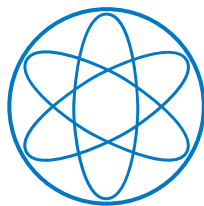# TECHNISCHE UNIVERSITÄT MÜNCHEN
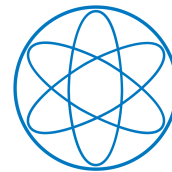
FAKULTÄT FÜR PHYSIK

On-Surface Synthesis of Covalent-Bonded Molecular Nanostructures: Reaction Strategies and Refined Control

Doctoral Dissertation

Nan Cao

TECHNISCHE UNIVERSITÄT MÜNCHEN

On-Surface Synthesis of Covalent-Bonded Molecular Nanostructures: Reaction Strategies and Refined Control

Nan Cao

Abstract

On-surface synthesis under ultra-high vacuum conditions is integral to the bottom-up approach to creating and characterizing molecule-based nanostructures. The controllable synthesis of novel conjugated covalent organic nanostructures is of particular interest for their application in nanoelectronic devices. With the development of nanoscale science, advanced analysis technologies facilitate the precise synthesis of functional organic nanostructures on surfaces. Indeed, scanning tunneling microscopy and non-contact atomic force microscopy - capable of atomic resolution and chemical bond-resolved imaging, can be exploited to investigate and determine the molecular structure on surfaces. X-ray photoelectron spectroscopy can be employed for assisting in the determination of the chemical structure of adsorbates, and density functional theory provides versatile means for modeling products and the reaction pathways underlying their formation.

In this thesis, using the on-surface synthesis strategy, we obtained different types of covalently connected molecular nanostructures based on the formation of different linkages. Firstly, we obtained conjugated enetriynes with high selectivity via tetramerization of alkynes on Ag(100) and trisubstituted aromatic derivatives on Au(111) through cyclotrimerization of alkynes. We used a precursor consisting of a biphenyl skeleton functionalized with alkynyl and hydroxyl groups at two para positions. For the formation of enetriyne, a two-step controlling strategy was applied to achieve high selectivity. Exposing O_2 to the well-ordered self-assembly structures facilitates the formation of organometallic dimers, then thermal annealing of the pretreated surface induces the formation of tetrameric enetriyne species. Comparative experiments and theoretical studies on this system demonstrate these excitations – gas-mediated pretreatment, thermal stimuli, and the suitable substrate are essential for the selective synthesis of the high-conjugated enetriyne. However, the cyclotrimerization of alkynes is prevailing on Au(111). By applying annealing steps at different temperatures, we achieved two regioselective trisubstituted aromatics and gained insights in selectivity.

Moreover, we present the synthesis of extended one-dimensional porphyrin nanostructures on Au(111) with alkyne-substituted porphyrins. The polymeric products form chains, as well as closed nanoring-like structures. We used porphyrins with alkyne substituents on two meso positions as precursors. Upon thermal annealing, in addition to intermolecular coupling – five-membered rings are formed through intramolecular cyclization reactions, and the products show a pronounced stereoselectivity towards *trans*-cyclized species. This behavior is explained in the framework of aromaticity and examined by theoretical calculations.

Finally, we demonstrate another conjugated porphyrin nanostructure synthesized from a benzaldehyde-substituted porphyrin monomer on Ag(111). The porphyrin nanostructure results from a McMurry-type reaction undertaken by the formyl groups. The obtained oligomers are connected through the vinylene (C=C) linkages, offering electron delocalization.

Contents

1. Introduction

Controllable construction of covalent nanostructures at the atomic level is a fascinating concept in nanotechnology. One requirement for the construction of molecular electronic and spintronic devices is to control the arrangements and connections between the molecular counterparts in a clean and atomically well-defined environment, [1, 2]. This has often been a great challenge for traditionally synthesized materials, particularly in the liquid phase. A promising strategy to overcome this challenge is to follow a bottom-up approach. This method is based on linking nano-sized building block units to create larger well-defined nanostructures with custom-designed properties. The characteristics of the synthesized materials can be tuned by variations of the building blocks, which gives a lot of flexibility to this approach. Bottom-up synthesis is often done at surfaces and interfaces, offering a two-dimensional environment. [3, 4] With the development of surface science as well as the advanced technologies, many tools and methodologies became available for the bottom-up construction and analysis of low-dimensional nanoarchitectures. [5]

Thus, in the past years, on-surface synthesis – i.e. designing and using bottom-up strategies towards covalently bonded molecular nanostructures – became more and more important and is now one of the most vibrant domains in surface science. [6, 7, 8, 9] A typical approach starts with a flat carrier (mostly a metal substrate) and deposition of a sub-monolayer of organic building blocks. Polymerization of the individual building blocks to larger nanostructures can then be induced by thermal annealing [6, 10], tip-manipulation [11, 12] or photo-irradiation [13, 14] of the submonolayer-covered substrate. These chemical reactions can be induced and investigated under highly controlled conditions, i.e. in ultra-high vacuum (UHV) environments and on single crystal substrates or 2D-sheet materials. Using this method, Grill and co-workers reported in 2007 for the first time on-surface in situ construction of porphyrin nanostructures. Porphyrin precursors with bromine substituents were coupled via thermally induced Ullmann-type coupling. [6] The chemical structure of the products could be controlled by tailoring the chemical structure of the building blocks, in particular by changing the positions of the active sites that then will link to neighboring molecules. This approach allows for a rational synthesis of various types of nanostructures on surfaces, with zero-dimensional (0D), one-dimensional (1D), and two-dimensional (2D) products.

One of the most famous 0D nanomaterials is the fullerene family, which was introduced to on-surface studies. For instance, Otero et al. reported the $C_{57}N_3$ triazafullerene formed after the cyclodehydrogenation process on Pt(111), and also demonstrated the catalytic effect of the platinum surface. [15] As a promising candidate for practical applications in digital electronics, 1D graphene nanoribbons (GNRs), [16, 17] were widely studied. Of particular interest are their electronic and transport properties. The first work from Cai et al. reported the fabrication of atomically precise graphene nanoribbons through debromination, C-C

coupling, and cyclodehydrogenation steps. [16] Since then, similar approaches have been widely used to synthesize GNRs in different morphologies. Additionally, various 2D covalent organic frameworks have been obtained with the strategy available in the field of on-surface synthesis. [18, 19, 20]

As yet, many on-surface reaction strategies were employed to build covalent linkages, including Ullmann coupling [21, 6, 22, 23, 24, 25, 26], Alkyne coupling [10, 27, 28], Schiff-base reaction, [29, 30, 31, 32] Bergman reaction [33, 34], Diels–Alder reaction, [35] aryl-aryl dehydrogenation, [36, 37, 38, 39] and boronic acid condensation, [18, 40, 41, 42]. Two aspects are essential for the successful construction of well-defined molecular nanostructures: practicable reaction strategies and efficient methods for reaction control. In particular, several factors need to be considered in the experiments, and these include the chemical and geometric design of the precursors, the chemical, physical and catalytic properties of the substrate, and the kinetic and thermodynamic parameters. These factors will critically affect the reaction pathways, selectivity, and yield of the respective reactions. Even though many molecular precursors are commercially available, it is in most cases desirable to use custom-design and deliberately synthesized molecular precursors as building blocks – often obtained in many iterations of precursor synthesis and on-surface synthesis. Of particular relevance are the chemical composition, functional groups, size/weight, symmetry and geometry, and mechanical properties. Such factors will critically affect the chemical reactivity and interaction with substrates and thus need to be considered when developing linking strategies. In this context, many functional groups are applied to tune molecular building blocks, such as carbene, [43, 44, 45] alkynyl, [10, 27, 34] alkenyl, [46, 35] halogen, [6, 16] carboxyl, [47, 14] formyl [48, 29] and acetyl groups, [19] etc..

In this thesis, we mainly focus on the synthesis of novel molecular nanostructures based on the formation of conjugated linkages, using the above mentioned reaction strategies and reaction control methodologies. More detailed motivations for each project will be given in the respective chapters.

Chapter 2 introduces the fundamental principles of the experimental methods used and techniques applied in this thesis. Scanning tunneling microscopy (STM) and non-contact atomic force microscopy (nc-AFM) is employed to image the surfaces. X-ray photoelectron spectroscopy (XPS) is utilized to investigate the chemical state of the molecules on surfaces. In addition, density functional theory (DFT) is applied to develop and study theoretical models describing the experiments. Furthermore, the last section of chapter 2 introduces the instruments and experimental setup for the studies.

The first project is presented in Chapter 3. We employed a precursor composed of a biphenyl skeleton functionalized with alkynyl and hydroxyl substituents. We developed a controllable approach toward the formation of enetriyne species with high selectivity on the Ag(100) surface. The enetriyne species were synthesized through the tetramerization of alkynes and aggregated into regular enetriyne arrangements. We notesly explored a multi-step synthesis strategy for the fabrication of enetriyne. Metal-organic Ag-bis-acetylide dimers can be first synthesized via O_2-mediation, which would aggregate into condensed assembly structures via the directing effect of dehydrogenated hydroxyl terminals, thus

avoiding homo-coupling that is otherwise preferred for terminal alkynes. These adjacent dimers serve as templates to facilitate the tetramerization reaction during the subsequent annealing treatment, forming a conjugated enetriyne core. The atomic structures and chemical states of intermediates and products were determined by a combination of STM, nc-AFM, and XPS measurements. The reaction mechanism for the two-step synthesis has been further elucidated by DFT calculations. In addition, we obtained trisubstituted aromatic derivatives with regioselectivity on Au(111) surface. Two species selectively dominate the molecular arrangements on the surface at different temperatures. The approach applied in this work introduces a novel approach for the selective construction of covalent linkages between functional organic units.

In Chapter 4, porphyrin was selected as the building block because of its potential optical and electronic properties, which can be fine-tuned by accommodating different metal centers. 1D porphyrin chains were synthesized via cyclization of alkynes and coupling reactions on Au(111). The aromaticity effects on the reactivity of alkyne-substituted free-base and Cu-metalated porphyrins were mainly investigated. We compared the reactivity of the aromatic versus olefinic carbon atoms at the β positions of the porphyrins. As these carbon atoms are in structurally equivalent environments, we can isolate the effect of aromaticity on the region-selectivity of the reactions from other parameters (such as steric effects). We found that the olefinic carbon atoms are more than five times more likely to participate in intramolecular cyclization reactions of the molecules. This behaviour is corroborated by extensive density functional theory calculations: The thermodynamic stability of the reaction products shows a direct correlation with the molecular aromaticity (quantified based on the bond length alteration along the aromatic pathways). Our results show that the aromaticity of porphyrins is preserved upon adsorption on the metal substrate and plays a major role in the on-surface reactivity of the molecules.

In Chapter 5, conjugated porphyrin oligomers were synthesized from the condensation of 4-benzaldehyde-substituted porphyrins on Ag(111). The formation of oligomers is based on the generation of C=C linkages, following a McMurry-type reaction scheme. The structural evolution and chemical transformation were thoroughly characterized. This approach provides a path for the on-surface synthesis of porphyrin-based oligomers coupled by C=C bridges – as a means to create functional conjugated nanostructures.

In the last, Chapter 6 summarizes the main achievements, the importance of the projects, and the implications of these results for future studies and exciting prospects are discussed.

2. Experimental Methods and Techniques

This chapter introduces the fundamental principles of the experimental methods and techniques applied during the presented studies. Scanning tunneling microscopy and non-contact atomic force microscopy were employed to image the surface-adsorbed molecules, whereas, X-ray photoelectron spectroscopy was used to investigate the chemical states of the molecules on surfaces. In addition, density functional theory was applied to study the theoretical models corresponding to the experiments.

2.1. Scanning tunneling microscopy (STM)

Scanning tunneling microscopy (STM) is a powerful technique for imaging surfaces and adsorbates with high spatial resolution. The first working STM was developed by Gerd Binning and Heinrich Rohrer at the IBM Zurich Research Laboratories, [49] for which they were awarded the Nobel Prize in physics in 1986.

STM is based on the tunneling effect (details are explained in section 2.1.1). [50] Due to this effect, a tunneling current starts to flow when a sharp metal tip moves close to a conductive surface. The electron wave functions of the atoms in the tip overlap with wave functions of the surface atom; when a voltage is applied, electrons can "tunnel" through the vacuum gap. The use of STM features the following advantages: (1) it has an atomic-level high resolution, i.e., commonly 1 Å in lateral and 0.1 Å vertical resolution or better; (2) STM can yield in-situ observations; (3) it works in a variety of environments (atmospheric pressure, under vacuum, in solution, and at various temperatures); In addition, combining with scanning tunneling spectroscopy, the electronic information of the material surface can also be obtained. The superior performance of STM makes it widely used in nanotechnology, material science, physical, chemical, and life sciences.

2.1.1. Basic principle of STM

The basic principle of STM is based on the quantum mechanical tunneling effect. In classical physics, a particle cannot penetrate through the potential barrier V_0 if its energy E is smaller than V_0. In quantum mechanics, however, there is a probability for a particle (electron in the case of the STM experiment) to overcome the energy barrier, even if the energy of the electron is lower than the potential barrier. We consider a particle with energy E tunneling through a rectangular potential barrier of height V_0 with width d, as presented in Figure 2.1.

There are three regions where the particle might be. In each region, the particle can be
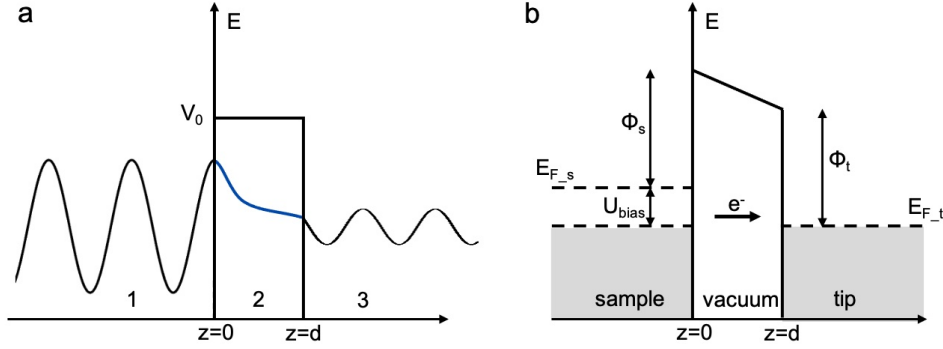
Figure 2.1.: Schematics of tunneling effect and STM tip-sample tunneling. (a) The electron wave function goes through the barrier V_0 from regions 1 to 3 with exponential decay of the wave function in the barrier. (b) STM tip-sample tunneling with a negative sample bias is applied. The applied bias alters the Fermi level alignment, allowing electron tunneling through the barrier. Without applying a bias, the electron tunneling probability is identical for both directions (positive and negative z), no current flows.

described by the Schrödinger equation:

$$-\frac{\hbar^2}{2m}\frac{d^2\Psi}{dz^2} + V(z)\Psi = E\Psi \tag{2.1}$$

where $\hbar$ is Planck constant divided by $2m$, and Ψ is the electron wave function solution of the Schrödinger equation. Considering a particle of mass m and energy $E < V_0$, as an incoming wave propagating in the positive z-direction (Figure 2.1, regions 1 to 3), the wave function solutions in different regions can be expressed by:

$$\Psi_{1,3} = e^{\pm ikz}, k = \frac{\sqrt{2mE}}{\hbar} \tag{2.2}$$

$$\Psi_2 = e^{-Kz}, K = \frac{\sqrt{2m(V_0 - E)}}{\hbar} \tag{2.3}$$

From the solutions of wave functions, the transmission probability T can be obtained:

$$T = \frac{16k^2K^2}{(k^2 + K^2)^2}e^{-2Kd} \tag{2.4}$$

The equation 2.4 shows that the transmission probability exponentially depends on the barrier width. This sensitivity of the electron tunneling on the barrier width is one of the main reasons that STM can achieve exceptionally high resolution.

In the case of STM, electron tunneling is between the sample and the tip. To describe the realistic tunneling current, an approach was developed by Bardeen, describing the tunneling

current produced in a metal-oxide-metal junction using the first-order time-dependent perturbation theory. [51] Later, Tersoff and Hamann extended this approach, [52] defining the following tunneling current:

$$I = \frac{2\pi e}{\hbar} \sum_{t,s} f(E_t) [1 - f(E_s + eU)] |M_{ts}|^2 \delta(E_t - E_s) \tag{2.5}$$

where $f(E)$ represents the Fermi function, U is the applied bias, M_{ts} is the tunneling matrix element, E_t and E_s are the energies of the wave functions of the tip (Ψ_t) and the sample (Ψ_s). The δ function describes the conversion of the energy in the case of elastic tunneling. To simplify this equation, the limits of small voltage and low temperature were considered, resulting in the following tunneling current:

$$I = \frac{2\pi}{\hbar} e^2 U \sum_{t,s} |M_{ts}|^2 \delta(E_s - E_F) \delta(E_t - E_F) \tag{2.6}$$

where E_F is the Fermi level. M_{ts} is the tunneling matrix element, which is defined as an integral over a surface, lying within the vacuum region separated by the tip and the sample. The tunneling matrix element is defined subsequently:

$$M_{ts} = -\frac{\hbar^2}{2m} \int_S \left(\Psi_t^* \overrightarrow{\nabla} \Psi_s - \Psi_s \overrightarrow{\nabla} \Psi_t^* \right) dS \tag{2.7}$$

From equation 2.7, it can be seen that the tunneling matrix element can be calculated only when the wave functions of the tip and the sample are known. It is difficult to determine the wave function of the tip due to the unknown shape, Tersoff and Hamann assumed the tip as a spherical shape, with a radius of R and the center position of $\overrightarrow{r_0}$. Now, assuming the identical work function Φ of tip and sample, the tunneling current can be expressed as:

$$I = \frac{32\pi^3 e^2 V \Phi^2 R^2 e^{2KR}}{\hbar K^4} D_t(E_F) \sum_s |\Psi_s(\overrightarrow{r_0})|^2 \delta(E_s - E_F) \tag{2.8}$$

In equation 2.8, D_t presents the density of states per unit volume of the tip. At the tip position of $\overrightarrow{r_0}$, the local density of state (LDOS) of the surface at E_F is:

$$\rho_s(\overrightarrow{r_0}, E_F) = \sum_s |\Psi_s(\overrightarrow{r_0})|^2 \delta(E_s - E_F) \tag{2.9}$$

In the direction perpendicular to the sample surface and oriented to the vacuum area, the surface wave function is:

$$\Psi_s(\overrightarrow{r_0}) \propto e^{-Kz}, z = d + R \tag{2.10}$$

where d is tip-sample distance. Therefore, the tunneling current shows exponential dependence on the tip-sample distance (see equations 2.8 and 2.10), and is also proportional to the LDOS (equation 2.8) of the surface. This means that STM measures the topographic and electronic information of the surface.
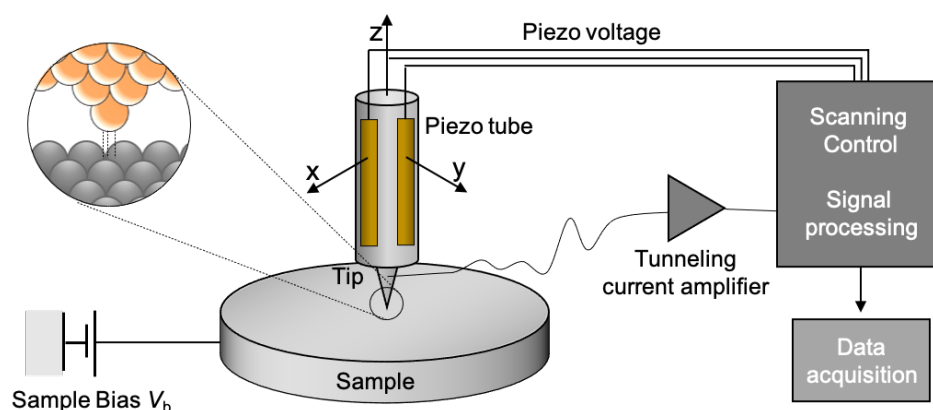
Figure 2.2.: Simplified working scheme of an STM. The piezo tube drives a tip moving above the sample surface. When the tip approaches very close to the sample and applies a voltage, the tunneling current flows between the tip and the sample.

2.1.2. STM imaging

Figure 2.2 shows a simplified working scheme of STM. Moving the tip very close to a sample surface, and applying a voltage between the tip and the sample, results in a tunneling current. The tip can be driven by the piezo tube and move in both lateral and vertical directions above the sample. When STM is working, the height of the sample or the tunneling current is recorded and serves as the signal for imaging.

There are two operation modes when STM imaging the surface, namely, constant height and constant current modes, as shown in Figure 2.3. In the constant height mode, the feedback loop is off and the z-position of the tip is kept constant, while the tunnel current is recorded as a function of the position $I_t(x,y)$. The variation of the tunneling current represents the changes in the tip-sample distance and electronic states. Therefore, the obtained image gives information about both the topography and local density of electronic states. However, this mode is not commonly used for large-scale and rough surface imaging because of the danger of crashing tips. In the constant current mode, the feedback loop controls the tip-sample distance in order to maintain the measured tunneling current constant. The z-position of the tip is recorded as a function of the position $z(x,y)$. Thus, the obtained image is related to the surface topography. This mode is more commonly used in STM measurements since the feedback loop can prevent the tip from crashing.

2.2. Atomic force microscopy (AFM)

In 1986, Binnig and his colleagues invented atomic force microscopy (AFM), [53] the invention of AFM enables atomic-precision real-space resolution for insulating samples. AFM measures the forces rather than the tunnel current and therefore applies equally to conductors and insulators.
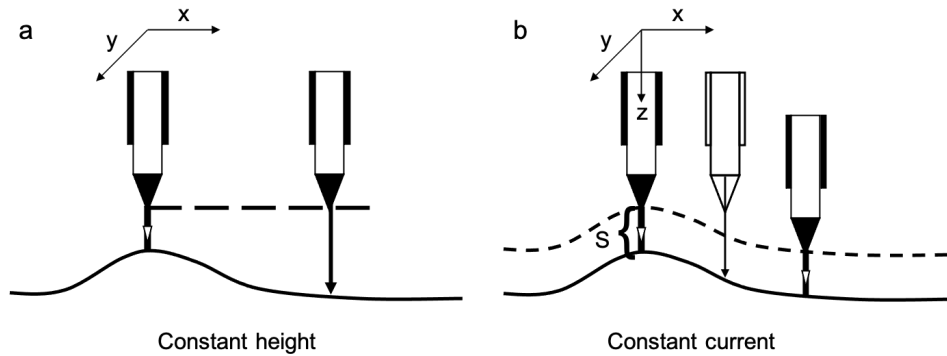
Figure 2.3.: Working modes of an STM. (a) In constant height mode, the feedback loop is off and the z-position of the tip is fixed; (b) In constant current mode, the current is fixed, and the feedback loop makes the tip height adjustable.

Since its invention, AFM has been extensively applied to investigate surface phenomena. In general, most AFM tools work under ambient conditions and in contact or tapping mode, in which the sensor makes physical contact with the sample. To maximize the resolution when imaging surfaces, it is advantageous to operate under very stable and clean conditions achieved by using cryogenic systems under ultrahigh vacuum. Imaging the surface can be non-destructive if mechanical contact between tip and sample is avoided, commonly referred as the non-contact AFM (nc-AFM).

In 1995, Giessibl, et al. successfully obtained atomically resolved images of the Si(111)-7 $\times$ 7 surface at room temperature using nc-AFM under frequency modulation. [54, 55] Meanwhile, Ueyama, et al. successfully achieved atomically resolved images of atomic vacancies on the cleaved InP(110) surface by nc-AFM [56], while Sugawara et al. observed the defect movement of atomic vacancies on the cleaved InP(110) surface. [57] Since then, nc-AFM has successfully demonstrated its ability to obtain atomic resolution using frequency modulation mode in an ultrahigh vacuum environment. [58]

2.2.1. Operation modes of AFM

AFM has two basic operation modes: the static mode – also called contact mode, and the dynamic mode or non-contact mode. In the static mode, the cantilever deflection $q = F_{ts}/k$ caused by the tip downforce is used as a feedback signal (F_{ts} is the force between the tip and the sample, k is the cantilever spring constant). When scanning the image, the tip is always in contact with the sample surface, thus both the tip and sample can be damaged. In dynamic mode, however, it is almost non-destructive, since the cantilever does not touch the surface. The cantilever oscillates around its resonant frequency f_0 driven by an external excitation.

There are two modulation methods in dynamic non-contact mode: amplitude modulation (AM) [59] and frequency modulation (FM). [60] In AM-AFM, the external excitation drives the cantilever to vibrate at a constant frequency slightly below its resonant frequency f_0 and with an initial amplitude A_0. When the tip approaches the sample surface, the amplitude A
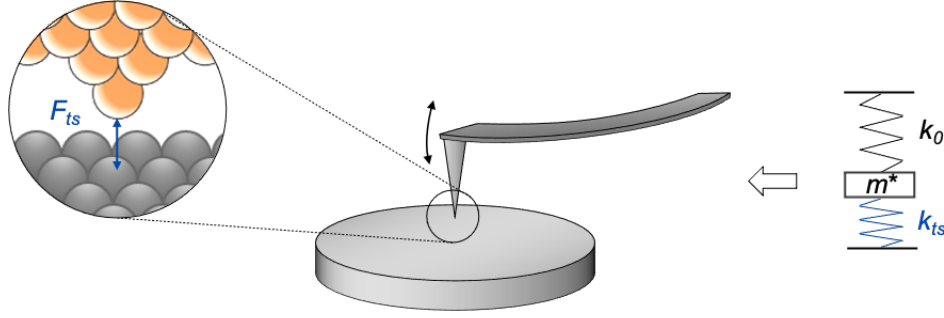
Figure 2.4.: Schematic of non-contact AFM. The cantilever with the attached tip is considered as an effective mass m^*, the mass connects to a base plate through a spring with its spring constant k_0. When the tip approaches the sample surface, the tip-sample force is considered as another spring with a spring constant k_{ts}.

changes with the variation of the tip-sample force. This change is used as the input signal in a feedback loop, and the feedback loop will modulate the tip height such that the amplitude still returns to A_0. The change in amplitude does not occur immediately with the change in tip-sample force but has a delay on a timescale of $T_{AM} \approx 2Q/f_0$. Thus AM mode is slow with high-quality (Q) factor cantilevers, which can reduce the noise. However, using high-Q cantilevers in FM mode makes the change in frequency shift settle on a timescale of $T_{FM}1/f_0$. [60]

In FM-AFM, on the contrary, the external excitation drives the cantilever to oscillate at its resonant frequency f_0 and a constant amplitude A. When the tip approaches the surface, the frequency f shifts with the variation of the tip-sample force. The frequency shifts $\Delta f = f - f_0$ are used as the input signal for the feedback loop. Using FM modulation, the imaging resolution can be greatly improved, and the atomic resolution was obtained by decreasing the tip-sample distance. The FM mode is now extensively used in non-contact AFM in ultra-high vacuum, and it has bond-resolve ability together with qPlus sensor and tip functionalization (details in section 2.2.4).

In this thesis, all the AFM measurements were carried out with FM-AFM mode based on the qPlus sensor, the tunneling current is integrated on the AFM probe, thus STM tunneling current and AFM frequency shift can be obtained concomitantly. The following mainly introduces the core parameters in the FM-AFM experiment: the relationship between the tip-sample force and the frequency shift, as well as the forces acting between the tip and the sample.

2.2.2. Frequency-modulation AFM

In FM-AFM, without the external force, the cantilever oscillates at a constant amplitude A and its resonant frequency f_0. In such a system, the vibration direction of the AFM tip is defined as being perpendicular to the sample. The movement of the tip can be expressed as $q(t) = A_0 cos(2\pi f_0 t)$. [61] The cantilever can be considered as a spring with a spring constant

of k_0, the tip attached on the cantilever as an effective mass m^*, as shown in Figure 2.4. The resonant frequency f_0 of the spring is:

$$f_0 = \frac{1}{2\pi}\sqrt{\frac{k_0}{m^*}} \tag{2.11}$$

When the tip approaches the sample surface, the tip-sample force F_{ts} can be treated as an additional spring with a spring constant of k_{ts}. When the oscillation amplitude is much smaller than the tip-sample distance, the effective spring constant of the whole system is approximated as [61]:

$$k^* = k_0 + k_{ts} = k_0 - \frac{\partial F_{ts}}{\partial z} \tag{2.12}$$

where $k_{ts} = \partial F_{ts}/\partial z$ represents the force gradient of the tip-sample force with respect to the vertical distance z. When the amplitude is small enough, the force gradient can be approximated as a constant, now the frequency shift Δf of the cantilever is [61]:

$$\Delta f = f - f_0 = \frac{1}{2\pi}\left(\sqrt{\frac{k^*}{m^*}} - \sqrt{\frac{k_0}{m^*}}\right) \approx -\frac{f_0}{2k_0}\frac{\partial F_{ts}}{\partial z} \tag{2.13}$$

Equation 2.13 shows that the frequency shift is proportional to the force gradient of the tip-sample force. This is only applicable when the oscillation amplitude is very small (< 0.1 nm). When using an arbitrary amplitude, the force gradient cannot be considered a constant. A more general expression can quantify the relationship between frequency shift and tip-sample force. [61, 62]

2.2.3. Tip-sample forces

In FM-AFM, the frequency shift is determined by the tip-sample force and as explained in the previous section, the relationship between the frequency shift value and the tip-sample distance is very complicated. In general, the frequency shift is determined by the total force – the sum of different types and strengths of forces. The major tip-sample forces include van der Waals forces, chemical forces, electrostatic forces, and magnetic forces. As the magnetic force was not implicated in this study, this effect will not be explained here.

Van der Waals force. The van der Waals (vdW) interaction is caused by fluctuations in the electric dipole moment of atoms and their mutual polarization. [58] The potential of this force between two atoms separated by z is expressed as:

$$E_{vdw}(z) \propto -\frac{1}{z^6} \tag{2.14}$$

In general, because of the large number of atoms at the tip and on the sample surface, the tip-sample vdW forces can be very large. The Hamaker formula gives a quantitative expression of the vdW forces. For a spherical tip with radius R next to a flat surface (z is the distance between the center of the tip atom and the center of the surface atom), the vdW force [63] is given by:

$$F_{vdw}(z) = -\frac{A_H R}{6z^2} \tag{2.15}$$

A_H is the Hamaker constant, depending on the type of materials of the tip and sample. The vdW force is long-ranged because it do not change significantly on the atomic scale. According to this equation, using a sharper tip can greatly reduce the van der Waals force.

Chemical force. When the tip-sample distance is very close, the electron wavefunctions of the atoms at the tip apex and the atoms of the surface overlap, and the chemical interactions dominate the total force (Figure 2.5). The chemical force can be either attractive or repulsive depending on the tip-sample distance z, the magnitude of which can be given semi-empirically by the Lennard-Jones (L-J) potential [64]:

$$E_{L-J}(z) = \epsilon \left[\left(\frac{z_m}{z} \right)^{12} - 2 \left(\frac{z_m}{z} \right)^6 \right] \tag{2.16}$$

Where ϵ is the binding energy at the equilibrium distance z_m, $(1/z)^{12}$ describes the repulsive force at a close distance due to the Pauli repulsion. The Pauli repulsion comes from the overlap of the electron wavefunctions of the atoms at the tip apex and the probed atoms of the surface. In this case, electrons tend to occupy higher-energy orbitals, thus generating repulsive forces. The other term $(1/z)^6$ describes the attractive force caused by the vdW interactions described above. The Lennard-Jones force (L-J-Force) can be derived from this potential:

$$F_{L-J}(z) = -\frac{\partial E_{L-J}(z)}{\partial z} = 12 \frac{\epsilon}{z_m} \left[\left(\frac{z_m}{z} \right)^{13} - \left(\frac{z_m}{z} \right)^7 \right] \tag{2.17}$$
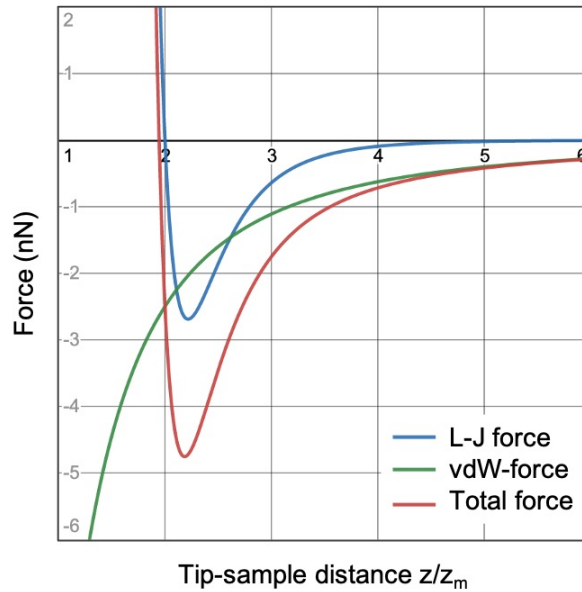

Figure 2.5.: Tip-sample forces in FM-AFM. Lennard-Jones force (blue), van der Waals force (green), and total force (red) as a function of the tip-sample distance z/z_m. Parameters used for plotting: ϵ = 2.0 eV, z_m = 2 Å, A_H = 3.0 eV, R = 2 nm.

Electrostatic force. When the tip and sample are conductive and have different electrostatic potentials (work functions), the electrostatic interaction arises. The electrostatic potential

difference results in a capacitor with a capacity $C(z)$ between the tip and the sample, the magnitude of which varies with the tip-sample distance. The electrostatic force between them is:

$$F_{el}(z) = \frac{1}{2}\frac{\partial C}{\partial z}(V - V_{CPD})^2 \tag{2.18}$$

Where V is the applied bias, V_{CPD} is the contact potential difference (CPD) between the tip and sample. Since this force is long-ranged and attractive and the AFM measurement here was done at a constant bias of zero, the electrostatic force did not play a dominant role in the tip-sample force compared to the chemical forces. However, the electrostatic force produced from the charged molecules on the surface can induce distortions in bond-resolved AFM images.

Total force. The total force is the sum of the effective forces acting between the tip and sample, i.e, the long-range vdW force and the short-range repulsive force.

The green curve (vdW-force) in Figure 2.5 shows the trend of van der Waals forces as calculated using Hamaker's formula, the functions of the Lennard-Jones force (blue curve, L-J force) and the sum of them (red curve, total force) as a function of the distance. Note that van der Waals forces dominate the sum force when the tip-sample distance is large, while chemical forces dominate the sum force when the tip-sample distance is small. Therefore, nc-AFM imaging can be performed at a close tip-sample distance, i.e., in the short-range repulsive interaction region, to obtain high-resolution molecular and chemical bond information.

2.2.4. High-resolution imaging

qPlus sensor. Traditionally, AFM uses silicon microcantilevers, because of the advantages of high-Q factor and photolithography fabrication. But there are limitations, such as the small size of silicon cantilevers making them difficult to customize and functionalize the AFM probe. In addition, in nc-AFM, a large amplitude is used to avoid sudden tip contact with the surface due to the low stiffness of the silicon cantilever. However, short-range forces operate in the sub-nanometer range, and the large amplitude means these forces cannot easily be isolated from long-range forces.

In 1996, Giessibl invented the qPlus sensor, [54, 65] which was made from a quartz tuning fork. As can be seen in Figure 2.6, the tuning fork is glued to the ceramic base with one side fixed, and a tip is glued to the free prong. The deflection signal is generated by the piezoelectric effect and can be read from the two electrodes attached to the tuning fork. The use of a qPlus sensor can greatly improve the performance of nc-AFM. Other than the high-Q factor and the micromachining techniques, qPlus sensors afford superior properties compared to the silicon cantilever: (1) The higher stiffness, [61] which endures higher forces before the jump to contact with the surface. The higher stiffness enables a smaller oscillation amplitude, such that measurements can be operated in the repulsive force region to achieve high-resolution images. (2) Self-sensing via the piezoelectric effect is applicable for low-temperature operation [66, 67]. (3) The thermal stability minimize the influence to the oscillation frequency [67, 68].
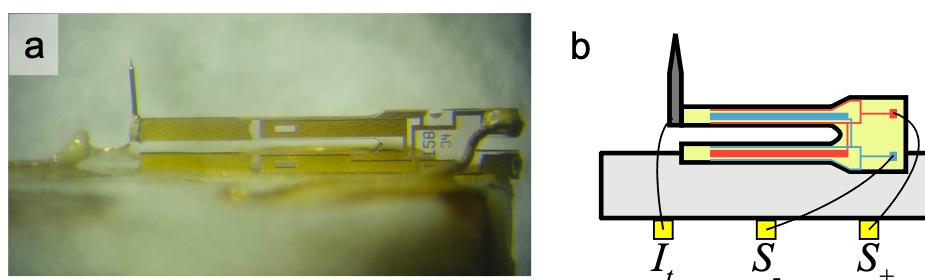
Figure 2.6.: qPlus sensor. (a) A picture of a qPlus sensor. A Tunning fork is mounted on the base plate. (b) Schematic diagram of qPlus sensor. The red and blue areas represent the two gold electrodes on the quartz tuning fork. (StirlingJulian, CC BY-SA 3.0 <https://creativecommons/org/licenses/by-sa/3.0>, via Wikimedia Commons)
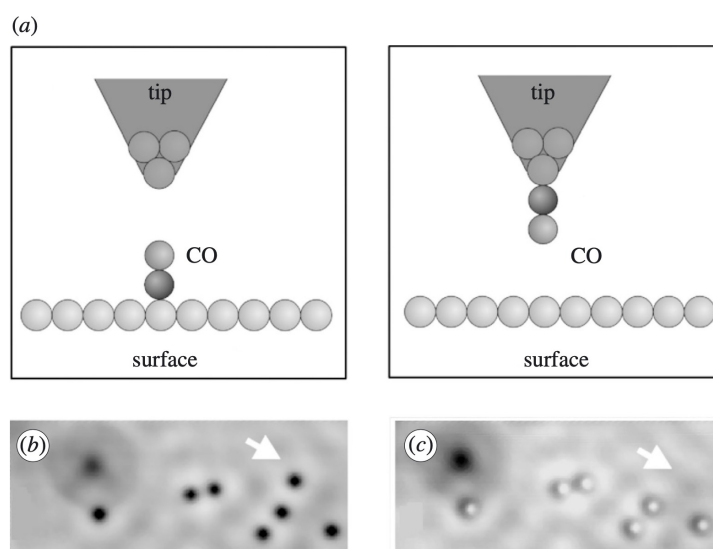

Figure 2.7.: STM tip functionalized with a CO. (a) Schematic of STM tip picking up a CO molecule by vertical manipulation from the surface to the tip apex. (b) and (c) STM images obtained with the tip before and after modified with a CO. Note that the image of the oxygen atom in the upper left corner is unaffected. The white arrow points to the CO molecule which was transferred intentionally to the tip. [69]

Tip functionalization. Modifying the tip with a single molecule or atom can significantly improve image contrast for both STM and AFM. There are different molecules or atoms reported for functionalization, including carbon monoxide (CO) [70, 71], Xenon (Xe) atoms, [72] Bromine (Br) atoms [73] and Chlorine (Cl) atoms. [70] CO is the most commonly used species for tip functionalization. The properties of the tip can affect the tip functionalization and greatly affect the image contrast and resolution of the image.

Functionalization of an AFM tip is realized by picking up a molecule or an atom (such as CO) via vertical manipulation, e.g., placing the tip over a CO molecule and applying a constant voltage in the direction of the tip to excite CO molecules to jump to the tip. [74] Figure 2.7a describes the tip picking up a CO molecule. The CO molecules appear as depressions in the constant-current image obtained with a metal tip (Figure 2.7b). The CO molecule indicated with a white arrow was picked up by vertical manipulation and the same area was imaged again with the CO modified tip. CO molecules show a bright spot in the center of the dark depression in the STM image (Figure 2.7c), whereas a single oxygen atom in the upper left corner of the images is always imaged as a depression. [74, 69] It is obvious that functionalization of the tip with different molecules may lead to chemical contrast, improving the image resolution.
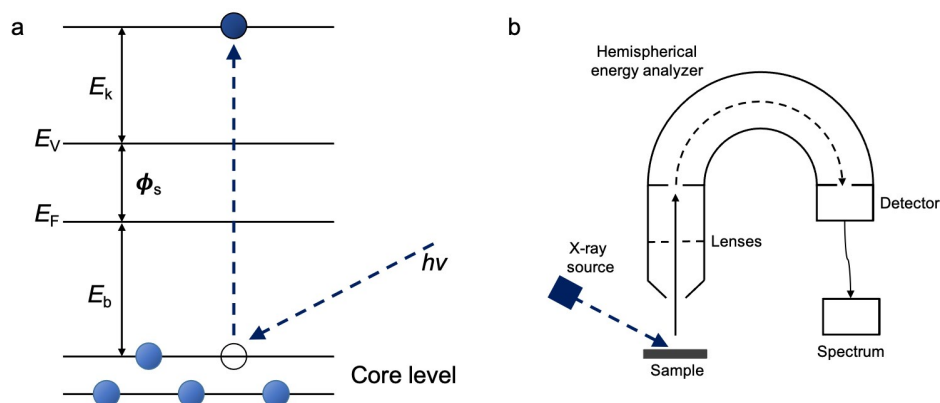

Figure 2.8.: Schematic illustration photoemission process and the energy analyzer setup. (a) A core-level electron is excited by an incident photon with energy $h\nu$. (b) The emitted photoelectron passes through the lenses, is collected by an energy analyzer, and is detected by the detector.

2.3. X-ray photoelectron spectroscopy (XPS)

X-ray photoelectron spectroscopy (XPS) is a surface-sensitive technique for identifying the elemental composition and the chemical state of the solid material. It is an essential method used throughout this thesis.

The physical concept behind XPS is based on the photoelectric effect, which was first explained by Albert Einstein. [75] An incoming photon with the energy $h\nu$ is absorbed by a

material (Figure 2.8), the photon energy is transferred to an electron and this electron can be emitted from the material into the vacuum. The kinetic energy of this photon-emitted electron is:

$$E_{kin} = h\nu - E_b - \phi_s \tag{2.19}$$

Here E_b is the binding energy of the atomic orbital from which the electron originates (with respect to the Fermi level), ϕ_s is the work function of the material, and represents the minimum energy required to emit an electron from the material; it can be seen as an energy barrier that electrons need to overcome in order to escape from the surface into the vacuum. From equation 2.19, the photon energy must at least exceed the sum of E_b and the ϕ for the electron to be excited. In standard XPS, the relatively high photon energy (typically in the range between 100 to 2000 eV) is used to probe core-level electrons, and the ejected electron is detected by the analyzer.

In XPS, monochromatic X-rays are usually used, which can be Mg $K\alpha$ (1253.6 eV), Al $K\alpha$ (1486.6 eV) X-rays, or synchrotron radiation. Using relatively high photon energy, the X-ray photons can penetrate the material to depths in the order of 1-10 μm; the detected electrons, however, only originate from the topmost atomic layers, due to the inelastic mean free path of electrons in solids which varies between 5 and 30 Å, depending on the material. [76] This makes XPS highly surface sensitivity.

Core level binding energies are different for each chemical element, photoemission spectra can serve as "fingerprints" of the respective elements. The relative abundance of each chemical composition can be quantified by the peak intensity. [77] This affords XPS the elemental sensitivity, which is very useful for determining the composition of an unknown sample.

XPS possesses the ability to identify the chemical states of elements. For a given element, the E_b of the element depends on the local chemical environment of the atoms. In particular, chemical shifts may occur when the same element is present in one species at nonequivalent positions, i.e, different oxidation states. In general, photoelectrons excited from atoms in a higher positive oxidation state have higher binding energy, because of the increased Coulomb interaction with the ion core upon withdrawal of valence charge due to chemical bonding. The binding energy shift is often used to determine oxidation states and to gain insight into the nature of the chemical bond formed by the atoms. Such a chemical state specificity is one of the major strengths of XPS for application in chemistry, surface physics, and materials research.

2.4. Density functional theory (DFT)

Basics. Density functional theory (DFT) is a quantum mechanical modeling method to study the electronic structure of multi-body systems by using electron density rather than single electrons. In practice, DFT simplifies the intractable problem involving electron-electron interaction into a non-interaction problem through various approximations, then puts all errors into a separate item, and analyzes this error.

Classical methods of electronic structure theory, especially the Hartree-Fock methods, are based on complex multi-electron wave functions. [78] The main goal of DFT is to replace the

wave function with the functional of electron density. As the multi-electron wavefunction has 3N spatial variables (N is the number of electrons, and each electron contains three spatial variables), whereas the functional of electron density contains only 3 variables. This reduction is more important for the larger system consisting of many atoms (complex molecules and condensed matter).

Although the concept of DFT originated from the Thomas-Fermi model, [79] there was no solid theoretical basis until the formulation of the Hohenberg-Kohn theorem (HK). [80] The HK theorems were originally only applicable to the ground state in which no magnetic field exists, although it has now been generalized to include these. The first HK theorem states that for an external potential $v(r)$, the ground state energy of a many-electron system is determined by the electron density $n(r)$. The second HK theorem defines an energy functional for the system and proves that the ground state electron density minimizes the energy functional:

$$E[n(r)] = \int v(r)n(r)dr + F[n(r)] \tag{2.20}$$

$F[n(r)]$ includes the kinetic energy, the Coulomb interaction, and exchange-correlation (XC) functional. The original HK theorem does not provide the specific expression of these parameters. Walter Kohn and Lu Jeu Sham further developed the HK theorems, [81] whereby, the many-electron problem (due to the interaction of electrons in an external electrostatic potential) is reduced to a problem of non-interacting electrons moving in an effective potential. The total energy of a system as defined by the Kohn-Sham method is described as:

$$E(n) = T_s(n) + \frac{e^2}{2} \int dr \int r' \frac{n(r)n(r)'}{|r - r'|} + \int V(r)n(r)dr + E_{XC}(n) \tag{2.21}$$

The first term of this definition pertains to the kinetic energy of non-interacting electrons, the second term is the external potential, the third term gives the electrons Coulomb energy, and the last term is the XC energy. The first three terms can be determined accurately, but the XC energy needs to be approximated. [81, 82]

Treating van der Waals forces. DFT is currently the leading method for electronic structure calculations in the field of surface science. Although DFT has been improved, it is still difficult to describe the van der Waals (vdW) forces. The vdW force arises from the electrostatic interactions and is important for describing the weak interactions between atoms or molecules. Different vdW density functional methods have been developed, two main methods are the dispersion-corrected DFT proposed by Grimme et al, based on semi-empirical corrections; [83, 84] and the van der Waals density functional (vdWDF) method proposed by Dion et al., introducing a non-local density functional. [85, 86]

Reaction mechanism calculations. The transition state theory is the most widely used approach to study the reaction pathways of reactions related to on-surface synthesis. This theory assumes that a reaction can be characterized by an initial state (**IS**), a transition state (**TS**), and a final state (**FS**), and the transition state has the maximal energy along the reaction path. The rate of passing the transition state is explained by the Arrhenius equation. The initial and final states are local minima on the potential energy surface, which can be

obtained by structural optimization, while specific methods are required for characterizing the transition state. The most commonly used methods to calculate the transition state are Nudged Elastic Band (NEB), the Climbing Image Nudged Elastic Band (CI-NEB), and the dimer method. [87, 88, 89]

In the NEB method, several images are interpolated between the **IS** and **FS**, and the reaction path is then found by minimizing the forces acting perpendicular to the tangents of the path (nudging). The spring forces are added between images along the path to maintain equal distances between neighboring images along the band (elastic bands). Although the NEB method can guarantee that the elastic band roughly falls on the path with the lowest energy, it is difficult to ensure that the image with the highest energy is precisely the **TS**. The CI-NEB method is a minor modification to the NEB method in which the highest energy image is driven up to the saddle point (**TS**). [89]

The combination of NEB and CI-NEB methods results in reliable approximations of the minimum-energy path, and provides a good initial guess for the reaction pathways. Since these methods usually employ several images (states) and converge slowly to the minimum-path energy, more efficient approaches are needed to calculate the transition state. These include the dimer method, one of the minimum-mode following methods, which is an efficient way of finding transition states. [87] The dimer method focuses on optimizing the transition state using three images: the central image and the dimer image consisting of two images. The dimer image can rotate and translate; thus, finding the transition state becomes a two-step optimization process. In the first step, the distance between the dimer and the central image is fixed, and the vector defined by the dimer is rotated into the lowest curvature mode of the potential energy at the central image. Then, the dimer and the central image are translated with a specific step, moving the central image to the highest energy position (**TS**). The position of the transition state can be determined by constant iterations through the two-step optimizations, until the forces on the central image are converged and the curvature of the potential energy at the central image is negative.

For the calculation of the reaction mechanism in the field of on-surface synthesis, the dimer method is usually used to refine the transition state based on the initial estimation of the reaction path obtained by NEB and CI-NEB.

2.5. Instrumentation

The instruments used for the experiments are available in TUM Physics Department (E20 labs) in Garching. The instrument techniques, sample preparation, and data analysis methods will be introduced.

2.5.1. Low temperature STM/AFM (LT-STM/AFM)

A contamination-free environment is a prerequisite for preparing a clean sample, especially for surface studies. In this thesis, all experiments were carried out in ultra-high vacuum (UHV) chambers. Most measurements were performed with a commercial LT-STM/AFM

instrument (CreaTec). Figure 2.9 gives a schematic diagram of the instrument, which mainly comprises three chambers (load-lock chamber, preparation chamber, and SPM chamber) separated by gate valves. The load-lock chamber is for loading samples or tips into the vacuum chamber, the preparation chamber is where the samples are stored and prepared, and the SPM chamber is where the measurements are performed. Between chambers, samples can be transferred with a manipulator, one of the supporting apparatuses of the instrument. In addition, there are pumps, a cryostat, as well as damping legs to maintain the regular operation of the instrument.
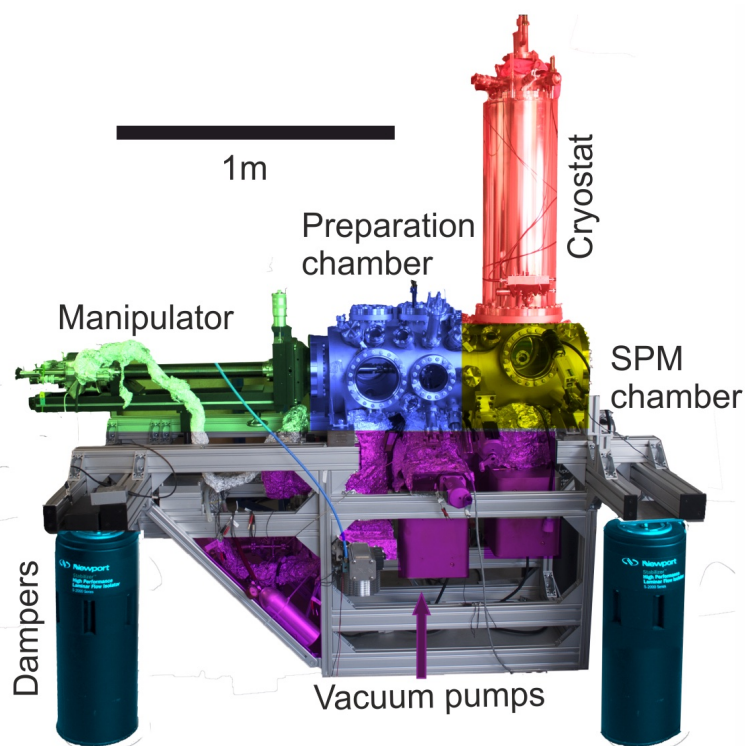

Figure 2.9.: Schematic diagram of the LT-STM/AFM setup (Adapted from [90]). Different components of the instrument are highlighted with colors. The load-lock chamber is mobile, not shown here but can be mounted on the preparation chamber.

Pumping system. The LT-STM/AFM setup maintains UHV through the use of a series of pumps connected to the preparation chamber; a roughing pump, turbo pumps, ion pumps, and a titanium sublimation pump (TSP). With different working principles, the base pressure can be lowered to $\leq 5^{-10} mbar$. A roughing pump and two turbo pumps are used in series to obtain a high vacuum in the order of $10^{-10} mbar$. Then with the ion pump working, the pressure can be reduced continuously and, more importantly, preserve this pressure in case the mechanical pumps need to be shut down for sensitive measurements. The TSP is also used occasionally to improve the pressure by trapping the small molecules which get bound to titanium evaporated from the heated filament. The high vacuum is monitored by ion

gauges. In addition, the preparation chamber is equipped with a cooling trap, which can be filled temporarily with liquid nitrogen, in order to minimize the pressure during sample preparation. For routine maintenance of the UHV, the roughing pump and turbo pumps are running continuously. Finally, in case the gate valve closes, a second ion pump is connected to the SPM chamber to keep the UHV.

Cooling and damping system. Atomic-scale imaging is performed at low temperatures for high resolution and low thermal drift. This low temperature is achieved using a cryostat setup; a schematic diagram of which is shown in Figure 2.10. The core components are the inner liquid helium (LHe) dewar and the outer liquid nitrogen (LN_2) dewar. The two dewars are separated by high vacuum insulation, to block heat convection. The scanner is fixed directly under the LHe dewar, connected by a thermal conductor which facilitates the cooling of the scanner. Additionally, the scanner is covered by two-layer shielding, LHe and LN_2 shields, each connected to the respective dewar, to block the external thermal radiation. With these cooling setups, the LT-STM/AFM typically works under a low temperature of ≈ 5 *K*.

The noise during imaging is commonly caused by external vibrations. To minimize external vibration, the instrument is mounted on four damping legs. The entire setup will be floating on these damping legs during the measurements. Equally, the cryostat can also induce vibrations. The gasification of LHe and LN_2 produces noise at a frequency of 500 to 800 *Hz* due to the outlet of the dewars directly connected to the atmosphere. To reduce this noise, the scanner is suspended by springs and equipped with eddy current damping. In addition, the whole instrument is grounded to isolate the electrical noise. These operations ensure that the measurements run in a highly stable environment.

Scanning system. The core parts of the scanning include a scanner (Figure 2.11), a qPlus sensor (Figure 2.6) and Nanonis controllers. The scanner is the core for all STM/AFM instruments, and its performance and noise level directly affect the imaging quality. The status of the controller, circuit noise level, etc. can also significantly affect the image quality. In general, before the measurements, it's necessary to achieve a stable status for both hardware and software of the instrument.

For STM measurements, a sharp metal tip is required. The material for making tips is platinum-iridium (Pt-Ir) or tungsten. The Pt-Ir tip is produced either by cutting platinum-iridium wire (diameter is 0.25 *mm*) or purchased commercially. The alternative is the tungsten tip, made by electrochemically etching tungsten wire (diameter is 0.25 *mm*). [92] The tungsten tip was selected as it performs better experimentally.

For nc-AFM measurement, the qPlus senor invented by Giessibl in 1995, [54, 65] is the most important unit. As shown in Figure 2.11, the tuning fork is glued to the ceramic base with one side fixed, and a tip (usually a tungsten tip) is glued to the free prong. The deflection signal is generated by the piezoelectric effect and can be read from the two electrodes of the tuning fork. Since the tungsten tip is conductive, the sensor can be used for combined STM/AFM measurements. In this thesis, a commercial qPlus sensor (CreaTec) was used for the nc-AFM measurements.
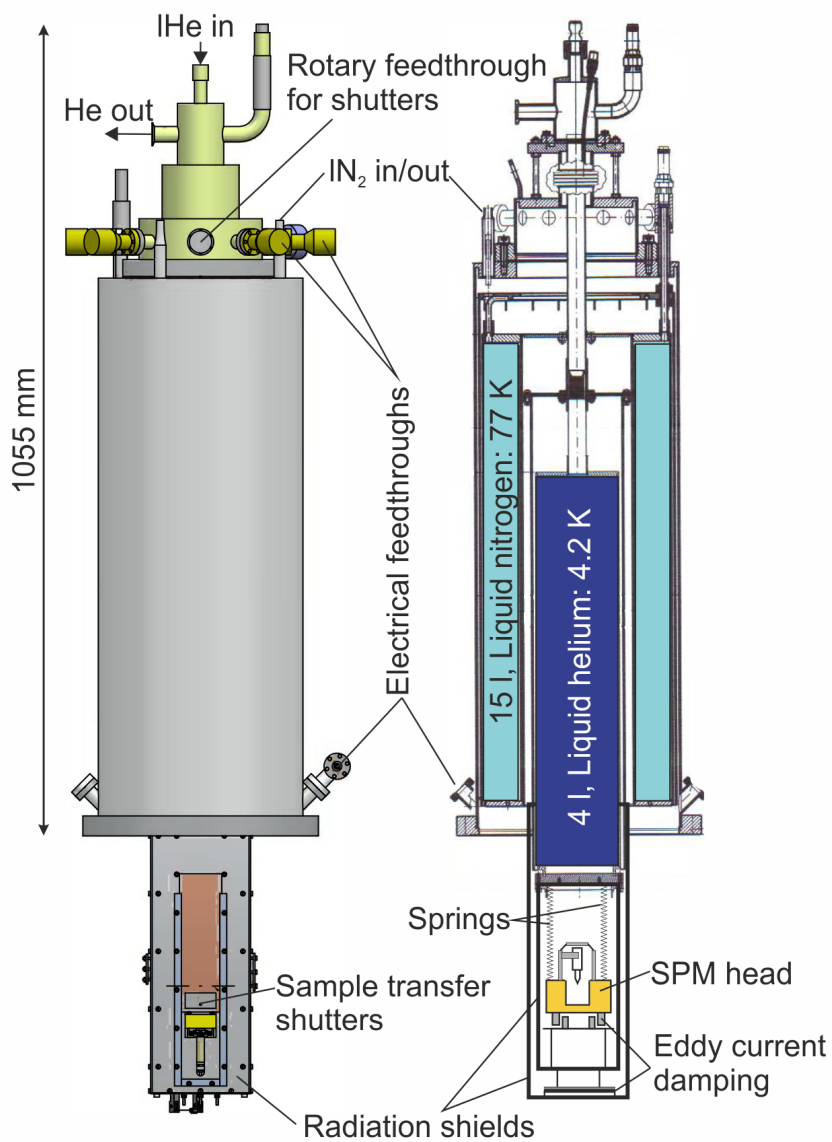
Figure 2.10.: Schematic diagram of the cryostat (The picture adapted from [91]. The dark blue region (the inner Dewar) is filled with LHe, and the light blue area (the outer Dewar) is filled with LN_2.
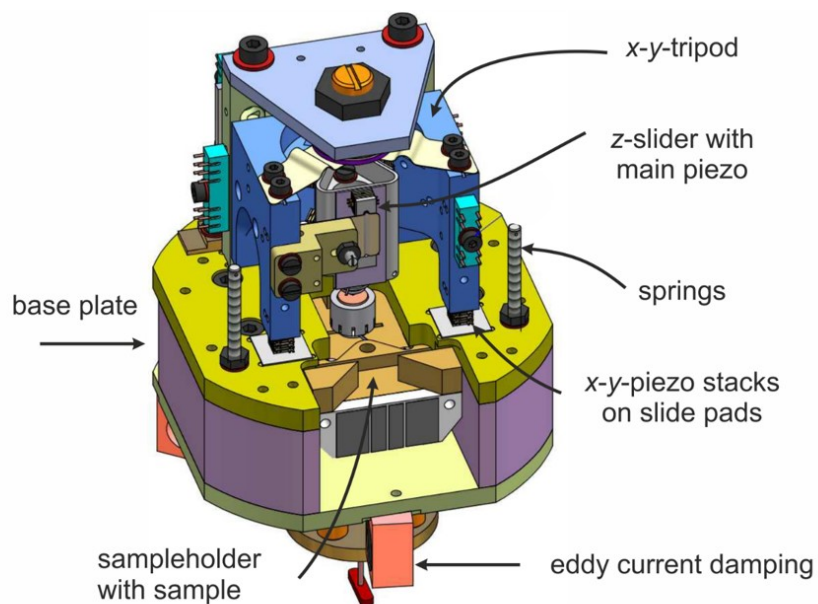
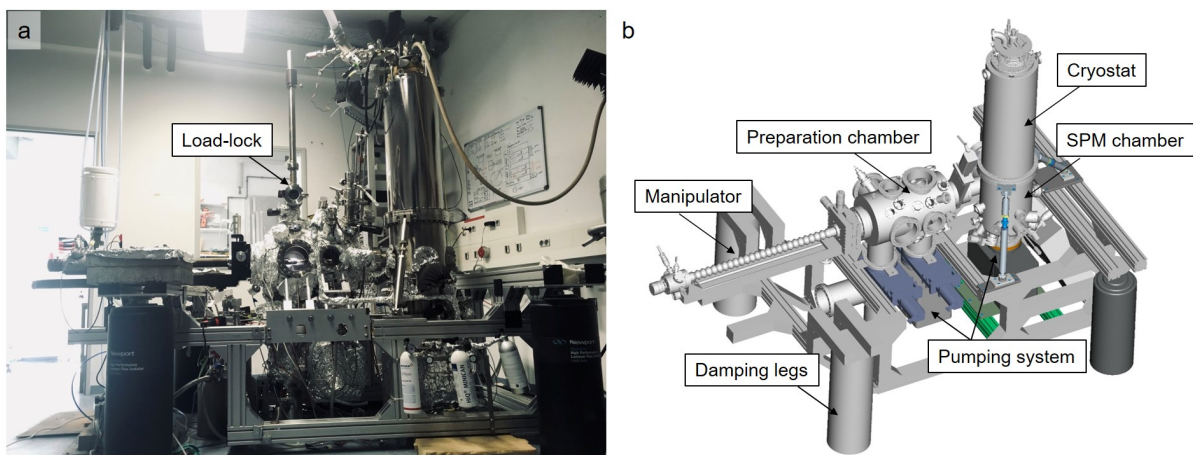Figure 2.11.: A schematic diagram of the STM scanner (Adapted from [93]).

Figure 2.12.: JT-STM setup and its Schematic diagram. The components of the instrument were indicated in the image.

2.5.2. Joule-Thomson STM (JT-STM)

Some of the STM measurements in this thesis were conducted in a commercial JT-STM system (Figure 2.12). This system comprises three main components: the cryostat, the JT cooler, and the actual STM. The pumping, cooling, and damping equipment of JT-STM are very similar to the LT-STM/AFM instrument. The main differences are in the STM scanner and sample holder, as illustrated in Figure 2.14. In the JT-STM system, the scanner is placed inside the JT shield. The crystal is mounted between two molybdenum plates, and the sample is facing down, above the tip in the scanner. The JT-cooler is the feature of this system, which can bring the temperature to $\approx 1.2\ K$, which is required for specific measurements (such as spectroscopic measurements).
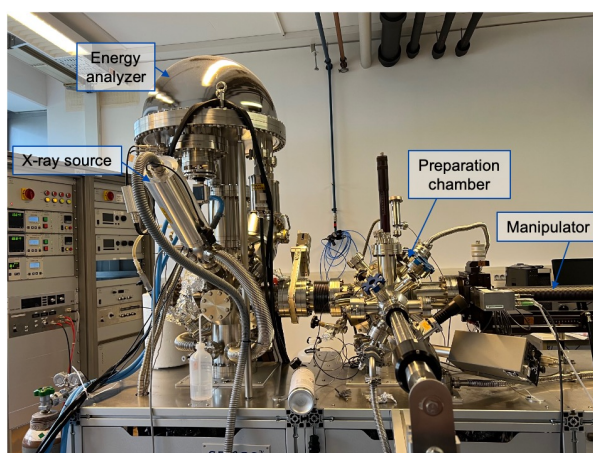

Figure 2.13.: Picture of the XPS set-up used for the XPS measurements in this thesis.

2.5.3. SPECS – XPS

Figure 2.13 is a picture of the actual instrument used for the XPS measurements in this thesis. This is a SPECS GmbH UHV system (base pressure of 3×10^{-10} mbar), including a PHOIBOS 150 hemispherical analyzer, and an XR50 X-ray source providing monochromatic Al and Mg Kα radiation. The instrument comprises three chambers, a load-lock chamber, a preparation chamber, and an analysis chamber. The analyzer is mounted on the analysis chamber. The sample can be transferred with a load-lock chamber from the atmosphere to the UHV chamber or prepared in the preparation chamber. Before the examination, the sample needs to be transferred to the analysis chamber using a manipulator.

2.5.4. Sample preparation

All sample preparations follow a similar procedure. First, the substrate surfaces are cleaned in UHV chamber, then organic chemicals are deposited onto the substrate by an organic molecular beam epitaxy (OMBE) method. The details are explained in the following.

The substrates used in this thesis are Ag(100), Ag(111), and Au(111) single crystals. The sample preparation is performed in the preparation chamber. The single crystals are mounted on the sample holder (Figure 2.14), and the crystal surface is cleaned by means of repeated argon ion sputtering and thermal annealing cycles. For sputtering, an ion gun is used to generate the electron beam with 10 mA emission current under ($\sim$ 1 kV) high voltage condition. Then the dosed Argon gas is ionized and accelerated to bombard the metal surfaces. Applying an Argon pressure of $1.5e^{-5}$mbar, typically produces an ion current of $\sim$ 5 uA. The bombardment of the surface with the argon ion efficiently removes the contaminants, but also causes a rough surface. The subsequent annealing is needed to obtain a well-defined surface and to remove residual species (argon atoms). The annealing temperature depends on the single crystal (below the melting point). In our case, annealing temperatures are 700 - 720 K for both Ag(100) and Ag(111), and 670 K for Au(111). After these cleaning procedures, the surface is ready for chemical deposition.
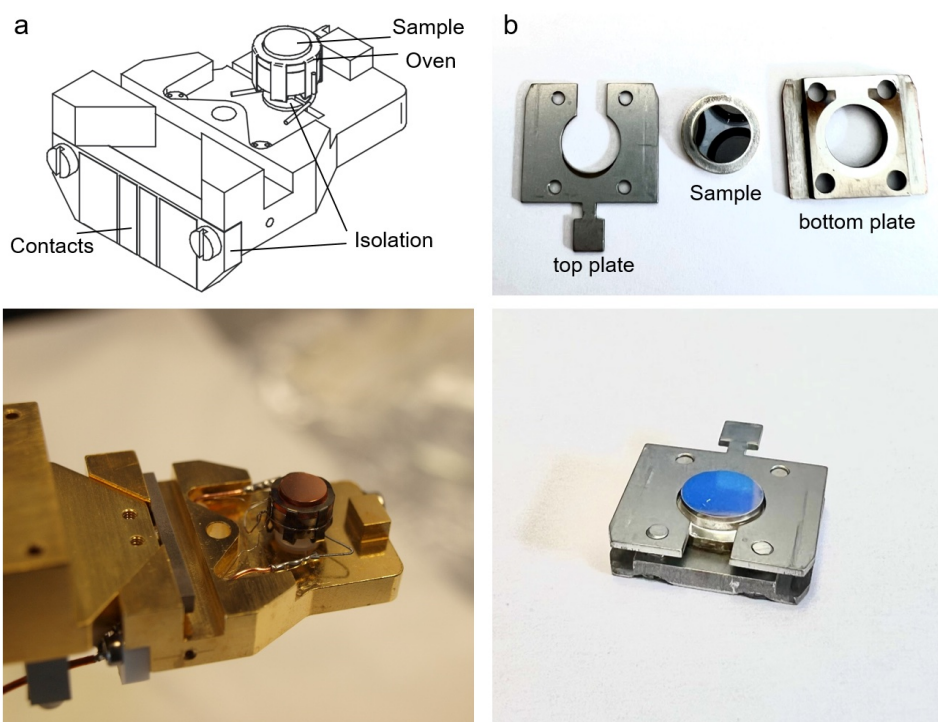

Figure 2.14.: Images of the sample holder used in LT-STM/AFM (a); (b) used in JT-STM and XPS.

Chemical compounds are deposited from a quartz crucible at their sublimation temperatures. Figure 2.15 shows the chemical structures of all used precursors. (5,10,15,20-tetrakis(4-formylphenyl)porphyrin (H$_2$TFPP) was synthesized according to a published procedure from 5,10,15,20-tetrakis(4-bromophenyl)porphyrin via a bromine-lithium exchange reaction [94] and was deposited at a sublimation temperature of 665 K. The compounds 5,15-bis((trimethylsilyl)ethynylporphyrin (**1a**) and (5,15-bis(trimethylsilyl)ethynylporphyrinato)

copper(ii) (**1b**) were synthesized according to literature process [95, 96] and proper purify operations and were deposited onto Au(111) substrate at 520 K and 550 K, respectively. The 4'-Ethynyl-[1,1'-biphenyl]-4-ol (EHBP) was purchased from TCI, and was deposited at 330 K onto the Ag(100) substrate. The deposition time was appropriately controlled to obtain a submonolayer.

In Chapter 4, to investigate reaction kinetics, we used different heating programs: (i) heating directly to 305 °C at a rate of 170 °C min^{-1}, (ii) heating directly to 305 °C at a rate of 30 °C min^{-1}, (iii) stepwise heating to 305 °C (200 °C to 245 °C for 10 min, 245 °C for 10 min, 245 °C to 275 °C for 10 min, 275 °C for 10 min and 275 °C to 305 °C for 10 min), (iv) stepwise heating to 305 °C (180 °C for 10 min, 205 °C for 40 min, and 225 °C, 245 °C, 275 °C and 305 °C for 10 min at each temperature). The average temperature ramp (as plotted in Figure 4.17) was calculated for temperatures above 100 °C.
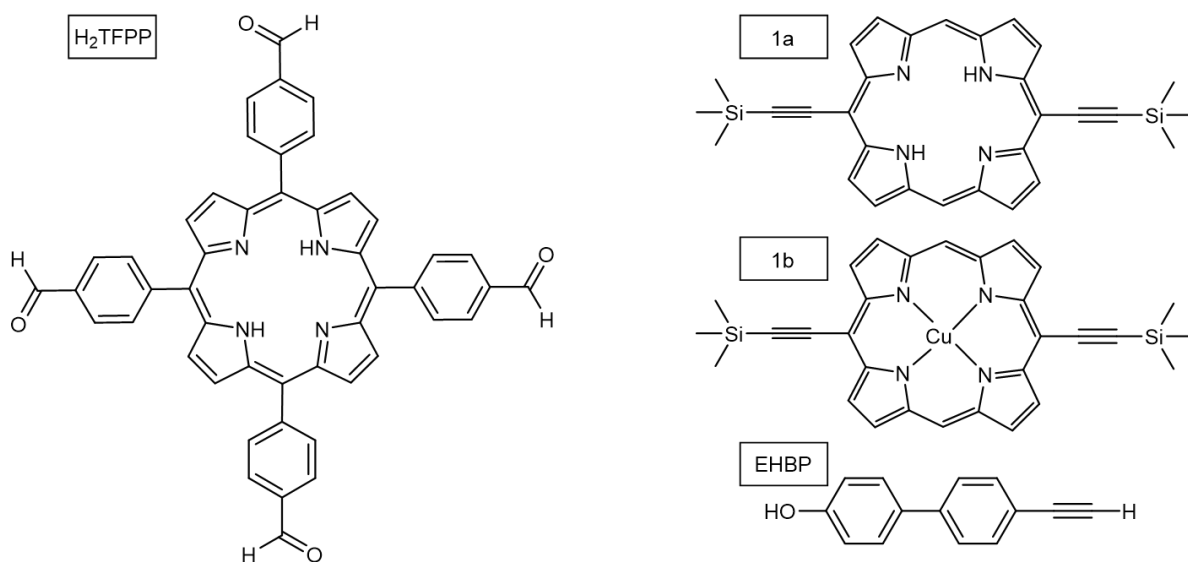

Figure 2.15.: Chemical structures of the molecules studied in this thesis.

2.5.5. Data acquisition and analysis

STM and AFM data. All STM images were taken using the constant current mode, and the bias voltage was applied to the sample. All AFM images were acquired at constant heights and V_s = 0 V using a qPlus tuning fork sensor [97] (resonance frequency ≈ 31 KHz, oscillation amplitude 60-80 pm, Q value > 100000, stiffness k ≈ 1800 Nm^{-1}) operated in frequency modulation mode. The measurements were performed with CO-terminated tips, [70, 74] obtained by vertical manipulation of adsorbed CO molecules that were deposited onto the substrate at T < 10 K. The scanning parameters (tunneling current I_t and sample bias V_s) are given in the respective figure captions. The data were analyzed using WSXM [98] and SpmImage Tycoon. [99]

XPS data. All XPS measurements were performed using the SPECS GmbH UHV system

described above. The monochromatic Al Kα radiation (hv = 1486.71 eV) was selected and spectra were recorded with a PHOIBOS 150 hemispherical analyzer in normal emission geometry, with the samples held at 300 K. The binding energy of all spectra was calibrated against the Ag $3d_{5/2}$ core level of the silver at 368.3 eV. Peak indentation and fitting were processed using CasaXPS software. [100]

DFT Calculations. The calculations were performed within the DFT framework using the Vienna ab-initio simulation package (VASP). [101] The projector-augmented wave (PAW) method was used to describe the interactions between ions and electrons. [102] The exchange-correlation interactions were treated by van der Waals density functional (vdWDF) in the version of rev-vdWDF2 proposed by Hamada. [86] The transition states were searched by a combination of Climbing Image Nudge Elastic Band and the Dimer methods. [87, 88, 89] Firstly, ten images were inserted in between the initial and final states. The central images were then used as the input for the Dimer calculations, in order to obtain precise transition states. Plane waves were used as a basis set with an energy cut-off of 400 eV. The Ag(100) and Au(111) substrates were all modelled by four-layered slabs where the bottom two layers were fixed, and the periodic image interactions were avoided by implying a 15 Å vacuum region. The atomic structures were relaxed until the energy was less than 10^{-6} eV and the residual forces on all unconstrained atoms were less than 0.01 eV/Å. For the modelling performed on Ag(100) substrate, the surface unit cell of $p(13 \times 13)$ was used for the tetramer model, $p\begin{pmatrix} 9 & 10 \\ -3 & 2 \end{pmatrix}$, for self-assembled organometallic dimers, $p\begin{pmatrix} 9 & 3 \\ 3 & -8 \end{pmatrix}$ for self-assembled enetriynes were used. For the modelling performed on the Au(111) substrate, a surface unit cell of $p(8 \times 8)$ was used. In the above calculations, the 1st Brillouin zone was sampled by the gamma point only. In addition, the Ag(100) surface unit cell of $p(14 \times 6)$ was used for the single organometallic dimer, together with 1×2 k-point sampling. The STM simulation images were calculated based on the Tersoff-Hamann approximation, [103] the AFM simulation images based on the geometries optimized by DFT were obtained on the website: http://ppr.fyu.cz/. The Probe Particle Model used in the simulation uses classical force-fields. [104, 105] Charge transfer values were obtained by Bader charge analysis. [106] The reaction energies were obtained by calculating the energy difference between the cyclization products (**2a-*cis***, **2a-*trans1***, **2a-*trans2***) and the corresponding precursor (**1a**).

HOMA index. The Harmonic Oscillator Model of Aromaticity (HOMA) [107, 108] index is defined as:

$$HOMA = 1 - \frac{1}{n} \sum_{i}^{n} V(d_{opt} - d_i)^2 \tag{2.22}$$

Here, n is the number of bonds in aromatic pathway, V is a normalization constant (257.7 Å^{-2} for C-C bonds and 93.52 Å^{-2} for C-N bonds), d_i is the respective bond length and d_{opt} is the "optimal" aromatic bond length. [108, 109] The optimal aromatic bond lengths were determined from the average DFT-computed C-C and C-N bond lengths in benzene and pyrrole, respectively: 1.396 Å for C-C bonds and 1.375 Å for C-N bonds. For a perfectly aromatic system (i.e., all bond lengths are equal to the "optimal" aromatic bond lengths), a

HOMA index of 1 is obtained.

Kinetic simulations. Kinetic simulations were performed by solving the system of rate equations for the transformation of **1a** as shown in Figure 4.17c, using an instant thermalization approximation without taking entropic effects into account. [110]

3. On-Surface Synthesis of Conjugated Molecules via the Controllable Addition Reaction of Alkynes

3.1. Tetramerization of alkynes on Ag(100)

3.1.1. Introduction

Enynes are a unique family of conjugated π-bond-rich compounds that are of broad interest due to their prevalence in both biochemistry and materials science. [111, 112] The enyne family consists of four basic units, namely enyne, enediyne, enetriyne, and enetetrayne, containing 1, 2, 3, or 4 substituted alkynyl groups, respectively (Figure 3.1). The low conjugated enyne and enediyne motifs have attracted much attention since the discovery of antitumor antibiotics over the last decades. [113, 114, 115, 116] Their biological activity stems from the generation of diradicals, which are responsible for DNA cleavage and cell destruction. [117] In addition to the exceptional anticancer properties in biomolecules, enynes are also fundamental scaffolds in synthetic chemistry and materials science, which undergo transformations to build functional compounds. For example, enyne metathesis has evolved into one of the most important chemical reactions to afford reactive intermediates, heterocycles, and natural products. [118, 119, 120] Higher conjugated enetetrayne frameworks are mainly applied in molecular systems in which their optical and electrical properties are explored. [121, 122, 123]

Motivated by these biological functions and application potentials, many efficient strategies have been developed to afford enyne species. Common transition-metal-catalyzed cross-coupling reactions are generally based on complex materials such as vinyl halides, [124] alkynyl halides [125] or organometallic alkenes. [126] Novel oxidative cross/homo-coupling reactions however are applied to simple terminal alkynes 17, [127] as this offers more sustainable synthesis routes. Practically, low conjugated enynes, such as enynes and enediynes, are easily synthesized and successfully applied in the construction of numerous functional materials. [112, 128, 129] Interesting, although there are many reports on the synthesis and application of enetetraynes, [114, 125, 130, 131] despite their conjugated π-systems and promising properties few papers have focused on enetriynes. [132, 133, 134, 135] Thus, the development of novel strategies to afford enetriyne motifs is of vital importance.

On-surface synthesis, [6, 136, 137, 8, 9] whereby synthesis occurs on single crystal surfaces under ultra-high vacuum (UHV) conditions, was shown to be an exciting new route towards the formation of conjugated nanostructures [16, 138, 139, 140] and functional organic

molecules. [141, 142, 143, 144, 145, 146] Substrate confinement and catalysis promote the transformation of reactive groups, thus constructing pre-designed nanostructures on surfaces. [147, 148] Specifically, aryl-alkynes, containing π-conjugated terminal alkynyl groups, have been widely studied [149, 150] using homo-coupling, [151, 152, 27, 14, 153, 154] cycloaddition [155, 156, 34, 157, 158, 159, 160] or cross-coupling with other active termini, [161, 162, 163, 164] to form a versatile covalent connection of functional nanostructures. [149] However, limited control over the reaction pathways of active carbon triple bonds inevitably results in side products, coincidentally, most in the forms of enynes. [14, 165, 166, 167, 168] Control over the desired synthesis is successfully improved via steric or template effects, inhibiting the undesired side reactions. [154, 169] On the other hand, one might achieve enynes as targeted products by introducing a directing group to an aryne precursor, thus suppressing the main homo-coupling pathway and creating spatial conditions for the cross-addition reaction mechanism. Recently, Wang et al. [170] synthesized the cis-enediynes on Ag(111) by introducing Br to a 4-ethynyl-1,1'-biphenyl precursor at either the phenyl side or the ethynyl end, whereby the Br adatoms aggregate the cis-enediynes into close-packed islands and pose a high steric barrier to further reactions.

Figure 3.1.: Examples of different enynes. The enyne family features elements with different electron-rich C-C bonding configurations. The marked enetriyne species is the main product obtained by the on-surface synthesis strategy developed in this work.

Here, we report a novel approach to highly selective enetriyne formation via tetramerization of terminal alkynes on Ag(100). By introducing a hydroxyl directing group to aryne, we designed a two-substituent precursor (4'-Ethynyl-[1,1'-biphenyl]-4-ol, EHBP, **1**, Figure 3.2), managed to control the reaction process and obtained uniform enetriyne species. With

the further development of on-surface reaction, using multicomponent precursors to synthesize complex surface structures has become a trend [155, 158, 170, 171] but remained challenging due to the difficulties in controlling the reaction pathway for each active group involved. [154, 171, 47] To achieve a high-quality sample, full control over the reaction pathway is required, which could be achieved via the design of molecular precursors with widely studied active groups. Thus, it would be of great importance to developing a method to control the on-surface reaction pathway step-by-step, which has been rarely done. In this work, we demonstrate a two-step synthesis strategy for the fabrication of enetriyne molecules using EHBP (**1**, Figure 3.2) as a template, which aggregates into regular assembly structures composed of mixed hydrogen bonds (**2**, Figure 3.2). According to recent studies, [172] metal-organic Ag-bis-acetylide dimers (**3**, Figure 3.2) can be first synthesized via O_2-mediation, which would aggregate into condensed assembly structures with the direction of the dehydrogenated hydroxyl termini, [173] thus avoiding the coupling reaction preferred by terminal alkynes. These adjacent dimers serve as templates to facilitate the tetramerization reaction during the further annealing process, forming a conjugated enetriyne core (**4**, Figure 3.2). The dehydrogenated hydroxyl termini, again, steer the aggregation of tetramer enetriynes to regular assembly structures, sterically hindering the diffusion and further reaction of conjugated products. The atomic structures and chemical states of intermediates and products were determined by a combination of scanning tunnelling microscopy (STM), non-contact atomic force microscopy (nc-AFM), and X-ray photoelectron spectroscopy (XPS) measurements. The reaction mechanism for the two-step synthesis has been further elucidated by density functional theory (DFT) calculations.

3.1.2. Supramolecular organic assemblies on Ag(100)

We initially deposited EHBP molecules onto a Ag(100) surface at a low temperature (150 K), to prepare a sample with pristine precursors, since both terminal alkynyl [151, 174, 168] and hydroxyl [173, 37, 175, 176] groups can be modified on silver surfaces at mild conditions. STM imaging (Figure 3.3a) of a medium coverage sample (45% of a full monolayer) shows a local aggregation of molecules adsorbed on the flat terrace. They typically assemble into tetrameric cross-shaped supramolecular modules, as highlighted in the inset in STM image Figure 3.3a. By careful inspection, the four-fold symmetric unit (high-symmetry D_{4h}) is cross-shape with mirror planes perpendicular to the surface, rather than the windmill-like structure with chirality which is usually formed by CH-π interaction between four ethynyls. Thus we infer the tetramer to be formed via intermolecular hydrogen bonds of the hydroxyl heads, resulting in the proposed structural model shown in Figure 3.3b. [177, 168, 170] Upon warming the initial sample up to room temperature (RT) or depositing EHBP on a Ag(100) substrate held at RT, large-area assembled islands were observed (Figure 3.5). When zooming into the assembly domain, the STM image (Figure 3.3c) shows an ordered rhombic network that seems to be made up of deformed tetramer units (3.3a). The high-resolution STM image (inset in Figure 3.3c) facilitates the close inspection of the vertex, with obviously reduced symmetry (C2). The rhombic-shaped unit contains four molecules, among which two are closer to each other in the head-to-head fashion, while the elongated heads of the other two
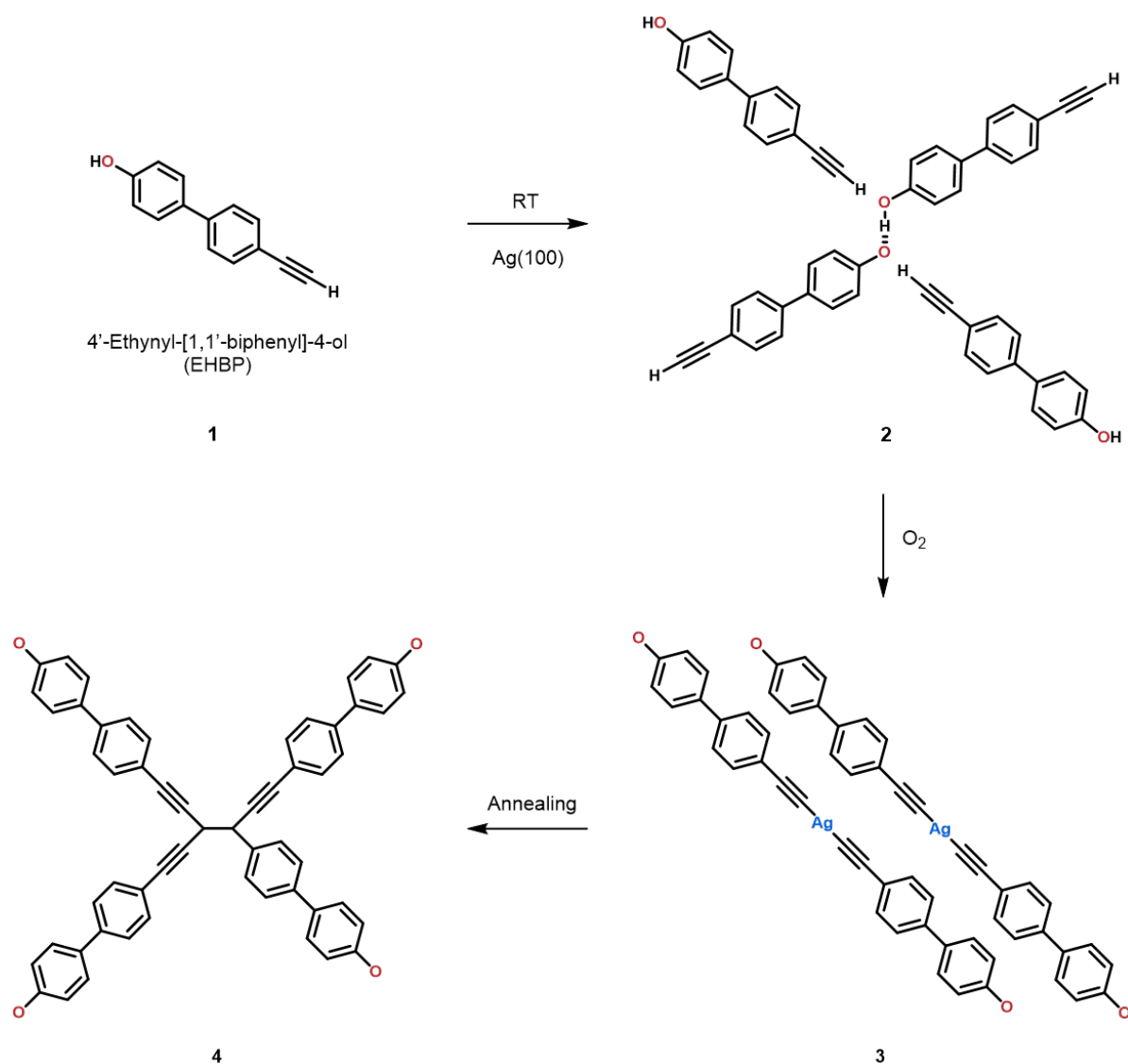
Figure 3.2.: Schematic illustration showing the molecular self-assembly and chemical transformations. The devised multi-step protocol involves a precursor with a directing group, gas-mediated pre-treatment, and thermally activated reactions to realize functional enetriyne species
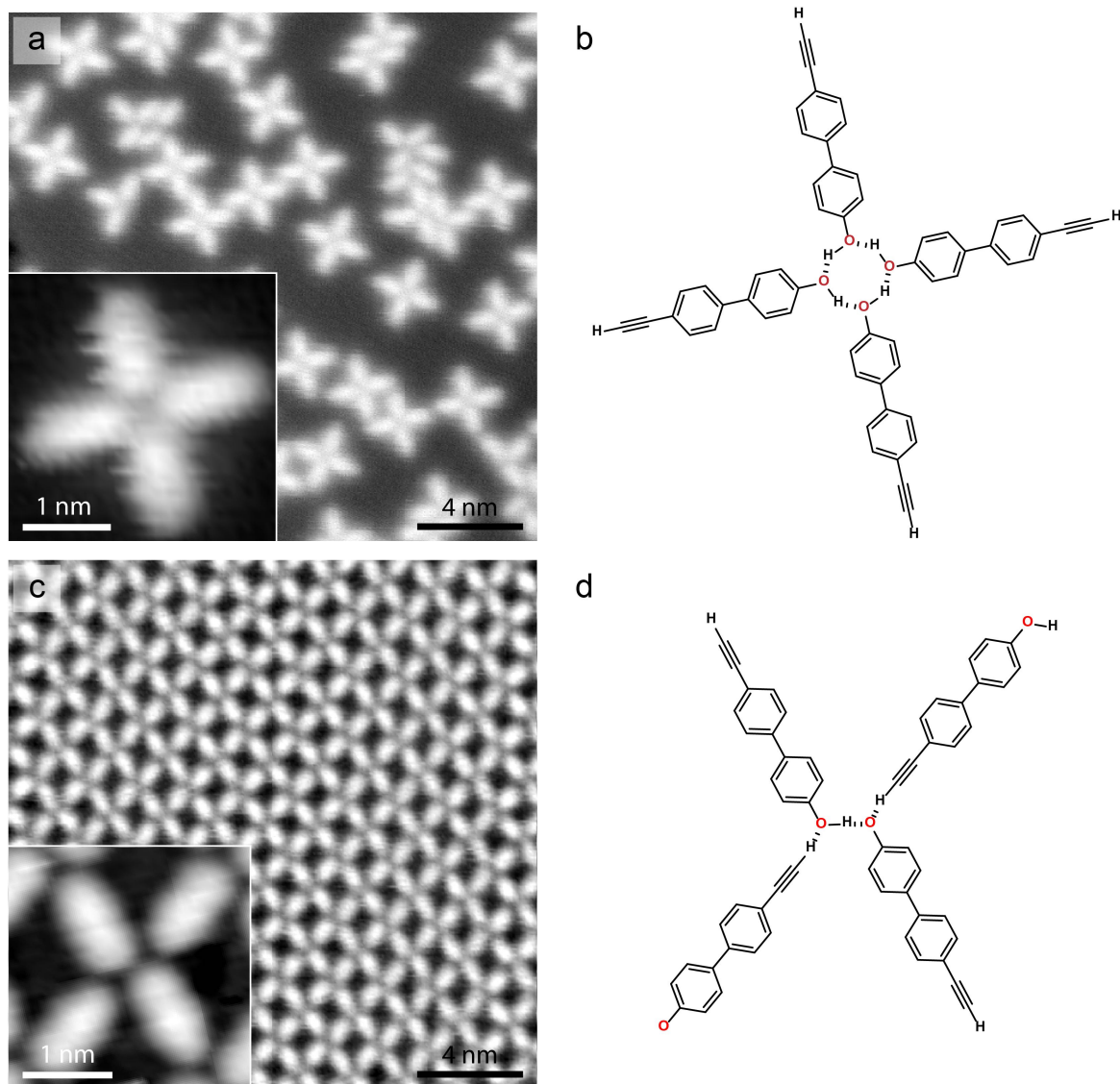
Figure 3.3.: Self-assembly structures of EHBP upon depositing on a clean Ag(100) substrate. (a) and (c) With the substrate held at 150 K and room temperature, respectively, either tetrameric units or extended networks evolve. (b) and (d) The models for vertices occurring in (a) and (c) explain the respective structural arrangements stabilized by different hydrogen bonding schemes. Scan parameters: (a) and (b) I_t = 1 nA, V_s = -100 mV.

approach from either side. This structural pattern transformation is ascribed to the variation of intermolecular interaction. Thus, we suggest a structural model for the ordered rhombic network, as shown in Figure 3.3d.
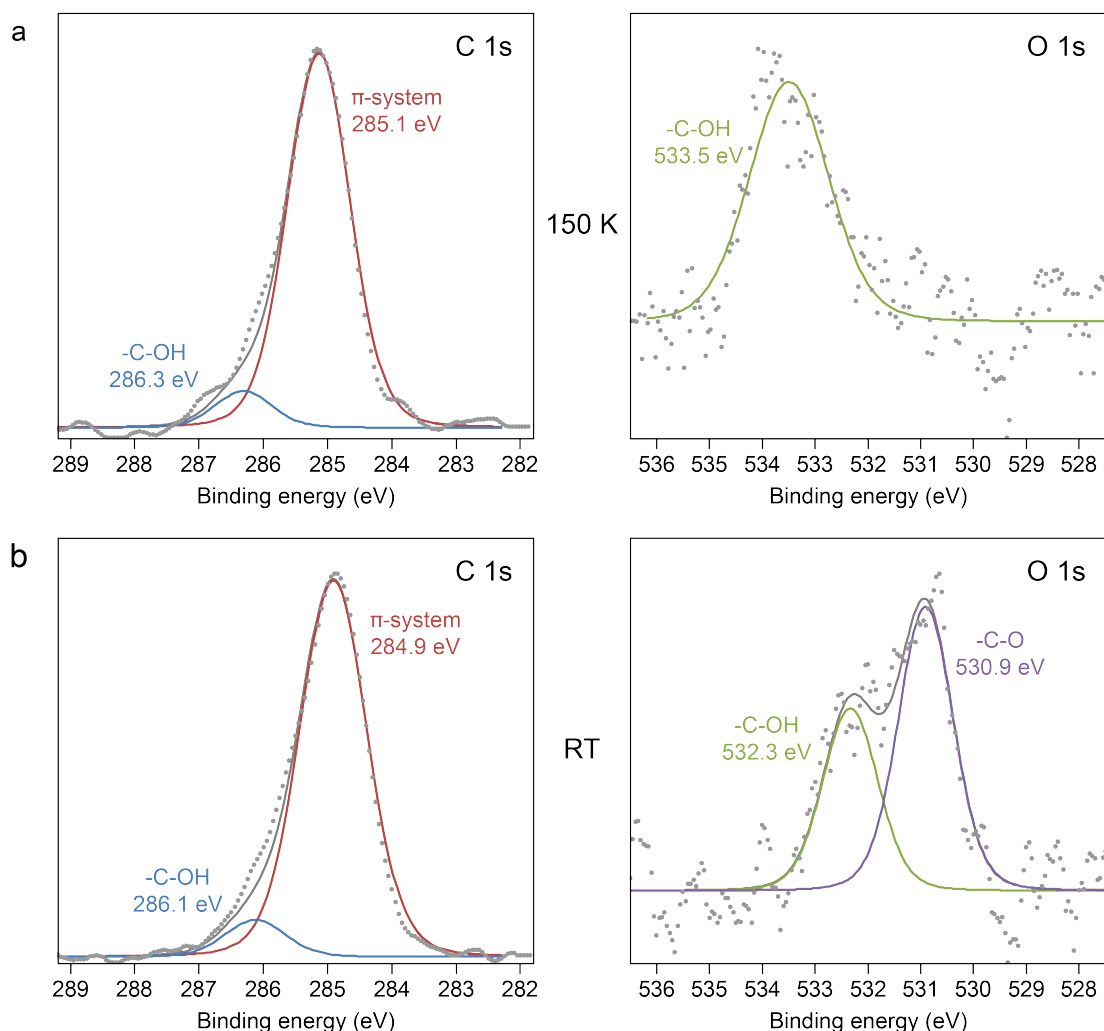
Figure 3.4.: XPS spectra of C 1s and O 1s core level for EHBP deposited on a clean Ag(100) surface held at 150 K and warming up to RT.

To clarify the chemical structures of self-assembled structures, we performed XPS measurements. As can be seen in Figure 3.4, at 150 K, the O 1s spectrum shows a sole peak centered at binding energy (BE) of 533.5 eV, which is related to the oxygen of -OH (right panel in Figure 3.4a). This is consistent with previously reported values for aromatic hydroxyl groups. [173, 37, 175, 176] Upon warming up to RT, the O 1s spectra split into two peaks at BE of 532.3 eV and 530.9 eV (right panel in Figure 3.4b), which are assigned to the oxygen of -OH and -C-O, respectively. In comparison, the alkyne termini remain pristine at RT according to the previous reports. These results reveal a partial dehydrogenation of hydroxyl groups, [168]

in which C-H$\cdots$O and O-H$\cdots$O mixed hydrogen bonds form between alkyne entities and (dehydrogenated) hydroxyl species, as depicted in Figure 3.3d.

It should be noted that the shifts of the O 1s signal of -OH could be related to the changes in the intermolecular interactions at different temperatures. Correspondingly, the C 1s spectra also display a slight downward shift. The C 1s spectra of the sample at 150 K present the main peak (left panel in Figure 3.4a). It can be fitted with two peaks, the high BE of 286.3 eV is the typical sign of -C-OH, and the low BE of 285.1 eV is assigned to the π-system consisting of phenyl and alkynyl groups. The peak intensity has a ratio of $\sim$ 1:11.5, close to the stoichiometric value of 1:13. After warming the sample up to RT (left panel in Figure 3.4b), the two C 1s peaks appear at lower BE of 286.1 eV and 284.9 eV, respectively. Therefore we propose that EHBP molecules remain pristine on the Ag(100) surface at 150 K; partial dehydrogenation occurs upon annealing to RT, as the chemical structures shown in Figure 3.3. Based on this speculation, the extended assembly structure obtained via DFT optimization also fits well with the experimental observations (Figure 3.3 e and f).
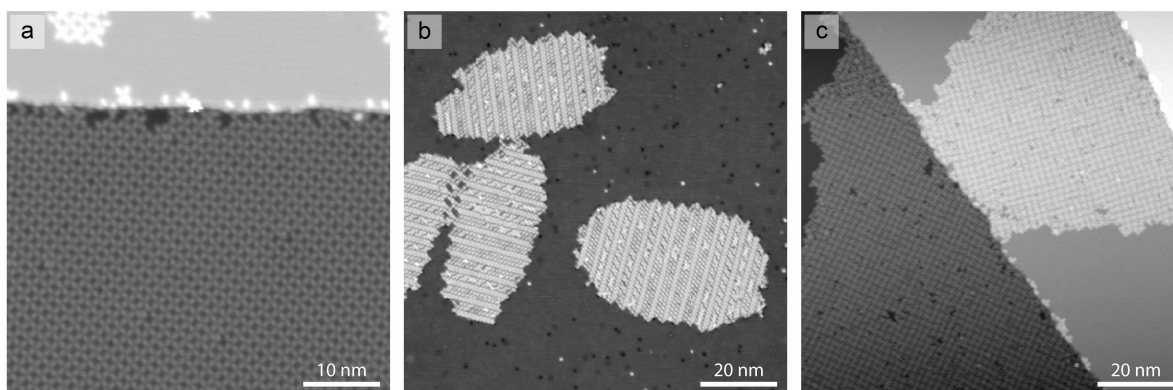
Figure 3.5.: Large-scale STM images of sample surfaces at different stages. (a) Upon deposition on a clean Ag(100) substrate held at RT. (b) After O2 exposure. (c) After annealing at 520 K. Scan parameters: (a) and (b) T_t = 100 pA, V_s = -100 mV, (c) I_t = 100 pA, V_s = -500 mV.

3.1.3. Organometallic dimers generated via oxygen-mediated oxidization

Upon exposing the self-assembled networks to O$_2$ ($\sim$45 L) at RT, shrinking islands were observed on Ag(100) surface, presenting ordered stripe sketches with different orientations (Figure 3.5). Figure 3.6a reveals the two kinds of stripes, which arrange alternately to form an extended domain. The repeated candy-like species in both stripes can be easily recognized as organometallic dimers composed of two EHBP monomers and a silver adatom. To characterize this alternate stripe configuration and the chemical structure of the linkages, bond-resolved AFM measurements were performed by using a CO-functionalized tip. AFM images (Figures 3.6b and 3.6d) reveal the structural details of the organometallic dimer array regions marked as I and II in Figure 3.6a, respectively. The biphenyl and alkynyl skeleton can be unambiguously
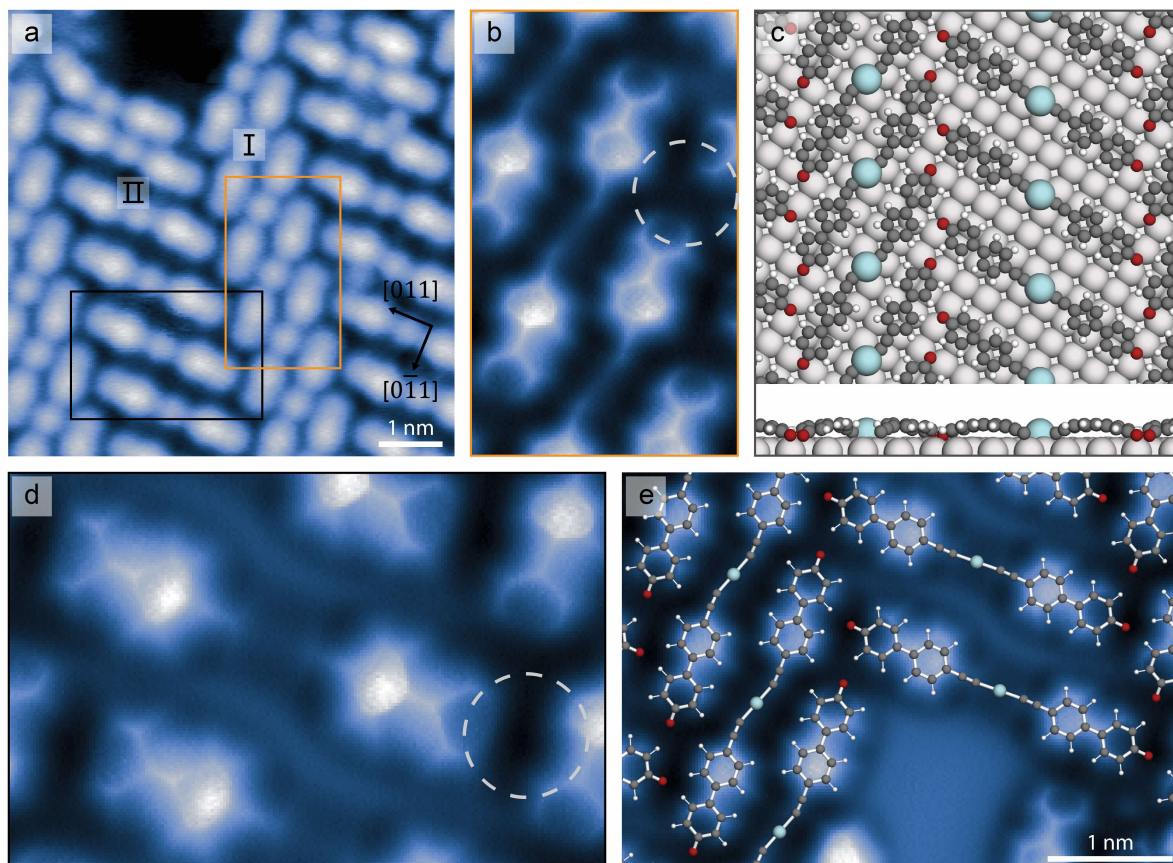
Figure 3.6.: Formation of organometallic dimers via O$_2$ mediation. (a) Representative STM image of revealing dimeric organometallic constituents and their mutual arrangement. (b) and (d) Bond-resolved nc-AFM images of the dimers corresponding to the area marked with orange and black rectangles in (a), respectively. (c) DFT optimized organometallic structures on Ag(100). (e) AFM image of the organometallic structure partially superimposed with the optimized structural model. Scan parameters: (a) I_t = 10 pA, V_s = 100 mV, (b), (d) and (e) V_s = 0 V, constant height.
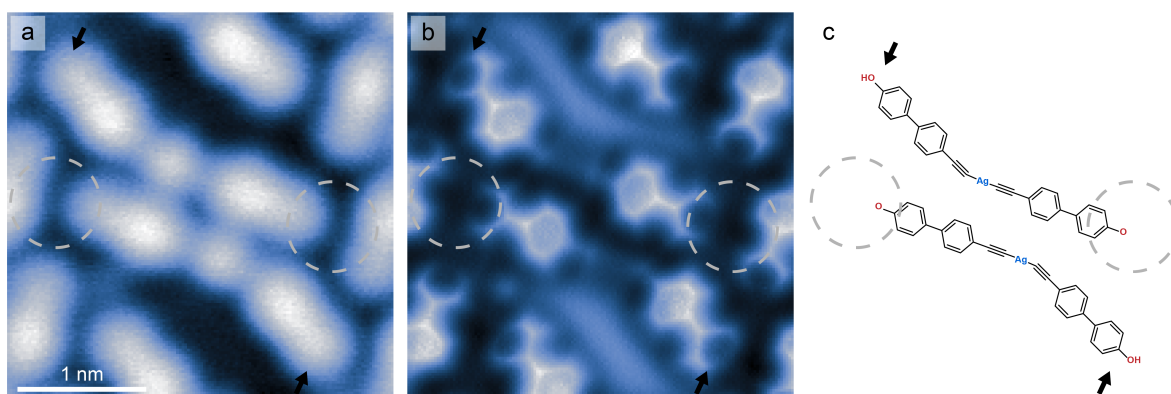
Figure 3.7.: STM and AFM images of a dimer pair showing different interactions in the vicinity of oxygen termini. (a) STM image of a dimer pair. (b) AFM image of the same area in (a). (c) Corresponding chemical structure of the dimers in (a) and (b). The two ends marked by gray circles are dehydrogenated hydroxyl entities, which point towards the biphenyl backbone of the adjacent dimer, analogous to the situation in Figure 2d in the main text. The two other ends bend outward (shown by black arrows) and are assigned to hydroxyl entities with relatively higher contrast compared to dehydrogenated ones. Scan parameters: (a) I_t = 10 pA, V_s = 100 mV, (b) V_s = 0 V, constant height.

distinguished as bright outlines while sliver adatoms in the center of the dimers are invisible in either array, leading to the determination of alkynyl-Ag-alkynyl organometallic linked dimers, which is in agreement with the O_2-mediated synthesized alkynyl-silver networks on Ag(111). [172] Similarly, both termini of the dimers exhibit a dark appearance in AFM images, coincident with the AFM studies on ketone groups. [178, 179] In addition, previous studies have reported that O_2 exposure may induce further dehydrogenation of hydroxyl groups on silver on the basis of partial dehydrogenation at RT. [180, 181] We thus hypothesized that both hydroxyl groups of the organometallic dimers in the ordered array structures are dehydrogenated. Further evidence thus will be provided by the XPS measurements, discussed in Figure 3.12.

It is interesting to note that dimers in array II (Figure 3.6d) show two-fold symmetry (D_{2h}), while the ones in array I (Figure 3.6b) have less symmetry (C_2), which is mainly reflected by the bending of the organometallic linkers. Another distinguishing feature is the different interplay in the vicinity of hydroxyl termini. The former is facing the middle part of the diphenyl backbone of the dimer in array I (indicated by the gray dashed circle in Figure 3.6d), while the latter points to the terminal benzene ring of the dimer in array II (indicated by the gray dashed circle in Figure 3.6b). To rationalize this stripe configuration, DFT calculations were performed on the organometallic dimers-Ag(100) system. Figure 3.6c shows the energetically most favorable configuration of the array assembly structures. The model shows all Ag adatoms adsorbing on the hollow sites, the oxygen termini, as well as the alkynyl-Ag-alkynyl organometallic species, match well with the two adjacent arrays in

the AFM image (Figure 3.6e). Besides this regular arrangement of individual organometallic dimers, some interesting pairs of dimers emerge in array II, as shown in the STM and AFM images in Figure 3.7. The two ends marked by gray circles face the middle of the biphenyl backbone of the dimer in the adjacent array, which are dehydrogenated hydroxyl entities, identical to the situation in Figure 3.6d. The two ends are bending outward (shown by black arrows), assigned to hydroxyl entities due to the non-depressed features relative to dehydrogenated entities. Taken together, this indicates a different interplay in the vicinity of the oxygen termini, due to the incomplete dehydrogenation of hydroxyl groups (detailed XPS analysis will be discussed later).
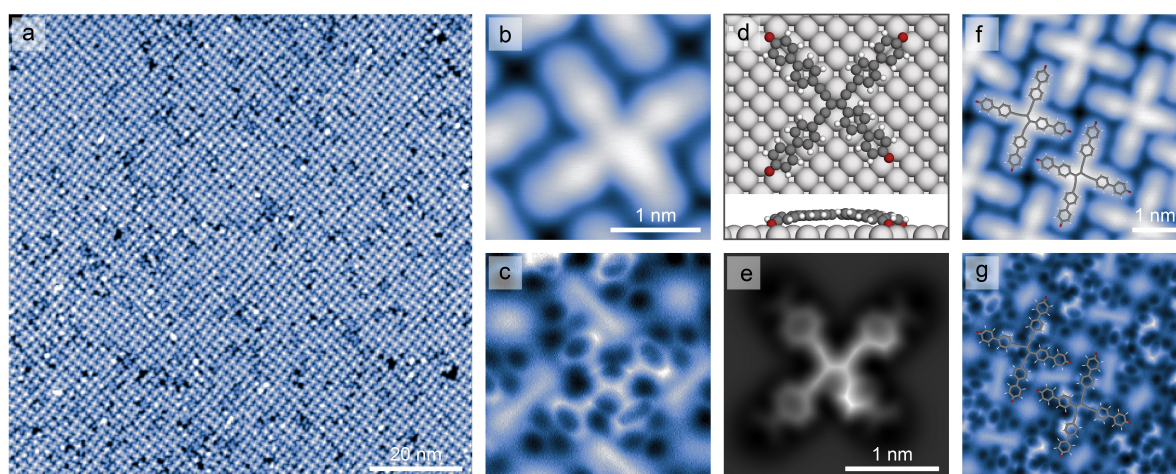
Figure 3.8.: Selective on-surface synthesis of enetriynes upon annealing the organometallic arrays at 520 K. (a) Representative large-scale STM image of tetramer superlattice. (b) High-resolution STM image of a tetramer unit. (c) The corresponding bond-resolved AFM characterization reveals the carbon backbone. (d) DFT calculated the structural model of an enetriyne species adsorbed on Ag(100). (e) Simulated AFM images of an enetriyne species. (f) and (g) STM and AFM images of an area of regular enetriyne arrays with partially overlaid structural models. Scan parameters: (a) I_t = 10 pA, V_s = 200 mV, (b) and (f) I_t = 10 pA, V_s = 100 mV, (c) and (g) V_s = 0 V, constant height.

3.1.4. Enetriyne formation via thermally activated tetramerization reaction

Following annealing of the O_2-treated sample described above to 520 K, a striking phase evolution was captured. The overview STM image (Figure 3.5) indicates a regular superlattice topography, i.e., the anisotropic organometallic dimer-array patches transformed into large-scale isotropic assembly structures. Figure 3.8a displays an overview STM image of the obtained ordered islands, revealing a self-assembly arrangement of newly formed cross-shape tetrameric species. For a better inspection of these novel products, a high-resolution STM image containing an intact tetramer is shown in Figure 3.8b. The latter consists of four

Optimized structure

Experimental AFM image

Simulated AFM image

Simulated STM
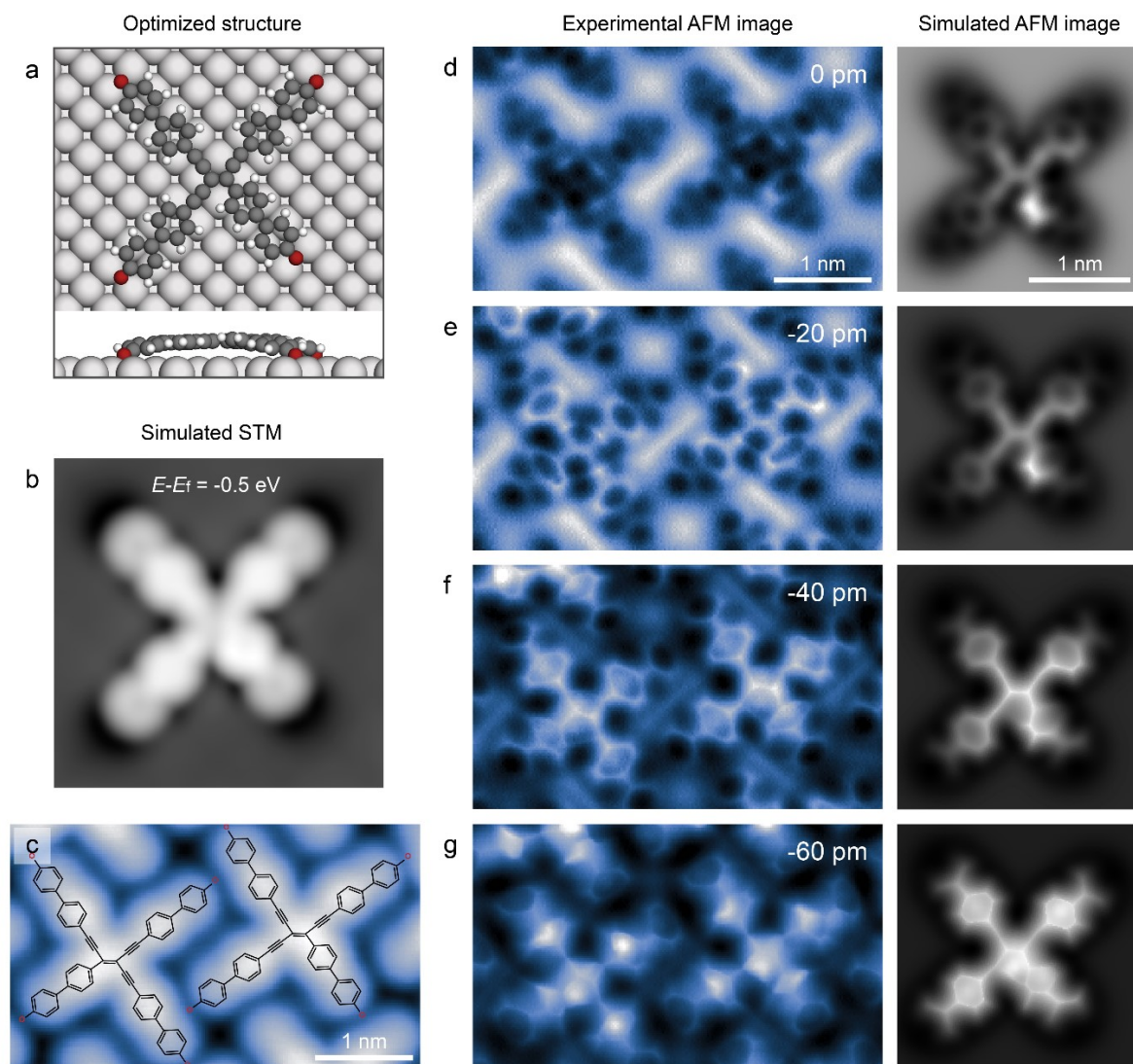
Figure 3.9.: Closer inspection of a small frame containing two tetramer products. (a) Optimized structural model of a tetramer for image simulation. (b) STM simulation of the single tetramer. (c) STM image of the scanned frame with two tetramers overlapped with the corresponding chemical structure. (d)-(g) Experimental and simulated AFM images at a series of decreasing tip-sample distances (as the labelled negative tip height showing). Scan parameters: (c) I_t = 10 pA, V_s = 100 mV, (d)-(g) V_s = 0 V, constant height.

cross-connected rod-like parts, which are straightforwardly assigned to four integrated EHBP precursors. Note that in all STM images there is no indication of embedded Ag atoms from the seamless contours, which strongly suggests covalent linkage at the crosses' centers, clearly differing from the supramolecular tetrameric constituents with different H-bonding nodes discussed above (Figure 3.3a).

Subsequently, bond-resolved AFM measurements again reveal details and the carbon scaffold of the covalent tetrameric products. Figure 3.8c shows an AFM image acquired at the same area of Figure 3.8b imaged by STM. The bond-resolved inspection clearly reveals that four biphenyl backbones are covalently connected at the center, i.e., there is a tetra-substituted skeleton. When focusing on the central moiety, three of the linkages (between phenyls and the central connection) display bright spot features, which can be unambiguously identified as ethynyl species according to previous AFM imaging experiments with a CO tip. [182, 183] Furthermore, a relatively short bond connects the fourth substituent and the central bond. This means that the central bond derives from the fourth monomer. Considering its same contrast as phenyl rings and the planar property of the entire tetramer, we confidently attribute the tetramer to be an enetriyne derivative (**4**, Figure 3.2).

Note that the phenyl rings in the periphery of the enetriyne tetrameric species appear darker and less sharp, due to a reduced adsorption height, which results from the strong interaction between terminal oxygen atoms and the substrate. [178, 179] This speculation is also supported by the DFT calculations. Figure 3.8d shows the most stable adsorption configuration of a tetramer on Ag(100), in which the molecular structural model resembles the shape of the observed tetramer products. The simulated AFM image (3.8e) acquired with DFT optimized structure compares well with its experimental counterpart (3.8c). Note that all oxygen atoms adsorb on bridge sites and bend the connected phenyl rings downward, in agreement with the AFM appearance. Hereby the oxygen atoms exist in the form of ketones engaging in intermolecular interaction with surrounding tetramers, which are observed in XPS and addressed in the next section. A closer inspection of the adjacent arrangement of two tetramer products clarifies the importance of the intermolecular hydrogen bond interactions for the formation of the well-ordered array (Figure 3.9). AFM images at different tip heights show more features of enetriynes. One can see the distortion of benzene rings at a lower tip-sample distance (Figure 3.9f and g), while the line-feature of alkynyl bonds are obvious at a higher tip-sample distance (Figure 3.9e). In addition, the termini of each enetriyne face the middle of the biphenyl backbone of the adjacent molecules.

In addition, Figures 3.8e and 3.8f show the STM and AFM images of a small area including four tetramer products. While all oxygen atoms face the middle of biphenyls of the adjacent tetramer, in the same way, the orientation of the central enetriyne skeleton varies between adjacent tetramers as the overlaid models show. However, with these different orientations, except for the slight difference in the length of the biphenyl skeleton, there are no morphological differences neither from experimental nor simulated STM images (Figure 3.10), in agreement with its highly conjugated electronic structure. It is worth noting that the chemoselectivity towards the enetriyne is significant (∼85%), according to the statistics (more than 2000 products were counted) from STM images obtained after annealing the

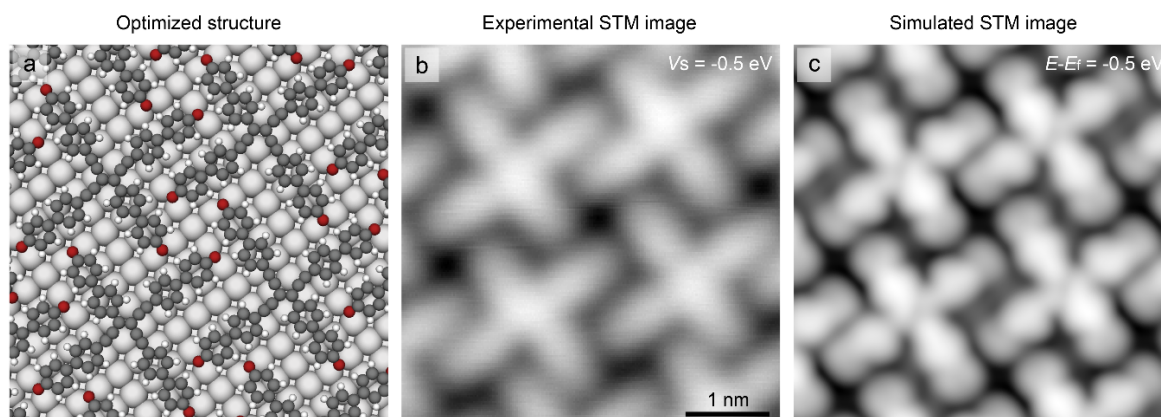| Optimized structure	Experimental STM image	Simulated STM image

Figure 3.10.: Extended assembly structure of the tetramer products. (a) Optimized structural model of the extended assembly. (b) and (c) experimental and simulated STM images of the assembly of tetramer products.

substrate at 520 K (Figure 3.11). There are some side products that can be seen, such as trimeric species and deformed tetramers, and some unknown species, with a ratio of 4%, 9%, and 2%, respectively.

3.1.5. Chemical shifts in the formation of enetriynes

We performed XPS measurements to inspect the chemical states of the EHBP molecules at different reaction stages (Figure 3.12). As explained in the previous section, due to the partial dehydrogenation of hydroxyl groups at RT (Figure 3.4), the as-deposited sample at RT already comprises a mix of chemical states. The O 1s spectrum in the upper panel of Figure 3.12 displays two comparable peaks at BEs of 532.2 eV and 530.7 eV, which are attributed to -C-OH and -C-O species, respectively. [173, 37, 175, 176] This chemical evidence confirms the proposed model of the RT assembly structure shown in Figure 3.3d. Following O_2 exposure, there is no evidence of oxygen uptake at the surface, and O 1s spectrum displays a pronounced reduction of the higher BE peak (532.2 eV) along with an increase of the lower BE signature (530.4 eV), which indicates the further dehydrogenation of the remaining hydroxyl groups, thus proving our hypothesis that the O termini of the organometallic dimers in the ordered array are dehydrogenated. In addition, the small contribution of hydrogenated oxygen (532.2 eV) is associated with the pairwise dimers that emerged in array II in Figure 3.6a, explaining the different interplay in the vicinity of oxygen termini. Post-annealing the O_2-treated sample at 520 K leads to a single O 1s peak at 530.2 eV, indicating fully enetriyne tetramers with exclusively -C-O endgroups. Note that the BE of the oxygen shifts slightly during the two-step treatment, which is presumably related to the modified intermolecular interactions in the different assemblies. In the C 1s spectrum, upon O_2 dosing, a new component appears at a low BE region of 283.7 eV. We attribute it to the signal of C-Ag, according to previous studies. [170, 171, 172] This result agrees well with the experimentally observed alkynyl-Ag-
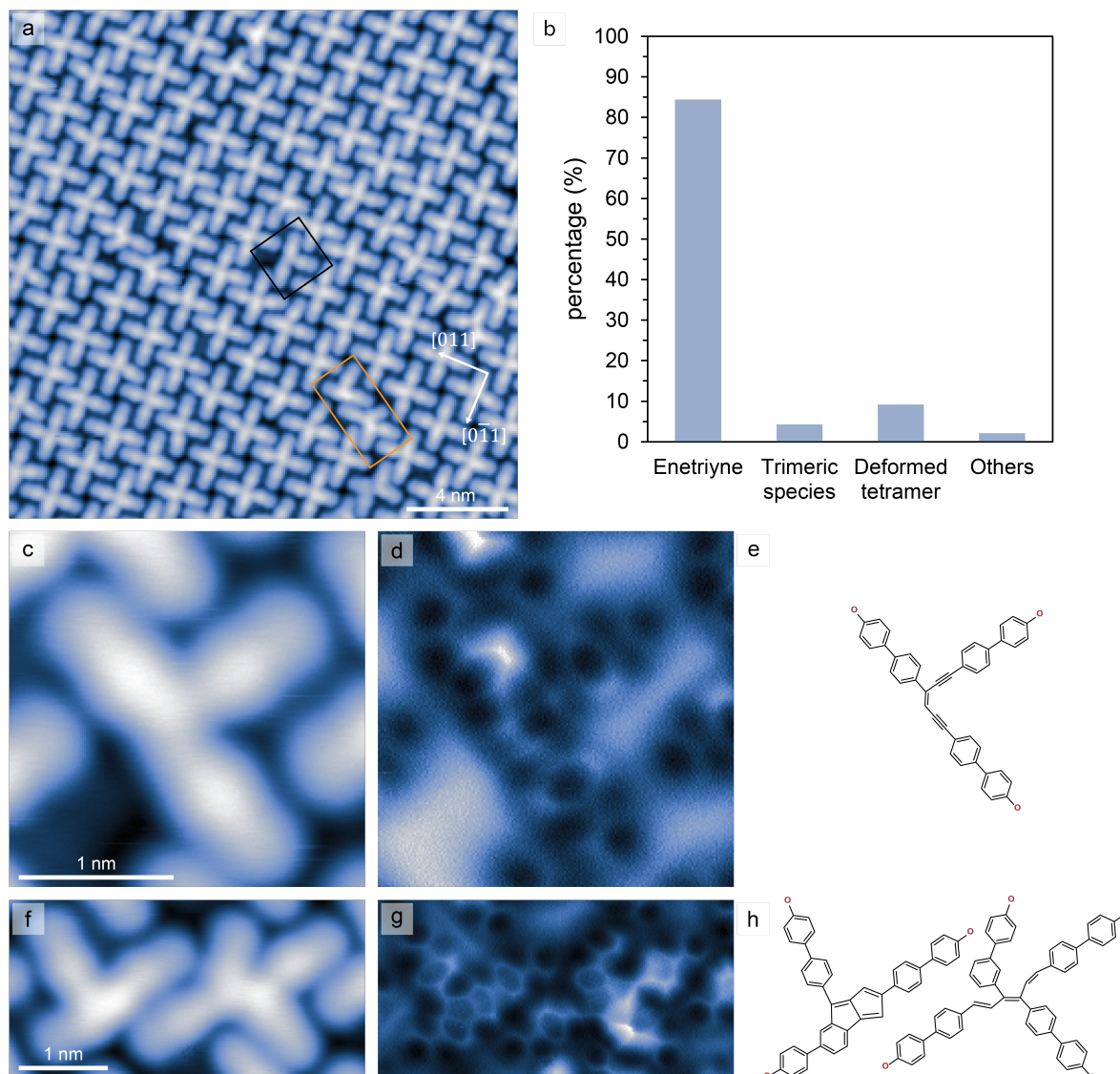
Figure 3.11.: Statistical analysis of the reaction products. (a) High-resolution STM image of the products after annealing substrate at 520 K. (b) Statistical distribution of different products on several high-resolution STM images. Counting more than 2000 products, the enetriyne is the dominant product with a large proportion of ~85%. Side products are mainly trimeric species, deformed tetramers, and unknown species, with ratios of 4%, 9%, and 2%, respectively. (c)-(d) STM and AFM images of an enediyne (the area marked by the black square in (a)) and its chemical structure in (e). (f)-(g) STM and AFM images of a trimeric species and a deformed tetrameric species (the orange rectangle in (a)), and their hypothesized chemical structures in (h).Scan parameters: (a), (c) and (f) I_t = 10 pA, V_s = 100 mV, (d) and (g): V_s = 0 V, constant height.
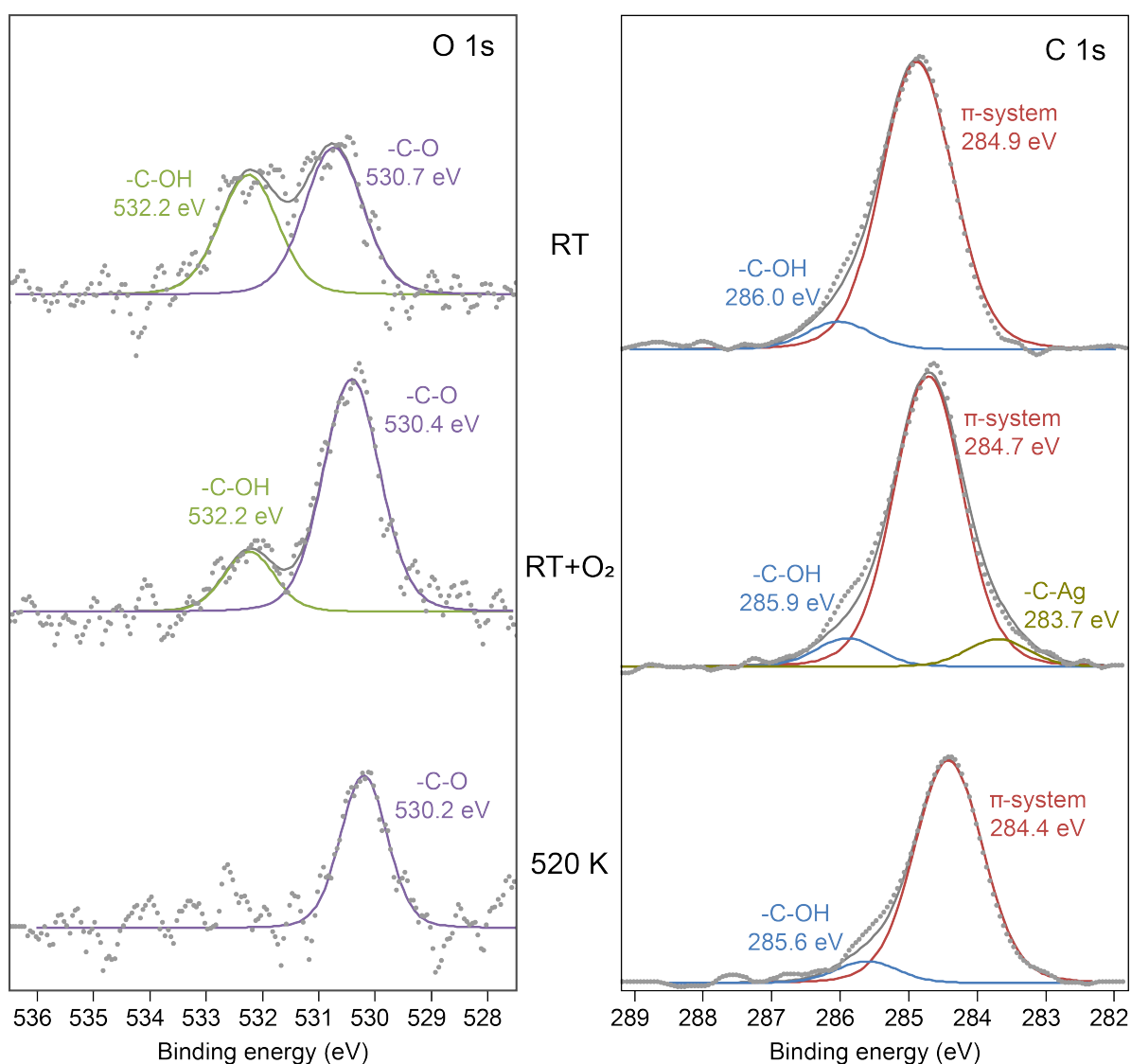
Figure 3.12.: XPS spectrum of O 1s and C 1s core level of EHBP at different reaction stages after depositing on a clean Ag(100) surface. The O 1s spectra recorded at RT display two peaks at 532.2 eV and 530.7 eV, indicating the partial dehydrogenation of hydroxyl entities. The peak at 532.2 eV vanishes after annealing the substrate at 520 K, revealing the fully dehydrogenated of hydroxyls.
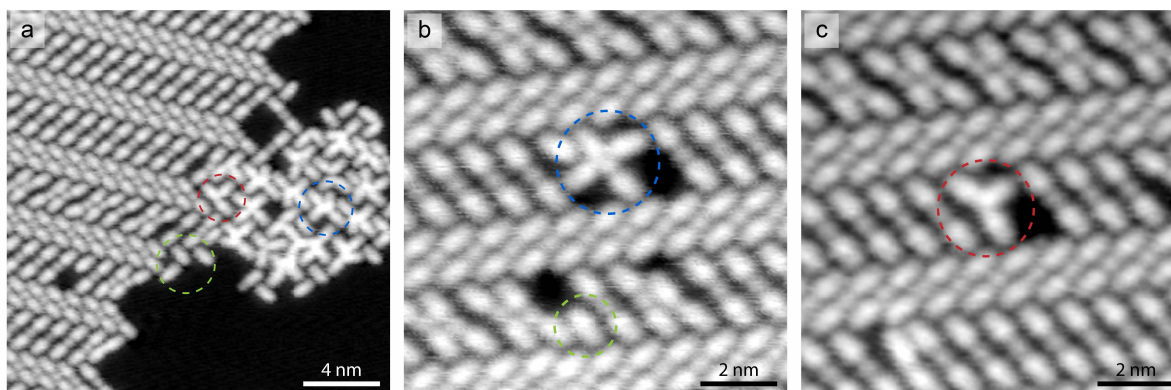
Figure 3.13.: Initial signs of the formation of enetriynes. (a) STM image of one domain edge of organometallic dimers after annealing the substrate at 450 K. It shows some broken dimers, trimeric and tetrameric species (marked by green, red, and blue dashed circles, respectively). (b) A close-up tetrameric species shows up in an organometallic dimers region, implying a possible intermediate state, Ag adatom not dissociated from the tetramer. (c) A close-up trimeric species appears in an organometallic dimers region, which could be the enediyne derivative. Scan parameters: (a) I_t = 100 pA, V_s = -100 mV, (b) and (c) I_t = 100 pA, V_s = -500 mV.

alkynyl organometallic dimers. Note that the main peak of C 1s spectra shows a downward shift from 284.7 eV to 284.4 eV, which is ascribed to the extended conjugation properties of enetriyne. Therefore, combining DFT optimization and XPS characterizations, as well as bond-resolved AFM images, we provide strong chemical and structural evidence for the on-surface synthesis of enetriyne tetramers.

3.1.6. Reaction mechanism of alkyne tetramerization on Ag(100)

In addition to the validation of synthesized products, it is also important to disentangle the pathway of the novel chemical reaction. The identification of intermediate states and incomplete products is an effective strategy to deduce the reaction process. The real-space structure analysis of STM is one of the advantages of on-surface reaction, which can capture trace intermediate state or byproduct structures for further analysis. With the help of STM and AFM observations, we found intermediate states in both steps of the synthetic process. For instance, after O_2 mediation, besides the regular dimer arrays, pairs of dimers emerge occasionally in array II. The structural difference allows us to understand the incomplete dehydrogenation of hydroxyl groups. The first stage of O_2-mediated organometallic dimer reaction is well understood, [172, 180, 182] while the second stage of thermally triggered tetramerization requires more detailed scrutiny. After annealing the organometallic dimer sample at 450 K, we found initial signs of the reaction at the edge of assembly domains and, importantly, containing many broken dimers, irregular trimeric and tetrameric species (as observed in Figure 3.13). These species can be assigned to intermediate states of the

tetramerization reaction, which may undergo stepwise organometallic bond scission and associated addition reactions.
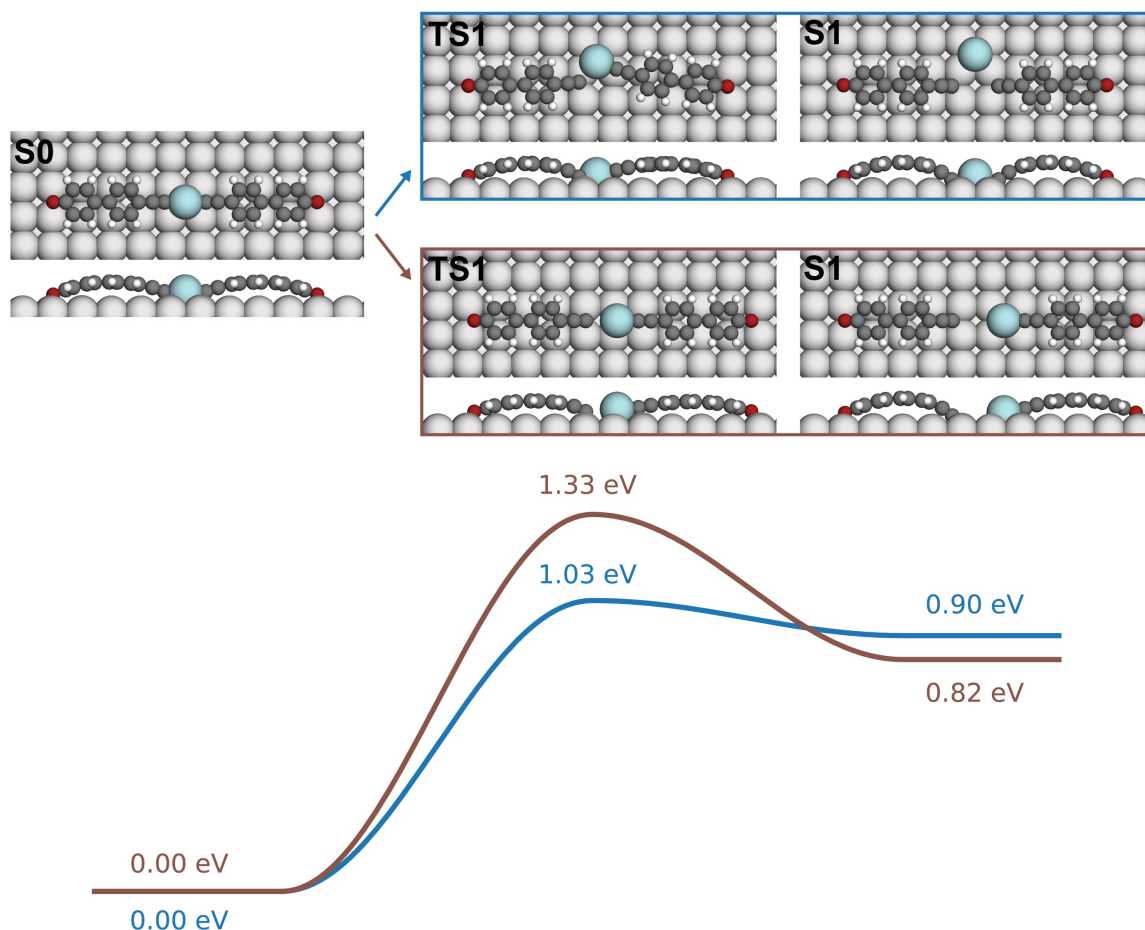
Figure 3.14.: Reaction pathways and energy profiles for the cleavage of an organometallic dimer. The reaction pathway with a blue outline is the most favorable one, in which Ag adatom is fully dissociated from alkynyl, with a barrier of 1.01 eV (corresponding to the blue energy profile). In the alternative reaction pathway (with a brown outline) the Ag adatom remains attached to one of the EHBP entities upon cleavage of the dimer, which gives an energy barrier of 1.33 eV (brown energy profile).

To analyze and rationalize the reaction pathway, we performed DFT-based transition state theory calculations. The most favorable free-energy pathway is depicted in Figure 3.15 (blue line). First, we performed calculations on the extraction of the Ag adatom of an organometallic dimer on Ag(100). The modeling indicates that the energetically most favorable pathway proceeds with the Ag adatom fully dissociated from the dimer, with an energy barrier of 1.01 eV (Figure 3.14). The resulting monomer has active -C≡C• head for further addition to the
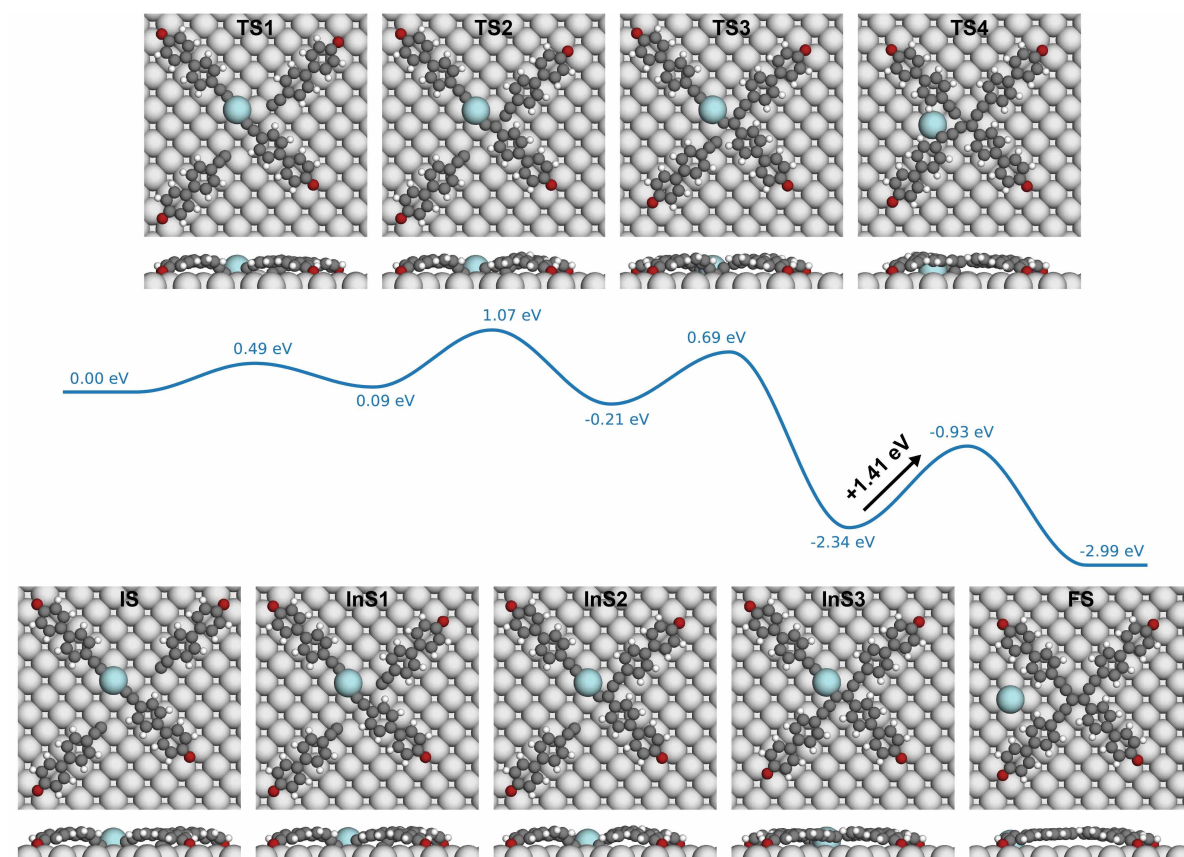
Figure 3.15.: Reaction pathway and energy profile from organometallic dimers toward the formation of enetriyne derivatives on Ag(100). C, H, O, surface Ag atom, and Ag adatom are represented by the dark gray, white, red, light gray, and cyan balls, respectively.

vicinal triple bond of an intact organometallic dimer. The addition reaction is triggered by the Ag adatom abstraction from organometallic dimers. Subsequently, the enetriyne species are formed through a three-step addition reaction. The first addition reaction proceeds through an EHBP entity added into an organometallic dimer (IS to InS2) with an energy barrier of 1.07 eV, whereas an energy barrier of 1.08 eV was obtained for the alternative pathway, shown in Figure 3.16. This process is followed by the addition of the second EHBP entity to the activated carbon of the trimeric species in InS2 (InS2 to InS3), with an energy barrier of 0.90 eV. During the final step, the dissociation of the second Ag adatom and the addition reaction of the third EHBP entity takes place, which requires a large energy input of 1.41 eV (InS3 to FS). It can be overcome at a substrate temperature of 520 K, according to the previous experimental results. [184]
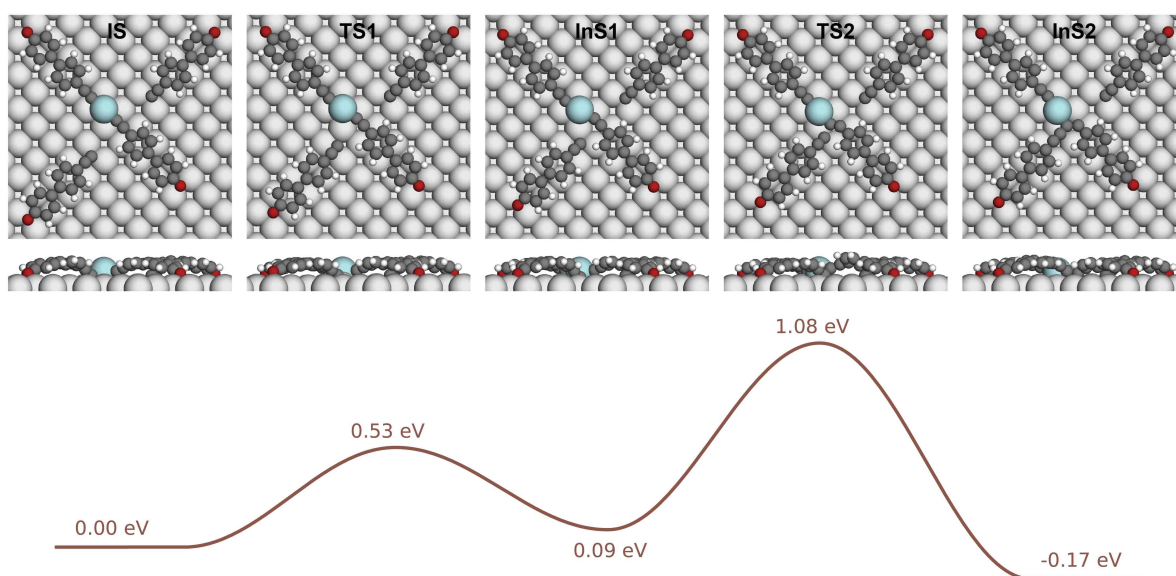
Figure 3.16.: The alternative reaction pathway of the first addition reaction with an energy barrier of 1.08 eV. At the reaction temperature of 520 K, reaction pathways of the first addition reaction exhibit mild activation energies (1.07 eV was obtained in the main text), both reaction pathways could take place.

3.1.7. Comparative experiments

The DFT calculations and analysis described above reveal this particular reaction mechanism is based on the alternative dimer arrays, which derive not only from the O_2 treatment but also from the directing effect of oxygen termini and Ag(100) substrate. To gain insight into the control parameters of the high selectivity of the formation of enetriynes, we performed comparative experiments without the O_2 dosage step and/or on Ag(111) surface.

Following deposition of EHBP molecules with medium coverage ($\sim$45% of a full monolayer) on the Ag(100) substrate held at RT, we observed an ordered rhombic network with a unit
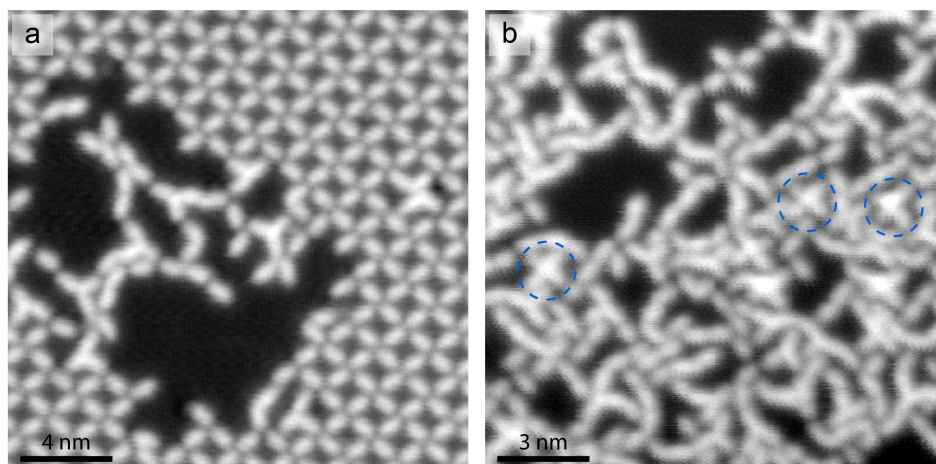
Figure 3.17.: Comparative experiment on Ag(100) without O_2 mediation. Deposition of EHBP molecules with medium coverage on Ag(100) substrate held at RT gives rise to an ordered rhombic network, identical to the one in Figure 1c. (a) Annealing the substrate at 370 K induces the formation of few short polymers and trimeric species on the edge of the rhombic network. (b) After annealing at 420 K, irregular structures and tetramer-like species can be found occasionally (marked by blue circles). This result indicates that O2 mediation is crucial for the formation of enetriynes. Scan parameters: (a) and (b) I_t = 1 nA, V_s = -100 mV.

cell of a = b = 3.05 $\pm$ 0.02 nm attaching an angle of 80°, identical to the one in Figure 3.3c. Annealing the substrate at 370 K, few short polymers and trimeric species were formed at the edge of the rhombic network, as shown in Figure 3.17a. After annealing at 520 K, the STM image in Figure 3.17b displays irregular structures, including occasional tetramer-like species (marked by blue circles). This result indicates that O_2 mediation is indispensable for the formation of enetriynes.

When depositing EHBP molecules with medium coverage on an Ag(111) substrate held at RT, we obtained rhombic networks (Figure 3.18a). The unit cell of the network can be described by a = b = 3.02 $\pm$ 0.02 nm with an angle of 80°, which is very close to the values measured on the Ag(100) surface. More interestingly, while exposing the rhombic network to O_2 (~45 L) at RT, we observed a close-packed organometallic dimers domain, shown in 3.18b. Note that the close-packed dimer is different from the alternative arrays obtained on Ag(100), which is attributed to the O_2-mediated deprotonation of alkynyl groups on Ag(111). Annealing the O_2-treated substrate at 520 K, disordered structures were obtained, and a close-up image (3.18c) presents trimeric species (red arrows) and short polymers (black arrows), randomly aggregated on the substrate. We propose that the condensed aggregation of organometallic structures does not allow effective control of the thermally triggered addition reaction when annealing at 520 K. These results again support our effective control of the synthesis of enetriynes.
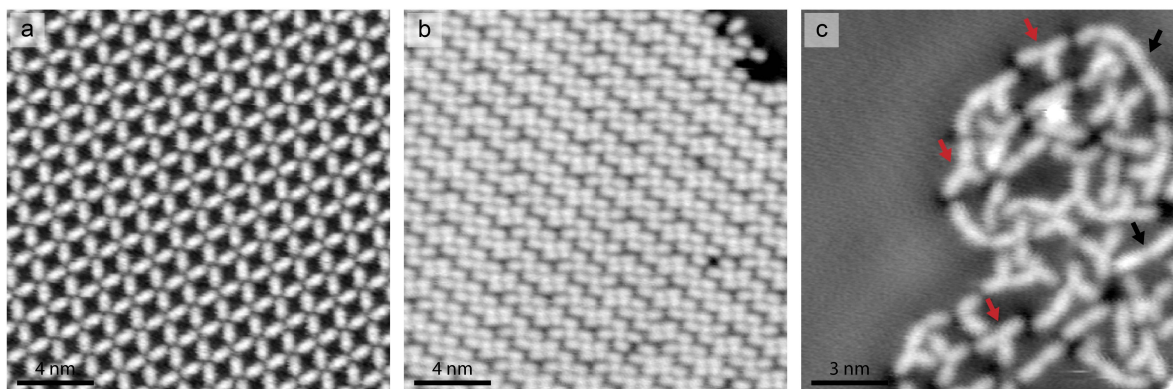
Figure 3.18.: Comparative experiment on Ag(111). (a) STM image of the rhombic network after deposition of EHBP molecules with medium coverage on Ag(111) substrate held at RT. (b) After exposing the rhombic network to O_2 at RT, we observed close-packed organometallic dimers domains. (c) Annealing the O_2-treated substrate at 520 K, disordered structures were obtained. Scan parameters: (a) I_t = 100 pA, V_s = -100 mV, (b) I_t = 1 nA, V_s = -100 mV, (c) I_t = 100 pA, V_s = -500 mV.

3.2. Cyclotrimerization of alkynes on Au(111)

As one of the most frequently used functional groups, alkynes are intensively studied in the field of on-surface synthesis. [151, 27, 165, 28] Among them, the alkyne polycyclotrimerization is promising for the synthesis of conjugated aromatics duo to its atom-economy. [177] It's noteworthy that noble metal surfaces, i.e, Cu, [165] Ag [10] and Au, [177, 185] display different reactivity for the reactions of alkynes. On the more reactive Cu(111) surfaces, it is difficult to obtain a uniform product because several reactions, including homo-coupling, cross-coupling, and trimerization, proceed simultaneously. On Ag(111) surfaces, homo-coupling of alkynes is favored, along with the catalyzed dehydrogenation of terminal alkynyl groups. Because of the low reactivity, Au(111) surfaces, comparatively, are the most suitable for the polycyclotrimerization of alkynes offering higher mobility and more addition chances to acetylenes. However, previously reported alkyne cyclotrimerization studies based on diyne and triyne monomers on Au(111) still show imperfection in the growth of extended conjugated structures due to the side reaction and steric shielding. Despite some attempts with monoyne monomers, the steric shielding of the other introduced functional groups was found to largely suppress the cycloaddition process after the dimerization of monomers. Therefore, it is necessary and useful to introduce suitable directing groups into monoynes to study the selectivity of cyclotrimerization.

Motivated by the highly selective synthesis of enetriynes via the tetramerization reaction of alkynes on the Ag(100) surface (above section), we studied the alkyne cyclotrimerization of EHBP molecules on Au(111) and analyzed the effects of the hydroxyl directing groups on the formation of regular molecular islands. In this section, we present a controllable synthesis of trisubstituted benzenes via the cyclotrimerization of alkynes on Au(111), schemat-
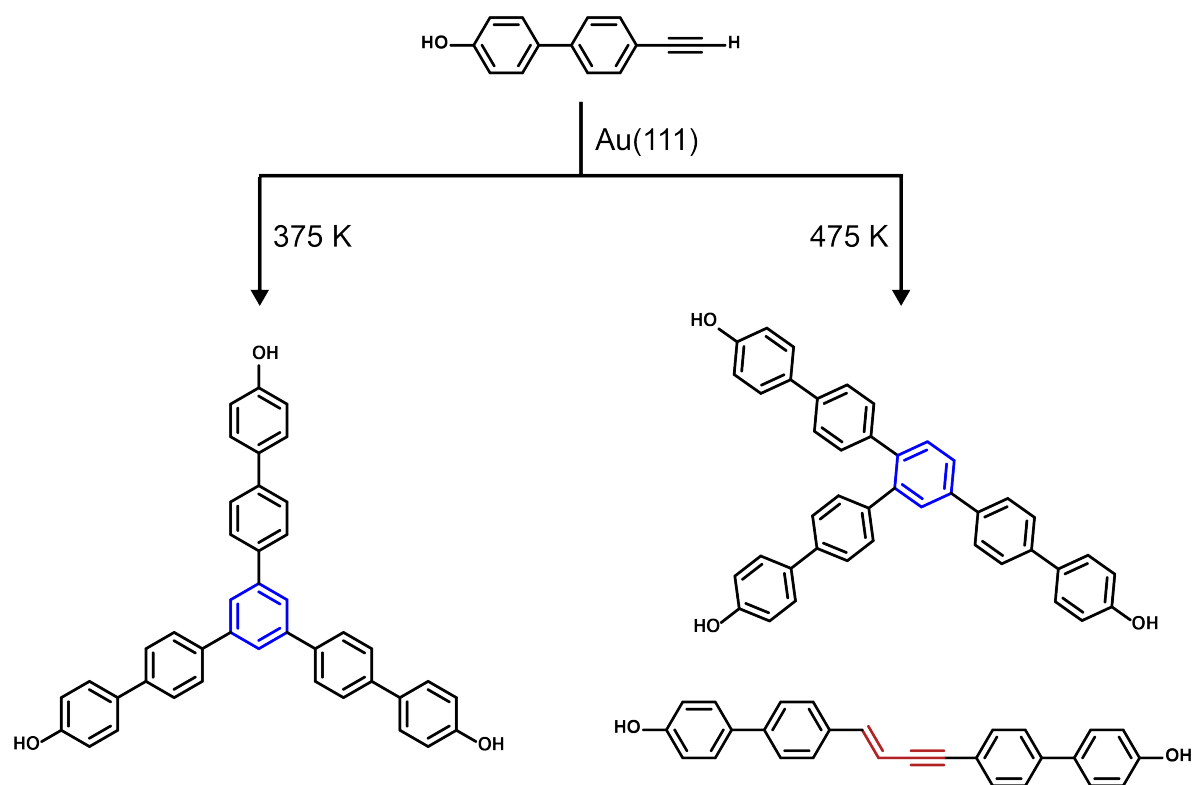
Figure 3.19.: Schematics of regioselective cyclotrimerization of alkynes. After depositing EHBP molecules on Au(111) surface kept at RT, cyclotrimerization of EHBP molecules was triggered by thermal annealing: three triple bonds are cyclotrimerized into one benzene ring by addition reaction. The addition products were selectively self-assemble into uniform molecular arrangements by annealing at different temperatures: 1,3,5-trisubstituted isomers at 375 K, 1,2,4-trisubstituted isomers, and dimers at 475 K.

ically depicted in Figure 3.19). Taking advantage of the hydroxyl directing groups and controllable thermal annealing, we managed to steer the reaction process and obtain uniform products. Controllable annealing of the preassembled structure induces the formation of the regioselective trimeric species, where 1,3,5-trisubstituted benzenes dominate at 375 K, and 1,2,4-trisubstituted benzenes dominate at 475 K. Uniform self-assembly islands, stabilized by intermolecular hydrogen bond interactions, can be obtained for both species. This study may provide a protocol to precisely fabricate functional trisubstituted benzene derivatives.

3.2.1. Supramolecular organic assemblies on Au(111)

Figure 3.20 shows typical STM images of self-assembly structures of EHBP after deposition on the Au(111) surface at RT with a coverage of ∼80% ML (monolayer). Most of the molecules aggregate into large uniform islands (Figure 3.20a), while some isolated stripes can be found between the large domains. Individual molecules can be distinguished in the magnified STM image (Figure 3.20b), in which a four-molecule unit is shown in the inset with the chemical structure superimposed. Similar to what we observed on Ag(100) at low temperatures, the four intact hydroxyl groups point to each other in an orthogonal arrangement, mediated by strong hydrogen bonds (Figure 3.3a). Figures 3.20c and 3.20d show regular self-assembly networks, exhibiting the extended structures of four-molecule units. The molecular arrangements in the two domains are chiral due to the reciprocal orientation of the alkynyl termini, leading to the enantiomeric islands, as indicated by the overlaid molecular models on the corresponding STM images. The unit cell parameters are a = b = 2.0 ± 0.02 nm with an angle of 90° for both chiral domains. Note that the intact EHBP molecules reveal the lower reactivity of Au(111) regarding to the dehydrogenation of ether hydroxyl and alkynyl groups, as compared to Ag(111) and Ag(100). Indeed, there is no phase transition even after the O_2 dosage treatment at RT on Au(111).

3.2.2. Alkyne cyclotrimerization via thermal activation

Annealing the substrate at 375 K induces pronounced changes in molecular arrangements, giving rise to the honey-comb islands and irregular molecular aggregates, as shown in the large-scale STM image in Figure 3.21a. Figure 3.21b shows an STM image, displaying the coexistence of regular and irregular molecular arrangements. The high-resolution images shown in Figure 3.22 reveal the uniform honey-comb structures consisting of triangular individuals with three-fold symmetry, denoted as trimer-I. Our constant-height STM image (Figure 3.22c) clearly shows the seamless connections in the center of the triangular individual, this immediately brings us to the formation of a benzene ring via the cyclotrimerization of three alkynes (rendering with blue in the proposed model in Figure 3.22d), as previously reported. [177, 185] The uniform structure can be expressed by a unit cell of a = b = 2.13 ± 0.02 nm, with an angle of 60°. Note the depression between the ends of three adjacent species, implying the non-covalent bonding. Thus, the large islands are formed by hydrogen bonding between hydroxyl groups; the proposed molecular model is shown in Figure 3.22d. The irregular molecular aggregates are composed of tree-fork trimers (denoted as trimer-II,
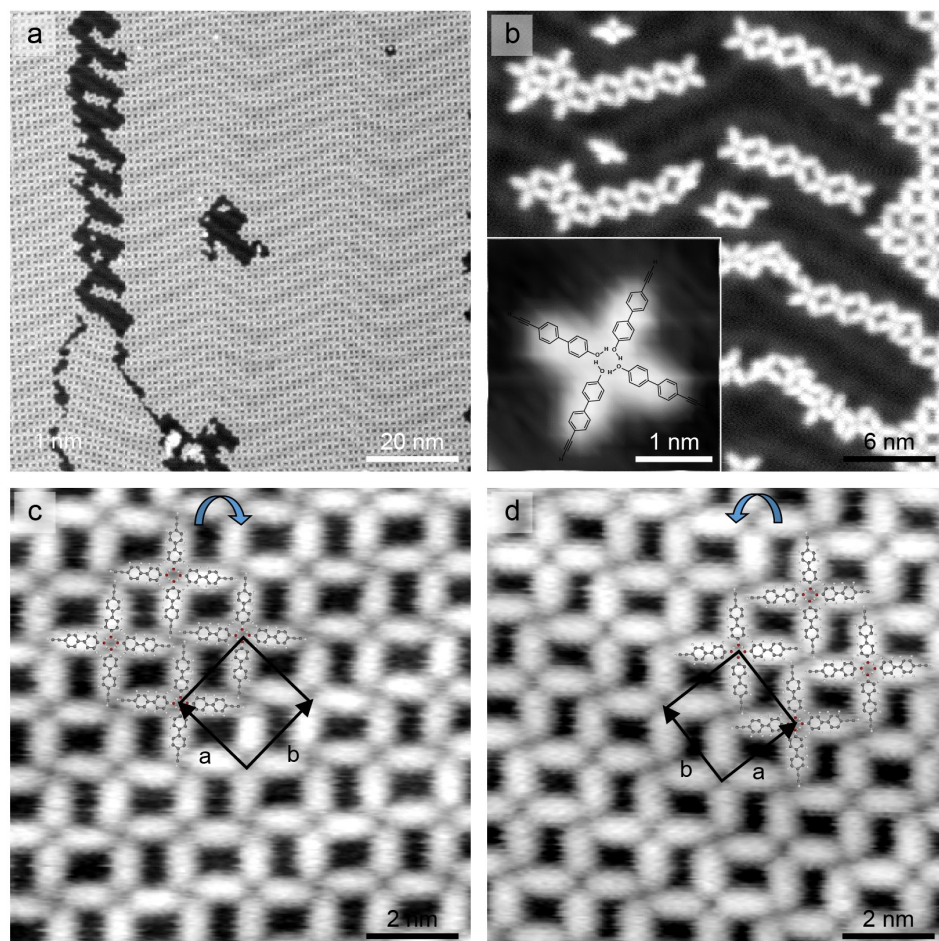
Figure 3.20.: Self-assembly of EHBP molecules after depositing on a Au(111) surface kept at RT. (a) Large-scale STM image of self-assembly of EHBP on Au(111). EHBP molecules self-assemble into molecular islands. (b) Magnified STM image of EHBP molecular stripes growing along the edge of a molecular island. The inset is a high-resolution STM image of one isolated four-molecule unit covered with the corresponding chemical structure. (c) and (d) Zoom-in STM images of chiral self-assembly domains, with the structural models superimposed, respectively. Scan parameters: (a) and (b) I_t = 100 pA, V_s = -100 mV, (c) and (d) I_t = 100 pA, V_s = -500 mV.
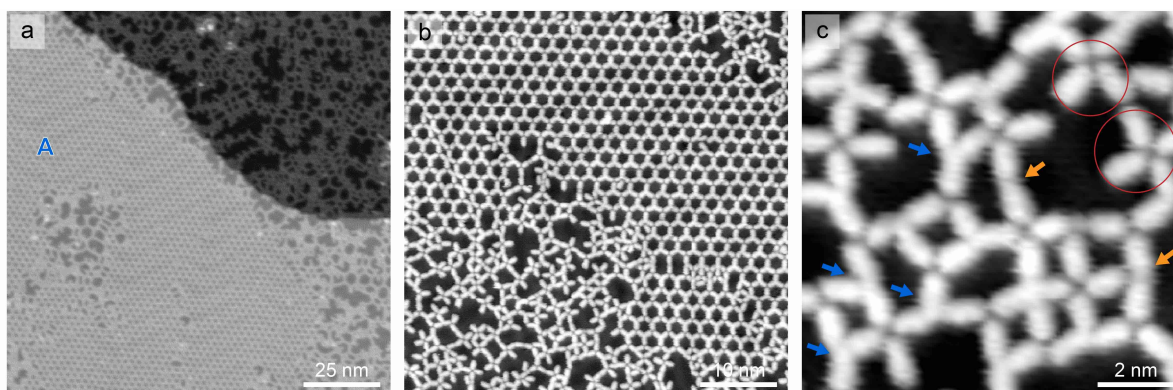
Figure 3.21.: Phase transition of the surface structures after annealing the predeposited sample at 375 K. (a) Large-scale STM image shows trimer species in an island. (b) A close-up STM image presents the coexistence of regular domains and irregular molecular arrangements. (c) Tree-fork shape trimers (blue arrows), dimers (orange arrows), and unreacted EHBP monomers (red circles) were also achieved, aggregating into disordered arrangements. Scan parameters: (a) I_t = 100 pA, V_s = -500 mV, (b) and (c) I_t = 100 pA, V_s = -100 mV.

blue arrows), dimer species (orange arrows), and unreacted EHBP monomers (red circles), as marked in Figure 3.21c. Trimer-II species are oblique triangular shapes, and possess angles close to 180°, 120° and 60°. These geometries are consistent with those proposed in previously reported works. [177] Therefore, we attributed trimer-I and trimer-II to the 1,3,5- and 1,2,4-isomers, respectively. The reaction mechanism for alkyne cyclotrimerization is clarified by Fasel et al, and Gao et al. [185, 177]

When further annealing the substrate at 475 K, the surface morphology changes, whereby in addition to **A**, three newly formed islands are prevailing, marked by **B**, **C** and **D** in a large-scale STM image (Figure 3.23a). The high-resolution STM image in Figure 3.23b presents the details of domain **B**, in which ladder shape arrangements composed of trimer-II and dimers are found, with a unit cell of a = 2.48 ± 0.02 nm, b = 4.0 ± 0.02 nm attaching an angle of 78°. The dimer can be recognized as two EHBP monomers connected by an enyne entity after the addition reaction. We proposed a structural model for the ladder shape arrangements in Figure 3.23c, which fits well with STM topologies. It is apparent that the hydrogen bonds of the hydroxyl groups of both dimer and trimer products play an important role in the aggregation process. Furthermore, other regular molecular patterns, consisting of different combinations of products, are also found on the surface. Figure 3.23d displays a small patch of the porous structure (**D**), the self-assembly of enyne dimers through hydrogen bonding between hydroxyl substituents. A more complex structure is also obtained (Figure 3.23e), including both trimer-I and II species with a unit cell of a = b = 5.85 ± 0.02 nm and an angle of 60°. This periodic unit is shown in Figure 3.23f.

Interestingly, when directly annealing the RT predeposited sample to 475 K, a different surface morphology was observed. Figure 3.24a presents a representative overview STM
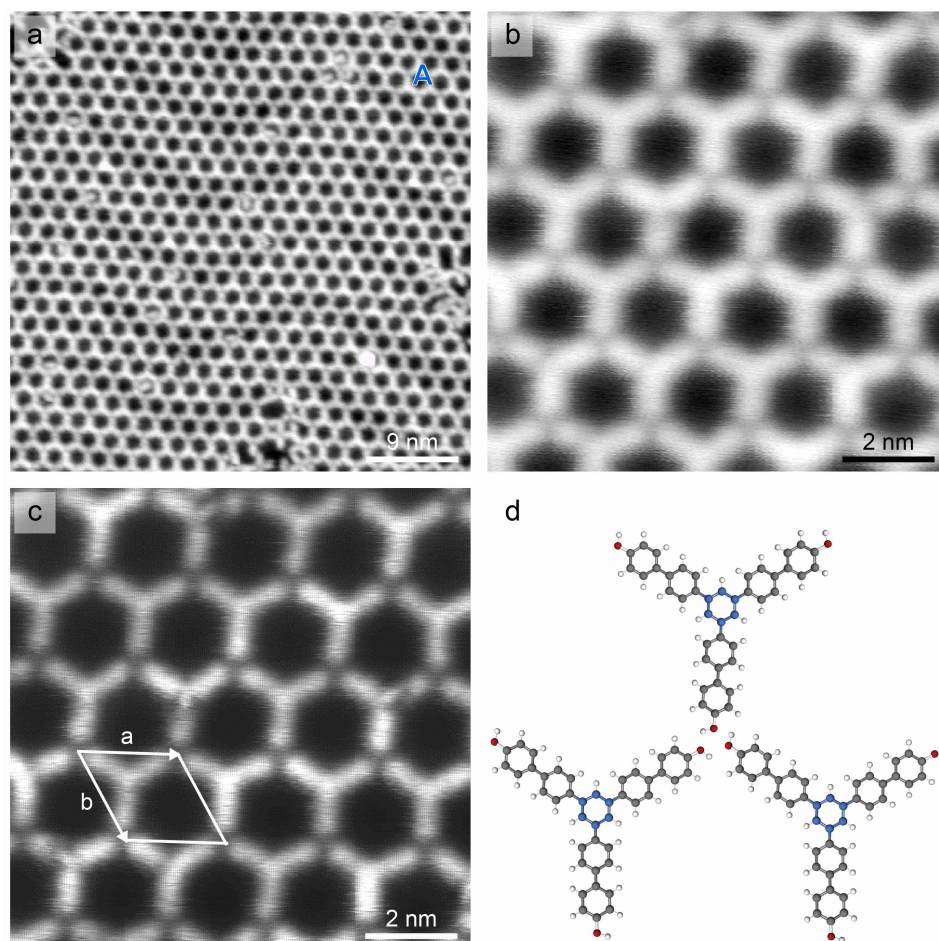
Figure 3.22.: High-resolution STM images of the trimer products after annealing the substrate at 375 K. (a) STM image of the regular honey-comb island (denoted as **A**), consisting of trimer species (denoted as trimer-I). (b) Zoom-in STM image of the trimer-I species. (c) Constant-height STM images were obtained in the same area as (a). (d) The proposed model for trimer-I, the newly formed benzene ring rendering with blue, and the well-ordered trimer stabilized by the hydrogen bonding. Scan parameters: (a) I_t = 100 pA, V_s = -500 mV, (b) I_t = 1 nA, V_s = -500 mV, (c) I_t = 1 nA, V_s = 100 mV.
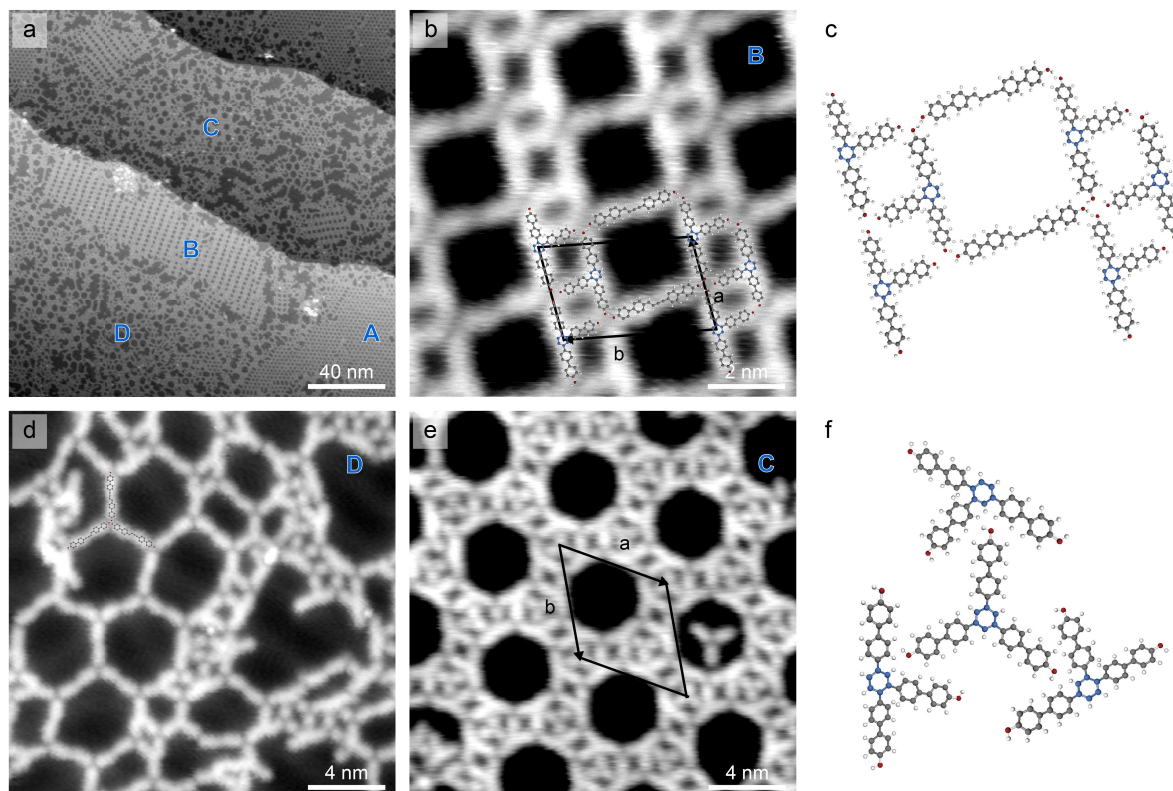
Figure 3.23.: Addition reaction of EHBP molecules after annealing the substrate at 475 K. (a) Large-scale STM image shows different molecular arrangements, denoted as domain **A**, **B**, **C** and **D**. Irregular molecular aggregates can also be found. (b) A zoom-in STM image of domain **B**, can be described by a unit cell of a = 2.48 ± 0.02 nm, b = 4.0 ± 0.02 nm, with an angle of 78°, consisting of trimer-II and dimers, as shown in the proposed model in (c). (d) STM image of domain **D**, dimer species self-assemble into a hexagonal shape arrangement. (e) STM image shows a more complex molecular arrangement (domain **C**). (f) A repeating unit of the pattern in (e), composed of trimer-I and II. Scan parameters: (a) I_t = 100 pA, V_s = -500 mV, (b), (d) and (e) I_t = 100 pA, V_s = -100 mV.
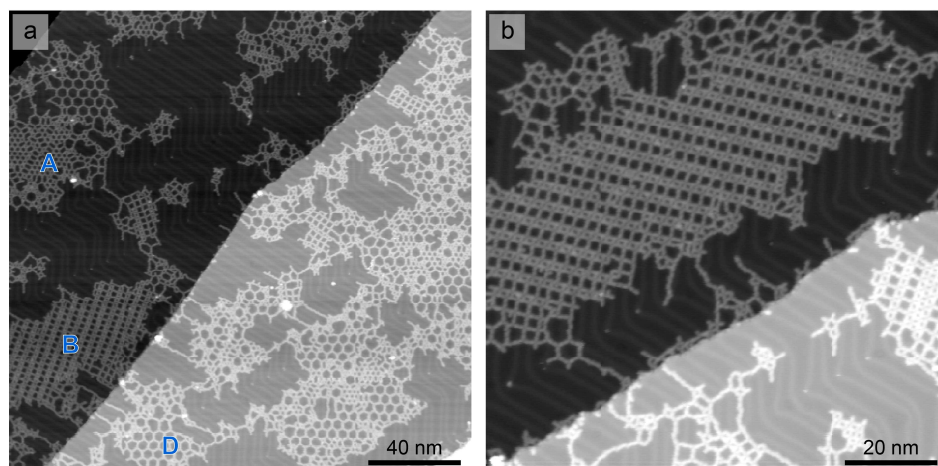
Figure 3.24.: STM images obtained after directly annealing the substrate at 475 K after the deposition of EHBP molecules on a Au(111) surface. In the different regular domains, the ladder shape arrangements tend to be the most common. Scan parameters: (a) and (b) I_t = 100 pA, V_s = -500 mV.

image of the structures, in which three regular islands can be distinguished, **A**, **B** and **D**. However, the ladder shape molecular arrangement (domain **B**), consisting of trimer-II and enyne dimers, is dominant over the surface. The comparison of the two thermal annealing processes reveals a temperature-dependent reaction preference for the alkyne addition reaction.

In contrast to the formation of enyne dimers on Ag surfaces with thermal activation, [186] cyclotrimerization is the dominant reaction pathway for alkynes on Au(111). [177, 185] To investigate the mechanism of the different cyclotrimerization products, it is interesting to consider the possible coupling schemes for the formation of 1,3,5- and 1,2,4-trisubstituted benzene. In the pioneering work on the cyclotrimerization of a diyne on Au(111), [177] a two-step [2+2+2] cyclization reaction involving Au adatoms is suggested, while a reaction pathway starting from the metallacyclopentadiene intermediate was proposed by a study on the use of 1,3,5-tris-(4-ethynylphenyl)benzene.[177] Structurally, the pre-dimerization of two monomers would inhibit the formation of 1,3,5-isomers (trimer-I) via the [2+2+2] cyclization reaction, facilitating, in contrast, the addition of a third alkyne to construct the 1,2,4-isomers (trimer-II). In our experiments, we did notice more accompanied enyne dimer formation along with the 1,2,4-isomers (trimer-II) at a higher annealing temperature. As mentioned in previous studies, Au adatoms would be involved in the dimerization step, whereas high temperatures increase the occurrence of Au adatoms at the surface. Thus we obtained the regioselectivity regarding the synthesis of benzene ring core via the alkyne cyclotrimerizations on Au(111). More important, the hydroxyl directing group facilitates the aggregation of uniform products, providing a suitable condition for product identification and separation.

3.3. Conclusion

In summary, we present a novel approach to synthesize enetriynes with a high selectivity (~85%) on Ag(100) surfaces. The high selectivity is achieved by: hydroxyl groups directing the arrangements in molecular domains; O_2 mediation of the ethynyl groups to organometallic species to avoid the homo-coupling; and the four-fold symmetry of the Ag(100) substrate favourable to the addition reaction to form tetrameric enetriynes. Comparative experiments without O_2-mediation and utilizing Ag(111) substrate accompanied by DFT calculations confirmed the importance of the above parameters and provide insights into the reaction pathways.

On the other hand, oxidative dehydrogenation does not occur on Au(111) with either O_2 dosage or thermal annealing treatments. We examined the trisubstituted benzene compounds. Interestingly, taking advantage of hydroxyl directing groups and controllable annealing, we managed to steer the regioselective alkyne cyclotrimerization and corresponding uniform arrangements were obtained. Controllable annealing of the preassembled system induces the formation of the trimeric species, 1,3,5-trisubstituted benzenes dominate at 375 K and 1,2,4-trisubstituted benzenes dominate at 475 K, which self-assemble into different regular islands. The approach applied in this work may provide an alternative avenue for precursor designing and selective synthesis.

4. Cyclization and Polymerization of Alkyne Substituted Porphyrins – the Role of Aromaticity

4.1. Introduction

Covalent coupled porphyrins architectures are sought-after for their remarkable stability and wide range of physical and chemical functionalities that can be exploited in nanoelectronic circuits, single-atom catalysis [187] and spintronic devices. [188, 189, 190] For instance, the conductance changes induced by tautomerization of the inner hydrogen atoms [191, 192] allow constructing coupled molecular switches and logical elements based on connected free-base porphyrins. The use of metalloporphyrins provides opportunities to embed catalytically active metal centers in a chemical matrix for superior stability at elevated temperatures. Furthermore, metalated porphyrins often exhibit magnetically active spin centers, the interaction of which can be tuned by exact positioning and chemical "locking" of the porphyrin units at defined distances. Such examples underline the importance of the precise and uniform control of the distances between porphyrin molecules. In many cases, it is advantageous to achieve short distances for efficient electronic or magnetic coupling between covalently coupled porphyrin units.

Nanostructures exhibiting short distances between and a high degree of regularity of the monomeric units can be more readily realized in one-dimensional nanostructures. Additionally, conceptually different morphologies (such as branched chains or closed circuits) provide further opportunities to tune the electronic properties of one-dimensional materials, as well as influence their chemical and catalytic behavior via regio- and stereo-selective centers emerging in the nanostructures.

While previous studies report covalent coupling of porphyrins via various synthetic strategies in solution, [193, 194, 195, 196, 197] many of these are limited in the number of coupled units – largely due to hampered solubility of extended structures in solution. This problem is circumvented in on-surface synthesis, which has been used to construct larger structures without solubility constraints. [198, 199, 200] The repertoire of synthetic strategies on surfaces, as of yet, is more limited than in solution; covalent C-C bonds are predominantly realized via Ullmann coupling on metal substrates, in which halogen atoms in the precursor molecules are cleaved off to form reactive carbon species that then form C-C bonds. [6] However, the formation of C-C bonds directly at the periphery of porphyrin molecules has not been demonstrated so far, likely due to steric constraints. Instead, additional "spacers" (i.e., phenyl rings, which the halogen atoms are attached to) have to be used, leading to increased distances

between the units in the resulting chains (1.70 to 1.80 nm center-to-center). [201] A different type of reaction, alkyne homocoupling, for which first attempts have been reported, [202] avoids the use of extra phenyl rings as spacers; however, due to the presence of the two alkyne units in the junction, the inter-porphyrin distance is still around 1.35 nm.
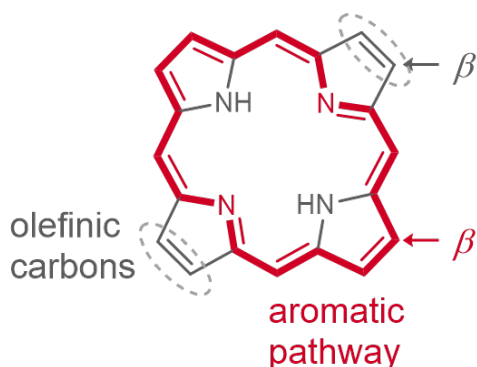
Figure 4.1.: Aromaticity-driven regioselectivity in free-base porphyrins. The aromatic 18 π-electron diaza[18]annulene pathway (red highlighted bonds) along the macrocycle of a free-base porphyrin omits four carbon atoms. Thus, there are two chemically different types of carbon atoms at the β positions: carbons with aromatic character and carbons with olefinic (i.e. double-bond) character. [203, 204, 205]

The smallest possible distance between porphyrins is obtained by "head-on" coupling of the units ($\sim$0.90 nm) to yield directly triply-fused bisporphyrins.ref Here, three C-C bonds are formed between equivalent carbon atoms (at beta, meso, and beta positions) directly at the peripheries of the porphyrins. In fact, such products have been synthesized on metal surfaces via catalytic dehydrogenative homocoupling of porphyrins. [206, 36, 207] However, the control of such homocoupling reactions is difficult because side reactions commonly occur, leading to other types of connections and therefore limiting the regularity and the lengths of the chains. Thus, the synthesis of extended nanostructures with regularly spaced porphyrin units at close distances remains a challenge, which demands the creation of localized reactive centers by functional groups that yield minimal spatial extension in the products.

Here we present the synthesis of extended one-dimensional (1D) porphyrin nanostructures on Au(111) with a center-to-center distance of 1.10 to 1.20 nm for porphyrin units. The selectivity of the coupling reaction is greater than 90% leading to regular chain segments whose lengths can exceed 50 units. In addition, we also observe the formation of closed one-dimensional circuits (i.e., rings). We use free base porphyrin precursors with alkyne substituents on two opposite meso positions (5,15-bis((trimethylsilyl)ethynyl)porphyrin, denoted as **1a**, see the chemical structure in Figure 4.2a). To prevent polymerization in the crucible during thermal sublimation, the alkyne groups are protected with trimethylsilyl groups (SiMe$_3$). After deposition of the precursors onto the metallic substrate, these protective SiMe$_3$ groups cleave off to generate undersaturated carbons atoms, which then direct coupling in one dimension. The alkyne groups additionally undergo cyclization reactions, thus

shrinking the porphyrin-porphyrin distance by ~15% compared to uncyclized alkyne-alkyne junctions.

By using scanning tunneling microscopy (STM) and bond-resolved atomic force microscopy (AFM), we determined the precise atomic-scale structure of the synthesized nanostructures and gained further insights into the regioselectivity of the reaction. Both, the intermolecular coupling, as well as the intramolecular cyclization proceed via two different routes, i.e., (Z)- and (E)-coupling which refers to the position of porphyrin units, as shown in Figure 4.2b; *cis* and *trans* cyclization refers to the positioning of five-membered ring formation linking a meso and β carbon (Figure 4.2b). The coupling does not show a very strong preference for one of the two pathways ((Z)- and (E)-); the situation is different, however, for the cyclization. Statistical analysis reveals that *trans*-cyclization is more than five times more common than *cis*-cyclization.

This behavior can be rationalized by the 18π diaza-annulene [203, 204] aromatic pathway of the porphyrin precursors, which gives rise to specific local reactivity for free base porphyrins – aromatic versus olefinic carbon atoms at the β positions (i.e. at the "corners") of the molecules (cf. Figure 4.1); And thus a preference for *trans*-cyclization. This is in agreement with the energetic description by density functional theory (DFT) calculations, which show that the *trans*-cyclized species are preferred to *cis*-cyclized species. Additionally, the thermodynamic stability of the reaction products shows a direct correlation with the molecular aromaticity (quantified based on the bond length alteration along the aromatic pathways).

Understanding the reactivity of porphyrins and porphyrin nanostructures has direct implications for preserving their remarkable stability – grounded in their 18π-electron aromaticity – and thus for utilization of their versatile chemical and physical functionalities in a wide range of environments.

4.2. Alkyne-substituted free-base porphyrins on Au(111)

4.2.1. The formation of 1D porphyrin nanostructures

We used free-base porphyrins with alkyne substituents on two opposite meso-positions as precursors: 5,15-bis((trimethylsilyl)ethynyl)porphyrin, denoted as **1a**, see the chemical structure in Figure 4.2. To prevent polymerization in the crucible during thermal sublimation, the alkyne groups were protected with trimethylsilyl groups (-SiMe$_3$). Deposition of **1a** on a Au(111) substrate kept at room temperature leads to the formation of small islands with self-assembled molecules and few isolated species (Figure 4.3a). The molecules appear rod-like with bright spots at the two termini, assigned to the bulky -SiMe$_3$ groups. Figure 4.4 gives the STM image and the corresponding AFM image of a small island of self-assembled molecules after annealing the substrate at 205 °C. The alignment of the molecules indicates interaction between the -SiMe$_3$ groups, which appear as bright spots at the termini of the rod-shaped molecules. The overlaid chemical structure on the corresponding AFM image reveals protrusions at the positions of the -SiMe$_3$ groups. The dashed gray circle marks a region with less brightness, which possibly emerged from an initial reaction step, in which the
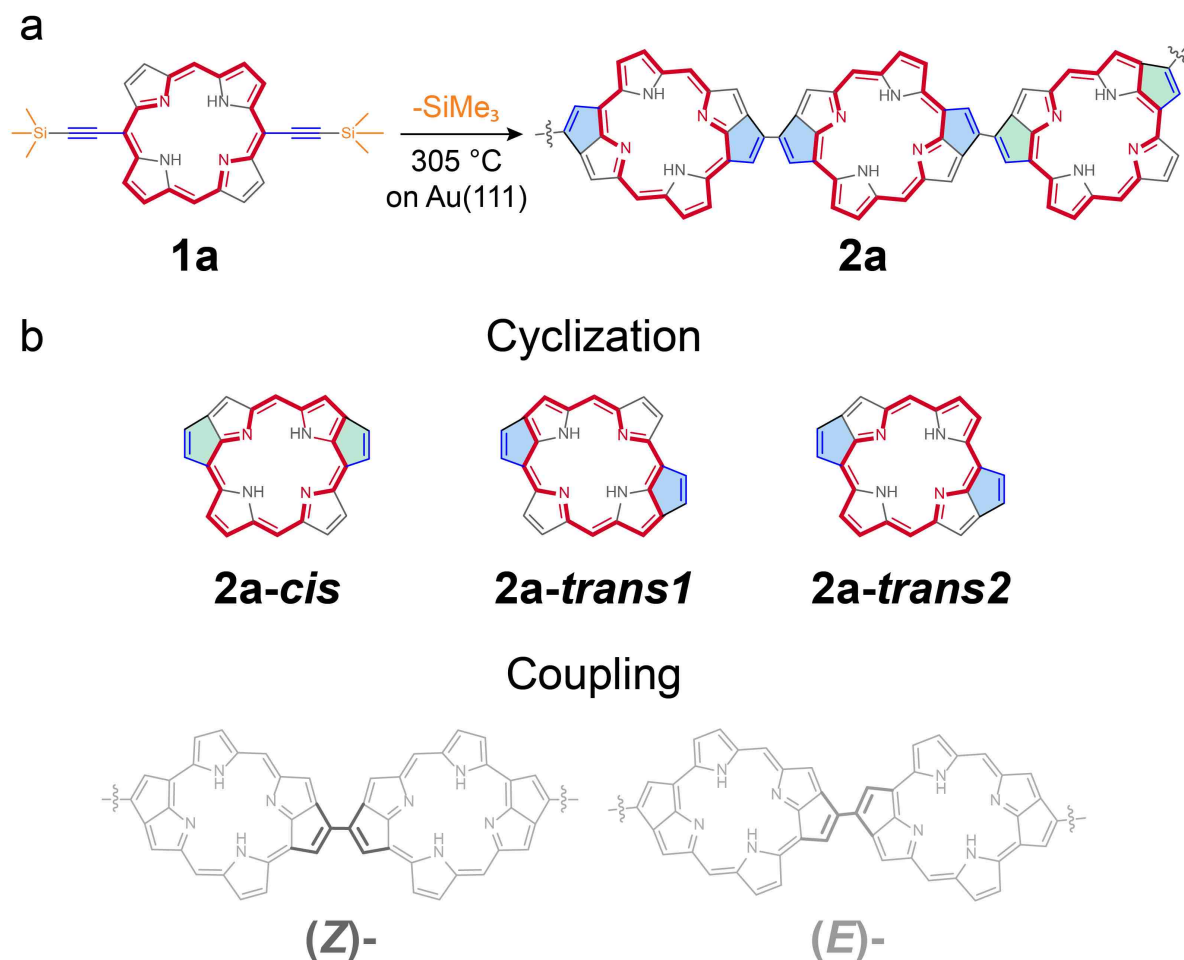
Figure 4.2.: Reaction scheme of cyclization and coupling of alkyne-substituted free-base porphyrins. (a) Reaction scheme of the transformation of the SiMe$_3$-alkyne-substituted porphyrin precursor **1a** towards covalently coupled one-dimensional porphyrin nanostructures **2a**. Thermally induced cleavage of the -SiMe$_3$ group exposes a reactive carbon atom, which participates in the formation of two new C-C bonds, leading to: (i) intramolecular cyclization to cyclopenta[*at*]porphyrin units via formation of five-membered rings (highlighted by green and blue fill-color), and (ii) intermolecular coupling. (b) Chemical structures of different isomeric reaction products emerging from the cyclization reactions (**2a-*cis***, **2a-*trans1***, **2a-*trans2***) and the coupling reactions ((*Z*)- and (*E*)-). The bold red highlight in the chemical models denotes the aromatic 18 π-electron diaza[18]annulene pathway observed in free-base porphyrins. [203, 204, 205]
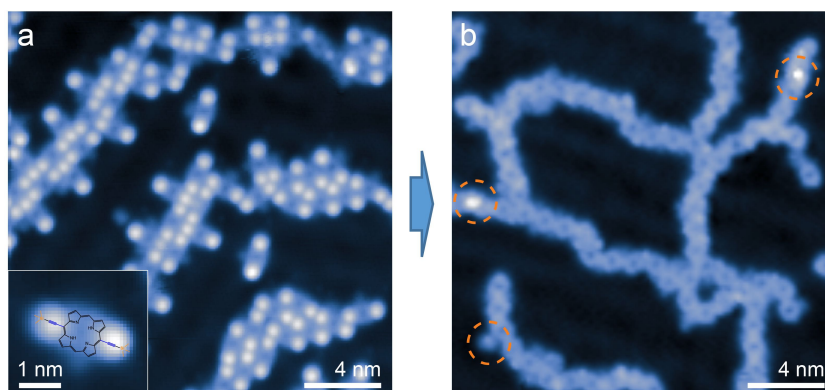
Figure 4.3.: Cyclization and polymerization of alkyne-substituted free-base porphyrins on Au(111). (a) STM image of the precursor **1a** after deposition on a Au(111) held at room temperature shows self-assembled structures. The inset shows an isolated molecule with two protrusions at the positions of the -SiMe$_3$ groups. (d) STM image after annealing at 305 °C showing the formation of covalently linked porphyrin nanostructures (**2a**), i.e., chains and ring-like elements, via cyclization and coupling. Scan parameters: (c) I_t = 10 pA, V_s = 50 mV, (d) I_t = 2 pA, V_s = 50 mV.
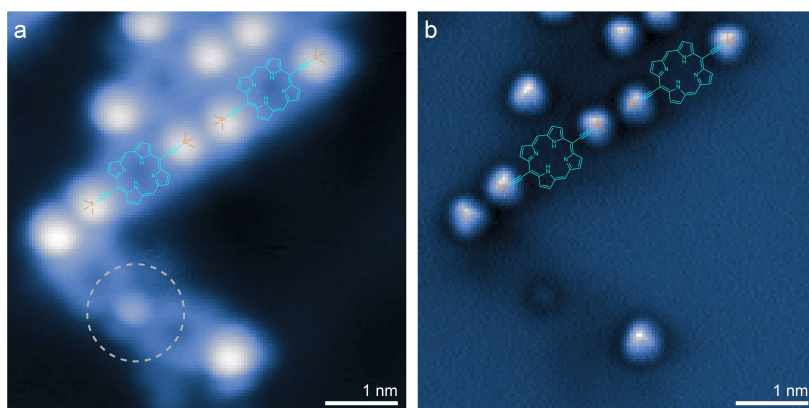
Figure 4.4.: Self-assembled structures of **1a**. (a) STM image of a small island of self-assembled molecules after annealing at 205 °C shows predominantly unreacted molecules (scan parameters: I_t = 2 pA, V_s = 50 mV). (b) The corresponding AFM image of the same area as (a) reveals protrusions at the positions of the -SiMe$_3$ groups (scan parameters: V_s = 0 V, constant height).

partial cleavage of -SiMe$_3$ leads to an intermediate connection motif between the molecules.

Step-wise annealing the substrate induced -SiMe$_3$ cleavage and coupling. As shown in Figures 4.4 and 4.5a, annealing at 205 °C, most of the precursors were seen to be in self-assembled islands; additionally, some reaction intermediates were formed (the dashed gray circle in Figure 4.4). Annealing at 245 °C, most of the bright spots (i.e., -SiMe$_3$) were removed, and 1D polymerized and ring-like structures emerged. At higher temperatures (275 °C), almost all bright spots were removed, and nearly all molecules participated in the formation of 1D nanostructures. The dark appearance of the molecular centers in the STM images does not unambiguously confirm the absence of metal centers, [208, 209, 198] but as no change in the appearance of the interior of the molecules was seen after annealing, we conclude that self-metalation with substrate atoms does not play a role, as expected from previous studies of porphyrins on Au(111). [206]
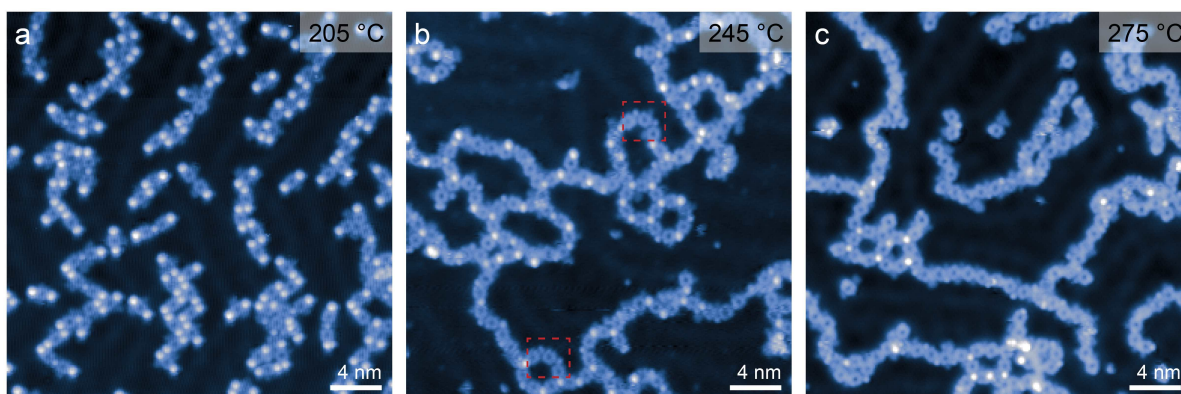
Figure 4.5.: Thermally induced -SiMe$_3$ cleavage and coupling. (a) After annealing at 205 °C, most of the precursors were seen to be in self-assembled islands. (b) After annealing at 245 °C, most of the bright spots (i.e. -SiMe$_3$) were removed. Putative reaction intermediates with less bright spots between molecules were seen (examples are marked by dashed red rectangles). (c) At higher temperatures (275 °C), almost all bright spots were removed, and almost all molecules have undergone cyclization and coupling reactions. The duration of all annealing steps was 10 minutes. Scan parameters: (a) and (c) I_t = 2 pA, V_s = 50 mV, (b) I_t = 2 pA, V_s = 100 mV.

Annealing the substrate at 305 °C induced a fully chemical transformation (bright spot cleavage) towards extended 1D nanostructures with lengths commonly exceeding 30 units (Figure 4.3b). The predominant products were chains with mostly regular arrangements of porphyrins forming straight, as well as angled connections, with few branching points (see also Figure 4.5). Some of the structures formed closed loops, i.e., nanorings, typically consisting of 5 to 6 units. Additionally, we observed that almost all of the bright features associated with -SiMe$_3$ groups disappeared and only very few putative -SiMe$_3$ remnants remained on the surface (see dashed orange circles in Figures 4.3b and 4.6a). We thus conclude that the -SiMe$_3$ groups cleaved off and desorbed upon annealing, in agreement with previous

studies. [210]

4.2.2. Bond-resolved imaging of 1D porphyrin nanostructures

To clarify the connection motifs between porphyrin units, we performed bond-resolved AFM measurements with CO-functionalized tips. [70] The AFM images of the polymeric structures (Figure 4.6) indicate covalent connections between the porphyrin units with center-to-center distances of 1.10 to 1.20 nm. Furthermore, the images reveal the formation of additional five-membered rings at the periphery of the porphyrins. Both reactions appear to be facilitated by the cleavage of the -SiMe$_3$ group, which exposes a reactive carbon atom; this atom then participates in the formation of two new C-C bonds associated with coupling and cyclization (Figure 4.2a).

For the coupling reaction, we observe two different reaction pathways. These lead to (Z)- and (E)-type stereoisomers, which are defined with respect to the orientation of two neighbouring porphyrin units about the connecting C-C bond (Figure 4.2b). Figure 4.6b shows a high-resolution image of a fragment composed of three porphyrin units showing both, (E)- and (Z)-type coupling. The coupling type is directly related to the morphologies formed: straight segments imply (E)-coupling, while (Z)-coupled sequences lead to the formation of curved and ring-like structures. Our experiments show that (Z)-coupling is slightly more common than (E)-coupling (Figure 4.6d).

The additional rings at the periphery of the porphyrins originate from cyclization reactions of the ethynyl residues. [110, 157] In the vast majority of cases (> 95%), five-membered rings are formed (the minority side products see in Figure 4.8). The relative position of the two formed rings at both sides of the porphyrin leads to different isomers: *cis-* and *trans-*isomers. These are associated with the regioselectivity of the cyclization reactions, i.e. which β-pyrrole carbons the reactive ethinyl carbon atoms connect to (see Figure 4.2b). The high-resolution images (Figure 4.6b, c) further reveal an increased brightness for some of the five-membered rings. This is likely caused by geometric distortions [72, 212, 213] and in some cases might be related to the degree of saturation at the specific carbon atoms, i.e., extra hydrogen atoms pointing away from the surface [214] (see also Figure 4.9)

Statistical analysis of more than 200 molecules (Figure 4.6d) reveals that *trans-*cyclization occurred much more frequently than *cis-*cyclization: 85% of molecules were found to be in *trans-*configuration, compared to 15% of *cis-*cyclized molecules (typical errors for these estimates are ± 3%). This preference for *trans-*cyclization was not dependent on whether the molecules were coupled or isolated: Analysis of more than 50 isolated molecules (about 3% of molecules remained isolated) similarly gave a four times the higher abundance of *trans-*cyclized species.

To clarify the *trans-*cyclization product, we observed AFM images of a chain of three *trans-*cyclized and one *cis-*cyclized molecule at different tip-sample distances (see Figure 4.7) and performed tip-manipulation experiments. We determined that the all or almost all *trans-*cyclized species are of type **2a-*trans2***). In Figure 4.10a, application of a voltage pulse (V_s = 3.2 V) close to the center of a *trans-*cyclized molecule within a chain leads to cleavage of an inner hydrogen atom. A substantial contrast change on the lower side can be observed,
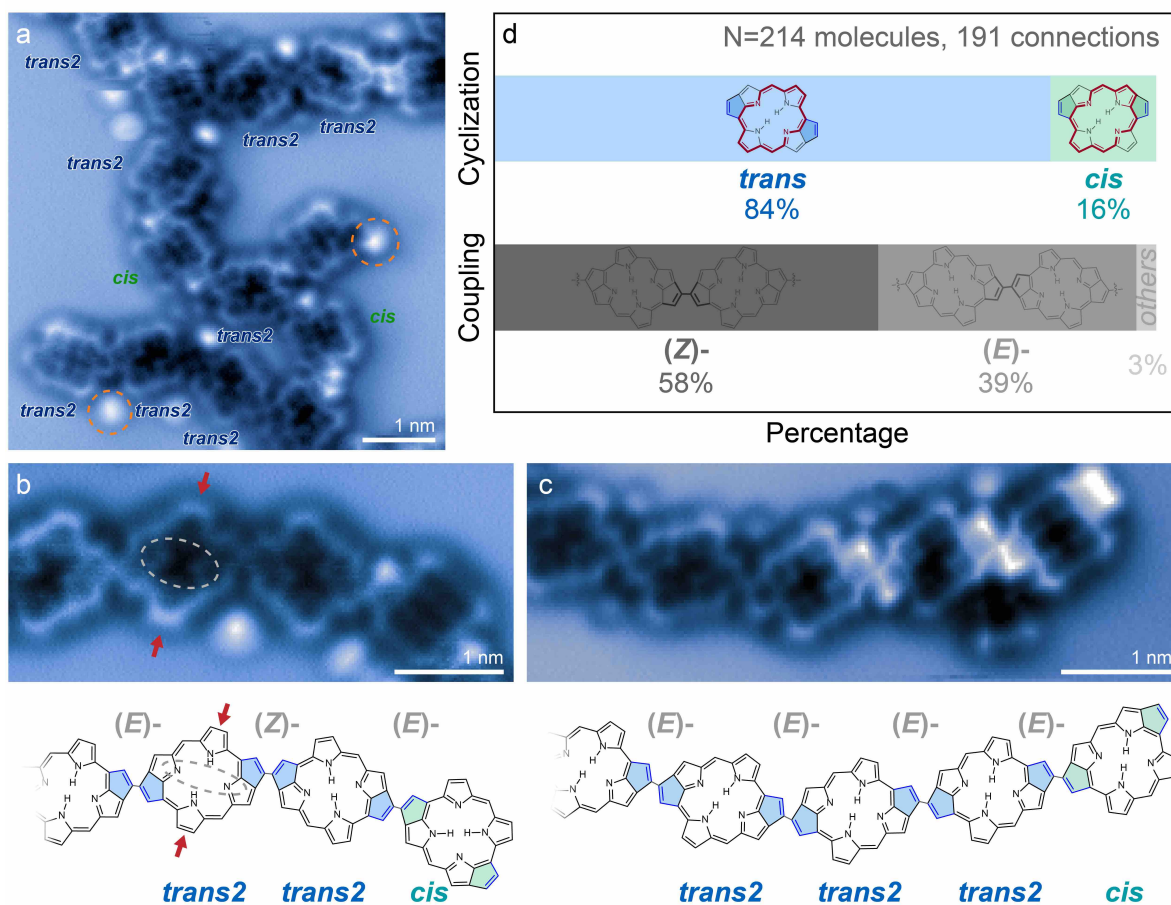
Figure 4.6.: Regio- and stereo-selectivity of cyclization and coupling reactions. (a) Bond-resolved AFM image of the porphyrin nanostructures (**2a**) shows regular segments and few irregular coupling motifs creating branches. Bright spots nearby the molecules (dashed orange circles) are likely related to remnants of -SiMe$_3$ or small adsorbed molecules (such as CO). (b), (c) High-resolution AFM images and their corresponding chemical structures highlight the different possible reaction products for coupling, i.e., (*Z*)- and (*E*)-, as well as for cyclization, i.e. *cis* and *trans*. Brighter features at larger tip heights indicate that the *trans*-species are of type **2a-trans2** (see Figure 4.7). Similar features can also be seen at the tip height shown here: the dashed grey ellipse marks brighter features inside the macrocycle associated with the iminic nitrogens. (d) Statistical analysis of reaction products for the different pathways for coupling and cyclization. For intramolecular cyclization, a strong preference for a *trans* product is evident, while intermolecular coupling shows a more balanced yield of (*Z*)- and (*E*)-coupled products. Scan parameters: $V_s = 0$ V, constant height.
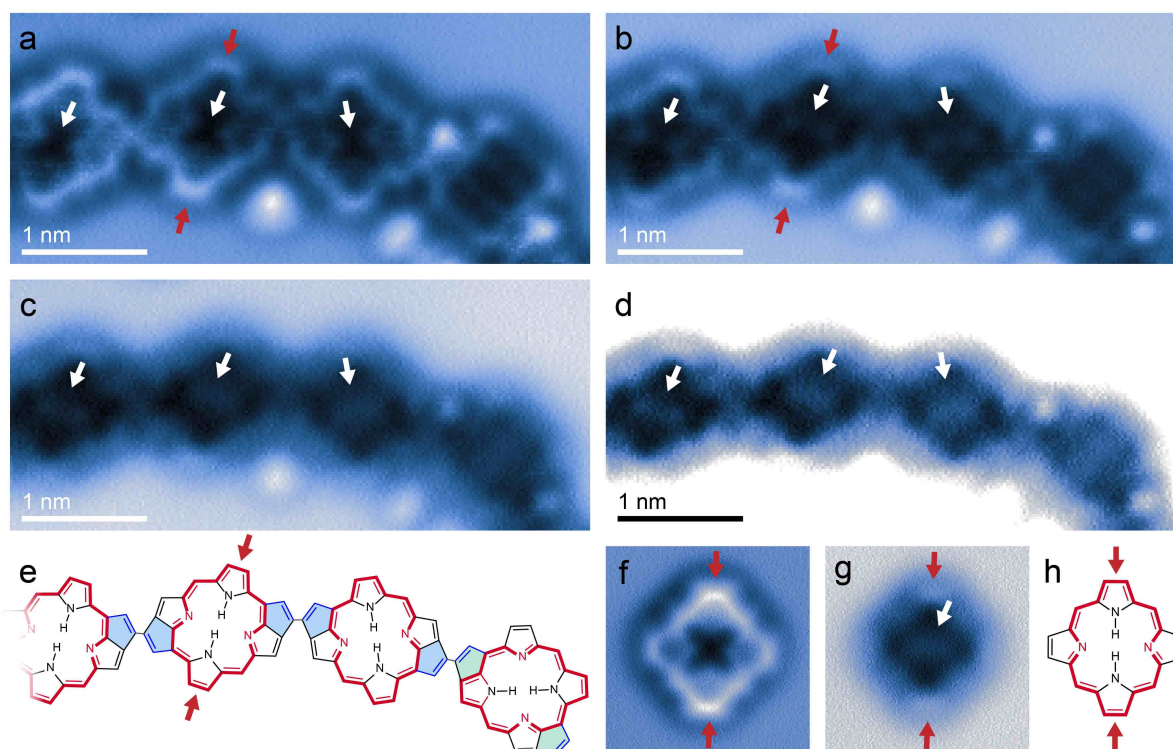
Figure 4.7.: Identification of hydrogen tautomers via AFM. (a-c) AFM images of a chain of three *trans*-cyclized and one *cis*-cyclized molecule at different tip-sample distances. The *trans*-cyclized species show brighter features associated with one pair of nitrogen atoms at opposite sides, as marked by white arrows. (d) The same image as in (c), but with increased contrast. Such bright features connecting one pair of opposing nitrogen atoms were observed in previous work and assigned to iminic nitrogen atoms, [211] i.e., nitrogen atoms within the pyrrole rings that do not carry internal hydrogens. This assignment corresponds to the **2a-*trans2***) type. (e) Proposed chemical structure of the chain, consisting of three **2a-*trans2***) and one **2a-*cis***) molecule. (f),(g) AFM images of an unsubstituted porphyrin molecule adsorbed on Au(111) show similar features at larger tip-sample heights: a line along the direction of the iminic nitrogen atoms can be seen, marked by the white arrow. (h) Chemical structure of the molecule in (f) and (g). Red arrows mark aminic pyrroles. We have investigated 165 *trans*-cyclized molecules, all of which exhibit these particular features, suggesting that (almost) all of the *trans*-cyclized species are of type **2a-*trans2***). Further support for this assignment is obtained by tip manipulation experiments (see Figure 4.10). Scan parameters: $V_s = 0$ V, constant height.
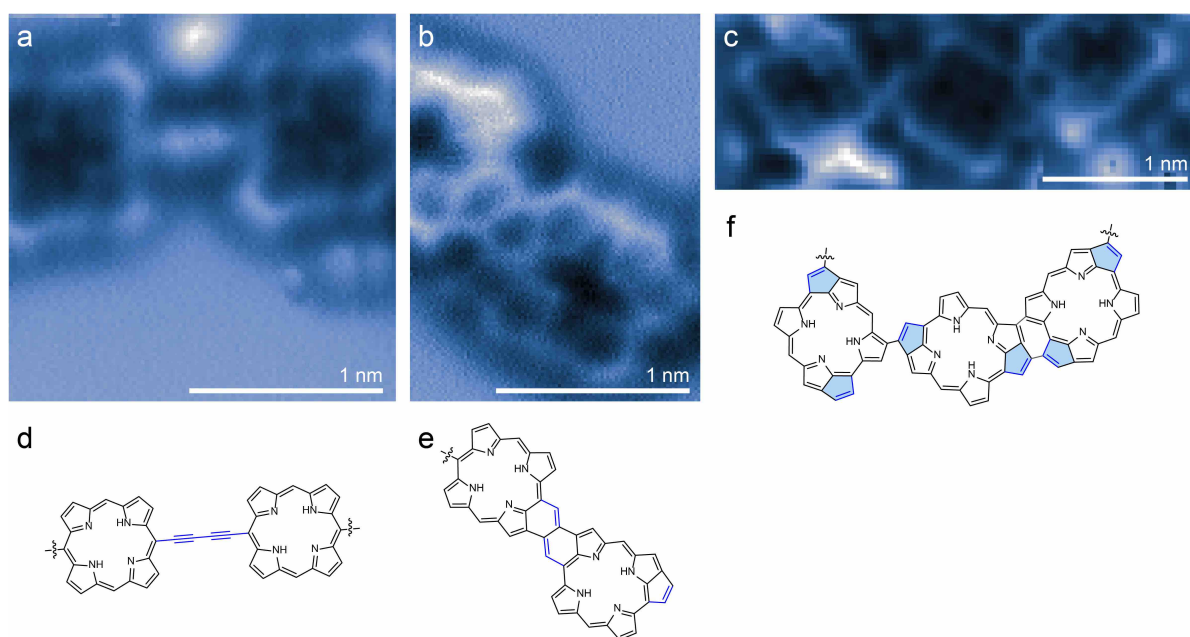
Figure 4.8.: Side products of the reaction of free-base porphyrins. Bond-resolved AFM images and derived chemical structures of minority products that emerged from side reactions of **1a**. (a) Alkyne homo-coupling. (b) Formation of six-membered rings. (c) Unspecific cyclodehydrogenative coupling at the porphyrin periphery. (d)-(f) Chemical structures derived from the bond-resolved AFM images of (a)-(c). Scan parameters: (a)-(c): $V_s = 0$ V, constant height.

as marked by filled (before manipulation) and outlined (after manipulation) red arrows. We thus deduce that the pyrrole ring at this position was carrying one of the inner hydrogen atoms before the manipulation. This assignment corresponds to a **2a-*trans2***) type molecule. A similar experiment (with a voltage pulse of V_s = 3.2 V, Figure 4.10b) shows the cleavage of both inner hydrogen atoms, inducing contrast changes at the top and bottom (marked by red arrows). Again, these positions are associated with the pyrroles that carry the inner hydrogen atoms, indicating that this molecule is of the type **2a-*trans2***). We have successfully performed such manipulation experiments on 10 molecules, all of which were confirmed to be of type **2a-*trans2***). Figure 4.10c shows an analogous experiment on unsubstituted porphyrin molecules adsorbed on Au(111). The two inner hydrogens can be cleaved off in two steps, both times associated with contrast changes at the respective hydrogen-carrying pyrrole rings (marked by red arrows).

It is noteworthy that tip-induced tautomerization was not observed in any of the experiments on the chains, neither in the STM or AFM measurements, nor in the manipulation experiments, even though we have exceeded the parameters typically used for such hydrogen switching. [215, 216, 217, 191, 218] This is in agreement with the theoretical predictions of the higher stability of one tautomer **2a-*trans2***). Thus, even though tautomerization in porphyrins is readily induced by thermal energy, [218, 219] it is expected that in our (symmetry-broken) case the residence time of the inner hydrogens is substantially skewed towards the positions associated with **2a-*trans2*** (as the response of the electronic system is always much faster than the proton displacement frequency, the distinction between olefinic and aromatic moieties still holds under reaction conditions at elevated temperatures). Nevertheless, it can be interesting to hypothesize what effect tautomerization may have on product distribution. First, tautomerization of the products can in principle interconvert between **2a-*trans1*** and **2a-*trans2***. The two tautomers of **2a-*cis*** are equivalent and correspond to different adsorption positions on the substrate (an effect we accounted for and discussed in Figure 4.15). Both, theory (see Figure 4.17) and experiment show that no (or almost no) **2a-*trans1*** species are formed, thus it is likely that tautomerization at this stage does not play a significant role (as expected from the absence of tip-induced switching). Importantly, even if tautomerization played a role, it would not affect the *cis/trans* ratio, as interconversion between *cis-* and *trans*-cyclized products by tautomerization is not possible.

Furthermore, we can consider interconversion between the half-cyclized intermediates **2a-*pre1*** and **2a-*pre2*** by tautomerization. Based on the theoretical calculations of the reaction pathways (Appendix Figures A.5-A.8), as well as the kinetic simulations (see Figure 4.17), **2a-*pre2*** is the preferred species. If some of the **2a-*pre2*** species were transformed into **2a-*pre1*** by tautomerization, theory predicts that more *cis*-cyclized species would be formed (see Figure 4.17). Tautomerization at this stage is thus also not the driving force behind the strong preference for *trans*-cyclized species. Instead, the high yield of *trans*-cyclized species is caused by differences in chemical reactivity for the cyclization reactions at the two types of β-carbons – such chemical differences are explained by the aromatic diaza[18]annulene pathway in porphyrins.
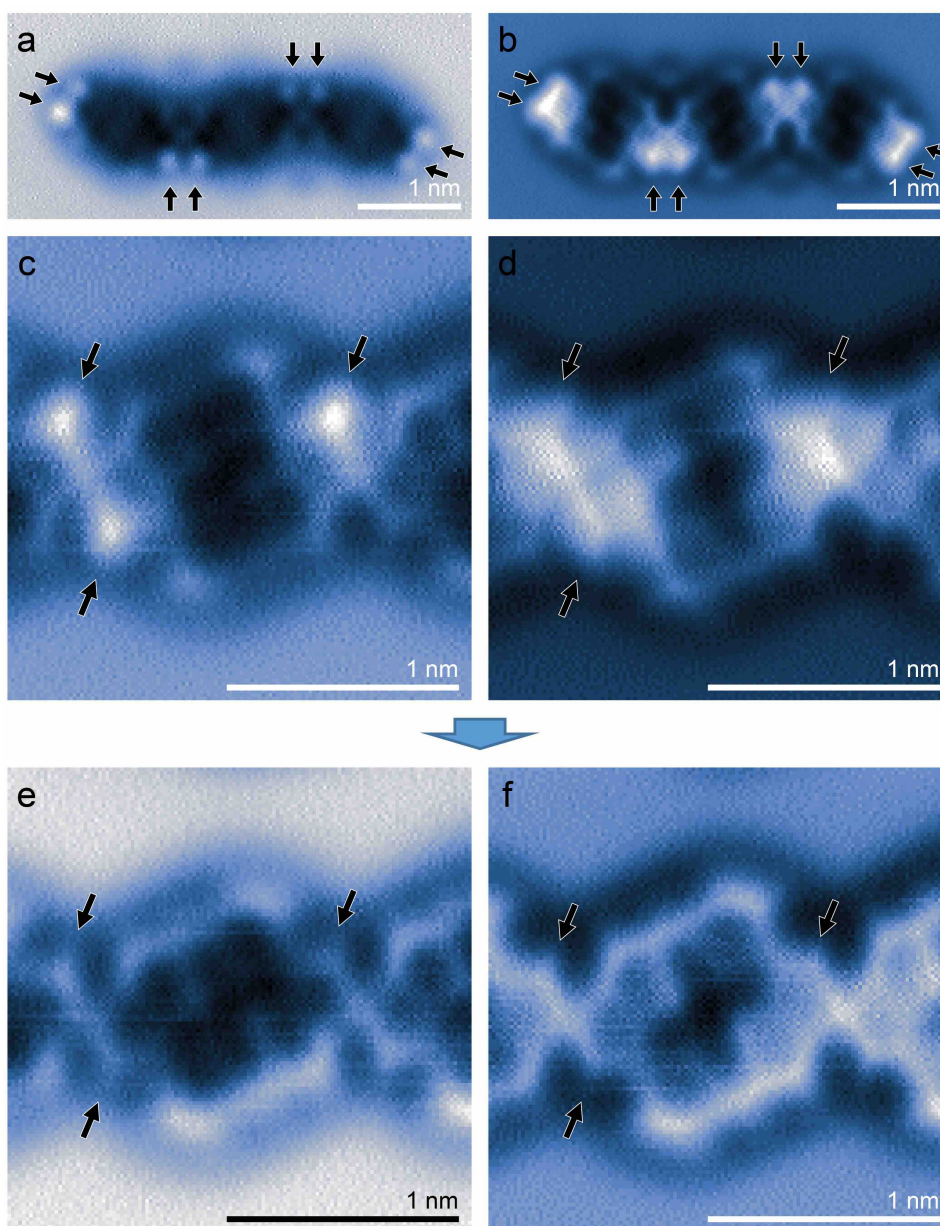
Figure 4.9.: Tip-induced transformation of the cyclization products. (a),(b) AFM images at two different tip-sample distances of a chain. The black arrows mark positions of increased brightness, suggesting geometric protrusions at the positions of the five-membered rings at the periphery of the porphyrin. (c),(d) Close-up AFM measurements of a molecule within a chain at two different tip-sample distances show similar features with increased brightness (black arrows). (e),(f) AFM images of the same molecule at two different tip-sample distances after the application of voltage pulses (V_s = 3.0 V). The molecule now appears mostly flat, suggesting a tip-induced cleavage of hydrogen atoms, [220, 221, 222] i.e., a transformation of sp3-hybridized carbon atoms within the five-membered rings towards sp2-hybridized atoms.
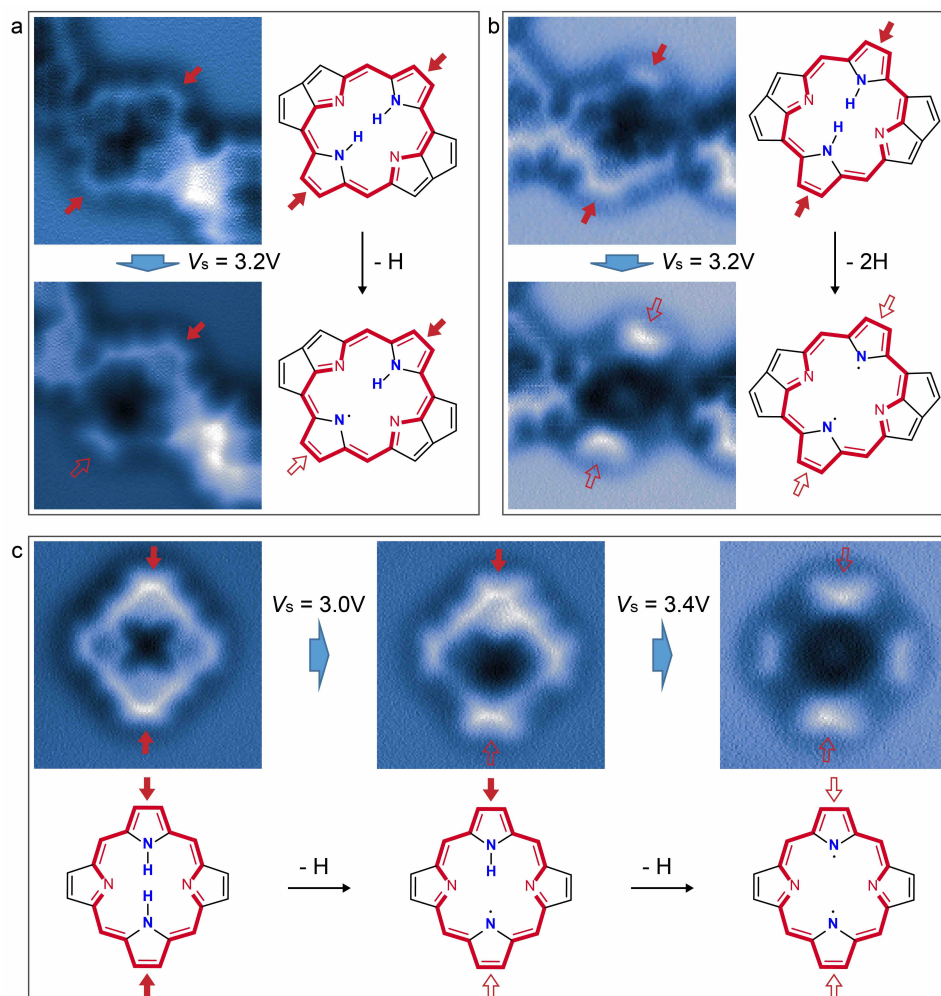
Figure 4.10.: Tip-induced cleavage of inner hydrogens. (a) Application of a voltage pulse (V_s = 3.2 V) close to the center of a *trans*-cyclized molecule within a chain leads to cleavage of an inner hydrogen atom. [215, 216, 217] A substantial contrast change on the lower side can be observed, as marked by filled (before manipulation) and outlined (after manipulation) red arrows. We thus deduce that the pyrrole ring at this position was carrying one of the inner hydrogen atoms before the manipulation. This assignment corresponds to a **2a-*trans2*)** type molecule. (b) A similar experiment (with a voltage pulse of V_s = 3.2 V) shows the cleavage of both inner hydrogen atoms, inducing contrast changes at the top and bottom (marked by red arrows). Again, these positions are associated with the pyrroles that carry the inner hydrogen atoms, indicating that this molecule is of the type **2a-*trans2*)**. (c) Analogous experiments on unsubstituted porphyrin molecules adsorbed on Au(111). The two inner hydrogens can be cleaved off in two steps, both times associated with contrast changes at the respective hydrogen-carrying pyrrole rings (marked by red arrows).

4.2.3. The role of aromaticity in the reactivity of free-base porphyrin

To understand the origin of this regioselectivity, we studied the energetics of the cyclization reaction by DFT calculations. In particular, we determined reaction energies for the three possible transformation pathways, i.e., the energy differences between the reactant molecule (**1a**) and the three possible products (**2a-cis**, **2a-trans1**, **2a-trans2**) adsorbed on Au(111). We modelled **1a** as an alkyne-substituted porphyrin (i.e., without the -SiMe$_3$ groups), such that the transformation does not entail any change of the number of atoms and the respective energies of the relaxed systems can be compared with each other. A different choice for the model of **1a** would not change any of the conclusions below, as we compare the products with each other (with respect to the reference point of **1a**).

The most stable adsorption configurations of the reactant and each of the three possible cyclization products are shown in Figure 4.11a. The two *trans*-cyclized products, **2a-trans1** and **2a-trans2**, are different N-H tautomers: Despite their otherwise equal chemical structure, the different positions of the inner hydrogen atoms cause a different optimal adsorption position on the substrate and, importantly, influence the aromatic pathway (which will be discussed in detail below). While other hydrogen tautomeric configurations are conceivable, [219, 223] we have restricted our calculations to the most common scenario of tautomers, in which the inner hydrogens are in opposite positions. [191, 192, 224, 225, 226, 227] For the *cis*-cyclized product (**2a-cis**), as well as for the reactant **1a**, different hydrogen tautomers can be seen as mirror images of each other and are thus equivalent.

The DFT simulations reveal that **2a-trans2** is the energetically most favourable product (ΔE = -2.17 eV), followed by **2a-cis** (ΔE = -2.04 eV), and **2a-trans1** (ΔE = -2.01 eV). This trend is still valid if the respective molecules occupy different adsorption sites, which might be the case for the porphyrin units within the chains (see below and Figure 4.12). The calculated energy differences directly explain why *cis*-cyclized species were less commonly observed in our experiments. However, since all the reaction pathways are exothermic with reaction energies differences of less than 0.2 eV, the coexistence of the different products is predicted (see Figure 4.13 for estimation of relative abundances of reaction products). This agrees with our experimental observations showing a coexistence of *cis*- and *trans*-cyclized species. The calculations furthermore suggest that the **2a-trans2** tautomer is more common, in agreement with the experimental assignments.

These findings can be interpreted in the chemical framework of aromaticity. The aromatic pathway in free-base porphyrins (diaza[18]annulene with 18 π-electrons, red-coloured bonds in Figures. 4.2b and 4.11a) does not include all atoms in the macrocycle, but instead omits two C$_\beta$=C$_\beta$ units at opposite "corners" (cf. Figure 4.1). Due to the olefinic character and the increased reactivity of these carbon atoms, [228, 229] it is expected that these carbon atoms preferably react with the terminal alkyne carbon atoms in the cyclization. This is exactly what happens in the formation of the energetically most stable product **2a-trans2**. For **2a-cis**, on the other hand, only one of the alkyne groups forms a ring involving an olefinic carbon atom, while the other one attaches to a β-carbon within the aromatic pathway. For **2a-trans1**, the least favourable product, both extra rings involve carbon atoms within the aromatic pathway.

To connect the two perspectives, i.e., the energetics based on DFT calculations and the intu-
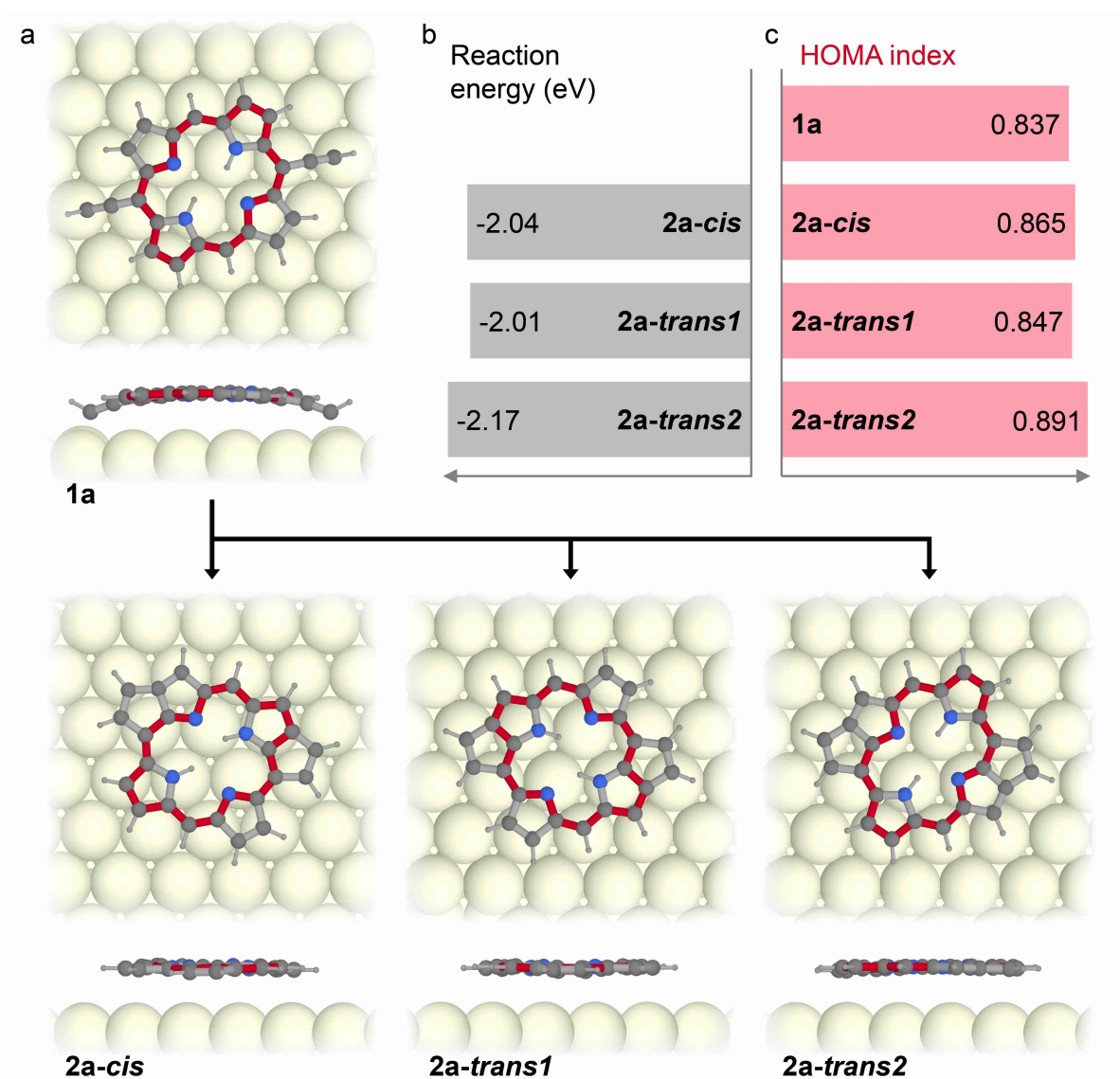
Figure 4.11.: Correlation between aromaticity and thermodynamical stability. (a) Top and side views of DFT relaxed structures of the precursor **1a** and the possible cyclization products: **2a-*cis***, **2a-*trans1*** and **2a-*trans2***. **2a-*trans1*** and **2a-*trans2*** correspond to different N-H tautomers (i.e., different configuration of the inner hydrogen atoms). The red bonds mark the aromatic 18 π-electron diaza[18]annulene pathway in the structures. (b) DFT-calculated reaction energies are correlated with (c) the HOMA-aromaticity indices for the respective cyclization products.

a

	fcc 15°	bridge	bridge	hcp 15°	fcc 45°	
$\Delta E_{reaction}$(eV)	-2.04	-2.03	-2.02	-1.98	-1.95	-2.08
ΔE_{ads}(eV)	-2.65	-2.64	-2.63	-2.59	-2.56	
HOMA	0.865	0.856	0.862	0.862	0.857	0.863

b

	bridge	fcc 0°	hcp 15°	fcc 15°	fcc 45°	bridge	
$\Delta E_{reaction}$(eV)	-2.01	-1.99	-1.99	-1.96	-1.93	-1.93	-2.03
ΔE_{ads}(eV)	-2.67	-2.65	-2.65	-2.62	-2.59	-2.59	
HOMA	0.847	0.844	0.848	0.848	0.848	0.848	0.849

c

	bridge	hcp 45°	bridge	fcc 45°	top	top	
$\Delta E_{reaction}$(eV)	-2.17	-2.15	-2.14	-2.13	-2.10	-2.05	-2.15
ΔE_{ads}(eV)	-2.71	-2.69	-2.68	-2.67	-2.64	-2.59	
HOMA	0.891	0.889	0.897	0.891	0.890	0.889	0.909
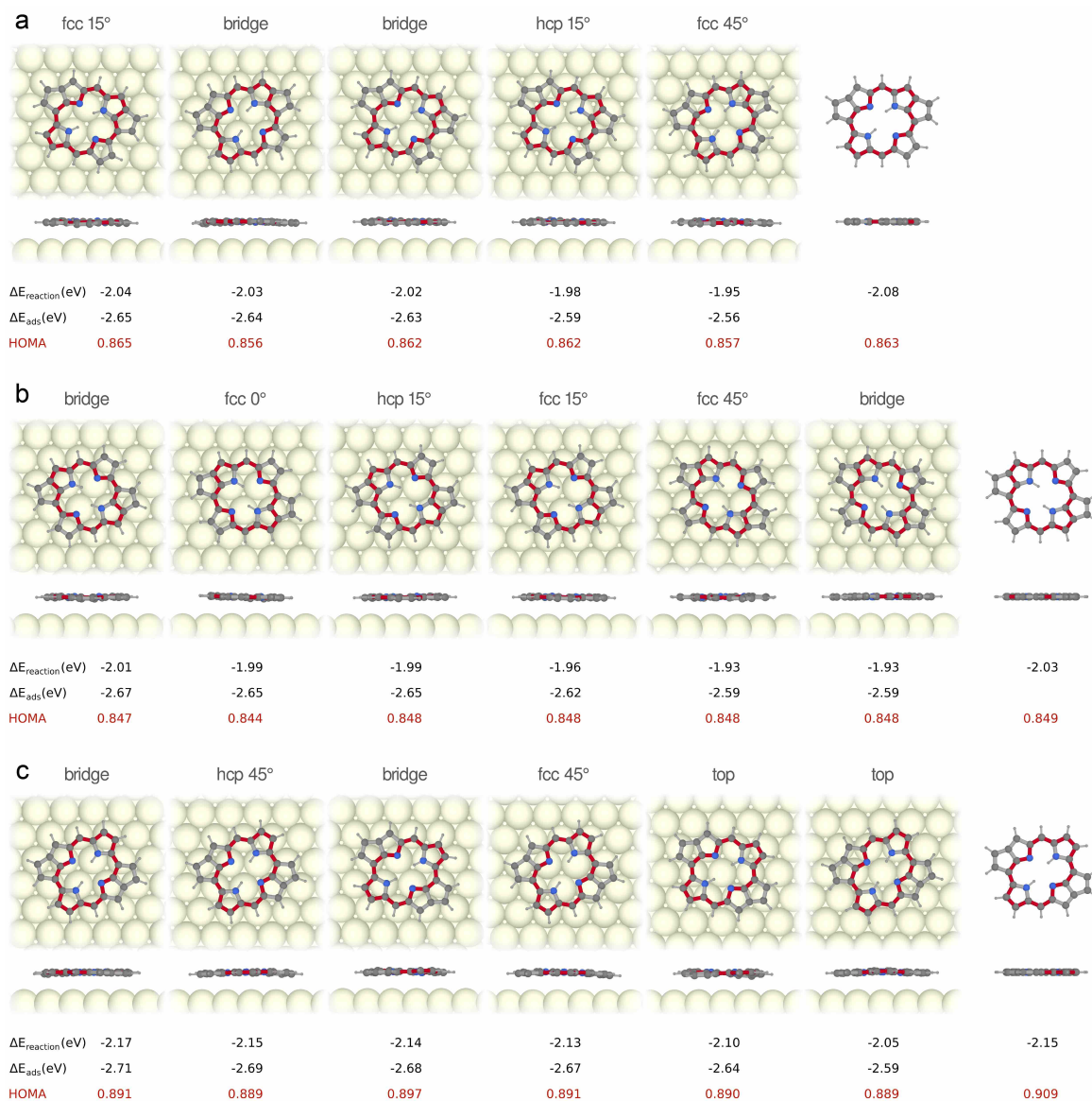
Figure 4.12.: Relaxed geometries of the cyclization products of free-base porphyrins. Top and side views of relaxed structures of (a) **2a-cis**, (b) **2a-trans1** and (c) **2a-trans2** at different adsorption positions, as well as in their free-standing geometry. For each structure, the reaction energies (with respect to the model of the precursor **1a**), the adsorption energies, as well as the HOMA indices associated with the aromatic diaza[18]annulene pathway are shown.
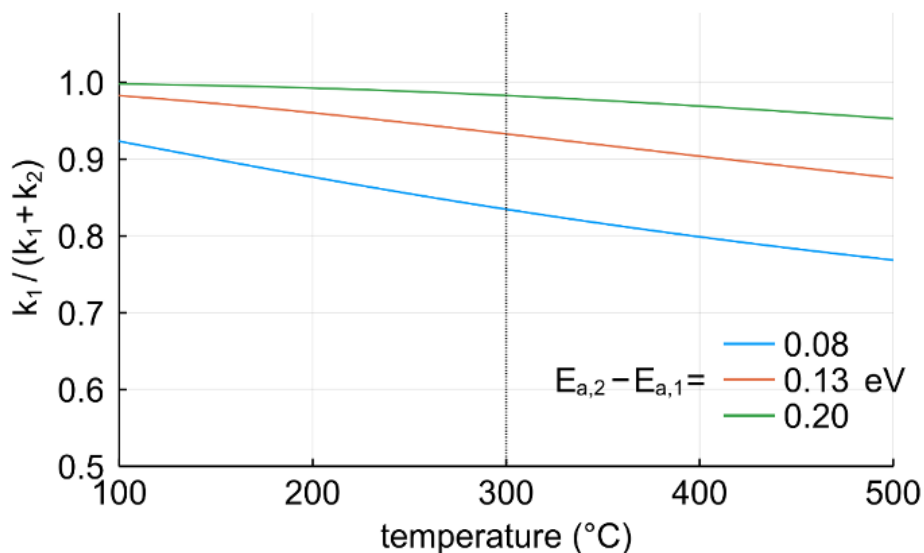
Figure 4.13.: Rate constants for a reaction with two competing pathways, *trans-* and *cis-*cyclization. The ratio of rate constants for two competing pathways, k_1 and k_2, respectively, can be estimated by the ratio of the Arrhenius equations: $k_2/k_1 = e^{-(E_{a,2}-E_{a,1})/k_B T}$, where $E_{a,1}$ and $E_{a,2}$ are the activation energies for the two pathways, k_B is the Boltzmann constant and T is the reaction temperature. k_2/k_1 corresponds to the ratio of product concentrations c_2/c_1. The graph plots the relative abundance of the first product, calculated as $k_1/(k_1 + k_2)$ for better comparison with the Figure 4.6d. The traces show the computed values for differences in activation energies of 0.20, 0.13 and 0.08 eV. These values are chosen to be in a similar range as the differences in reaction energies as computed by DFT (0.13 eV for $\Delta E_{\textbf{2a-cis}}$- $\Delta E_{\textbf{2a-trans2}}$; see Figure 4.11b). The reaction barriers for the same type of reaction are expected to be correlated with the reaction energies according to the Bell-Evans-Polanyi principle. [230, 231] Based on such assumptions, the simulations yield relative abundances of the energetically preferred product at the reaction temperature of around 300 °C (dotted vertical line) in the range between 0.83 to 0.98, similar to the relative abundance of 0.85 obtained experimentally for the *trans-*cyclized product (see Figure 4.6d). The results are comparable to the yields computed by kinetic simulations based on the calculations of transformation barriers for the reaction pathways.

itive chemical aromaticity interpretation, we turned towards a more quantitative assessment of aromaticity: the Harmonic Oscillator Model of Aromaticity (HOMA) index. [107, 108] The HOMA index is one of the most widespread measures of structural aspects of aromaticity, mostly due to its versatility and direct chemical interpretation. The HOMA index measures the deviation of the observed bond lengths from the "optimal" aromatic bond lengths. The normalized sum of the squared deviations is subtracted from 1, such that a HOMA index close to 1 is obtained for a strongly aromatic system (i.e., with all bond lengths close to the optimal values); see the Data acquisition and analysis section (2) for the formal definition. We choose the HOMA index because it is sensitive to geometrical changes induced by the adsorption of the molecules, as opposed to topological aromaticity descriptors. [232, 233, 234] Also, it can be used to quantify the aromaticity of extended macrocyclic pathways, which is more difficult with Nucleus-Independent Chemical Shift (NICS) calculations. [205, 206] We used the DFT-computed bond lengths to calculate the HOMA indices, [109, 235] because it is not feasible to accurately extract absolute or even relative bond length from the AFM measurements due to substantial distortions in the images. [236, 237, 104] The calculations confirm the twofold symmetry of the aromatic system and reveal two types of pyrrole rings with different aromaticity, in accordance with the model introduced in Figure 4.1 (see Figure 4.14 for calculations of local pyrrolic aromaticity). Figure 4.11c shows the HOMA values associated with the macrocyclic diaza[18]annulene aromatic pathways for the reactant (**1a**) as well as for the three products (**2a-*cis*, 2a-*trans1*, 2a-*trans2***). Strikingly, the HOMA values correlate with the DFT-calculated reaction energies (Figure 4.11b): the highest aromaticity index is obtained for the energetically most favourable product (**2a-*trans2***), while the product with the lowest HOMA index is also the energetically least preferred (**2a-*trans1***).

Thus, all three perspectives, i.e., the energetics based on DFT, the qualitative chemical intuitive picture, as well as the quantitative assessment of aromaticity, are in agreement – and, importantly – also match the experimentally observed relative abundance of cyclization products (see Figure 4.13 for estimates of predicted product abundances). However, two important aspects warrant further discussion. These concerns: (i) the role of the substrate and (ii) the role of the adjacent molecules on the energetics of the cyclization reaction.

To shed light on the influence of the substrate, we performed calculations for the products (**2a-*cis*, 2a-*trans1*, 2a-*trans2***) at different adsorption sites. The reaction energies for one product at different adsorption sites can vary by up to 0.1 eV (see Figure 4.15a). This variation reflects different adsorption energies of the respective molecules on the substrate (Figure 4.15b). And while this variation is on the same order of magnitude as the variation of reaction energies between the different products, our initial conclusions remain unchanged: for all investigated adsorption positions the product **2a-*trans2*** is energetically preferred over the other two products (**2a-*cis*, 2a-*trans1***). The same trend holds true for the reaction of free-standing molecules, i.e. without the substrate (dashed lines in Figure 4.15).

It is remarkable that the variation of the calculated HOMA indices for one product at different adsorption sites is much smaller than the variation between the different products (Figure 4.15c). This suggests that the aromaticity is not noticeably altered for different adsorption configurations. However, our calculations reveal that the HOMA indices for the
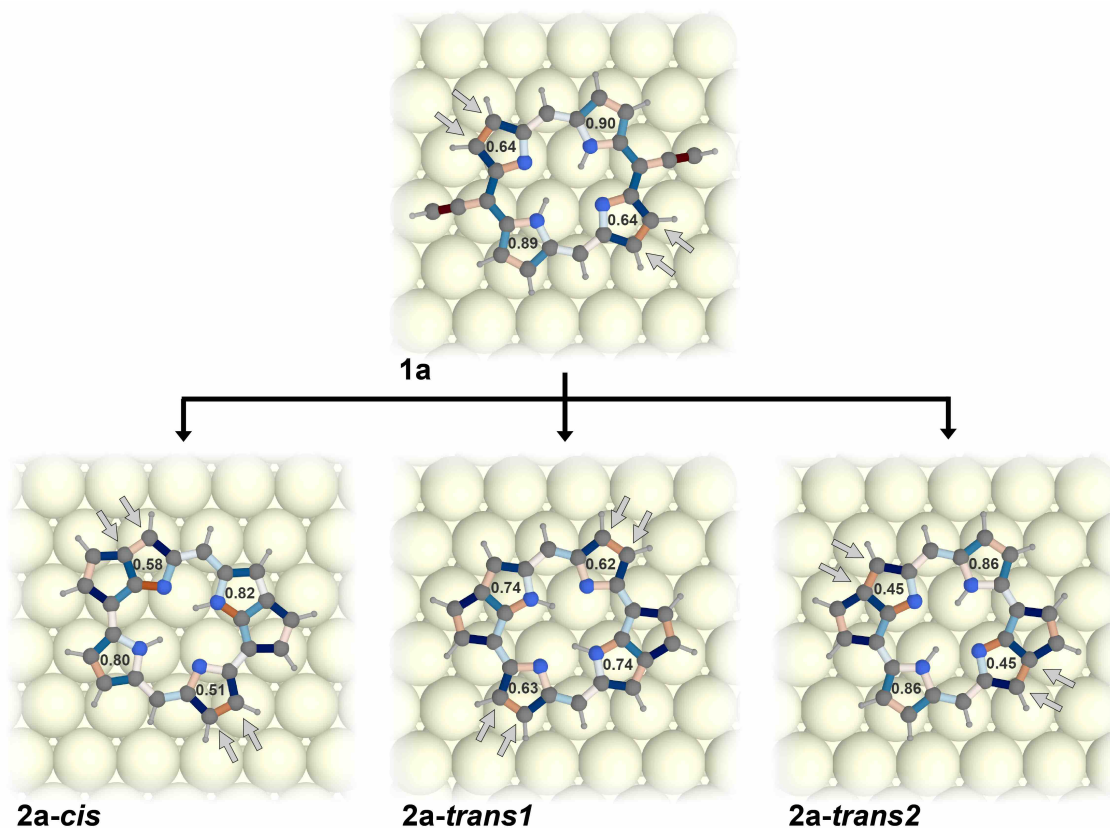
Figure 4.14.: Local HOMA indices and relative bond lengths of free-base porphyrins. The images show the local HOMA indices for the pyrrole rings, as well as the relative bond lengths of each C-C and C-N bond (red for shortened and blue for elongated bond lengths, compared with the "optimal" aromatic bond lengths). The precursor **1a** exhibits a significant asymmetry, with one pair of two pyrrole rings at opposite "corners" having higher HOMA indices than the other pair. This is in line with the aromatic diaza[18]annulene pathway (see Figure 4.1) observed in porphyrins. [238, 239, 240] The two pairs of carbon atoms with olefinic character outside of the aromatic pathway are indicated by gray arrows. The cyclized products also exhibit this twofold symmetry, but there are significant changes in the HOMA indices for the rings. The newly formed five-membered rings lead to a reduction of the HOMA indices of the pyrrole rings that they are attached to.
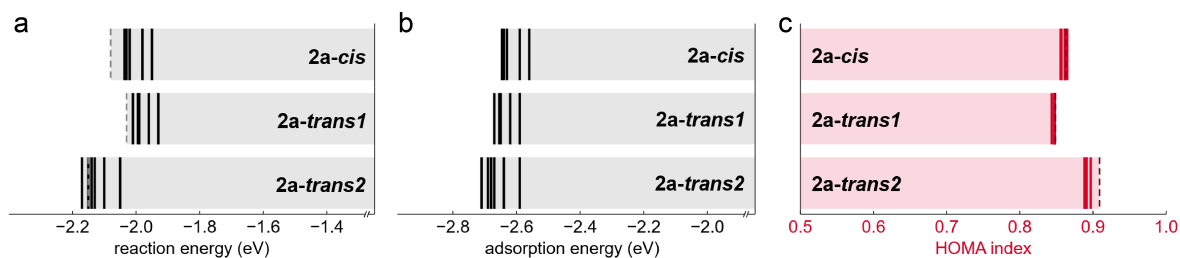
Figure 4.15.: Influence of different adsorption positions. The graphs show the variation of (a) reaction energies, (b) adsorption energies and (c) HOMA indices of the products **2a-*cis***, **2a-*trans1***, **2a-*trans2*** as a function of their adsorption configurations. Free-standing configurations are denoted by dashed lines. The notable variation of the adsorption energies for each molecule is reflected in the respective reaction energies. Nevertheless, in all cases the most stable product remains **2a-*trans2***. Adsorption typically decreases the HOMA index compared with the free-standing molecules (dashed lines), but only a rather small variation is observed for different adsorption sites.
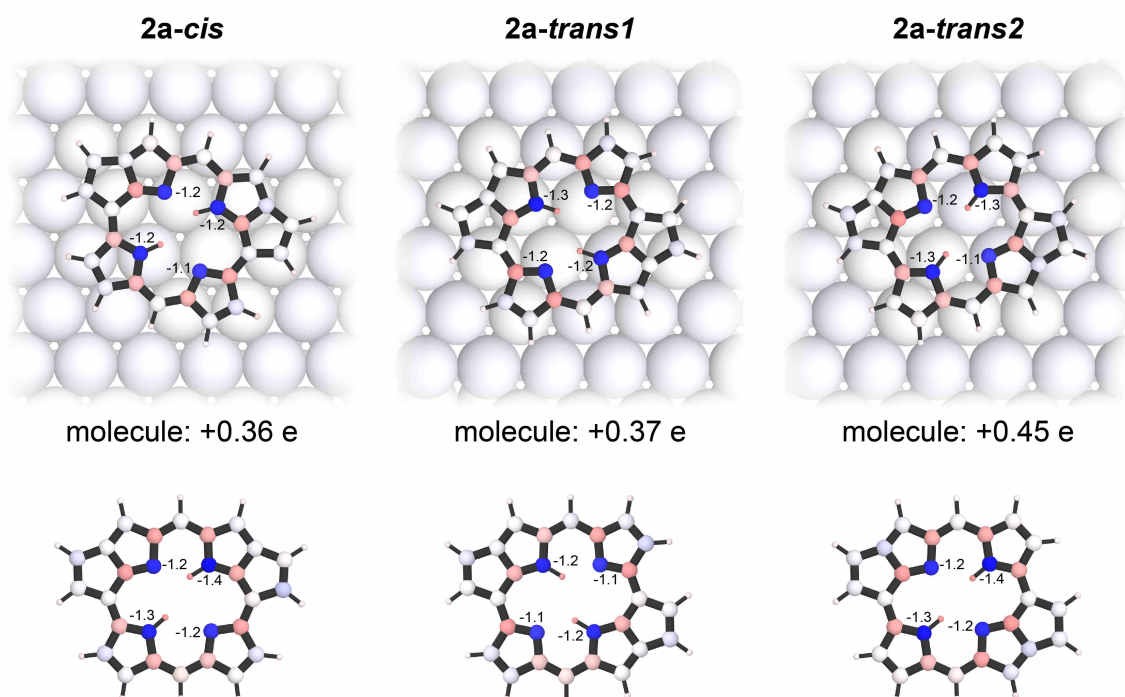
Figure 4.16.: Bader charge analysis for **2a-*cis***, **2a-*trans1*** and **2a-*trans2***. The DFT calculations for the most stable adsorption configurations show a charge transfer of ∼0.4 electrons from the molecules to the substrate. For all structures, the nitrogen atoms are negatively charged (-1 e), which is balanced by positively charged carbon neighbors.

surface-adsorbed species typically are slightly lower than for their free-standing counterparts. This can be explained by a small perturbation of the atom positions upon adsorption of the molecules on the substrate, inducing additional deviations of the bond lengths from their "optimal" aromatic lengths. In addition, charge transfer between the molecule and the substrate can play a role here (see Figure 4.16). The DFT calculations for the most stable adsorption configurations show a charge transfer of ∼0.4 electrons from the molecules to the substrate. For all structures, the nitrogen atoms are negatively charged (-1 e), which is balanced by positively charged carbon neighbors.

Most of our explanations regarding cyclization were based on the understanding of single molecules. It is conceivable that cyclization is influenced by the coupling reaction (which occurs at similar temperatures), as well as by non-covalent interactions with nearby molecules (molecular aggregates can even form for diluted surface concentrations). Due to computational complexity, it was not feasible to perform calculations that thoroughly investigate these effects. But the statistical analysis of our experiments indicates that coupling does not change the regioselectivity of the cyclization: both, the coupled, as well as the isolated molecules, show the same preference for *trans*-cyclization. Non-covalent interactions within molecular aggregates will likely "push" the molecules away from their most stable positions on the substrate (the same is expected to happen at elevated temperatures). And while changes in adsorption positions do not significantly alter the HOMA indices, they do have a noticeable effect on the reaction energies (Figure 4.15). But, based on the calculations, this effect is unlikely to change the trends in reaction energies for the different products.

The cyclization reaction might also be influenced by other parameters that our models do not capture, such as steric effects or energy dissipation to the substrate. [110] But as the pathways towards *cis*- and *trans*-cyclized species are remarkably similar, such effects would very likely influence these pathways in a similar way and therefore would not lead to a notable preference for one of the products. Thus, despite such potential complexities, we believe that our theoretical models adequately describe the reaction and therefore correctly explain the pronounced preference of *trans*-cyclized species that has been experimentally observed for both, isolated, as well as coupled molecules. Beyond that, the reduced reactivity of aromatic *β*-carbons can directly explain the product distributions observed in previous studies of planarization reactions of tetraphenyl-porphyrins, which report comparable preferences for certain isomers. [241, 242, 243]

Finally, we closely examine and model the reaction kinetics. The transformation of 1a involves two cyclization steps with two possibilities for each (Figure 4.17c,d): formation of bonds with *β*-carbon atoms at the porphyrin periphery that are either within or outside of the aromatic pathway. The first cyclization yields the half-cyclized intermediates **2a-*pre1*** and **2a-*pre2***. These then can transform into **2a-*trans1*** and **2a-*cis1***, as well as **2a-*cis2*** and **2a-*trans2***. Note that **2a-*cis1*** and **2a-*cis2*** are equivalent structures (that can be seen as mirror images of each other), but they emerge from different reaction pathways and thus are distinguishable in this analysis. DFT calculated reaction barriers for all four possible pathways show that the coupling steps with aromatically stabilized carbon atoms have higher barriers by up to 0.3 eV (see Appendix Figures A.5-A.8). Considering the multiple steps for each transformation,
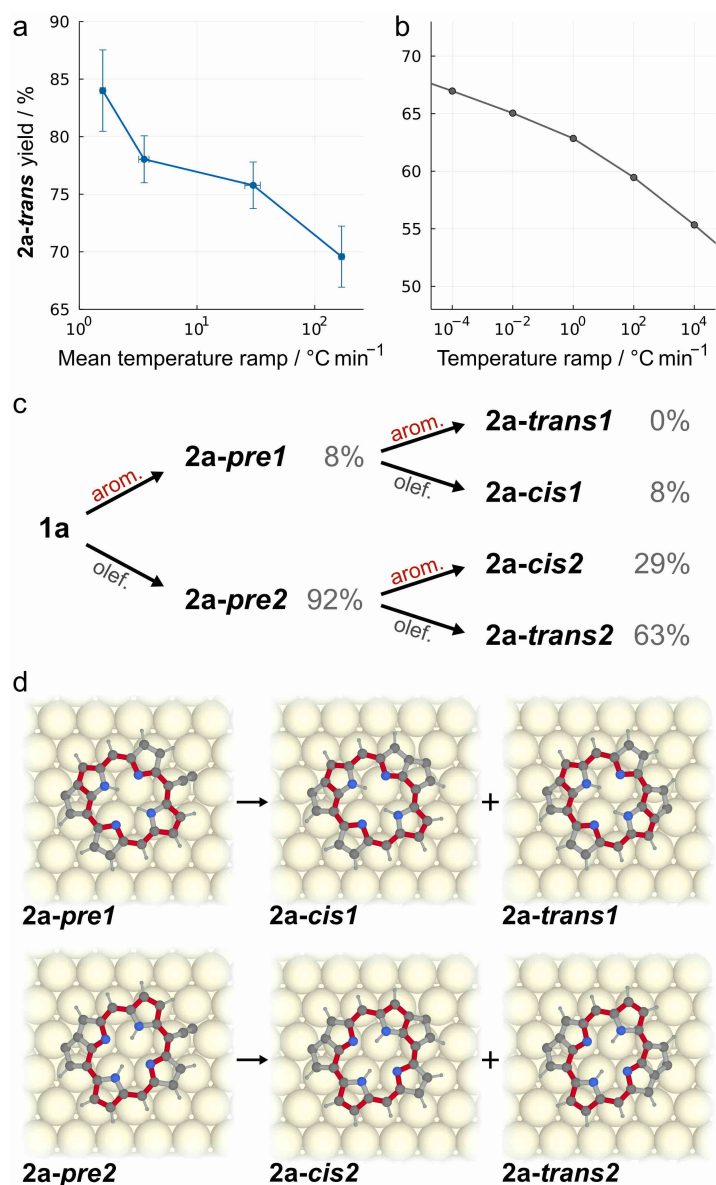
Figure 4.17.: Reaction kinetics. (a) The experimental yield of *trans*-cyclized species as a function of the average heating ramp (final annealing temperature of 305 °C). The total number of counted molecules for each data point was 200, 601, 611, and 355, respectively. (b) Kinetic simulations based on DFT-calculated reaction barriers show a similar trend of an increased yield of **2a-trans2** with a slower annealing ramp. (c) Scheme of the cyclization cascade of 1a towards the half-cyclized intermediates **2a-pre1** and **2a-pre2** and the products **2a-trans1**, **2a-cis1**, **2a-cis2**, **2a-trans2**. Both cyclization steps preferentially occur at the olefinic β-carbon atoms at the porphyrin periphery. The calculated yields of intermediates and products with respect to the precursor **1a** are given for a heating ramp of 1 °C min^{-1}. (d) Structural models of the DFT-relaxed intermediates and products.

we use the calculated barriers to simulate the reaction kinetics by solving the system of rate equations associated with the pathways shown in Figure 4.17c. The simulations confirm the preference for the pathway towards **2a-trans2** (Figure 4.17c). Furthermore, a pronounced dependence on the heating rate is revealed (Figure 4.17b): the slower the heating rate, the stronger the preference for the reaction path towards **2a-trans2**. This can be intuitively explained by considering that with faster heating rates a wider energy range is accessed earlier in the reaction progress, which helps to overcome the reaction barriers associated with less preferred pathways. Following these predictions, we have conducted experiments with different temperature programs (Figure 4.17a). The experiments show a higher yield of **2a-trans2** and a stronger dependence on the heating ramp than the simulations. However, both, experiment and simulation (Figure 4.17a and b, respectively) reveal the same trend: slower heating rates increase the *trans*-cyclized product yields, clearly demonstrating the existence and prospects of kinetic reaction control.
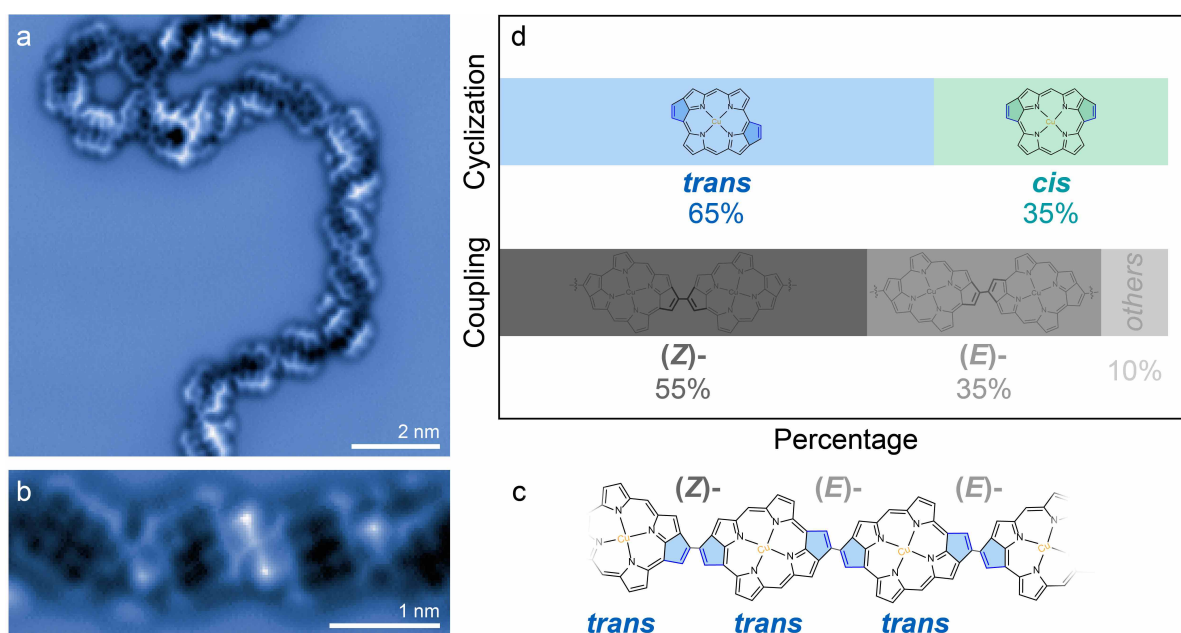
Figure 4.18.: Regio- and stereo-selectivity of cyclization and coupling of SiMe$_3$-ethynyl-substituted Cu-metalated porphyrin precursors (**1b**) on Au(111). (a) AFM image of a porphyrin nanostructure (**2b**) formed after annealing at 305 °C (average temperature ramp of 3 °C *min*$^{-1}$). (b) High-resolution AFM image of a chain segment and (c) the derived chemical structure showing that **1b** similarly undergoes cyclization and coupling reactions. (d) Statistical analysis of reaction products for intramolecular cyclization and intermolecular coupling. Compared with the reaction products of free-base porphyrins, a significantly smaller preference for *trans*-cyclization was observed, while for coupling the behaviour is similar. Scan parameters: V_s = 0 V, constant height.

4.3. Alkyne-substituted Cu-metalated porphyrins on Au(111)

To further explain the effect of aromaticity on cyclization, we performed comparative measurements using a metalated precursor: (5,15-bis(trimethylsilyl)ethynylporphyrinato)copper(II), denoted as **1b**. As opposed to the twofold symmetry (D_{2h}) of the porphyrin core of the free-base precursor, this species is fourfold symmetric (D_{4h}), we expect that the carbon atoms at the periphery exhibit rather similar chemical behavior instead of the pronounced difference in reactivity outlined above.

We deposited **1b** on Au(111) held at room temperature and post-annealing to 305 °C with a similar coverage as **1a**. We obtained similar morphologies of extended 1D porphyrin nanostructures (Figure 4.18a) with linear segments, ring-like structures, and some branches. (see also Appendix section) The high-resolution image in Figure 4.18b reveals the same types of intramolecular cyclization and intermolecular coupling reactions as observed for **1a**, the corresponding chemical structures shown in Figure 4.18c. In fact, the stereo-selectivity of intermolecular coupling reaction for both species is consistent, showing a slight preference for (Z)-type coupling: the reaction yield of (Z)-coupling is roughly 55% for both **1a** and **1b**. This result might be expected, since the electronic conjugation for both, *cis-* as well as *trans*-coupled segments are likely comparable.

For the intramolecular cyclization reaction, the Cu-metalated precursor **1b** forms the same types of products as observed for the free-base precursor **1a**, i.e. *cis-* and *trans*-cyclized products (Figure 4.18). However, our statistics reveal an obvious difference, for **1b** the preference for *trans*-cyclization is strongly reduced: compared to 85% of the free-base products **2a**, only 65% were in a *trans* configuration for **2b** (determined by single-molecule counting of more than 200 molecules in each case). But the ratio of *cis-* and *trans*-cyclized species is still slightly skewed towards *trans*-species. Such more subtle differences can have their origins in other effects (for instance the energy differences for different adsorption positions, see above).

DFT calculated reaction energies are in line with the experimental observations (more discussion refer to Appendix A.1 section). **2b-*trans*** (ΔE = -2.06 eV) is slightly more favourable than **2b-*cis*** (ΔE = -2.05 eV). The difference of reaction energies between *cis* and *trans* products is on the order of 10 meV for 1b –> 2b, while for 1a –> 2a it was more than 100 meV. Such energy differences can in fact lead to the relative ratios of products that are similar to what we observed in the experiments (see Figure 4.13 for simulation of reaction rates as a function of activation energy differences). Hence, these results further strengthen the conclusions obtained from the analysis of the behaviour of the free-base precursor **1a**; i.e., that its reactivity is substantially influenced by the aromatic diaza[18]annulene pathway.

4.4. Conclusion

In this chapter, SiMe$_3$-alkyne-substituted porphyrins were used to construct covalently coupled nanostructures. And we successfully obtained one-dimensional porphyrin nanostructures on Au(111), commonly exhibiting length above 30 units. The precursors undergo intramolecular cyclization and intermolecular coupling reactions, making the distance shrink

to near 1.10 nm between porphyrin units. The two coupling pathways directly induced different morphologies of the nanostructures, regular chain structures, and nanorings. While cyclization was found to be strongly affected by the local reactivity of the free base porphyrins, which leads to a strong preference for *trans*-cyclization, in agreement with theoretical estimates of reaction energy differences on the order of 100 meV. The reaction energies of the products are correlated with their aromaticity as determined by calculation of their HOMA indices, which were found to be remarkably robust against adsorption on the substrate. Our results show that the predictive power of chemical reasoning based on the concept of aromaticity can be extended to on-surface chemistry – and can directly explain preferences for porphyrin cyclization pathways in previous studies. [241, 242, 243] These insights will help to guide the design of precursors to optimize yields and selectivity of reactions for the synthesis of surface-supported porphyrin architectures.

5. Surface-Confined Formation of Conjugated Porphyrin-Based Nanostructures

5.1. Introduction

Porphyrins constitute a group of natural and synthetic compounds with unique chemical, optical, and electronic properties, [244, 245] which are widely used in photomedicine, catalysis, photovoltaics, and photonics. Their optoelectronic and structural properties can be tuned at interfaces through their macrocycle, functional groups, and central metal atom, which altogether affords versatile and promising candidates for the construction of functional organic nanomaterials. [6, 200, 9, 199, 8] Recent efforts to obtain porphyrinic interfacial nanostructures include studies on the formation of porphyrin-based nanochains, [246, 247, 248, 249, 250, 251, 207] covalent, [22, 252] and metal-organic networks. [253, 254]

Construction of robust nanomaterials containing porphyrin backbones requires the formation of covalent bonds between the reacting monomers. [6, 251, 207, 22, 252, 255] As such, several schemes have been explored, in which the geometry and chemical nature of the linkages determine the topology and electron delocalization along the nanostructures formed. In this context, a number of carbon-carbon (C-C) coupling reactions, mostly obtained by Ullmann coupling as well as other reactions such as CH_3 activation and Glaser coupling, have been reported. [6, 22, 256, 208, 257, 202] Notably, the formation of porphyrin nanostructures linked by ethylene bridges (-C=C=), which allows for the electron delocalization or conjugation along the molecular structure, has not been explored at interfaces. Alkenyl units also render the conjugated structures flexible via *cis/trans*-configurations. This has constituted the motivation of the present work where C=C is formed as the result of the surface reaction through which porphyrin molecules are connected to form conjugated porphyrin-based nanostructures. Hence, this study offers another avenue for making nanostructures whose electronic properties can be tailored. [258, 259, 260, 261, 157, 149]

A classic approach to generate -CH=CH- units is the McMurry reaction, [262, 263] where aldehyde condensation is catalyzed by low-valent titanium, already demonstrated for aldehyde-substituted porphyrins in solutions. [264, 265, 266] Simple aldehyde units have been previously used in on-surface reaction studies under ultra-high vacuum (UHV) conditions. [267, 48, 268, 269] For example, Fuchs et al. [48] reported the formation of polyphenylene vinylene oligomers on Au(111) by the coupling reaction of 2,5-dihexylterephthalaldehyde. However, photoelectronically active compounds such as porphyrins have not been used to generate -C=C- units via interfacial coupling reactions.
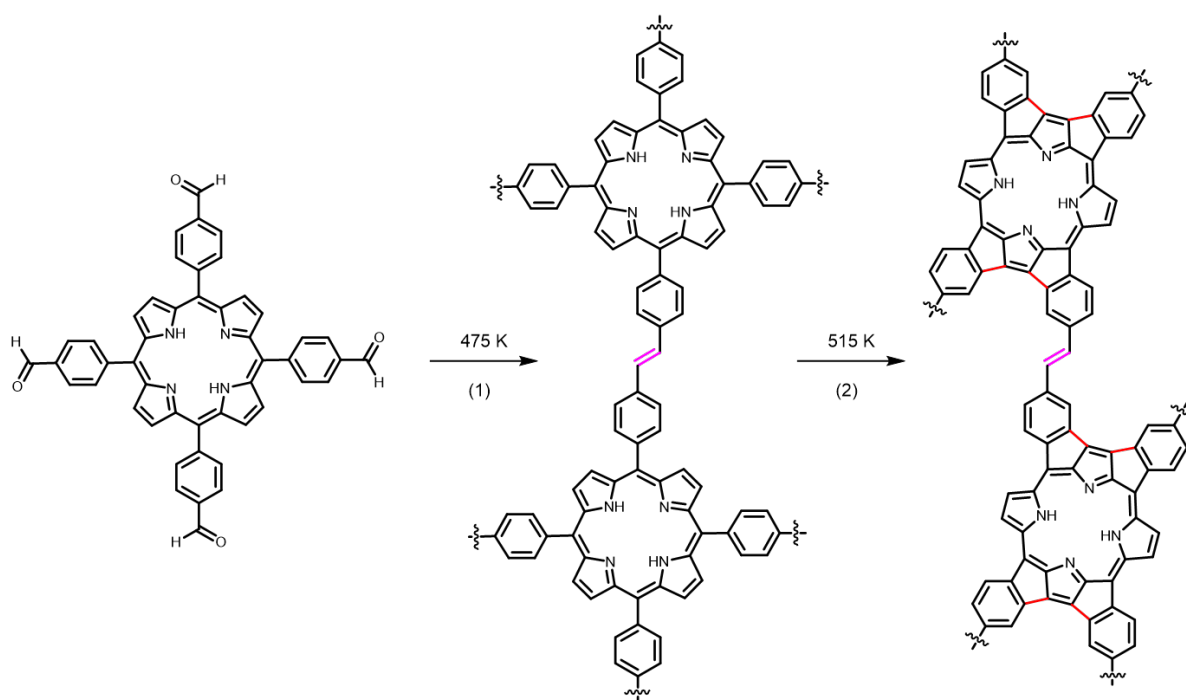
Figure 5.1.: On-surface reaction of H$_2$TFPP on Ag(111). (1) Coupling reaction of aldehyde groups. (2) Cyclodehydrogenation and ring-closure reaction.

The present work reports the self-condensation of metal-free (5,10,15,20-tetrakis(4-formyl-phenyl)porphyrin (H$_2$TFPP) [94] on Ag(111) - a benzaldehyde-substituted porphyrin undertaking the surface-confined "McMurry-type"[1] reaction to generate porphyrin-based nanostructures stabilized by -C=C- linkages (Figure 5.1). The molecule's structural evolution and chemical transformation were characterized by a multi-technique approach, using low-temperature scanning tunneling microscopy (LT-STM), high-resolution non-contact atomic force microscopy (nc-AFM) with CO-functionalized tips, and X-ray photoelectron spectroscopy

---

[1]The reactant molecule, H$_2$TFPP, studied in the present work is a porphyrin containing benzaldehyde functional group. The reaction was carried out on silver single crystal surfaces, Ag(111) and Ag(100), under UHV conditions, which is different from the classical McMurry reaction proceeded in solution. [262, 263] However, the present on-surface reaction, performed in UHV systems, resulted in the formation of C=C, similar to the solution-based McMurry reaction. Therefore, we define the reaction in this work as the "McMurry-type" reaction.

(XPS). Formation of C=C linkages from the formyl-substituted tetraphenyl-porphyrin precursor was achieved through stepwise thermal annealing of the adsorbed molecular layers, resulting in molecular nanostructures with porphyrin-vinylene-porphyrin units.

5.2. Porphyrin oligomers on Ag(111)
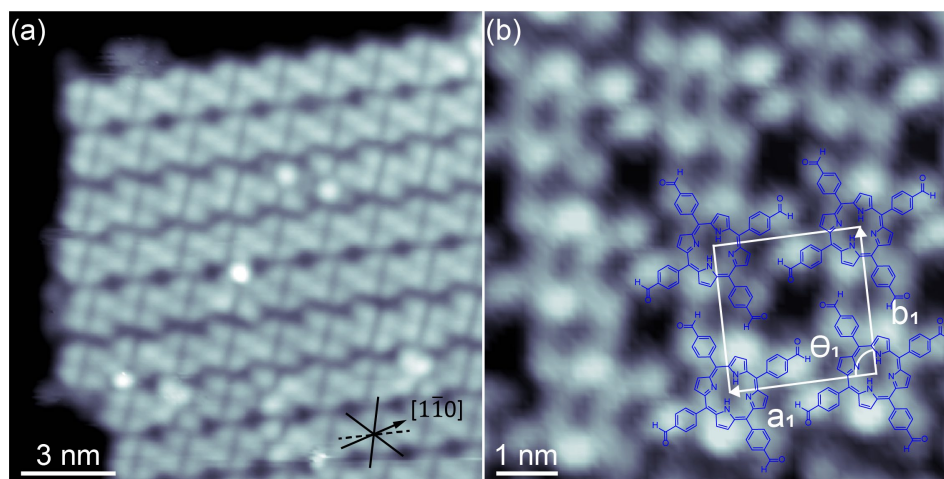
Figure 5.2.: STM images of H$_2$TFPP on Ag(111) after deposition at 300 K. (a) Close-packed assembled structure. (b) High-resolution STM image of (a). Scan parameters: (a) I_t = 100 pA, V_s = 1 V, (b) I_t = 12 pA, V_s = 100 mV.

Figure 5.2 shows STM data of H$_2$TFPP for a sub-monolayer coverage on Ag(111) after deposition at 300 K, featuring close-packed self-assembled domains (Figure 5.2a). The direction of molecular rows (black dashed line) deviates by 16° from the [1$\bar{1}$0] high symmetry direction of the Ag(111) substrate. The high-resolution STM image distinctly reveals the individual molecules (cf. Figure 5.2b), exhibiting a saddle-shaped geometry resulting from the deformation of the porphyrin macrocycle upon adsorption on the surface. [215] The central depression of the single molecule is attributed to the macrocycle core, whereas the four surrounding terminal protrusions are assigned to the 4-formylphenyl moieties. [215] The self-assembled arrangement with a structural model overlaid shown in Figure 5.2b, can be described by a unit cell with lattice vector lengths of $a_1 = b_1 = 1.59 \pm 0.02$ nm, and an enclosed angle of $\theta_1 = 91 \pm 1°$.

The ordered self-assembled structure is stable up to 455 K (Figure 5.3). Postannealing to 475 K drives the formation of small islands, consisting of short oligomers and sparse isolated monomers (Figure 5.4a and Figure 5.5). The chain-like oligomers comprise two or more monomer subunits, whereby one terminal site in each monomer is linked to an adjacent one. From the appearance of two coupled molecules in a trimer, depicted in the close-up STM image (Figure 5.4b), the protruding linkage is consistent with the covalent coupling. To further resolve this unit, nc-AFM measurements were performed. Indeed, the
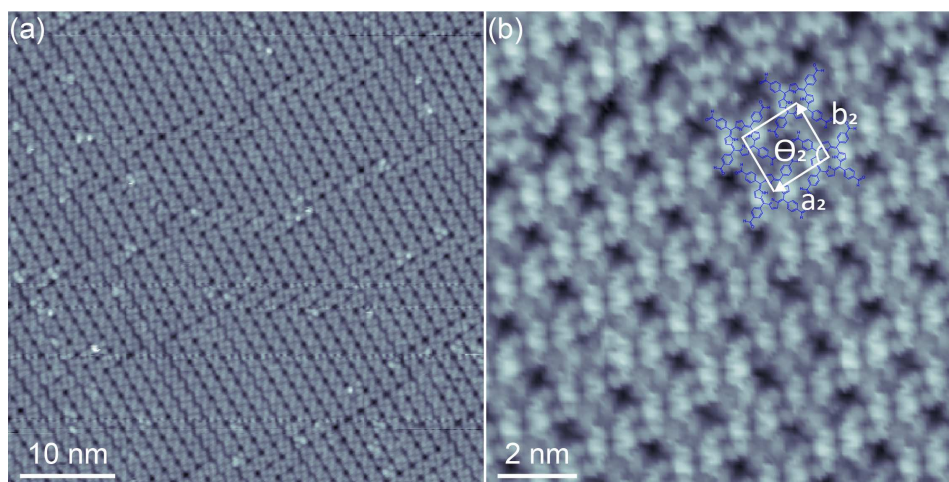
Figure 5.3.: Self-assembled structure of H_2TFPP on Ag(111) upon annealing the sample at 455 K. (a) The close-packed self-assembled structure. (b) The molecular model is overlaid on the close-up image, with the lattice vectors of $a_2 = 1.61 \pm 0.02$ nm, $b_2 = 1.56 \pm 0.02$ nm and an angle of $\theta_2 = 92 \pm 1°$. This is comparable with the self-assembled structure obtained at 300 K (Figure 5.2). Scan parameters: (a) $I_t = 10$ pA, $V_s = 1$ V, (b) $I_t = 30$ pA, $V_s = 30$ mV.

AFM image of Figure 5.4b shows features indicative of a vinylene (-C=C-) bridge between the phenyl rings along with a kinked shape as expected; [270] and the distorted conformation of the molecular backbone (Figure 5.4c). This bonding motif is in line with earlier results of reductively coupled 2,5-dihexylterephthalaldehyde on Au(111). [48] A typical STM image (Figure 5.5) upon annealing the sample at 475 K displays molecules aggregated into small islands, which consist of oligomers (marked with the blue outline) and monomers (marked with the red outline). Statistical analysis shows that 65% of the molecules (out of 500 counted molecules) have undergone coupling reactions, and 32% of the terminal aldehyde groups had reacted. In another word, the fraction of formed -C=C- connections is 32% of the theoretical maximum. Of the reacted molecules, about 25%, 26%, and 49% formed dimers, trimers, and oligomers (some of them with branches) consisting of more than four units, respectively.

Upon annealing the surface at 515 K, a large-scale STM image (Figure 5.7a) shows no changes in molecular coverage ($\approx$ 35%) compared to the sample annealed at 475 K, indicating no molecular desorption upon annealing. A close-up STM image shows the appearance of oligomers different from those at 475 K, illustrating features with the 'H' shape connected (Figure 5.4e and 5.4f). To further delineate the oligomer structure, high-resolution AFM measurements were performed on two coupled molecules (Figure 5.4g). The AFM image shows a planarized molecular backbone, with a sharp kinked connection between two monomers at a similar brightness (marked by the dashed blue circles). Note that the linkage between the bonded porphyrin units is not straight but exhibits two kinks and thus appears staggered, similar to the appearance of -C=C- motifs reported by Cai et al. [270] This excludes an aryl-aryl coupling after removal of the aldehyde groups, which would have led to the
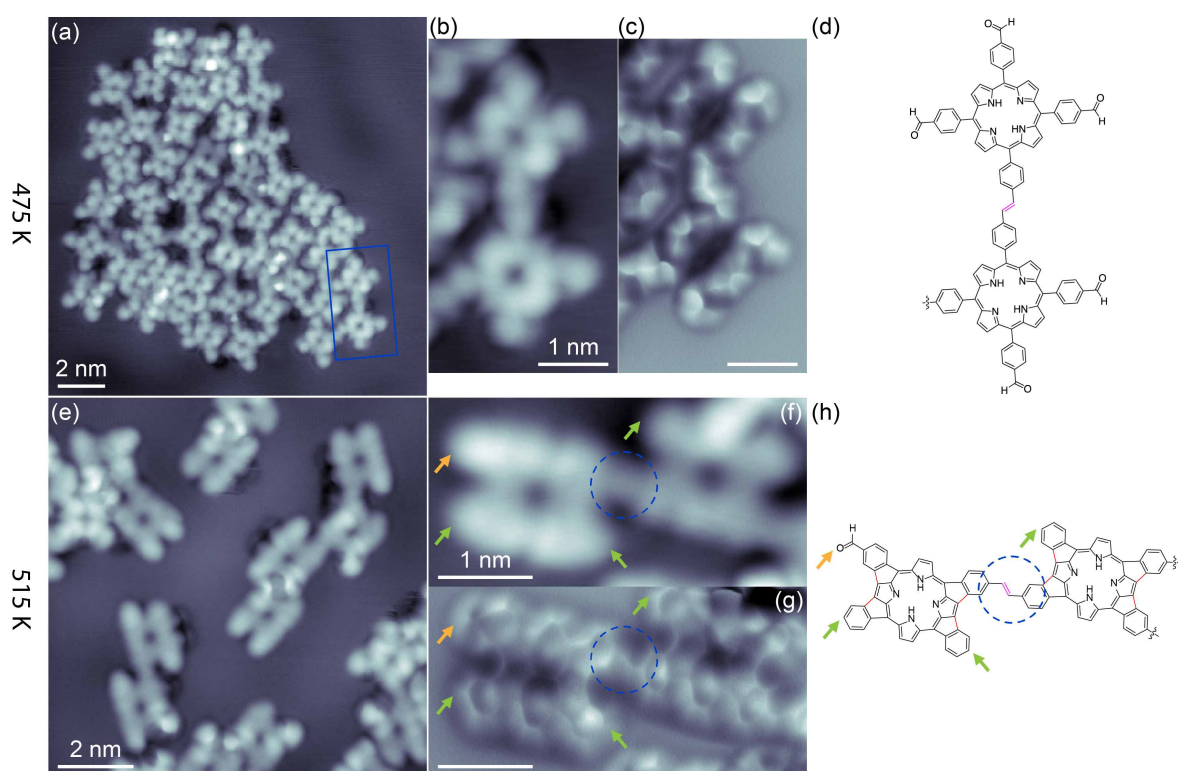
Figure 5.4.: On-surface synthesis of porphyrin-based oligomers via a coupling reaction of H$_2$TFPP on Ag(111). (a) STM image of covalently coupled porphyrins upon annealing at 475 K, showing the oligomeric chains aggregated in an island. (b) - (c) High-resolution STM and nc-AFM images of the oligomeric coupling marked by a blue rectangle shown in (a). (d) The proposed chemical structures of (b) and (c). (e) STM image of planarized oligomers due to ring-closure upon annealing at 515 K. (f) - (g) Close-up STM and corresponding nc-AFM images of a *trans*-dimer structure. (h) The proposed chemical structures of (f) and (g). Scan parameters: (a) and (e) I_t = 12 pA, V_s = 50 mV, (b) and (f) I_t = 10 pA, V_s = 50 mV.
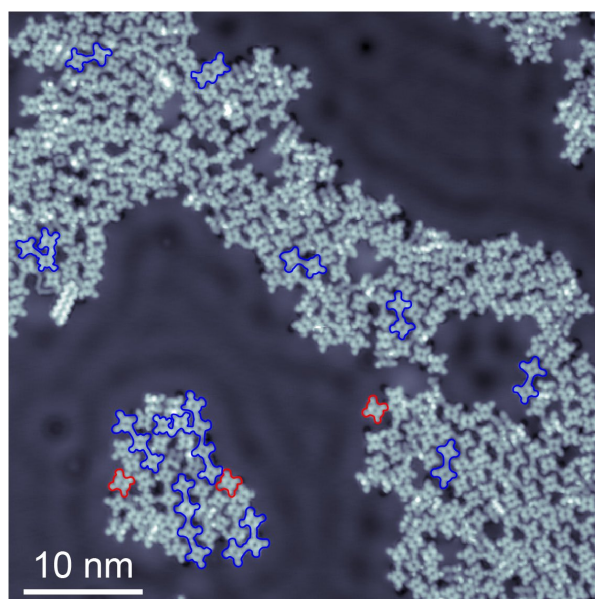
Figure 5.5.: The overview STM image upon annealing the sample at 475 K. The ordered self-assembled structure transformed into small molecular islands, which consist of oligomers (marked with the blue outline) and monomers (marked with the red outline). Scan parameters: (a) I_t = 12 pA, V_s = 50 mV.
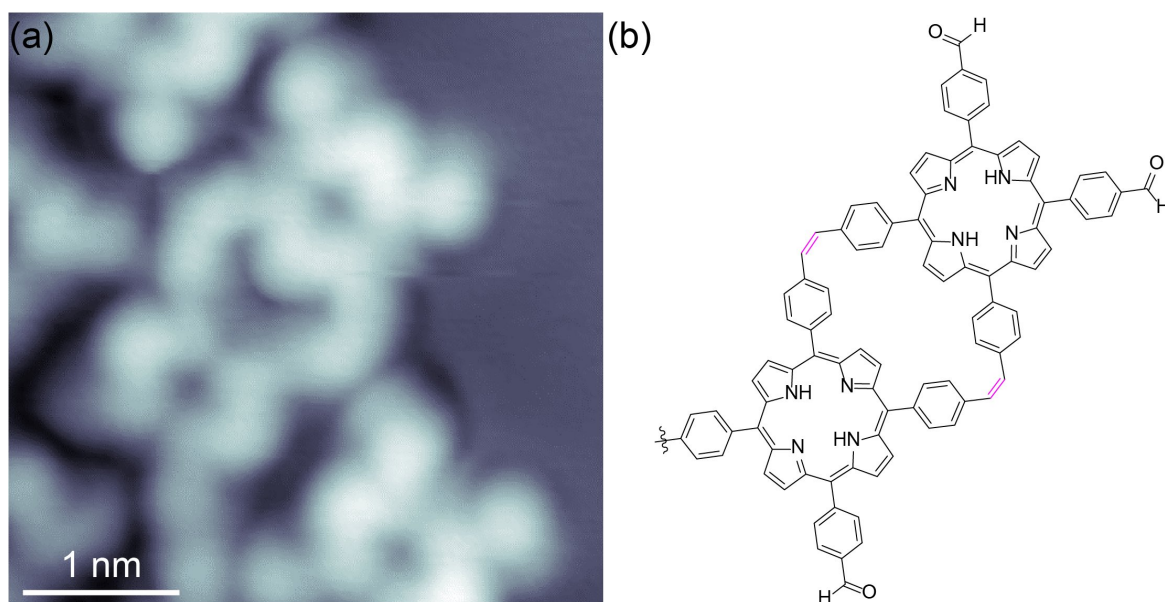
Figure 5.6.: STM image of a *cis*-dimer upon annealing the sample at 475 K (a), and the corresponding chemical structure (b). Scan parameters: (a) I_t = 10 pA, V_s = 50 mV.

formation of single C(sp2)-C(sp2) bonds between the adjacent porphyrin units, appearing as a straight line with a shorter length. [208] These data thus support a "McMurry-type" coupling scheme. Subsequent postannealing illustrated that the oligomers are stable up to the annealing temperature of 515 K. AFM images also reveal the occurrence of *trans-* (Figure 5.4g) and *cis-*configured (Figure 5.6) -C=C- linkages. Similar C=C linked oligomers also can be found after annealing the sample at 535 K (Figure 5.8), which indicates the rigidity of the C=C linkage.

In addition, the enhancement of the uniform brightness observed in the nc-AFM image (Figure 5.4g) indicates an intramolecular cyclodehydrogenation and ring-closure reaction, as the result of fusing of the pyrrole and phenyl rings of the porphyrin macrocycle. In agreement with previous reports, [271, 272, 273] the planarization of the molecular backbone is further evidenced by the chemical shift of the C 1s main peak towards lower binding energy upon annealing (Figure 5.9). This interfacial ring-closure was previously reported, [208, 272, 273, 274, 243, 275, 276] and initially described for meso-phenyl porphyrins in solution. [277] The cyclodehydrogenation reaction gives rise to four different types of planarized H_2TFPP derivatives (Figure 5.7), which is in agreement with earlier studies. [208, 243, 275]

Note that some of the terminal aldehyde entities are cleaved off after the thermal stimuli at 515 K, as indicated by the green arrows in Figure 5.4f and 5.4g, which can explain the predominance of short oligomeric chains. Contrarily, the feature marked by an orange arrow in Figure 5.4g signifies unreacted aldehyde entities. The formation of C=C resulting from the coupling reaction of aldehyde implies a "McMurry-type" reaction, which is further evidenced by the removal of oxygen atoms, as supported by XPS data, hereafter.

5.3. Chemical shifts in the formation of porphyrin oligomers

Our XPS experiments provide detailed information on the chemical transformations upon coupling of H_2TFPP on Ag(111). Figure 5.9 shows the C 1s and O 1s spectra, corresponding to different annealing steps. Following the deposition of H_2TFPP onto a Ag(111) surface at 300 K, the C 1s region shows distinct peaks at binding energies of 287.8 and 285.0 eV. The C 1s signature can be fitted with four components representing the four carbon contributions defined by the colors in Figure 5.9a. These peaks correspond to the formyl carbon (287.8 eV, blue); [180] α-pyrrole carbons (C-N and C=N, 285.7 eV, green); [260, 272, 279] the C-C carbons of phenyl, which are not attached to hydrogen atom, and the carbon of porphyrin bonded to the phenyl (285.2 eV, violet); [260, 280] and the β-pyrrole carbons and CH=CH carbons of phenyl (284.8 eV, red),8c,20 respectively. Quantitative analysis (Table 5.1) of the carbon composition of the H_2TFPP derives a ratio, approximately as 9%:17%:24%:50% from the higher to lower binding energy, which closely matches with the stoichiometric composition (1:2:3:6) of H_2TFPP monomers or dimers. A single O 1s peak is detected at a binding energy of 532.2 eV (orange), corresponding to the aldehyde oxygen.11b After annealing the surface at 475 K, this peak almost disappears, indicating C=O dissociation. Meantime, the previously observed C 1s peak at 287.8 eV (CHO), is significantly reduced. Quantitative analysis indicates that the ratio of C 1s at 287.8 eV reduces from 9% to 4%. On the other hand, the peak area
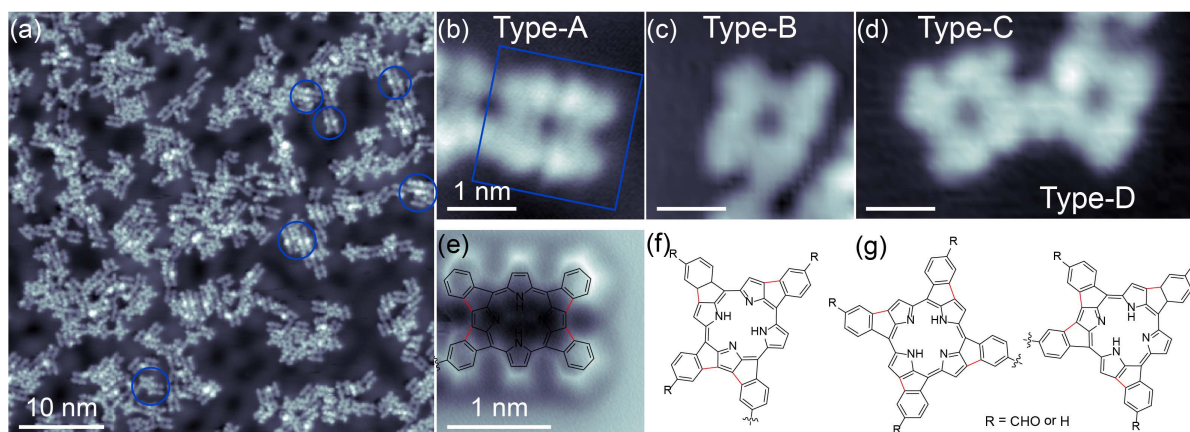
Figure 5.7.: STM and AFM images upon annealing the sample at 515 K. (a) The large scale STM image shows no changes in molecular coverage ($\approx$ 35%) compared to the sample annealed at 475 K, indicating no molecular desorption upon annealing. The small islands observed at 475 K underwent a further phase transition towards more disordered structures. Extended oligomeric or polymeric structures are not observed, potentially due to the loss of terminal aldehyde groups (see the main text). In addition to the -C=C- linked oligomers, other possible coupling motifs were also observed, [36, 278, 206] marked with the blue circles. (b) - (d) STM images of four planarized H_2TFPP derivatives, Type-A, -B, -C, -D, respectively. (e) AFM image of a Type-A molecule with the chemical structure overlaid. The terminal alkyne groups appear cleaved off. (f) The chemical structure of a Type-B molecule corresponds to the image (c). (g) The chemical structure of Type-C and Type-D molecules, correspond to image (d). Note that none of the images exhibit bright features in their center (observed for self-metalated porphyrins), originating from thermally induced self-metalation by substrate Ag atoms. [36, 278, 198] Scan parameters: (a) - (c) I_t = 12 pA, V_s = 50 mV, (d) I_t = 10 pA, V_s = 50 mV.
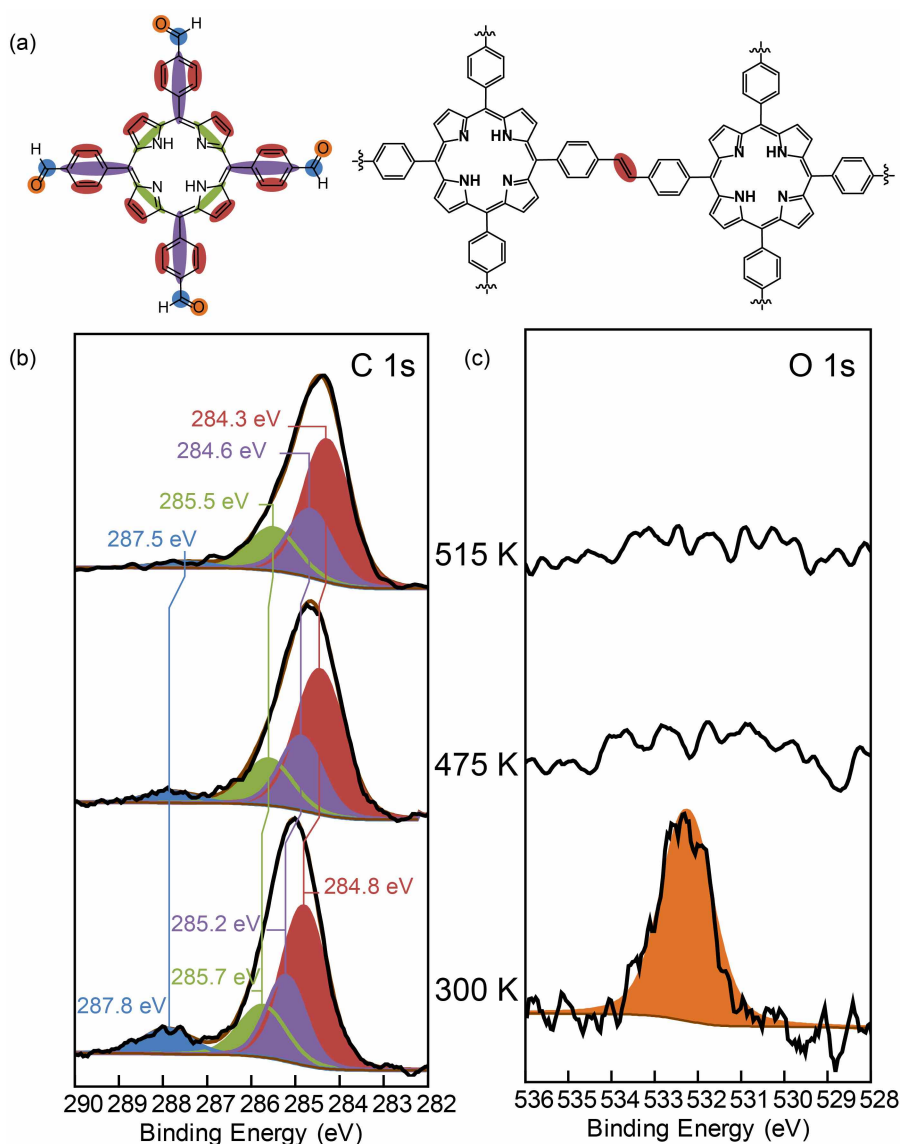
Figure 5.8.: XPS spectra of H$_2$TFPP adsorbed on Ag(111) at 300 K with a sub-monolayer coverage followed by stepwise annealing to 475 K and 515 K. (a) The chemical structures of H$_2$TFPP monomer and dimer. The color scheme represents the chemically equivalent carbon (and oxygen) atoms corresponding to the fitted peaks in (b) and (c). (b) C 1s spectra at 300 K, followed by postannealing to 475 K and 515 K. (c) O 1s peak at 532.2 eV vanishes after annealing. The decrease of the C 1s peak at 287.8 eV and the O 1s peak at 532.2 eV indicates the dissociation of the aldehyde group. The increase of the surface area in the C 1s peak in red is associated with the formation of C=C linkages. A quantitative analysis of C 1s and O 1s spectra is given in Table 5.1, and the compromises of the XPS analysis are also explained at the end of this section.
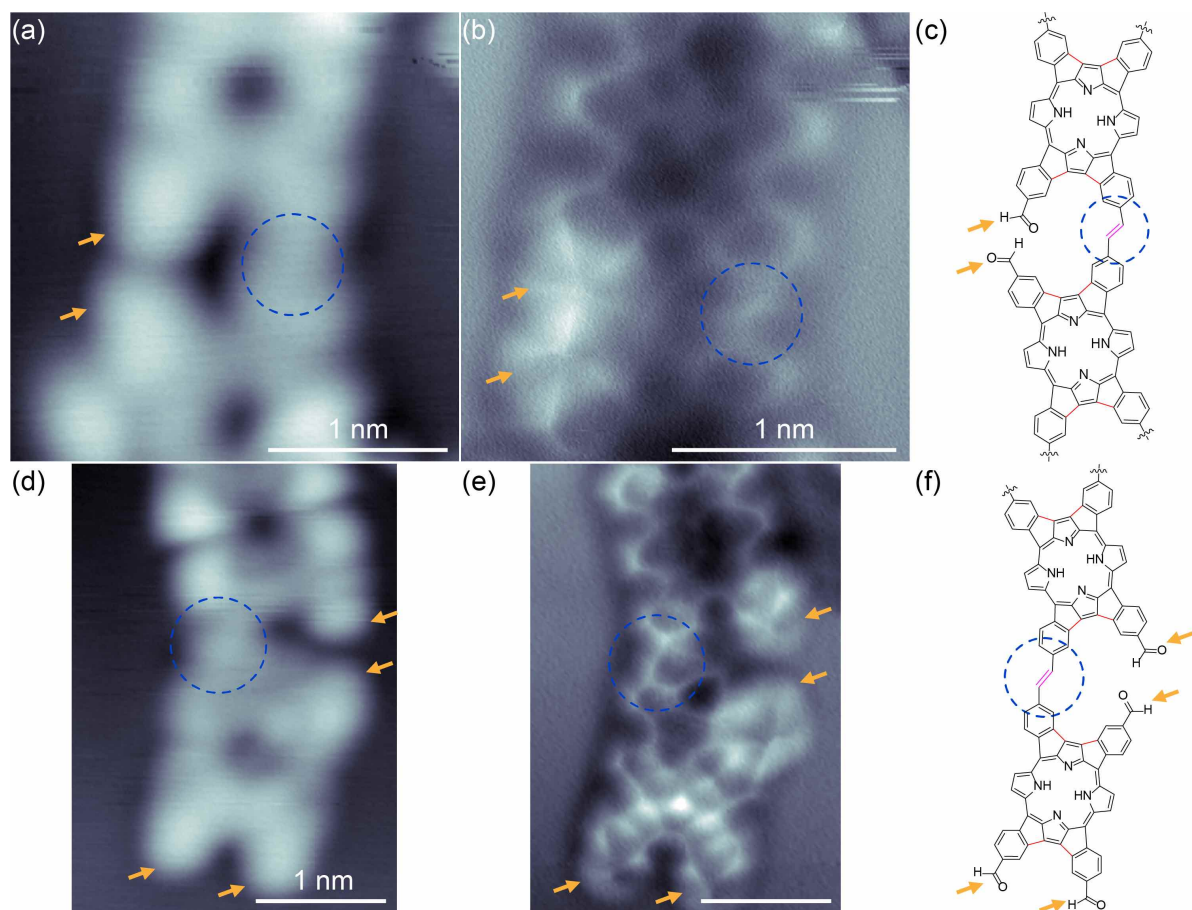
Figure 5.9.: Close-up STM and AFM images of planarized *trans*-dimers upon annealing the sample at 535 K. (a) and (d) STM images of two dimers. (b) and (e) AFM images corresponding to (a) and (d), respectively. (c) and (f) The proposed chemical structures corresponding to (b) and (e), respectively. The STM images show a pronounced bright appearance at the unreacted aldehyde groups, in contrast to a more uniform brightness observed for the -C=C- bond. The -C=C- linkage is marked by the dashed blue circles, and the unreacted aldehyde groups are marked by orange arrows. Scan parameters: (a) and (d) I_t = 10 pA, V_s = 50 mV.

of the C 1s attributed to β-pyrrole and CH=CH carbons of phenyl increases from 50% to 55%. This supports the proposed "McMurry-type" reaction and formation of the C=C–linkage reported here. The shift to the lower binding energy of two fitted carbon peaks (in violet and red) is also an indication of the coupling reaction, as the resultant -C=C- makes the molecular backbone more planar.15 The C 1s peak at 287.8 eV nearly vanishes after annealing the sample at 515 K, whereas no change has taken place in the intensity of C 1s peak corresponding to the CH=CH of phenyl and β-pyrrole carbons. This implies the cleavage of aldehyde groups, corresponding to the loss of unreacted terminal entities as suggested by the AFM data.

Table 5.1.: Contributions of C 1s spectra collected from H_2TFPP on Ag(111) upon depositing at 300 K and stepwise annealing. All XPS measurements are taken at 300 K.

Temperature C 1s	300 K Binding energy/Ratio	475 K Binding energy/ Ratio	515 K Binding energy/Ratio
-CHO (blue)	287.8 eV / 9%	287.8 eV / 4%	287.5 eV / 2%
C=N, C-N (green)	285.7 eV / 17%	285.6 eV / 17%	285.5 eV / 18%
C-C carbons (violet)	285.2 eV / 24%	284.8 eV / 25%	284.6 eV / 25%
CH=CH (red)	284.8 eV / 50%	284.5 eV / 54%	284.3 eV / 55%

In our XPS analysis, the C/O atomic ratio is about 11.6 for precursors adsorbed on the substrate at 300 K, which is very close to the stoichiometric ratio of 12 for intact molecules. Upon thermal annealing the substrate to 475 K, the C/O ratio increases to approximately 25, indicating the 50% loss of oxygen, which is considerably greater than the reaction yield of 32% obtained from the statistical analysis of the molecular features imaged by STM (Figure 5.5). It should be pointed out that an accurate statistical analysis of the cleaved aldehyde groups is difficult to perform due to the limited resolution of STM images. Therefore, the 50% loss of oxygen, retrieved from the XPS data, includes the cleavage of the aldehyde group and the portion of the molecules that have undergone the coupling reaction.

It should be mentioned that very few XPS spectra for porphyrin-containing compounds have been reported where the carbon peaks have been resolved experimentally (in synchrotron facilities) or fitted accordingly. In most studies, all carbon atoms (except C-N) have been fitted with one peak. [272, 279] However, based on a few publications where CH=CH carbons and C-C carbons have been fitted separately or resolved, [260, 281] and to illustrate the generation of newly formed C=C in our study, we have fitted accordingly to separate CH=CH carbons from C-C carbons, which can also be supported by theoretical XPS fitting. [282]

5.4. Porphyrin oligomers on Ag(100)

Motivated by the formation of porphyrin-based oligomers via C=C coupling of H_2TFPP on Ag(111), we studied the reaction of H_2TFPP on Ag(100), exploring the templating effect of a square substrate lattice. STM data reveal self-assembled islands after depositing H_2TFPP monomers on Ag(100) (Figure 5.10), similar to the assembly observed on Ag(111). Annealing
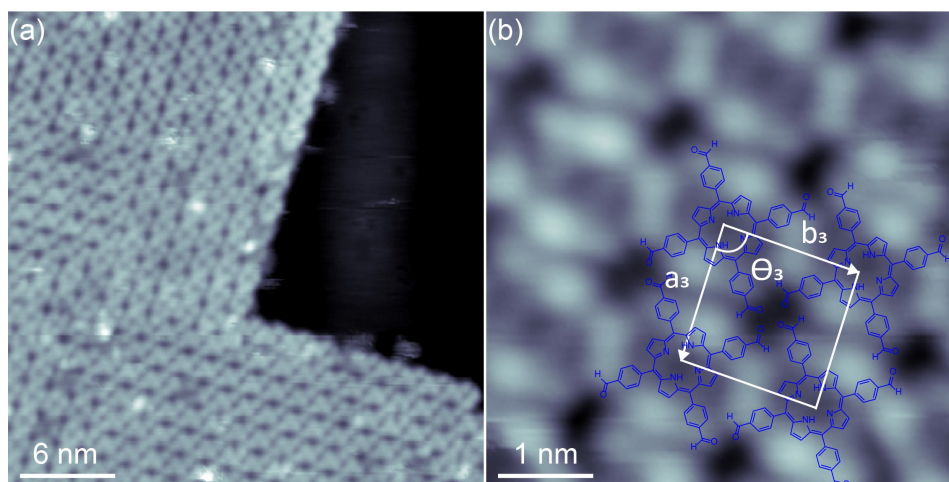
Figure 5.10.: Self-assembled structure of H_2TFPP on Ag(100) after deposition at 300 K. (a) An overview STM image of the self-assembled structure. (b) Zoom-in image of (a) with the chemical structure overlaid. The unit cell can be described by $a_3 = b_3 = 1.56 \pm 0.02$ nm with an angle of $\theta 3 = 89 \pm 1\circ$, which is very close to the values measured from the self-assembled structure achieved on Ag(111). Scan parameters: (a) $I_t = 10$ pA, $V_s = 500$ mV, (b) $I_t = 10$ pA, $V_s = 100$ mV.
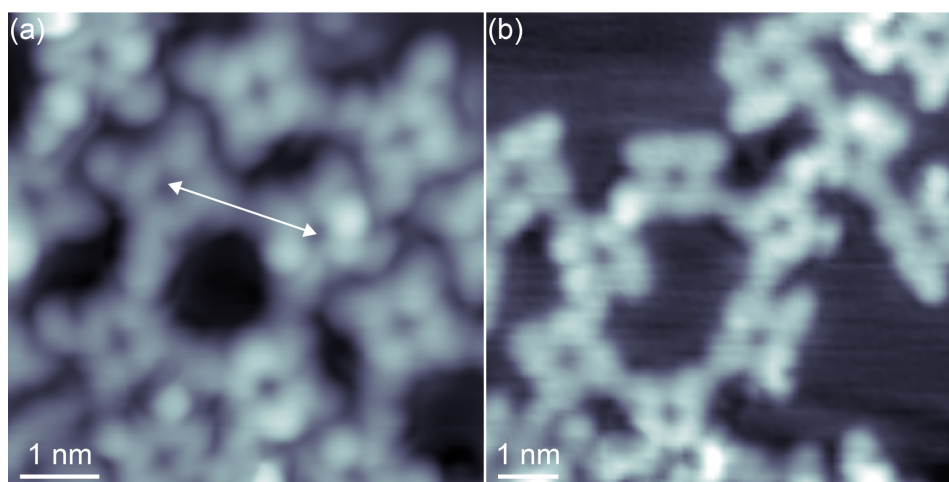
Figure 5.11.: Synthesis of porphyrin-based cyclic oligomers on Ag(100). STM images of (a) four-membered cyclic, and (b) six-membered cyclic structures upon annealing at 475 K and 555 K, respectively. Scan parameters: (a) $I_t = 10$ pA, $V_s = 50$ mV.

the substrate induces the oligomerization of H_2TFPP, and in selected cases, even gives rise to the formation of four-membered cyclic structure and six-membered cyclic structures (cf. data in Figures 5.11a and 5.11b, obtained after annealing at 475 and 555 K, respectively). The center-to-center distance of two connected units in Figure 5.10a (marked by a white arrow) is 1.96 ± 0.02 nm, which is comparable to the 1.94 ± 0.02 nm on Ag(111). The formation of such cyclic products indicates the possibility to construct 2D porous covalently bonded porphyrin sheet structures using the strategy outlined herein. Note, the porphyrin-based oligomers obtained in this work are limited in length and regularity, which could be related to the misalignment and cleavage of the aldehyde groups. This might be improved by using substrates in which molecules would have lower diffusion energy barriers to afford mobility and suitable orientation of the molecules to undergo the reaction.

5.5. Conclusion

In conclusion, we synthesized fully conjugated porphyrin-based oligomers linked by C=C-units through the coupling of 4-formylphenyl substituted porphyrin units. The present study offers a promising UHV-based approach for the on-surface fabrication of conjugated one-dimensional and two-dimensional porphyrin-based nanostructures. This approach is self-contained as the titanium catalyst and other chemical agents necessary in the solution chemistry counterpart are not required in the presented on-surface McMurry-type reaction. Other designer formyl-containing derivates or improved fabrication protocols may provide the long-range expression of regular covalent nanostructures on surfaces.

6. Conclusion and Outlook

In this thesis, several covalently-coupled nanostructures were constructed via different on-surface synthesis schemes. From self-assembly to in-situ synthesis, we precisely controlled the reaction pathways and characterized the products by using advanced scanning probe microscopy. We performed a comprehensive study of the reactivity, geometric and chemical properties of the designed molecular systems, combined with X-ray photoelectron spectroscopy and computational modeling using density functional theory.

Chapter 3 presents an approach to synthesizing enetriynes with a high selectivity (∼85%) on the Ag(100) surface. We used a biphenyl precursor with functional alkynyl and hydroxyl groups at the two opposite ends. As a directing group, hydroxyl substituents induced the arrangement of reactants in each step, while alkynes act as the reactive group leading to the addition reaction. Comparative experiments and DFT calculations provide insights into the factors determining the high selectivity: 1, the hydroxyl substituents direct the arrangement of the molecular domains via the intermolecular hydrogen bonds; 2, O_2 mediates the dehydrogenation of alkyne groups to form alkynyl-Ag-alkynyl organometallic species, preventing the alkynes from homo-coupling; 3, the four-fold symmetric Ag(100) substrate directs the addition reaction at elevated temperature to form tetrameric enetriynes. Furthermore, DFT calculations provided further evidence of the reaction pathways. With our controllable synthesis methods, large self-assembly domains of enetriyne products are obtained on Ag(100) surface. Additionally, bringing this precursor to an Au(111) surface, different thermal annealing treatments resulted in the selective trimerization of alkynes, and regular molecular islands were formed by the directing of hydroxyl substituents. The approach used in this study provides an intriguing avenue for precursor design and selective synthesis.
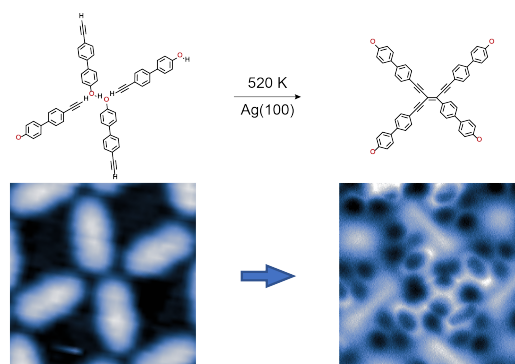
In Chapter 4, we synthesized one-dimensional porphyrin nanostructures by employing alkyne-substituted porphyrins as precursors on Au(111). The precursor had undergone intramolecular cyclization and intermolecular coupling reactions to form covalent nanostructures. The intermolecular coupling induced the formation of chains with lengths commonly exceeding 30 units, nanorings with 5 to 6 porphyrin units, and some branches. More-

over, the morphological diversity is directly related to the two different coupling pathways.
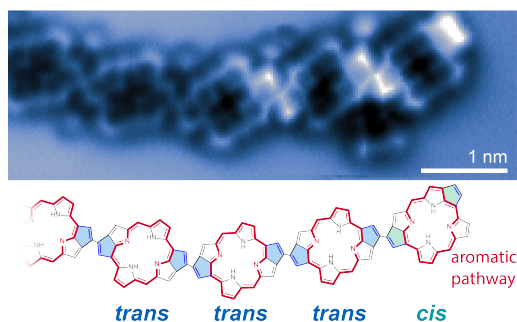
The intramolecular cyclization reaction towards the formation of five-membered rings at the periphery of porphyrins is regio-selective. The statistical analysis indicates a strong preference for *trans*-cyclized products compare to *cis*-cyclized products. These can be rationalized in the framework of aromaticity. The aromatic diaza[18]annulene pathway of free-base porphyrins stabilizes selected carbon atoms at the porphyrin periphery and this can explain the regioselectivity of the cyclization reactions. These observations agree with theoretical estimates of reaction energy differences in the order of 100 *me*V. The reaction energies of the products are directly correlated with their aromaticity, as determined by the calculation of their HOMA indices, which were found to be remarkably robust against adsorption on the substrate. This comprehensive analysis demonstrates that the predictive power of chemical reasoning based on the concept of aromaticity can be extended to on-surface chemistry. The strategy used in this work provides an alternative approach for the construction of long-extended porphyrin nanostructures.

In Chapter 5, we synthesized fully conjugated porphyrin-based oligomers on an Ag(100) surface, with porphyrin units linked by C=C units. A porphyrin with formyl-phenyl substituents at four meso positions was introduced as the precursor. With proper thermal stimuli, the C=C bonds were formed by a McMurry-type reaction of formyl substituents. STM, bond-resolved AFM, and XPS characterizations provide detailed evidence of the topographic and chemical states of products. The chemical reaction presented
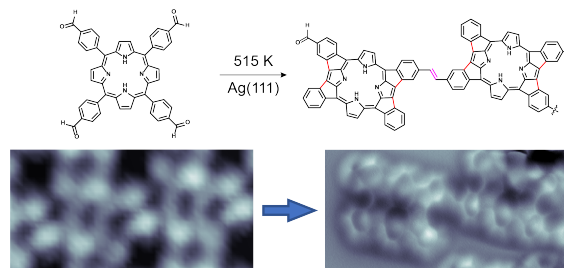
in this work offers a promising bottom-up approach for the on-surface fabrication of conjugated one-dimensional porphyrin nanostructures. This approach is self-contained, as the titanium catalyst and other chemical agents necessary in the solution are not required in the presented on-surface McMurry-type reaction. In further, the combination of the presented new insights with formyl-containing derivatives or improved fabrication protocols may lead to the long-range expression of regular covalent nanostructures on surfaces.

This thesis presents extensive studies of covalent molecular nanostructures on noble metal surfaces. Several novel on-surface synthesis strategies were used to achieve these nanoarchitectures. These comprehensive studies provide new insights into the fundamental

aspects of on-surface synthesis: molecular design, effects of reactant reactivity, reaction control, and the development of new rational reaction protocols. The employed approaches, in-depth analysis, and elaborated progress provide novel perspectives for the on-surface synthesis of covalent molecular nanostructures.

A. Appendix – Supplementary data for porphyrins on Au(111)
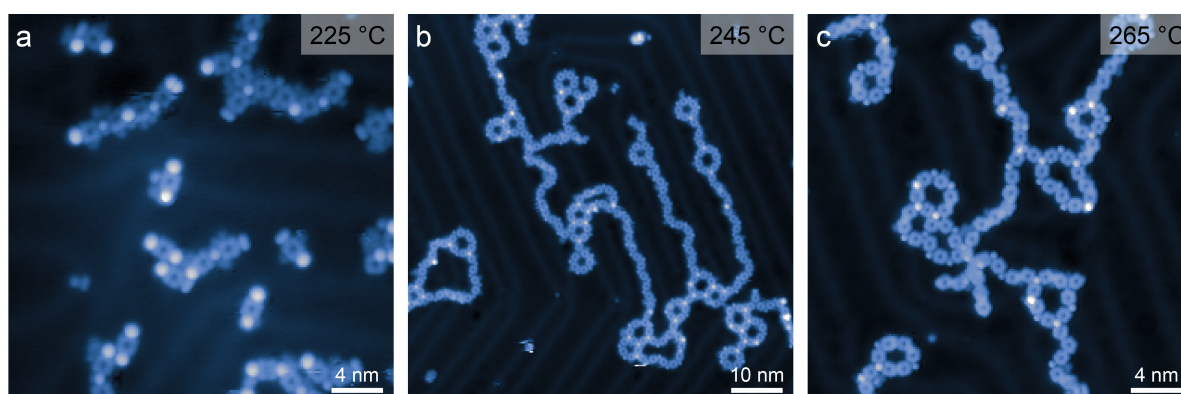
Figure A.1.: Thermally induced -SiMe$_3$ cleavage and coupling for **1b** on the Au(111) surface. Stepwise cleavage of TMS groups increases with the elevated annealing temperatures. The behavior is similar for both, the free-base species **1a**. (a) The first reaction intermediates can be seen at the onset reaction temperature of 225 °C. (b) Annealing the substrate at 245 °C, the reaction further proceeds, where the majority of the bright spots ((i.e. -SiMe$_3$)) are dissociated. (c) Almost all bright spots were removed after annealing at 275 °C, and almost all molecules participated in the formation of 1D porphyrin nanostructures. Scan parameters: (a) and (c) I_t = 10 pA, V_s = 100 mV, (b) I_t = 10 pA, V_s = 200 mV.

Depositing the Cu-metalated porphyrin (**1b**) on a Au(111) surface kept at room temperature, stepwise annealing induces TMS cleavage and coupling of the precursors. STM images (Figure A.1) show a very similar morphology, the extended 1D porphyrin nanostructures, to those observed for free-base porphyrin precursor (**1a**). Note that we cannot identify the central Cu atom for **1b** on Au(111), as no bright features of the molecular center were observed in the images.

In addition to the observed cyclization and coupling reactions for **1b**, the images also show the subtle differences at the junctions between (Z)-type coupled porphyrin units: with 30% of cases, the formed five-membered rings appear dark in AFM images (Figure A.2). The dark features indicate the bending towards the surface (Fig. 4b. black arrow), possibly due to the presence of unsaturated carbon atoms interacting with the substrate. While the AFM measurements did not directly resolve the exact bond configuration of this junction, we note that the geometry of the connected molecules is very similar to the geometry observed for
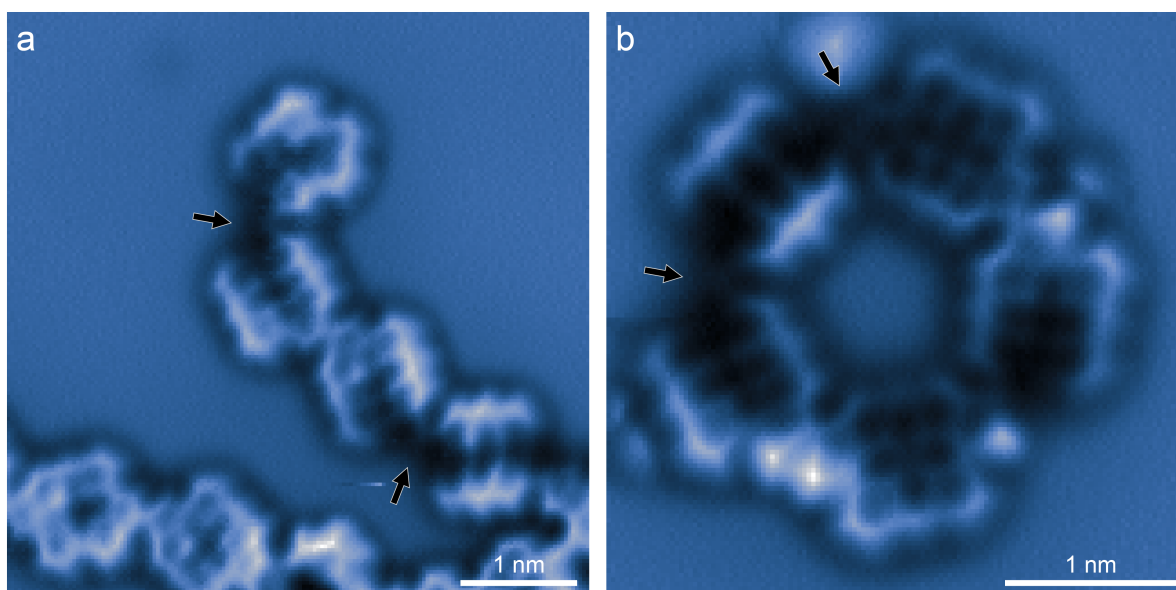
Figure A.2.: 1D porphyrin nanostructures achieved for Cu-metalated porphyrins on Au(111). (a) Zoom-in AFM image of porphyrin chain structures (**2b**) formed after annealing the substrate at 305 °C. (b) A nanoring consisting of five porphyrin units. The black arrows denote the dark (Z)-type junction. Scan parameters: (a) and (b) I_t = 10 pA, V_s = 100 mV, (c) and (d) V_s = 0 V, constant height.

the "normal" bright connections. Our STM manipulation experiments demonstrate that both of these bonding motifs correspond to (Z)-type coupling (Figure A.3).

Before STM manipulation (Figures A.3a and b), the junction region appears dark in the AFM image (marked by a black arrow), which indicates downward-bending of the corresponding carbon atoms, potentially due to unsaturation and thus stronger interaction with the substrate. Additionally, a bright protrusion is seen, which might be related to remnants of TMS or any other adsorbates. The STM Manipulation, i.e., tip movement along the line at decreased height (corresponding to V_s = 50 mV and I_t = 1 nA), induces several changes: The angle between the two molecules decreases; the bright spot disappears, And the junction region appears uniform in brightness. The images (Figures A.3c and d) clearly reveal a regular (Z)-coupling motif consisting of two connected five-membered rings. The contrast change in Figure A.3b is due to a deliberate change of tip height (not due to a tip change). We thus conclude that the coupling shown in Figures A.3a and c is related to the regular (Z)-type coupling.

Similar to the discussion for **2a** on the preferred *trans*-cyclization, we also get insights into the quantitative assessment of aromaticity for **2b**. Figure A.4 shows the HOMA index associated with the 18π diaza-annulene aromatic pathway within the porphyrin for **1b** and two cyclization products (**2b-cis**, **2b-trans**), indicated by the red bonds. The HOMA values are correlated to the DFT calculated reaction energies: the magnitude of HOMA values for products is parallel to their energetic stability, and the preference of the *trans*-cyclization is
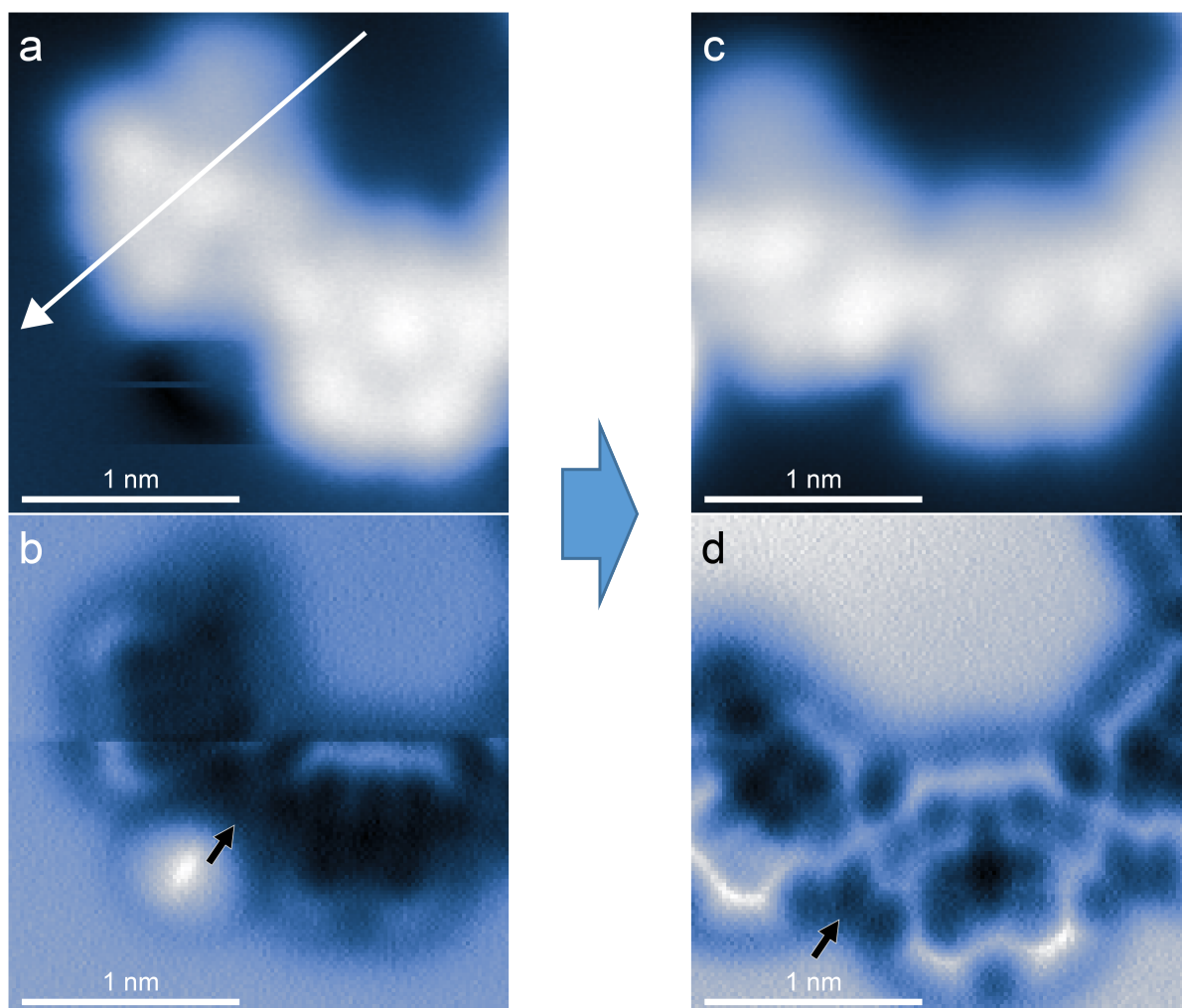
Figure A.3.: Manipulation experiments of (Z)-type coupled connections. (a) and (b) STM and AFM images of (Z)-coupled connection of two Cu-metalated porphyrin units. porphyrin units. (c) and (d) STM and AFM images after the manipulation experiments on the (Z)-coupled connection in (a). Scan parameters: (a) and (b) I_t = 10 pA, V_s = 100 mV, (c) and (d) V_s = 0 V, constant height.
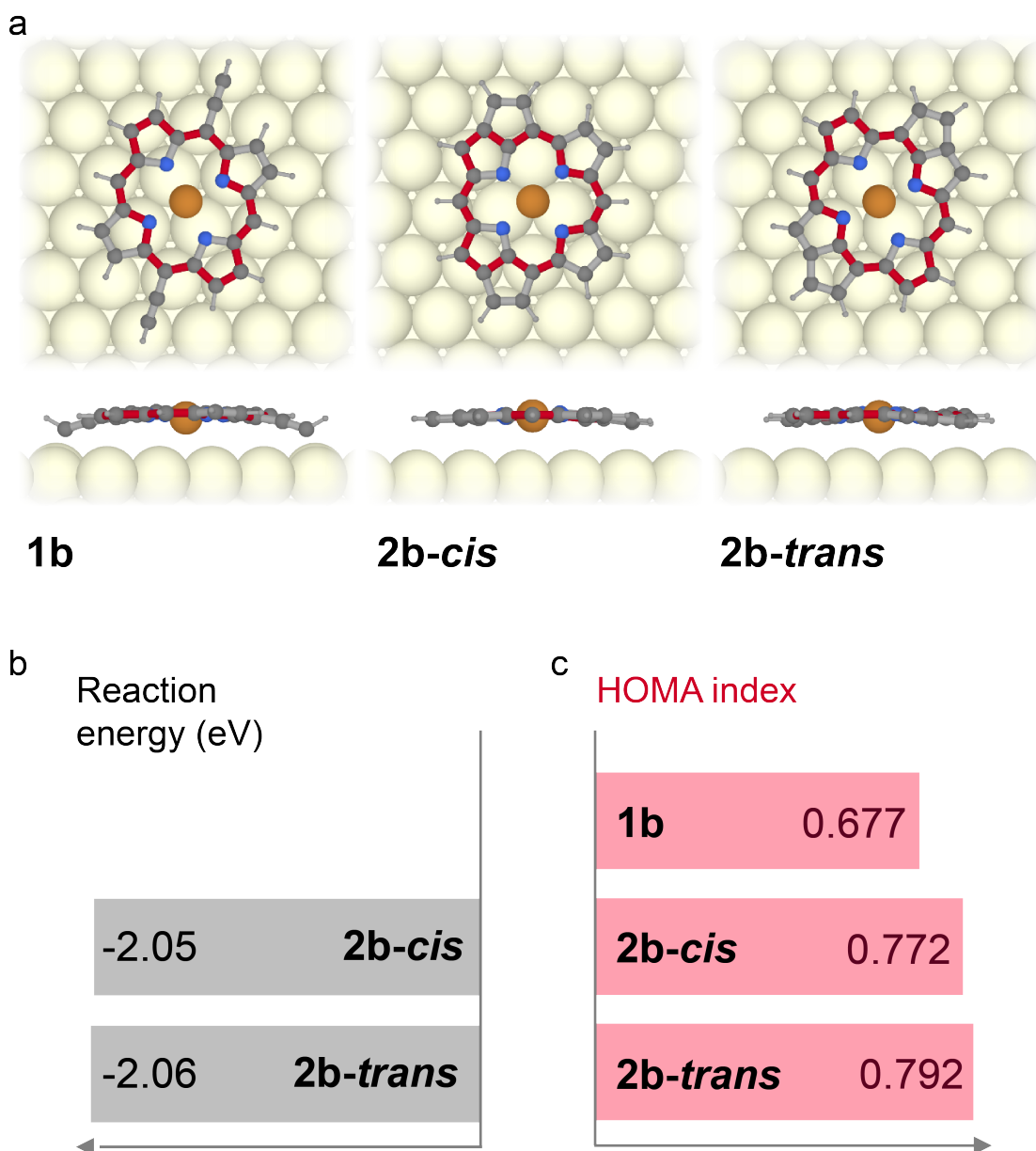
Figure A.4.: Correlation between aromaticity and thermodynamical stability for **2b** species. (a) Top and side views of DFT optimized structures of the precursor **1b** and two cyclization products: **2b-cis** and **2b-trans**. The red bonds denote the aromatic pathway used to calculate the HOMA index. (b) DFT-calculated reaction energies are correlated with (c) the HOMA-aromaticity indices for the respective cyclization products.

valid for both perspectives. Note that the highest aromaticity index for **2b-*cis*** is not obtained from the commonly used 18π diaza-annulene aromatic pathway in chapter 4, rather the path marked by red bonds shown in the structural model. But it does not affect our conclusion of the preferred *trans*-cyclization. Thus, the assessment of aromaticity is in line with the DFT calculations and, more importantly, the experimental observations (refer to the analysis in chapter 4/section:4.3).
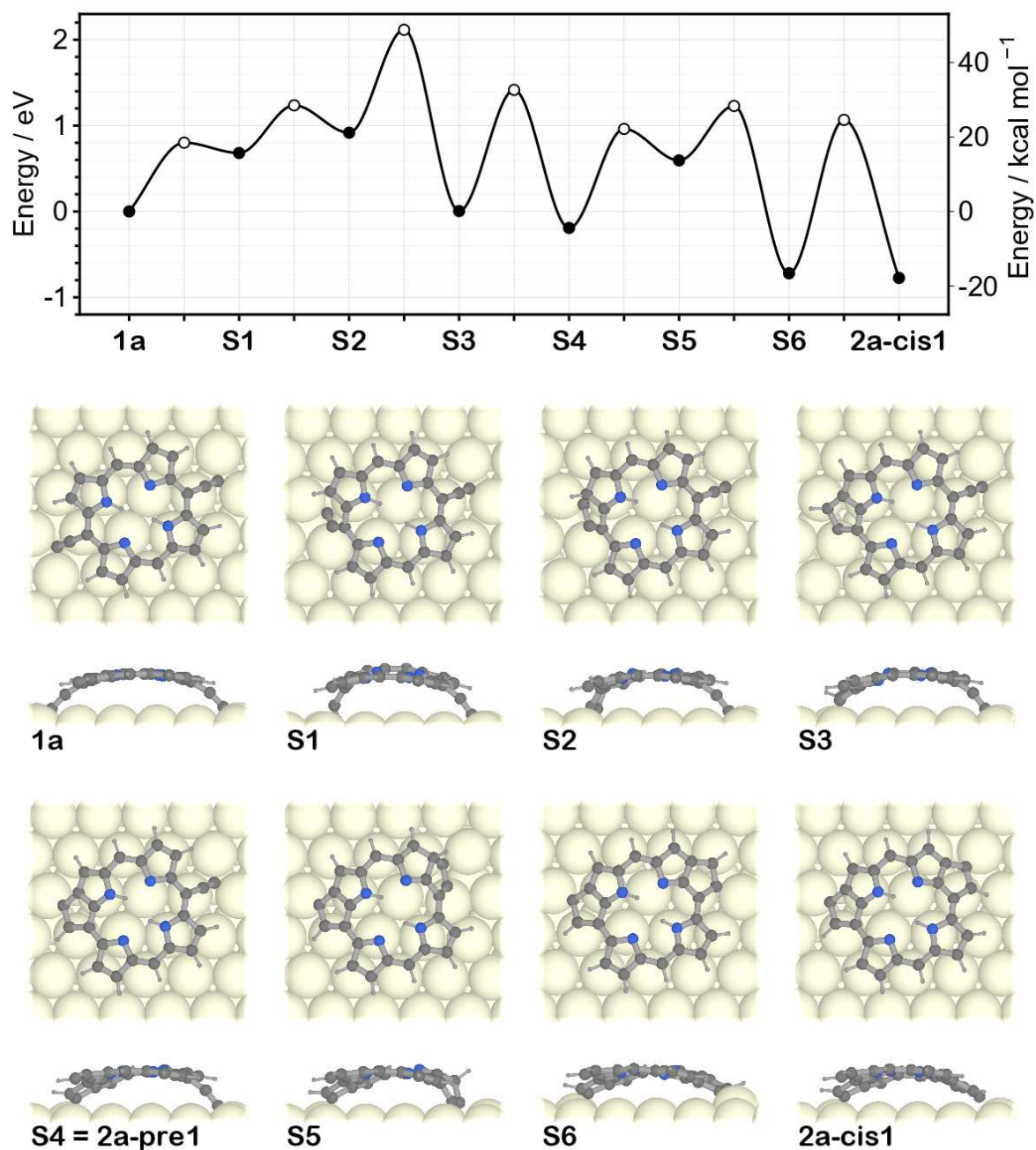
Figure A.5.: Calculated reaction pathway of the transformation of **1a** to **2a-*cis1***. The graph shows the energies and transformation barriers of the respective species. The top and side views of the relaxed structures are shown below. For these calculations, we have opted to use radical-terminated species for reduced complexity, i.e., to avoid additional hydrogen transfer reactions. The transformation barriers for the ring formation reactions are 0.55 eV for **S1** to **S2** (1.36 eV for **1a** to **S2**, respectively) and 1.15 eV for **S4** to **S5**.
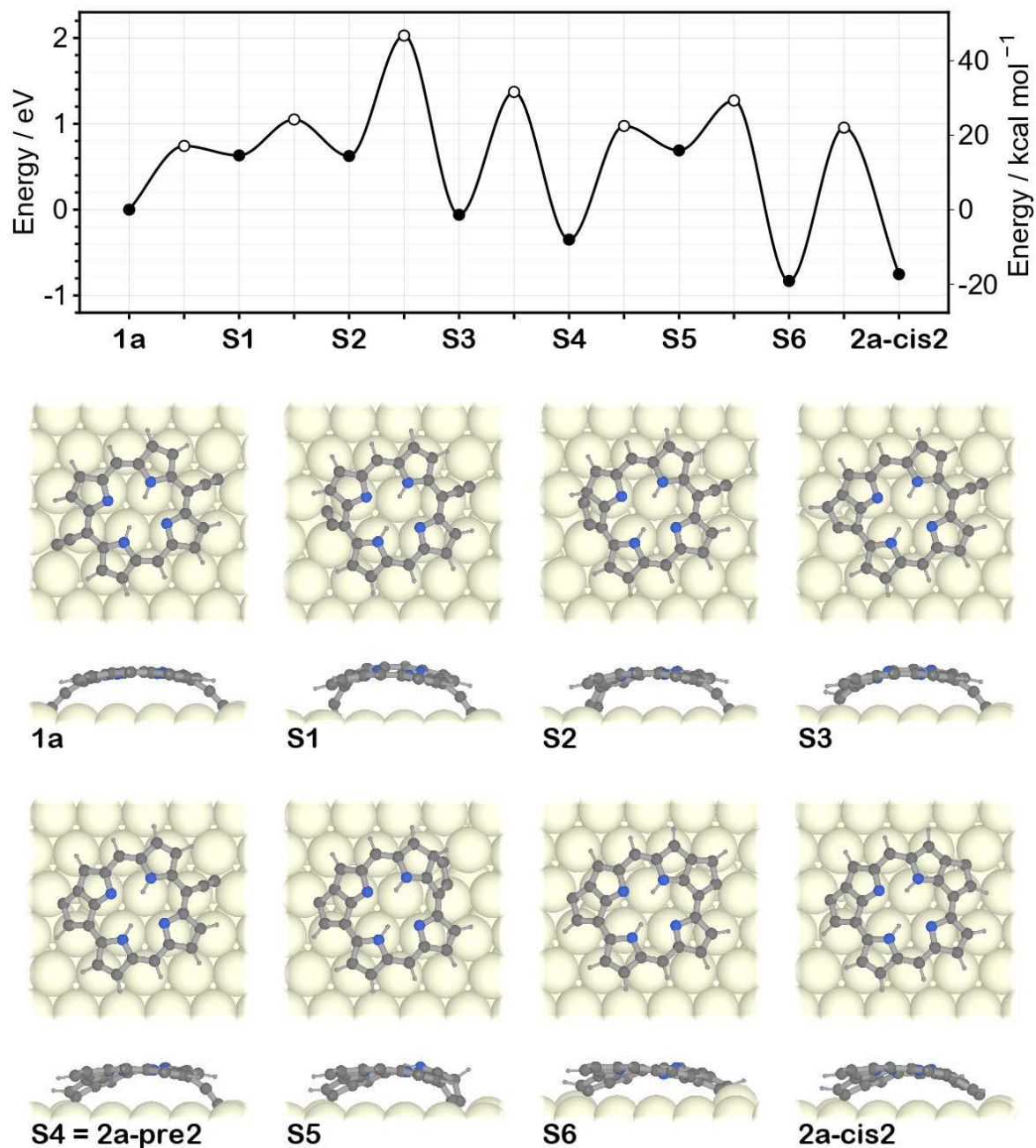
Figure A.6.: Calculated reaction pathway of the transformation of **1a** to **2a-*cis2***. The graph shows the energies and transformation barriers of the respective species. The top and side views of the relaxed structures are shown below. The transformation barriers for the ring formation reactions are 0.42 eV for **S1** to **S2** (1.16 eV for **1a** to **S2**, respectively) and 1.32 eV for **S4** to **S5**.
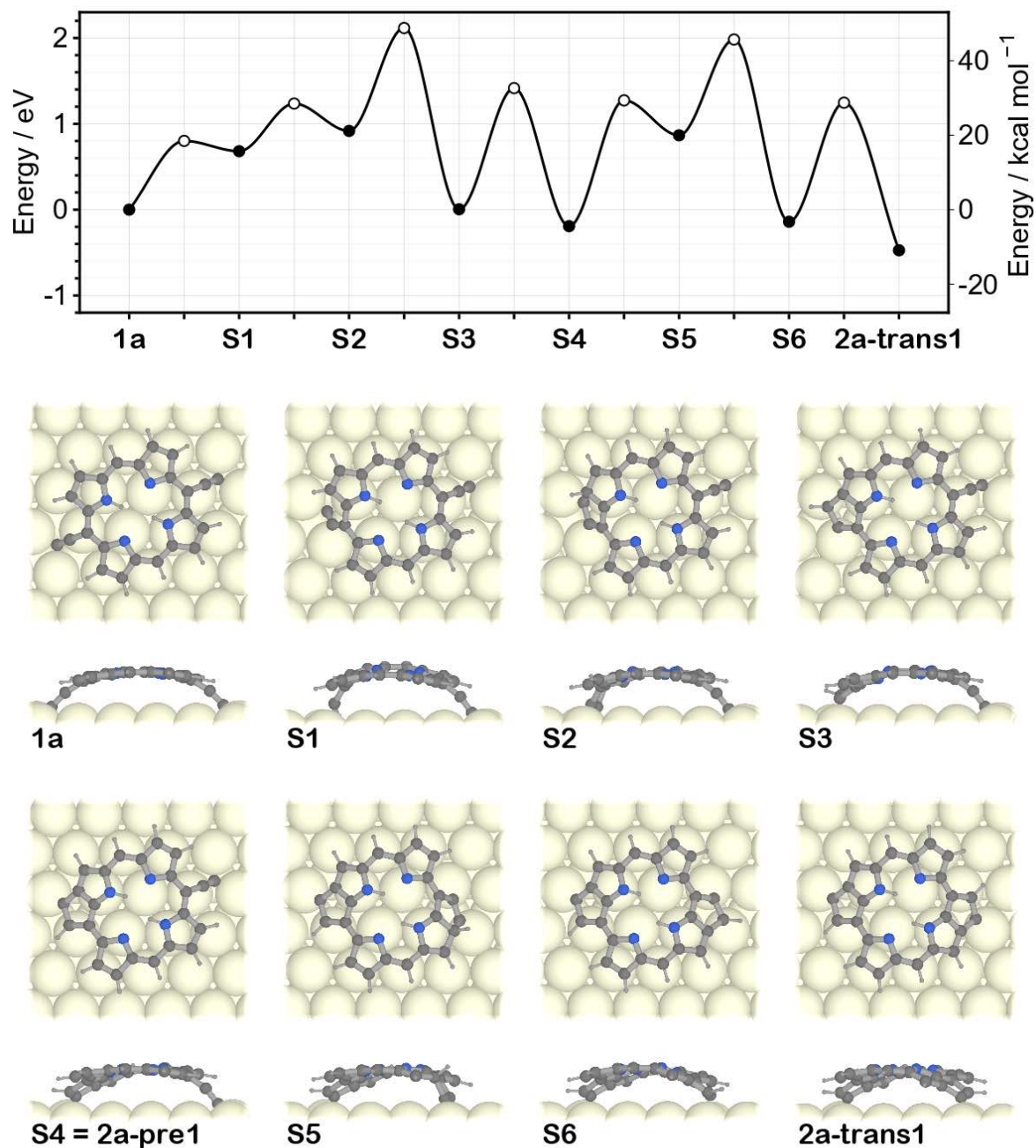
Figure A.7.: Calculated reaction pathway of the transformation of **1a** to **2a-*trans1***. The graph shows the energies and transformation barriers of the respective species. The top and side views of the relaxed structures are shown below. The transformation barriers for the ring formation reactions are 0.55 eV for **S1** to **S2** (1.36 eV for **1a** to **S2**, respectively) and 1.47 eV for **S4** to **S5**.
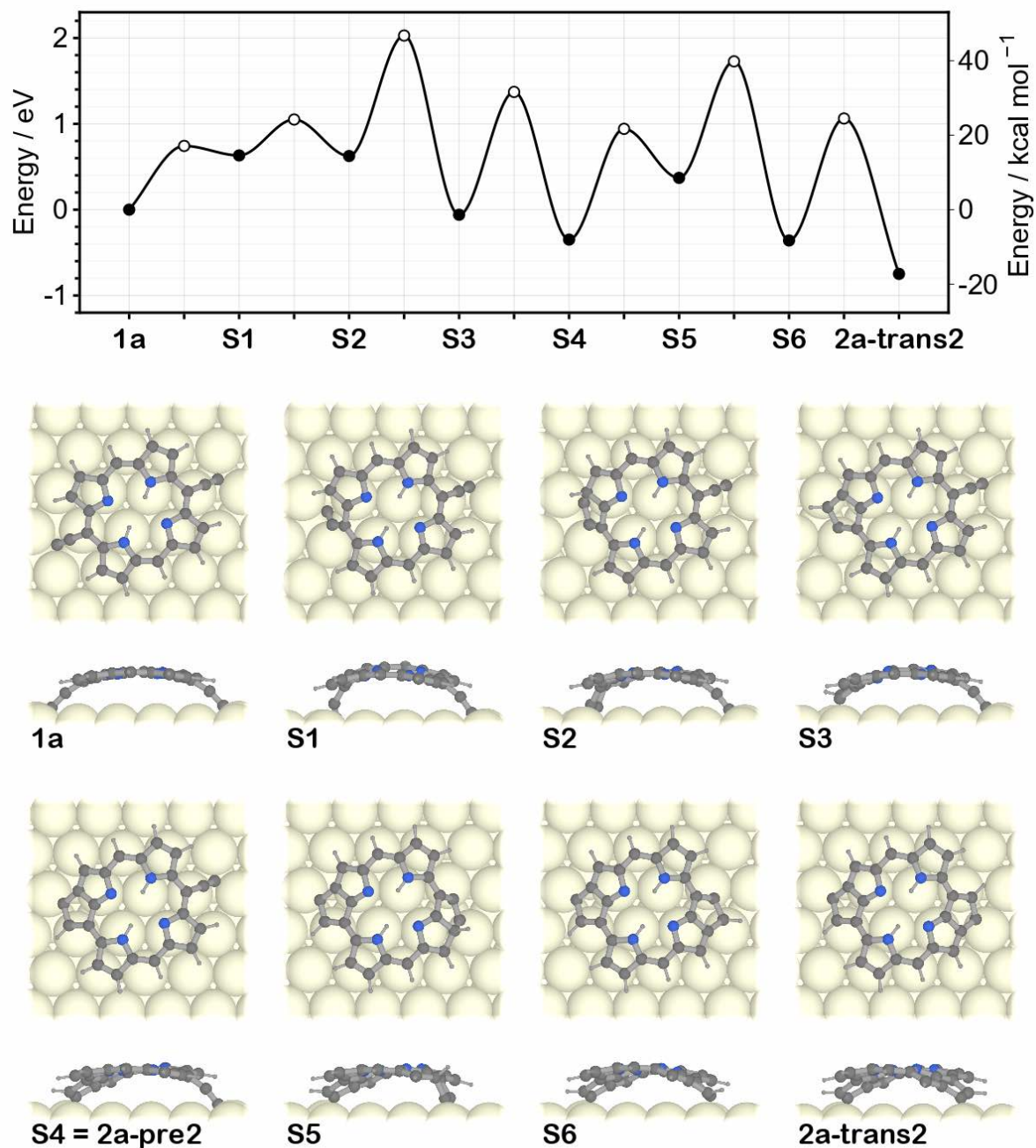
Figure A.8.: Calculated reaction pathway of the transformation of **1a** to **2a-*trans2***. The graph shows the energies and transformation barriers of the respective species. The top and side views of the relaxed structures are shown below. The transformation barriers for the ring formation reactions are 0.42 eV for **S1** to **S2** (1.16 eV for **1a** to **S2**, respectively) and 1.29 eV for **S4** to **S5**.

B. Appendix – Supplementary data for EHBP on Ag(100)
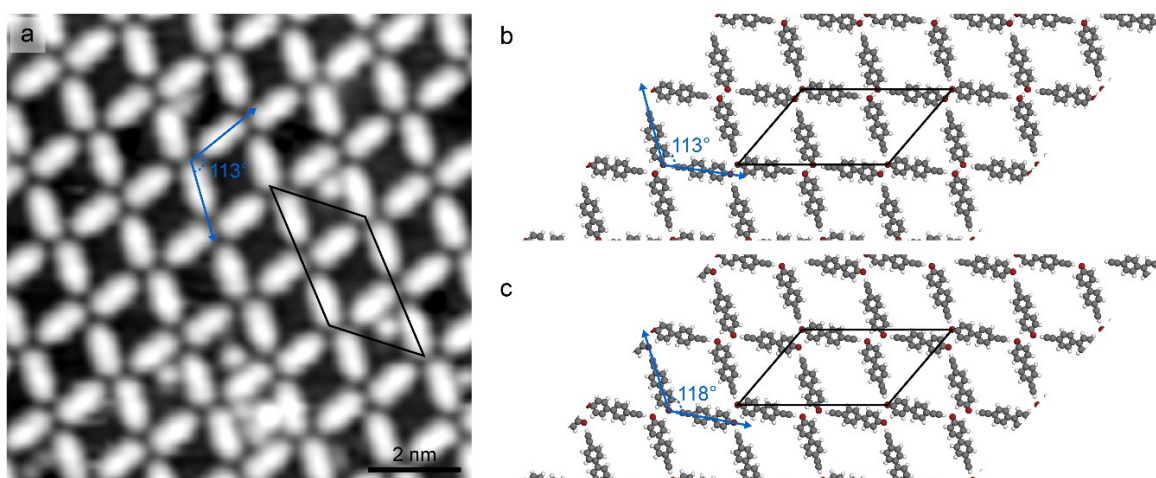
Figure B.1.: Determination of the self-assembly structural model of EHBP at RT. (a) High-resolution STM image of self-assembly structure at RT. Optimized structural models with half-dehydrogenated hydroxyl groups and fully dehydrogenated hydroxyl groups are shown in (b) and (c), respectively. The black framework shows the unit cell of the self-assembly structure, the unit cell of structural models in (b) and (c) is identical to the experimental value in (a). Blue arrows display the direction of the molecular axis. It shows that the angle between the molecular axis in (b) is comparable with the angle measured on the STM image in (a). This agrees well with the examination of XPS (Figure 3.4). Scan parameters: (a) I_t = 10 pA, V_s = 100 mV,

Optimized structure   E-Ef = 0.5 eV   E-Ef = -0.5 eV
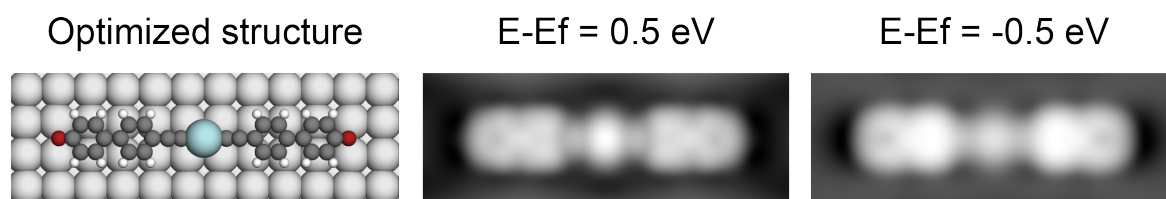
Figure B.2.: The most stable adsorption configuration (right) as well as the simulated STM images of a single organometallic dimer.

Experimental STM image   Simulated STM image

a V_s = -0.5 eV   b   E-Ef = -0.5 eV

1 nm

c V_s = 2.0 eV   d   E-Ef = 2.0 eV
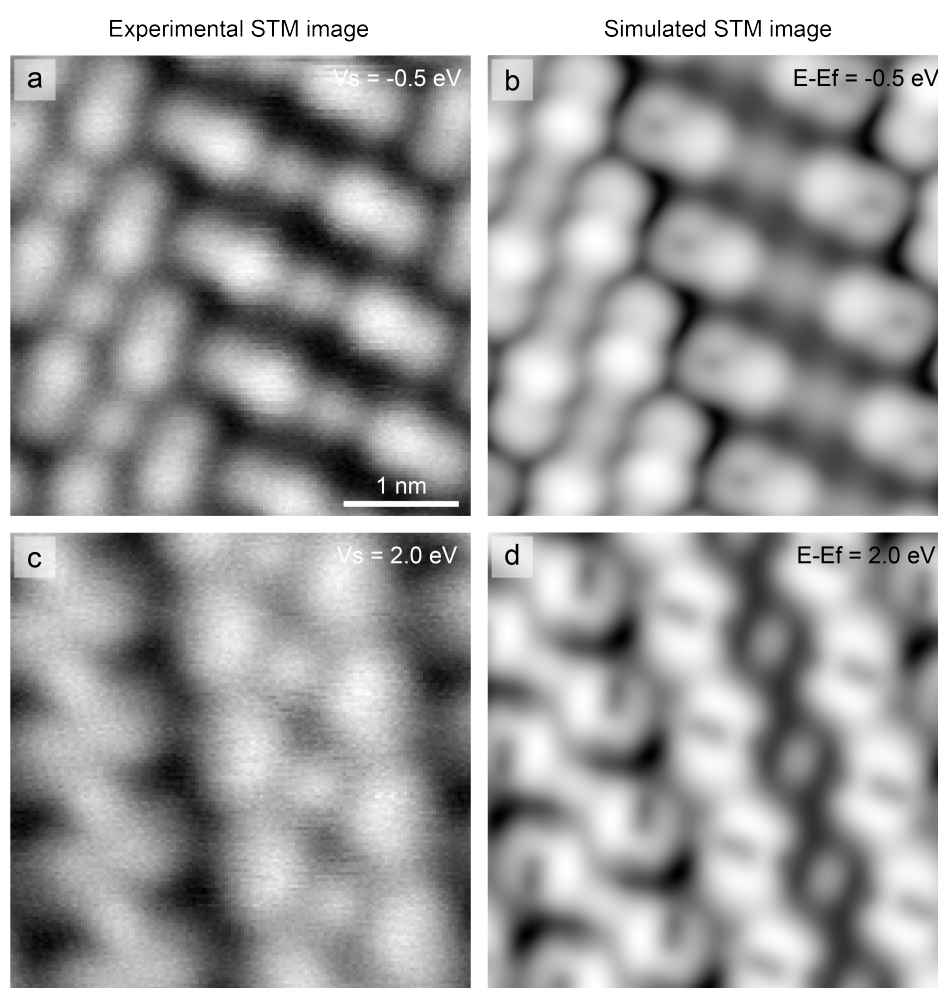
Figure B.3.: Experimental and simulated bias-dependent STM images of the array assembly of the organometallic dimers on Ag(100) surfaces. The simulated STM images agree well with the experimental ones. Scan parameters: (a) I_t = 10 pA, V_s = 500 mV, (c) I_t = 10 pA, V_s = 200 mV.

List of Figures

List of Tables

List of Publications

[1] N. Cao, A. Riss, E. Corral-Rascon, A. Meindl, W. Auwärter, M. O. Senge*, M. Ebrahimi*, and J. V. Barth. **Surface-confined formation of conjugated porphyrin-based nanostructures on Ag(111)**. *Nanoscale*, 2021, 13, 19884-19889.

[2] N. Cao, J. Björk, E. Corral-Rascon, Z. Chen, M. Ruben, M. O. Senge, J. V. Barth, and A. Riss*. **The role of aromaticity in the cyclization and polymerization of alkyne-substituted porphyrins on Au(111)**. *Under review in Nat. Chem.*.

[3] N. Cao, B. Yang*, A. Riss, J. Rosen, J. Björk*, and J. V. Barth. **On-surface synthesis of enetriynes**. *Under review in Nat.Commun.*.

[4] B. Yang*, K. Niu, F. Haag, N. Cao, J. Zhang, H. Zhang, Q. Li, F. Allegretti, J. Björk, J. V. Barth*, and L. Chi*. **Abiotic formationof an amide bond via surface-supported direct carboxyl–amine coupling**. *Angew. Chem. Int. Ed.*, 2022, 61, e202113590.

Bibliography

[1] V. Barone, O. Hod, and G. E. Scuseria. "Electronic Structure and Stability of Semi-conducting Graphene Nanoribbons". In: *Nano Letters* 6.12 (2006), pp. 2748–2754. DOI: 10.1021/nl0617033. URL: https://doi.org/10.1021/nl0617033.

[2] Y.-W. Son, M. L. Cohen, and S. G. Louie. "Half-metallic graphene nanoribbons". In: *Nature* 444.7117 (2006), pp. 347–349. DOI: 10.1038/nature05180.

[3] J. V. Barth, H. Brune, G. Ertl, and R. J. Behm. "Scanning tunneling microscopy observations on the reconstructed Au(111) surface: Atomic structure, long-range superstructure, rotational domains, and surface defects". In: *Phys. Rev. B* 42 (15 1990), pp. 9307–9318. DOI: 10.1103/PhysRevB.42.9307. URL: https://link.aps.org/doi/10.1103/PhysRevB.42.9307.

[4] J. V. Barth. "Molecular architectonic on metal surfaces". In: *Annu. Rev. Phys. Chem.* 58 (2007), pp. 375–407. DOI: 10.1146/annurev.physchem.56.092503.141259.

[5] J. V. Barth, J. Weckesser, C. Cai, P. Günter, L. Bürgi, O. Jeandupeux, and K. Kern. "Building Supramolecular Nanostructures at Surfaces by Hydrogen Bonding". In: *Angewandte Chemie International Edition* 39.7 (2000), pp. 1230–1234. DOI: https://doi.org/10.1002/(SICI)1521-3773(20000403)39:7<1230::AID-ANIE1230>3.0.CO;2-I.

[6] L. Grill, M. Dyer, L. Lafferentz, M. Persson, M. V. Peters, and S. Hecht. "Nano-architectures by covalent assembly of molecular building blocks". In: *Nature Nanotechnology* 2.11 (2007), pp. 687–691. ISSN: 17483395. DOI: 10.1038/nnano.2007.346.

[7] F. Klappenberger, Y.-Q. Zhang, J. Björk, S. Klyatskaya, M. Ruben, and J. V. Barth. "On-Surface Synthesis of Carbon-Based Scaffolds and Nanomaterials Using Terminal Alkynes". In: *Accounts of Chemical Research* 48.7 (2015), pp. 2140–2150. DOI: 10.1021/acs.accounts.5b00174. URL: https://doi.org/10.1021/acs.accounts.5b00174.

[8] S. Clair and D. G. de Oteyza. "Controlling a chemical coupling reaction on a surface: tools and strategies for on-surface synthesis". In: *Chemical reviews* 119.7 (2019), pp. 4717–4776.

[9] L. Grill and S. Hecht. "Covalent on-surface polymerization". In: *Nature Chemistry* 12.2 (2020), pp. 115–130. ISSN: 17554349. DOI: 10.1038/s41557-019-0392-9. URL: http://dx.doi.org/10.1038/s41557-019-0392-9.

[10] Y.-Q. Zhang, N. Kepčija, M. Kleinschrodt, K. Diller, S. Fischer, A. C. Papageorgiou, F. Allegretti, J. Björk, S. Klyatskaya, F. Klappenberger, et al. "Homo-coupling of terminal alkynes on a noble metal surface". In: *Nature communications* 3.1 (2012), pp. 1–8. DOI: 10.1038/ncomms2291.

[11] Y. Okawa and M. Aono. "Nanoscale control of chain polymerization". In: *Nature* 409.6821 (2001), pp. 683–684.

[12] Q. Zhong, A. Ihle, S. Ahles, H. A. Wegner, A. Schirmeisen, and D. Ebeling. "Constructing covalent organic nanoarchitectures molecule by molecule via scanning probe manipulation". In: *Nature chemistry* 13.11 (2021), pp. 1133–1139. DOI: 10.1038/s41557-021-00773-4.

[13] L. Grossmann, B. T. King, S. Reichlmaier, N. Hartmann, J. Rosen, W. M. Heckl, J. Björk, and M. Lackinger. "On-surface photopolymerization of two-dimensional polymers ordered on the mesoscale". In: *Nature Chemistry* 13 (2021), pp. 730–736. DOI: 10.1038/s41557-021-00709-y. URL: https://doi.org/10.1038/s41557-021-00709-y.

[14] H.-Y. Gao, D. Zhong, H. Moenig, H. Wagner, P.-A. Held, A. Timmer, A. Studer, and H. Fuchs. "Photochemical Glaser Coupling at Metal Surfaces". In: *Journal of Physical Chemistry C* 118.12 (2014), pp. 6272–6277. ISSN: 1932-7447. DOI: 10.1021/jp411889e.

[15] G. Otero, G. Biddau, C. Sánchez-Sánchez, R. Caillard, M. F. López, C. Rogero, F. J. Palomares, N. Cabello, M. A. Basanta, J. Ortega, et al. "Fullerenes from aromatic precursors by surface-catalysed cyclodehydrogenation". In: *Nature* 454.7206 (2008), pp. 865–868. DOI: 10.1038/nature07193.

[16] J. Cai, P. Ruffieux, R. Jaafar, M. Bieri, T. Braun, S. Blankenburg, M. Muoth, A. P. Seitsonen, M. Saleh, X. Feng, K. Müllen, and R. Fasel. "Atomically precise bottom-up fabrication of graphene nanoribbons". In: *Nature* 466.7305 (2010), pp. 470–473. ISSN: 1476-4687. DOI: 10.1038/nature09211. URL: https://www.nature.com/articles/nature09211.

[17] P. Ruffieux, S. Wang, B. Yang, C. Sánchez-Sánchez, J. Liu, T. Dienel, L. Talirz, P. Shinde, C. A. Pignedoli, D. Passerone, et al. "On-surface synthesis of graphene nanoribbons with zigzag edge topology". In: *Nature* 531.7595 (2016), pp. 489–492. DOI: 10.1038/nature17151.

[18] N. A. A. Zwaneveld, R. Pawlak, M. Abel, D. Catalin, D. Gigmes, D. Bertin, and L. Porte. "Organized Formation of 2D Extended Covalent Organic Frameworks at Surfaces". In: *Journal of the American Chemical Society* 130.21 (2008), pp. 6678–6679. DOI: 10.1021/ja800906f. URL: https://doi.org/10.1021/ja800906f.

[19] B. Yang, J. Björk, H. Lin, X. Zhang, H. Zhang, Y. Li, J. Fan, Q. Li, and L. Chi. "Synthesis of Surface Covalent Organic Frameworks via Dimerization and Cyclotrimerization of Acetyls". In: *Journal of the American Chemical Society* 137.15 (2015), pp. 4904–4907. DOI: 10.1021/jacs.5b00774. URL: https://doi.org/10.1021/jacs.5b00774.

[20] C. Chen, T. Joshi, H. Li, A. D. Chavez, Z. Pedramrazi, P.-N. Liu, H. Li, W. R. Dichtel, J.-L. Bredas, and M. F. Crommie. "Local Electronic Structure of a Single-Layer Porphyrin-Containing Covalent Organic Framework". In: *ACS Nano* 12.1 (2018), pp. 385–391. DOI: 10.1021/acsnano.7b06529. URL: https://doi.org/10.1021/acsnano.7b06529.

[21] L. Lafferentz, F. Ample, H. Yu, S. Hecht, C. Joachim, and L. Grill. "Conductance of a Single Conjugated Polymer as a Continuous Function of Its Length". In: *Science* 323.5918 (2009), pp. 1193–1197. DOI: 10.1126/science.1168255. URL: https://www.science.org/doi/abs/10.1126/science.1168255.

[22] L. Lafferentz, V. Eberhardt, C. Dri, C. Africh, G. Comelli, F. Esch, S. Hecht, and L. Grill. "Controlling on-surface polymerization by hierarchical and substrate-directed growth". In: *Nature Chemistry* 4.3 (2012), pp. 215–220. ISSN: 17554330. DOI: 10.1038/nchem.1242.

[23] W. Wang, X. Shi, S. Wang, M. A. Van Hove, and N. Lin. "Single-molecule resolution of an organometallic intermediate in a surface-supported Ullmann coupling reaction". In: *Journal of the American Chemical Society* 133.34 (2011), pp. 13264–13267. DOI: 10.1021/ja204956b.

[24] M. Bieri, M.-T. Nguyen, O. Gröning, J. Cai, M. Treier, K. Aıt-Mansour, P. Ruffieux, C. A. Pignedoli, D. Passerone, M. Kastler, et al. "Two-dimensional polymer formation on surfaces: insight into the roles of precursor mobility and reactivity". In: *Journal of the American Chemical Society* 132.46 (2010), pp. 16669–16676. DOI: 10.1021/ja107947z.

[25] C. Nacci, A. Viertel, S. Hecht, and L. Grill. "Covalent Assembly and Characterization of Nonsymmetrical Single-Molecule Nodes". In: *Angewandte Chemie International Edition* 55.44 (2016), pp. 13724–13728. DOI: https://doi.org/10.1002/anie.201605421. URL: https://onlinelibrary.wiley.com/doi/abs/10.1002/anie.201605421.

[26] Q. Fan, C. Wang, Y. Han, J. Zhu, W. Hieringer, J. Kuttner, G. Hilt, and J. M. Gottfried. "Surface-Assisted Organic Synthesis of Hyperbenzene Nanotroughs". In: *Angewandte Chemie International Edition* 52.17 (2013), pp. 4668–4672. DOI: https://doi.org/10.1002/anie.201300610. URL: https://onlinelibrary.wiley.com/doi/abs/10.1002/anie.201300610.

[27] H.-Y. Gao, H. Wagner, D. Zhong, J.-H. Franke, A. Studer, and H. Fuchs. "Glaser Coupling at Metal Surfaces". In: *Angewandte Chemie-International Edition* 52.14 (2013), pp. 4024–4028. ISSN: 1433-7851. DOI: 10.1002/anie.201208597.

[28] B. Cirera, Y.-Q. Zhang, J. Björk, S. Klyatskaya, Z. Chen, M. Ruben, J. V. Barth, and F. Klappenberger. "Synthesis of Extended Graphdiyne Wires by Vicinal Surface Templating". In: *Nano Letters* 14.4 (2014), pp. 1891–1897. DOI: 10.1021/nl4046747. URL: https://doi.org/10.1021/nl4046747.

[29] Z. Gong, B. Yang, H. Lin, Y. Tang, Z. Tang, J. Zhang, H. Zhang, Y. Li, Y. Xie, Q. Li, and L. Chi. "Structural Variation in Surface-Supported Synthesis by Adjusting the Stoichiometric Ratio of the Reactants". In: *ACS Nano* 10 (2016), pp. 4228–4235. DOI: 10.1021/acsnano.5b07601. URL: www.acsnano.org.

[30] L. Jiang, A. C. Papageorgiou, S. C. Oh, Ö. Sağlam, J. Reichert, D. A. Duncan, Y.-Q. Zhang, F. Klappenberger, Y. Guo, F. Allegretti, et al. "Synthesis of pyrene-fused pyrazaacenes on metal surfaces: toward one-dimensional conjugated nanostructures". In: *ACS nano* 10.1 (2016), pp. 1033–1041. DOI: 10.1021/acsnano.5b06340.

[31] S. Weigelt, C. Busse, C. Bombis, M. M. Knudsen, K. V. Gothelf, E. Laegsgaard, F. Besenbacher, T. R. Linderoth, M. M. Knudsen, K. V. Gothelf, S. Weigelt, C. Busse, C. Bombis, A. E. Laegsgaard, F. Besenbacher, and A. T. R Linderoth. "Surface Synthesis of 2D Branched Polymer Nanostructures". In: *Angew. Chem. Int. Ed* 47 (2008), pp. 4406–4410. DOI: 10.1002/anie.200705079. URL: http://www.angewandte.orgorfromtheauthor..

[32] S. Weigelt, C. Busse, C. Bombis, M. M. Knudsen, K. V. Gothelf, T. Strunskus, C. Wöll, M. Dahlbom, B. Hammer, E. Laegsgaard, F. Besenbacher, T. R. Linderoth, M. M. Knudsen, K. V. Gothelf, C. Busse, T. Strunskus, and C. Wöll. "Scanning Tunneling Microscopy Covalent Interlinking of an Aldehyde and an Amine on a Au(111) Surface in Ultrahigh Vacuum". In: *Angew. Chem. Int. Ed* 46 (2007), pp. 9227–9230. URL: http://www.angewandte.orgorfromtheauthor.angewandtechemie.

[33] D. G. de Oteyza, P. Gorman, Y.-C. Chen, S. Wickenburg, A. Riss, D. J. Mowbray, G. Etkin, Z. Pedramrazi, H.-Z. Tsai, A. Rubio, M. F. Crommie, and F. R. Fischer. "Direct Imaging of Covalent Bond Structure in Single-Molecule Chemical Reactions". In: *Science* 340.6139 (2013), pp. 1434–1437. DOI: 10.1126/science.1238187. URL: https://www.science.org/doi/abs/10.1126/science.1238187.

[34] Q. Sun, C. Zhang, Z. W. Li, H. H. Kong, Q. G. Tan, A. G. Hu, and W. Xu. "On-Surface Formation of One-Dimensional Polyphenylene through Bergman Cyclization". English. In: *Journal of the American Chemical Society* 135.23 (2013), pp. 8448–8451. ISSN: 0002-7863.

[35] A. C. Aragonès, N. L. Haworth, N. Darwish, S. Ciampi, N. J. Bloomfield, G. G. Wallace, I. Diez-Perez, and M. L. Coote. "Electrostatic catalysis of a Diels-Alder reaction". In: *Nature* 531 (2016), pp. 88–91. DOI: 10.1038/nature16989.

[36] A. Wiengarten, K. Seufert, W. Auwärter, D. Ecija, K. Diller, F. Allegretti, F. Bischoff, S. Fischer, D. A. Duncan, A. C. Papageorgiou, F. Klappenberger, R. G. Acres, T. H. Ngo, and J. V. Barth. "Surface-assisted dehydrogenative homocoupling of porphine molecules". In: *Journal of the American Chemical Society* 136.26 (2014), pp. 9346–9354. ISSN: 15205126. DOI: 10.1021/ja501680n.

[37] Q. Li, B. Yang, H. Lin, N. Aghdassi, K. Miao, J. Zhang, H. Zhang, Y. Li, S. Duhm, J. Fan, and L. Chi. "Surface-Controlled Mono/Diselective ortho C-H Bond Activation". In: *Journal of the American Chemical Society* 138.8 (2016), pp. 2809–2814. ISSN: 0002-7863. DOI: 10.1021/jacs.5b13286.

[38] K. Amsharov, N. Abdurakhmanova, S. Stepanow, S. Rauschenbach, M. Jansen, and K. Kern. "Towards the isomer-specific synthesis of higher fullerenes and buckybowls by the surface-catalyzed cyclodehydrogenation of aromatic precursors". In: *Angewandte Chemie - International Edition* 49.49 (2010), pp. 9392–9396. ISSN: 14337851. DOI: 10.1002/anie.201005000.

[39] M. Treier, C. A. Pignedoli, T. Laino, R. Rieger, K. Müllen, D. Passerone, and R. Fasel. "Surface-assisted cyclodehydrogenation provides a synthetic route towards easily processable and chemically tailored nanographenes". In: *Nature Chemistry* 3.1 (2011), pp. 61–67. ISSN: 17554330. DOI: 10.1038/nchem.891.

[40] X.-H. Liu, C.-Z. Guan, S.-Y. Ding, W. Wang, H.-J. Yan, D. Wang, and L.-J. Wan. "On-Surface Synthesis of Single-Layered Two-Dimensional Covalent Organic Frameworks via SolidVapor Interface Reactions". In: (2013). DOI: 10.1021/ja403464h. URL: https://pubs.acs.org/sharingguidelines.

[41] J. F. Dienstmaier, D. D. Medina, M. Dogru, P. Knochel, T. Bein, W. M. Heckl, and M. Lackinger. "Isoreticular two-dimensional covalent organic frameworks synthesized by on-surface condensation of diboronic acids". In: *ACS nano* 6 (2012), pp. 7234–7242. DOI: 10.1021/nn302363d.

[42] J. F. Dienstmaier, A. M. Gigler, A. J. Goetz, P. Knochel, T. Bein, A. Lyapin, S. Reichlmaier, W. M. Heckl, and M. Lackinger. "Synthesis of well-ordered COF monolayers: surface growth of nanocrystalline precursors versus direct on-surface polycondensation". In: *ACS nano* 5.12 (2011), pp. 9737–9745. DOI: 10.1021/nn2032616.

[43] C. M. Crudden, J. H. Horton, I. I. Ebralidze, O. V. Zenkina, A. B. McLean, B. Drevniok, Z. She, H.-B. Kraatz, N. J. Mosey, T. Seki, et al. "Ultra stable self-assembled monolayers of N-heterocyclic carbenes on gold". In: *Nature chemistry* 6.5 (2014), pp. 409–414. DOI: 10.1038/NCHEM.1891.

[44] M. Matena, T. Riehm, M. Stöhr, T. A. Jung, and L. H. Gade. "Transforming surface coordination polymers into covalent surface polymers: Linked polycondensed aromatics through oligomerization of N-heterocyclic carbene intermediates". In: *Angewandte Chemie* 120.13 (2008), pp. 2448–2451. DOI: 10.1002/anie.200704072.

[45] Q. Sun, L. Cai, S. Wang, R. Widmer, H. Ju, J. Zhu, L. Li, Y. He, P. Ruffieux, R. Fasel, et al. "Bottom-up synthesis of metalated carbyne". In: *Journal of the American Chemical Society* 138.4 (2016), pp. 1106–1109. DOI: 10.1021/jacs.5b10725.

[46] Q. Sun, L. Cai, Y. Ding, L. ei Xie, C. Zhang, and Q. inggang Tan. "Dehydrogenative Homocoupling of Terminal Alkenes on Copper Surfaces: A Route to Dienes". In: *Angew. Chem. Int. Ed.* 54 (2015), pp. 4549–4552. DOI: 10.1002/ange.201412307. URL: http://dx.doi.org/10.1002/anie.201412307..

[47] P. A. Held, H.-Y. Gao, L. Liu, C. Mueck-Lichtenfeld, A. Timmer, H. Moenig, D. Barton, J. Neugebauer, H. Fuchs, and A. Studer. "On-Surface Domino Reactions: Glaser Coupling and Dehydrogenative Coupling of a Biscarboxylic Acid To Form Polymeric Bisacylperoxides". In: *Angewandte Chemie-International Edition* 55.33 (2016), pp. 9777–9782. ISSN: 1433-7851. DOI: 10.1002/anie.201602859.

[48] O. Díaz Arado, H. Mönig, J. H. Franke, A. Timmer, P. A. Held, A. Studer, and H. Fuchs. "On-surface reductive coupling of aldehydes on Au(111)". In: *Chemical Communications* 51.23 (2015), pp. 4887–4890. ISSN: 1364548X. DOI: 10.1039/c4cc09634g.

[49] G. Binning, H. Rohrer, C. Gerber, and E. Weibel. "Surface studies by scanning tunneling microscopy". In: *Phys. Rev. L.* 49.1 (1982), pp. 57–61.

[50] F. Hund. "Zur Deutung der Molekelspektren. III." In: *Zeitschrift für Physik* 43.11 (1927), pp. 805–826.

[51] J. Bardeen. "Tunnelling from a Many-Particle Point of View". In: *Phys. Rev. Lett.* 6 (2 1961), pp. 57–59. DOI: 10.1103/PhysRevLett.6.57. URL: https://link.aps.org/doi/10.1103/PhysRevLett.6.57.

[52] J. Tersoff and D. R. Hamann. "Theory of the scanning tunneling microscope". In: *Phys. Rev. B* 31 (2 1985), pp. 805–813. DOI: 10.1103/PhysRevB.31.805. URL: https://link.aps.org/doi/10.1103/PhysRevB.31.805.

[53] G. Binnig, C. F. Quate, and C. Gerber. "Atomic Force Microscope". In: *Phys. Rev. Lett.* 56 (9 1986), pp. 930–933. DOI: 10.1103/PhysRevLett.56.930. URL: https://link.aps.org/doi/10.1103/PhysRevLett.56.930.

[54] F. J. Giessibl. *Atomic resolution of the silicon (111)-(7×7) surface by atomic force microscopy.* Tech. rep. 1995, pp. 68–71. DOI: 10.1126/science.267.5194.68. URL: https://www.science.org.

[55] S.-i. Kitamura and M. Iwatsuki. "Observation of 7×7 Reconstructed Structure on the Silicon (111) Surface using Ultrahigh Vacuum Noncontact Atomic Force Microscopy". In: *Japanese Journal of Applied Physics* 34.Part 2, No. 1B (1995), pp. L145–L148. ISSN: 00214922. DOI: 10.1143/JJAP.34.L145. URL: https://iopscience.iop.org/article/10.1143/JJAP.34.L145.

[56] H. Ueyama, M. Ohta, Y. Sugawara, and S. Morita. "Atomically Resolved InP(110) Surface Observed with Noncontact Ultrahigh Vacuum Atomic Force Microscope". In: *Japanese Journal of Applied Physics* 34.Part 2, No. 8B (1995), pp. L1086–L1088. ISSN: 00214922. DOI: 10.1143/JJAP.34.L1086. URL: https://iopscience.iop.org/article/10.1143/JJAP.34.L1086.

[57] Y. Sugawara, M. Ohta, H. Ueyama, and S. Morita. *Defect Motion on an InP(110) Surface Observed with Noncontact Atomic Force Microscopy.* Tech. rep. 1995, p. 1274. URL: https://www.science.org.

[58] F. J. Giessibl. "Advances in atomic force microscopy". In: *Rev. Mod. Phys.* 75 (3 2003), pp. 949–983. DOI: 10.1103/RevModPhys.75.949. URL: https://link.aps.org/doi/10.1103/RevModPhys.75.949.

[59] Y. Martin, C. C. Williams, and H. K. Wickramasinghe. "Atomic force microscope-force mapping and profiling on a sub 100-Å scale ARTICLES YOU MAY BE INTERESTED IN". In: *Journal of Applied Physics* 61 (1987), p. 4723. DOI: 10.1063/1.338807. URL: https://doi.org/10.1063/1.338807.

[60] T. R. Albrecht, P. Grütter, and D. Horne. "Frequency modulation detection using high-Q cantilevers for enhanced force microscope sensitivity ARTICLES YOU MAY BE INTERESTED IN". In: *Journal of Applied Physics* 69 (1991), p. 668. DOI: 10.1063/1.347347. URL: https://doi.org/10.1063/1.347347.

[61] F. J. Giessibl. "Forces and frequency shifts in atomic-resolution dynamic-force microscopy". In: *Physical Review B* 56 (1997), pp. 16010–16015.

[62] J. E. Sader and S. P. Jarvis. "Accurate formulas for interaction force and energy in frequency modulation force spectroscopy". In: *Cite as: Appl. Phys. Lett* 84 (2004), p. 1801. DOI: 10.1063/1.1667267. URL: https://doi.org/10.1063/1.1667267.

[63] H. C. Hamaker. "The London–Van der Waals Attraction Between Spherical Particles". In: *Physica* 4 (1937), pp. 1058–1072.

[64] J. E. Jones. *On the determination of molecular fields - II From the equation of state of a gas*. Tech. rep. 1924, pp. 463–477. URL: https://royalsocietypublishing.org/.

[65] F. J. Giessibl. "High-speed force sensor for force microscopy and profilometry utilizing a quartz tuning fork". In: *Applied Physics Letters* 73.26 (1998), pp. 3956–3958. DOI: 10.1063/1.122948.

[66] J. Rychen, T. Ihn, P. Studerus, A. Herrmann, and K. Ensslin. "A low-temperature dynamic mode scanning force microscope operating in high magnetic fields". In: *Review of Scientific Instruments* 70.6 (1999), pp. 2765–2768. DOI: 10.1063/1.1149842.

[67] S. Hembacher, F. J. Giessibl, and J. Mannhart. "Evaluation of a force sensor based on a quartz tuning fork for operation at low temperatures and ultrahigh vacuum". In: *Applied surface science* 188.3-4 (2002), pp. 445–449. DOI: 10.1016/S0169-4332(01)00976-X.

[68] F. J. Giessibl, H. Bielefeldt, S. Hembacher, and J. Mannhart. "Calculation of the optimal imaging parameters for frequency modulation atomic force microscopy". In: *Applied Surface Science* 140.3-4 (1999), pp. 352–357. DOI: 10.1016/S0169-4332(98)00553-4.

[69] J. R. Morgenstern, S. Foelsch, and L. Bartels. "The scanning tunnelling microscope as an operative tool: doing physics and chemistry with single atoms and molecules". In: *Phil. Trans. R. Soc. Lond. A* 362 (2004), pp. 1207–1216. DOI: 10.1098/rsta.2004.1373.

[70] L. Gross, F. Mohn, N. Moll, P. Liljeroth, and G. Meyer. "The chemical structure of a molecule resolved by atomic force microscopy". In: *Science* 325.5944 (2009), pp. 1110–1114. DOI: 10.1126/SCIENCE.1176210. URL: https://www.science.org/doi/abs/10.1126/science.1176210.

[71] N. Moll, L. Gross, F. Mohn, A. Curioni, and G. Meyer. "The mechanisms underlying the enhanced resolution of atomic force microscopy with functionalized tips". In: *New Journal of Physics* 12 (2010), p. 125020. ISSN: 13672630. DOI: 10.1088/1367-2630/12/12/125020.

[72] B. Schuler, W. Liu, A. Tkatchenko, N. Moll, G. Meyer, A. Mistry, D. Fox, and L. Gross. "Adsorption geometry determination of single molecules by atomic force microscopy". In: *Physical Review Letters* 111.10 (2013), p. 106103.

[73] F. Mohn, B. Schuler, and L. Gross. "Different tips for high-resolution atomic force microscopy and scanning tunneling microscopy of single molecules". In: *Appl. Phys. Lett* 102 (2013), p. 73109. DOI: 10.1063/1.4793200. URL: https://doi.org/10.1063/1.4793200.

[74] L. Bartels, G. Meyer, and K. H. Rieder. "Controlled vertical manipulation of single CO molecules with the scanning tunneling microscope: A route to chemical contrast". In: *Applied Physics Letters* 71.2 (1997), pp. 213–215. ISSN: 0003-6951. DOI: 10.1063/1.119503.

[75] Albert Einstein. "über einen die Erzeugung und Verwandlung des Lichtes betreffenden heuristischen Gesichtspunkt". In: *Ann. Phys. Chem.* 322 (1905), pp. 132–148.

[76] T. L. Alford, L. C. Feldman, and J. W. Mayer. *Fundamentals of nanoscale film analysis*. Springer Science & Business Media, 2007.

[77] T. A. Carlson. "Basic assumptions and recent developments in quantitative XPS *". In: *Surface and Interface analysis* 4 (1982), pp. 125–134.

[78] C. Froese Fischer. "General Hartree-Fock program". In: *Computer Physics Communications* 43.3 (1987), pp. 355–365. ISSN: 0010-4655. DOI: 10.1016/0010-4655(87)90053-1.

[79] N. March. "The Thomas-Fermi approximation in quantum mechanics". In: *Advances in Physics* 6.21 (1957), pp. 1–101. DOI: 10.1080/00018735700101156.

[80] P. Hohenberg and W. Konnt. "PHYSICAL REVIEW". In: *Physical Review* 136(3B) (1964), B864. DOI: 10.1103/PhysRev.136.B864.

[81] W. Kohn and L. J. Sham. "Self-consistent equations including exchange and correlation effects*". In: *Physical Review* 140 (1965), A1133.

[82] J. P. Perdew and W. Yue. "Accurate and simple density functional for the electronic exchange energy: Generalized gradient approximation". In: *Phys. Rev. B* 33 (12 1986), pp. 8800–8802. DOI: 10.1103/PhysRevB.33.8800. URL: https://link.aps.org/doi/10.1103/PhysRevB.33.8800.

[83] S. Grimme. "Semiempirical GGA-type density functional constructed with a long-range dispersion correction". In: *Journal of Computational Chemistry* 27.15 (2006), pp. 1787–1799. DOI: https://doi.org/10.1002/jcc.20495. eprint: https://onlinelibrary.wiley.com/doi/pdf/10.1002/jcc.20495. URL: https://onlinelibrary.wiley.com/doi/abs/10.1002/jcc.20495.

[84] V. G. Ruiz, W. Liu, E. Zojer, M. Scheffler, and A. Tkatchenko. "Density-functional theory with screened van der Waals interactions for the modeling of hybrid inorganic-organic systems". In: *Physical review letters* 108.14 (2012), p. 146103. DOI: 10.1103/PhysRevLett.108.146103.

[85] M. Dion, H. Rydberg, E. Schröder, D. C. Langreth, and B. I. Lundqvist. "Van der Waals Density Functional for General Geometries". In: *Phys. Rev. Lett.* 92 (24 2004), p. 246401. DOI: 10.1103/PhysRevLett.92.246401. URL: https://link.aps.org/doi/10.1103/PhysRevLett.92.246401.

[86] I. Hamada. "Van der Waals density functional made accurate". In: *Physical Review B* 89.12 (2014), p. 121103. ISSN: 1550235X. DOI: 10.1103/PhysRevB.89.121103.

[87] G. Henkelman and H. Jonsson. "A dimer method for finding saddle points on high dimensional potential surfaces using only first derivatives". English. In: *Journal of Chemical Physics* 111.15 (1999), pp. 7010–7022. ISSN: 0021-9606. DOI: Doi10.1063/1.480097.

[88] G. Henkelman and H. Jonsson. "Improved tangent estimate in the nudged elastic band method for finding minimum energy paths and saddle points". English. In: *Journal of Chemical Physics* 113.22 (2000), pp. 9978–9985. ISSN: 0021-9606. DOI: 10.1063/1.1323224.

[89] G. Henkelman, B. P. Uberuaga, and H. Jonsson. "A climbing image nudged elastic band method for finding saddle points and minimum energy paths". English. In: *Journal of Chemical Physics* 113.22 (2000), pp. 9901–9904. ISSN: 0021-9606. DOI: 10.1063/1.1329672.

[90] J. S. Ducke. "Scanning Probe Microscopy Investigation of Hybrid Nano Systems Comprising Functional Molecules and Two-Dimensional Layers". Dissertation. München: Technische Universität München, 2018.

[91] M. Pörtner. "Adsorption of phthalocyanine-complexes on hexagonal boron nitride templates". Dissertation. München: Technische Universität München, 2020.

[92] J. P. Ibe, P. P. Bey, S. L. Brandow, R. A. Brizzolara, N. A. Burnham, D. P. DiLella, K. P. Lee, C. R. K. Marrian, and R. J. Colton. "On the electrochemical etching of tips for scanning tunneling microscopy". In: *Journal of Vacuum Science & Technology A* 8.4 (1990), pp. 3570–3575. DOI: 10.1116/1.576509. URL: https://doi.org/10.1116/1.576509.

[93] C. F. Co. "Manual: How to install the LT-STM head". In: (2013).

[94] E. Önal, V. Ahsen, J. Pécaut, D. Luneau, and C. Hirel. "Bromine-lithium exchange as a straightforward method to obtain meso-tetrakis(4-formylphenyl)porphyrin: A versatile intermediate". In: *Tetrahedron Letters* 56.37 (2015), pp. 5157–5160. ISSN: 18733581. DOI: 10.1016/j.tetlet.2015.07.021.

[95] H. L. Anderson. "Meso-alkynyl porphyrins". In: *Tetrahedron Letters* 33.8 (1992), pp. 1101–1104. ISSN: 0040-4039. DOI: 10.1016/S0040-4039(00)91871-9.

[96] N. Hayashi, M. Sato, K. Miyabayashi, M. Miyake, and H. Higuchi. "Synthesis and electronic properties of trimeric octaethylporphyrin (OEP) derivative connected with diacetylene linkage. A comparative study with vinylene-group connected OEP trimer". In: *Science and Technology of Advanced Materials* 7.3 (2006), pp. 237–242. ISSN: 14686996. DOI: 10.1016/J.STAM.2005.12.006. URL: https://www.tandfonline.com/doi/abs/10.1016/j.stam.2005.12.006.

[97] F. J. Giessibl. "The qPlus sensor, a powerful core for the atomic force microscope". In: *Review of Scientific Instruments* 90.1 (2019), p. 011101. ISSN: 0034-6748. DOI: 10.1063/1.5052264. URL: https://aip.scitation.org/doi/abs/10.1063/1.5052264.

[98] I. Horcas, R. Fernandez, J. M. Gomez-Rodriguez, J. Colchero, J. Gomez-Herrero, and A. M. Baro. "WSXM: A software for scanning probe microscopy and a tool for nanotechnology". In: *Review of Scientific Instruments* 78.1 (2007), p. 13705. ISSN: 0034-6748. DOI: 10.1063/1.2432410.

[99] A. Riss. *SpmImage Tycoon*. 2021. URL: https://github.com/alexriss/SpmImageTycoon.jl.

[100] N. Fairley, V. Fernandez, M. Richard-Plouet, C. Guillot-Deudon, J. Walton, E. Smith, D. Flahaut, M. Greiner, M. Biesinger, S. Tougaard, D. Morgan, and J. Baltrusaitis. "Systematic and collaborative approach to problem solving using X-ray photoelectron spectroscopy". In: *Applied Surface Science Advances* 5 (2021), p. 100112. ISSN: 2666-5239. DOI: https://doi.org/10.1016/j.apsadv.2021.100112. URL: https://www.sciencedirect.com/science/article/pii/S2666523921000581.

[101] G. Kresse. "Efficient iterative schemes for ab initio total-energy calculations using a plane-wave basis set". In: *Physical Review B* 54.16 (1996), pp. 11169–11186. ISSN: 9789896540821.

[102] P. E. Blöchl. "Projector augmented-wave method". In: *Physical Review B* 50.24 (1994), pp. 17953–17979. ISSN: 01631829. DOI: 10.1103/PhysRevB.50.17953.

[103] J. Tersoff and D. R. Hamann. "Theory and application for the scanning tunneling microscope". In: *Physical review letters* 50.25 (1983), p. 1998.

[104] P. Hapala, G. Kichin, C. Wagner, F. S. Tautz, R. Temirov, and P. Jelínek. "Mechanism of high-resolution STM/AFM imaging with functionalized tips". In: *Physical Review B* 90.8 (2014), p. 085421.

[105] P. Hapala, R. Temirov, F. S. Tautz, and P. Jelínek. "Origin of high-resolution IETS-STM images of organic molecules with functionalized tips". In: *Physical review letters* 113.22 (2014), p. 226101.

[106] G. Henkelman, A. Arnaldsson, and H. Jónsson. "A fast and robust algorithm for Bader decomposition of charge density". In: *Computational Materials Science* 36.3 (2006), pp. 354–360. ISSN: 09270256. DOI: 10.1016/j.commatsci.2005.04.010.

[107] J. Kruszewski and T. M. Krygowski. "Definition of aromaticity basing on the harmonic oscillator model". In: *Tetrahedron Letters* 13.36 (1972), pp. 3839–3842. ISSN: 0040-4039. DOI: 10.1016/S0040-4039(01)94175-9.

[108] T. M. Krygowski, H. Szatylowicz, O. A. Stasyuk, J. Dominikowska, and M. Palusiak. "Aromaticity from the viewpoint of molecular geometry: Application to planar systems". In: *Chemical Reviews* 114.12 (2014), pp. 6383–6422. DOI: 10.1021/CR400252H. URL: https://pubs.acs.org/doi/full/10.1021/cr400252h.

[109] K. Radula-Janik, K. Kopka, T. Kupka, and K. Ejsmont. "Substituent effect of nitro group on aromaticity of carbazole rings". In: *Chemistry of Heterocyclic Compounds* 50.9 (2014), pp. 1244–1251. ISSN: 1573-8353. DOI: 10.1007/S10593-014-1586-0. URL: https://link.springer.com/article/10.1007/s10593-014-1586-0.

[110] A. Riss, A. P. Paz, S. Wickenburg, H.-Z. Tsai, D. G. De Oteyza, A. J. Bradley, M. M. Ugeda, P. Gorman, H. S. Jung, M. F. Crommie, et al. "Imaging single-molecule reaction intermediates stabilized by surface dissipation and entropy". In: *Nature chemistry* 8.7 (2016), pp. 678–683.

[111] B. M. Trost and J. T. Masters. "Transition metal-catalyzed couplings of alkynes to 1,3-enynes: modern methods and synthetic applications". In: *Chemical Society Reviews* 45.8 (2016), pp. 2212–2238. ISSN: 0306-0012 1460-4744. DOI: 10.1039/c5cs00892a.

[112] Y. Zhou, Y. Zhang, and J. Wang. "Recent advances in transition-metal-catalyzed synthesis of conjugated enynes". In: *Org. Biomol. Chem.* 14.28 (2016), pp. 6638–6650. ISSN: 1477-0520 1477-0539. DOI: 10.1039/c6ob00944a.

[113] N. Zein, A. M. Sinha, W. J. Mcgahren, and G. A. Ellestad. "Calicheamicin-Gamma-1-I - an Antitumor Antibiotic That Cleaves Double-Stranded DNA Site Specifically". English. In: *Science* 240.4856 (1988), pp. 1198–1201. ISSN: 0036-8075. DOI: DOI10.1126/science.3240341.

[114] S. L. Iverson and J. P. Uetrecht. "Identification of a Reactive Metabolite of Terbinafine: Insights into Terbinafine-Induced Hepatotoxicity". In: *Chemical Research in Toxicology* 14.2 (2001), pp. 175–181. ISSN: 0893-228X 1520-5010. DOI: 10.1021/tx0002029.

[115] J. Golik, G. Dubay, G. Groenewold, H. Kawaguchi, M. Konishi, B. Krishnan, H. Ohkuma, K. Saitoh, and T. W. Doyle. "Esperamicins, a novel class of potent antitumor antibiotics. 3. Structures of esperamicins A1, A2, and A1b". In: *Journal of the American Chemical Society* 109.11 (1987), pp. 3462–3464. ISSN: 0002-7863 1520-5126. DOI: 10.1021/ja00245a049.

[116] M. D. Lee, T. S. Dunne, C. C. Chang, G. A. Ellestad, M. M. Siegel, G. O. Morton, W. J. McGahren, and D. B. Borders. "Calichemicins, a novel family of antitumor antibiotics. 2. Chemistry and structure of calichemicin .gamma.1I". In: *Journal of the American Chemical Society* 109.11 (1987), pp. 3466–3468. ISSN: 0002-7863 1520-5126. DOI: 10.1021/ja00245a051.

[117] J. W. Grissom, G. U. Gunawardena, D. Klingberg, and D. Huang. "The chemistry of enediynes, enyne allenes and related compounds". In: *Tetrahedron* 52.19 (1996), pp. 6453–6518. ISSN: 00404020. DOI: 10.1016/0040-4020(96)00016-6.

[118] T. J. Katz and T. M. Sivavec. "Metal-catalyzed rearrangement of alkene-alkynes and the stereochemistry of metallacyclobutene ring opening". In: *Journal of the American Chemical Society* 107.3 (1985), pp. 737–738. ISSN: 0002-7863 1520-5126. DOI: 10.1021/ja00289a054.

[119] S. T. Diver and A. J. Giessert. "Enyne Metathesis (Enyne Bond Reorganization)". In: *Chemical Reviews* 104.3 (2004), pp. 1317–1382. ISSN: 0009-2665 1520-6890. DOI: 10.1021/cr020009e.

[120] H. Villar, M. Frings, and C. Bolm. "Ring closing enyne metathesis: A powerful tool for the synthesis of heterocycles". In: *Chem. Soc. Rev.* 36.1 (2007), pp. 55–66. ISSN: 0306-0012 1460-4744. DOI: 10.1039/b508899m.

[121] V. Mazzanti, H. Jiang, H. Gotfredsen, T. J. Morsing, C. R. Parker, and M. B. Nielsen. "The Gilded Edge in Acetylenic Scaffolding: Pd-Catalyzed Cross-Coupling Reactions of Phosphine–Gold(I) Oligoynyl Complexes". In: *Organic Letters* 16.14 (2014), pp. 3736–3739. ISSN: 1523-7060 1523-7052. DOI: 10.1021/ol5015587.

[122] J. Li, Z. Xie, Y. Xiong, Z. Li, Q. Huang, S. Zhang, J. Zhou, R. Liu, X. Gao, C. Chen, L. Tong, J. Zhang, and Z. Liu. "Architecture of *β*-Graphdiyne-Containing Thin Film Using Modified Glaser-Hay Coupling Reaction for Enhanced Photocatalytic Property of TiO2". In: *Advanced Materials* 29.19 (2017), p. 1700421. ISSN: 09359648. DOI: 10.1002/adma.201700421.

[123] E. Westley, M. J. Sowden, N. L. Magann, K. L. Horvath, K. P. E. Connor, and M. S. Sherburn. "Substituted Tetraethynylethylene–Tetravinylethylene Hybrids". In: *Journal of the American Chemical Society* 144.2 (2022), pp. 977–986. ISSN: 0002-7863 1520-5126. DOI: 10.1021/jacs.1c11598.

[124] J. Burdon, P. L. Coe, C. R. Marsh, and J. C. Tatlow. "Reactions of organocopper compounds with halogeno-olefins". In: *Chemical Communications (London)* 24 (1967), p. 1259. ISSN: 0009-241X. DOI: 10.1039/c19670001259.

[125] Y. Hori, K. Noda, S. Kobayashi, and H. Taniguchi. "Synthesis and properties of tetrakis(phenylethynyl)ethylene". In: *Tetrahedron Letters* 10.40 (1969), pp. 3563–3566. ISSN: 00404039. DOI: 10.1016/s0040-4039(01)88450-1.

[126] C. W. Cheung and X. Hu. "Stereoselective Synthesis of Trisubstituted Alkenes through Sequential Iron-Catalyzed Reductiveanti-Carbozincation of Terminal Alkynes and Base-Metal-Catalyzed Negishi Cross-Coupling". In: *Chemistry - A European Journal* 21.50 (2015), pp. 18439–18444. ISSN: 09476539. DOI: 10.1002/chem.201504049.

[127] J. T. D. Lee and Y. Zhao. "Access to Acyclic Z-Enediynes by Alkyne Trimerization: Cooperative Bimetallic Catalysis Using Air as the Oxidant". In: *Angewandte Chemie International Edition* 55.44 (2016), pp. 13872–13876. ISSN: 14337851. DOI: 10.1002/anie.201608192.

[128] Y. Jiang, J. T. Pan, T. Yang, Y. Zhao, and M. J. Koh. "Nickel-catalyzed site- and stereoselective reductive alkylalkynylation of alkynes". In: *CHEM* 7.4 (2021), pp. 993–1005. ISSN: 2451-9294. DOI: 10.1016/j.chempr.2020.12.024.

[129] L. Liu, H. Klaasen, M. C. Witteler, B. Schulze Lammers, A. Timmer, H. Kong, H. Mönig, H. Y. Gao, J. Neugebauer, H. Fuchs, and A. Studer. "Polymerization of silanes through dehydrogenative Si–Si bond formation on metal surfaces". In: *Nature Chemistry* 13.4 (2021), pp. 350–357. ISSN: 17554349. DOI: 10.1038/s41557-021-00651-z.

[130] Y. Rubin, C. B. Knobler, and F. Diederich. "Tetraethynylethene". In: *Angewandte Chemie International Edition in English* 30.6 (1991), pp. 698–700. ISSN: 0570-0833 1521-3773. DOI: 10.1002/anie.199106981.

[131] O. F. Koentjoro, P. Zuber, H. Puschmann, A. E. Goeta, J. A. K. Howard, and P. J. Low. "A simple synthesis of tetraethynylethenes and representative molecular structures of some dicobalt derivatives". In: *Journal of Organometallic Chemistry* 670.1-2 (2003), pp. 178–187. ISSN: 0022328X. DOI: 10.1016/s0022-328x(02)02191-5.

[132] R. Rossi, A. Carpita, and C. Bigelli. "A PALLADIUM-PROMOTED ROUTE TO 3-ALKYL-4-(1-ALKYNYL)-HEXA-1,5-DYN-3-ENES AND OR 1,3-DIYNES". English. In: *Tetrahedron Letters* 26.4 (1985), pp. 523–526. ISSN: 0040-4039. DOI: 10.1016/s0040-4039(00)61928-7.

[133] M. Alami, B. Crousse, and G. Linstrumelle. "A STEREOSELECTIVE ROUTE TO 1-CHLORO-1-HALO-ENYNES, VERSATILE PRECURSORS FOR THE SYNTHESIS OF CHLOROENEDIYNES AND ENETRIYNES". In: *Tetrahedron Letters* 36.21 (1995), pp. 3687–3690. ISSN: 0040-4039. DOI: 10.1016/0040-4039(95)00612-g.

[134] T. Rankin and R. R. Tykwinski. "Synthesis and Derivatization of Ethynyl α,α-Dibromomethyl Ketones: Formation of Highly Functionalized Vinyl Triflates". In: *Organic Letters* 5.2 (2003), pp. 213–216. ISSN: 1523-7060 1523-7052. DOI: 10.1021/ol027267i.

[135] C. Xi, C. Chen, Z. Ai, J. Lin, and X. Hong. "Palladium-Catalyzed Self-Coupling Reaction of Terminal Alkynes in the Presence of p-Chloranil: A Practical Method for the Synthesis of Triethynylethenes". In: *Synlett* 2006.15 (2006), pp. 2454–2458. ISSN: 0936-5214 1437-2096. DOI: 10.1055/s-2006-950416.

[136] R. Lindner and A. Kuhnle. "On-surface reactions". In: *Chemphyschem* 16.8 (2015), pp. 1582–1592. ISSN: 1439-7641 (Electronic) 1439-4235 (Linking). DOI: 10.1002/cphc.201500161. URL: https://www.ncbi.nlm.nih.gov/pubmed/25965579.

[137] P. A. Held, H. Fuchs, and A. Studer. "Covalent-Bond Formation via On-Surface Chemistry". In: *Chemistry-a European Journal* 23.25 (2017), pp. 5874–5892. ISSN: 1521-3765 (Electronic) 0947-6539 (Linking). DOI: 10.1002/chem.201604047. URL: https://www.ncbi.nlm.nih.gov/pubmed/28097707.

[138] G. Franc and A. Gourdon. "Covalent networks through on-surface chemistry in ultra-high vacuum: state-of-the-art and recent developments". In: *Physical Chemistry Chemical Physics* 13.32 (2011), pp. 14283–14292. ISSN: 1463-9076. DOI: 10.1039/c1cp20700h.

[139] Q. Fan, J. M. Gottfried, and J. Zhu. "Surface-catalyzed C-C covalent coupling strategies toward the synthesis of low-dimensional carbon-based nanostructures". In: *Acc Chem Res* 48.8 (2015), pp. 2484–2494. ISSN: 1520-4898 (Electronic) 0001-4842 (Linking). DOI: 10.1021/acs.accounts.5b00168. URL: https://www.ncbi.nlm.nih.gov/pubmed/26194462.

[140] Q. Sun, R. Zhang, J. Qiu, R. Liu, and W. Xu. "On-Surface Synthesis of Carbon Nanostructures". In: *Advanced Materials* 30.17 (2018), p. 1705630. ISSN: 09359648. DOI: 10.1002/adma.201705630.

[141] B. Yang, H. Lin, K. Miao, P. Zhu, L. Liang, K. Sun, H. Zhang, J. Fan, V. Meunier, Y. Li, Q. Li, and L. Chi. "Catalytic Dealkylation of Ethers to Alcohols on Metal Surfaces". In: *Angew. Chem. Int. Ed.* 55.34 (2016), pp. 9881–9885. ISSN: 1521-3773 (Electronic) 1433-7851 (Linking). DOI: 10.1002/anie.201602414. URL: https://www.ncbi.nlm.nih.gov/pubmed/27432690.

[142] D. Y. Li, Y. Wang, X. Y. Hou, Y. T. Ren, L. X. Kang, F. H. Xue, Y. C. Zhu, J. W. Liu, M. X. Liu, X. Q. Shi, X. H. Qiu, and P. N. Liu. "On-Surface Synthesis of [3]Radialenes via [1+1+1] Cycloaddition". English. In: *Angewandte Chemie-International Edition* (2022), e202117714. ISSN: 1433-7851. DOI: ARTNe20211771410.1002/anie.202117714.

[143] B. Yang, B. Dong, and L. Chi. "On-Surface Intramolecular Reactions". In: *ACS Nano* 14.6 (2020), pp. 6376–6382. ISSN: 1936-0851 1936-086X. DOI: 10.1021/acsnano.0c03766.

[144] J. Su, M. Telychko, S. Song, and J. Lu. "Triangulenes: From Precursor Design to On-Surface Synthesis and Characterization". In: *Angewandte Chemie International Edition* 59.20 (2020), pp. 7658–7668. ISSN: 1433-7851 1521-3773. DOI: 10.1002/anie.201913783.

[145] Z. Zeng, D. Guo, T. Wang, Q. Chen, A. Matěj, J. Huang, D. Han, Q. Xu, A. Zhao, P. Jelínek, D. G. de Oteyza, J.-S. McEwen, and J. Zhu. "Chemisorption-Induced Formation of Biphenylene Dimer on Ag(111)". In: *Journal of the American Chemical Society* 144.2 (2021), pp. 723–732. ISSN: 0002-7863 1520-5126. DOI: 10.1021/jacs.1c08284.

[146] J. I. Urgel, S. Mishra, H. Hayashi, J. Wilhelm, C. A. Pignedoli, M. Di Giovannantonio, R. Widmer, M. Yamashita, N. Hieda, P. Ruffieux, H. Yamada, and R. Fasel. "On-surface light-induced generation of higher acenes and elucidation of their open-shell character". In: *Nature Communications* 10.1 (2019), p. 861. ISSN: 2041-1723. DOI: 10.1038/s41467-019-08650-y.

[147] Q. Shen, H.-Y. Gao, and H. Fuchs. "Frontiers of on-surface synthesis: From principles to applications". In: *Nano Today* 13 (2017), pp. 77–96. ISSN: 17480132. DOI: 10.1016/j.nantod.2017.02.007.

[148] T. Wang and J. Zhu. "Confined on-surface organic synthesis: Strategies and mechanisms". In: *Surface Science Reports* 74.2 (2019), pp. 97–140. ISSN: 01675729. DOI: 10.1016/j.surfrep.2019.05.001.

[149] F. Klappenberger, Y. Q. Zhang, J. Björk, S. Klyatskaya, M. Ruben, and J. V. Barth. "On-surface synthesis of carbon-based scaffolds and nanomaterials using terminal alkynes". In: *Accounts of Chemical Research* 48.7 (2015), pp. 2140–2150. ISSN: 15204898. DOI: 10.1021/acs.accounts.5b00174.

[150] J. Liu, Q.-W. Chen, and K. Wu. "On-surface construction of low-dimensional nanostructures with terminal alkynes: Linking strategies and controlling methodologies". In: *Chinese Chemical Letters* 28.8 (2017), pp. 1631–1639. ISSN: 10018417. DOI: 10.1016/j.cclet.2017.04.022.

[151] Y. Q. Zhang, N. Kepcija, M. Kleinschrodt, K. Diller, S. Fischer, A. C. Papageorgiou, F. Allegretti, J. Bjork, S. Klyatskaya, F. Klappenberger, M. Ruben, and J. V. Barth. "Homocoupling of terminal alkynes on a noble metal surface". In: *Nature Communications* 3 (2012), p. 1286. ISSN: 2041-1723 (Electronic) 2041-1723 (Linking). DOI: 10.1038/ncomms2291. URL: https://www.ncbi.nlm.nih.gov/pubmed/23250416.

[152] J. Lawrence, M. S. Mohammed, D. Rey, F. Aguilar-Galindo, A. Berdonces-Layunta, D. Peña, and D. G. De Oteyza. "Reassessing alkyne coupling reactions while studying the electronic properties of diverse pyrene linkages at surfaces". In: *ACS Nano* 15.3 (2021), pp. 4937–4946. ISSN: 1936086X. DOI: 10.1021/acsnano.0c09756.

[153] J. Liu, Q. Chen, L. Xiao, J. Shang, X. Zhou, Y. Zhang, Y. Wang, X. Shao, J. Li, W. Chen, G. Q. Xu, H. Tang, D. Zhao, and K. Wu. "Lattice-Directed Formation of Covalent and Organometallic Molecular Wires by Terminal Alkynes on Ag Surfaces". In: *ACS Nano* 9.6 (2015), pp. 6305–6314. ISSN: 1936-0851. DOI: 10.1021/acsnano.5b01803.

[154] L. Colazzo, F. Sedona, A. Moretto, M. Casarin, and M. Sambi. "Metal-Free on-Surface Photochemical Homocoupling of Terminal Alkynes". In: *Journal of the American Chemical Society* 138.32 (2016), pp. 10151–10156. ISSN: 0002-7863 1520-5126. DOI: 10.1021/jacs.6b03589.

[155] O. Diaz Arado, H. Moenig, H. Wagner, J.-H. Franke, G. Langewisch, P. A. Held, A. Studer, and H. Fuchs. "On-Surface Azide-Alkyne Cycloaddition on Au(111)". In: *ACS Nano* 7.10 (2013), pp. 8509–8515. ISSN: 1936-0851. DOI: 10.1021/nn4022789.

[156] F. Bebensee, C. Bombis, S.-R. Vadapoo, J. R. Cramer, F. Besenbacher, K. V. Gothelf, and T. R. Linderoth. "On-Surface Azide-Alkyne Cycloaddition on Cu(111): Does It "Click" in Ultrahigh Vacuum?" In: *Journal of the American Chemical Society* 135.6 (2013), pp. 2136–2139. ISSN: 0002-7863. DOI: 10.1021/ja312303a.

[157] A. Riss, S. Wickenburg, P. Gorman, L. Z. Tan, H. Z. Tsai, D. G. De Oteyza, Y. C. Chen, A. J. Bradley, M. M. Ugeda, G. Etkin, S. G. Louie, F. R. Fischer, and M. F. Crommie. "Local electronic and chemical structure of oligo-acetylene derivatives formed through radical cyclizations at a surface". In: *Nano Letters* 14.5 (2014), pp. 2251–2255. ISSN: 15306992. DOI: 10.1021/nl403791q.

[158] T. Paintner, J. Björk, P. Du, S. Klyatskaya, M. Paszkiewicz, R. Hellwig, M. Uphoff, M. A. Öner, E. Cuniberto, P. S. Deimel, Y.-Q. Zhang, C.-A. Palma, F. Allegretti, M. Ruben, J. V. Barth, and F. Klappenberger. "Quantum Tunneling Mediated Interfacial Synthesis of a Benzofuran Derivative". In: *Angewandte Chemie International Edition* 58.33 (2019), pp. 11285–11290. ISSN: 1433-7851 1521-3773. DOI: 10.1002/anie.201904030.

[159] T. Wang, H. Lv, J. Huang, H. Shan, L. Feng, Y. Mao, J. Wang, W. Zhang, D. Han, Q. Xu, P. Du, A. Zhao, X. Wu, S. L. Tait, and J. Zhu. "Reaction selectivity of homochiral versus heterochiral intermolecular reactions of prochiral terminal alkynes on surfaces". In: *Nature Communications* 10.1 (2019), p. 4122. ISSN: 2041-1723. DOI: 10.1038/s41467-019-12102-y.

[160] G. Shi, J. Zhou, Z. Li, Y. Sun, L. N. Kantorovich, Q. Fang, F. Besenbacher, and M. Yu. "Graphene-Like Covalent Organic Framework with a Wide Band Gap Synthesized On Surface via Stepwise Reactions". In: *Angewandte Chemie International Edition* 59 (2020), pp. 15958–15962. ISSN: 1433-7851 1521-3773. DOI: 10.1002/anie.202006176.

[161] T. Wang, J. Huang, H. Lv, Q. Fan, L. Feng, Z. Tao, H. Ju, X. Wu, S. L. Tait, and J. Zhu. "Kinetic Strategies for the Formation of Graphyne Nanowires via Sonogashira Coupling on Ag(111)". In: *Journal of the American Chemical Society* 140.41 (2018), pp. 13421–13428. ISSN: 0002-7863 1520-5126. DOI: 10.1021/jacs.8b08477.

[162] V. K. Kanuru, G. Kyriakou, S. K. Beaumont, A. C. Papageorgiou, D. J. Watson, and R. M. Lambert. "Sonogashira Coupling on an Extended Gold Surface in Vacuo: Reaction of Phenylacetylene with Iodobenzene on Au(111)". In: *Journal of the American Chemical Society* 132.23 (2010), pp. 8081–8086. ISSN: 0002-7863. DOI: 10.1021/ja1011542.

[163] C. Sanchez-Sanchez, N. Orozco, J. P. Holgado, S. K. Beaumont, G. Kyriakou, D. J. Watson, A. R. Gonzalez-Elipe, L. Feria, J. Fernandez Sanz, and R. M. Lambert. "Sonogashira cross-coupling and homocoupling on a silver surface: chlorobenzene and phenylacetylene on Ag(100)". In: *J Am Chem Soc* 137.2 (2015), pp. 940–947. ISSN: 1520-5126 (Electronic) 0002-7863 (Linking). DOI: 10.1021/ja5115584. URL: https://www.ncbi.nlm.nih.gov/pubmed/25531937.

[164] R. Zhang, G. Lyu, D. Y. Li, P. N. Liu, and N. Lin. "Template-controlled Sonogashira cross-coupling reactions on a Au(111) surface". In: *Chem Commun (Camb)* 53.10 (2017), pp. 1731–1734. ISSN: 1364-548X (Electronic) 1359-7345 (Linking). DOI: 10.1039/c6cc10091k. URL: https://www.ncbi.nlm.nih.gov/pubmed/28106195.

[165] J. Eichhorn, W. M. Heckl, and M. Lackinger. "On-surface polymerization of 1,4-diethynylbenzene on Cu(111)". English. In: *Chemical Communications* 49.28 (2013), pp. 2900–2902. ISSN: 1359-7345. DOI: 10.1039/c3cc40444g.

[166] H.-Y. Gao, J.-H. Franke, H. Wagner, D. Zhong, P.-A. Held, A. Studer, and H. Fuchs. "Effect of Metal Surfaces in On-Surface Glaser Coupling". In: *Journal of Physical Chemistry C* 117.36 (2013), pp. 18595–18602. ISSN: 1932-7447. DOI: 10.1021/jp406858p.

[167] Z. Chen, T. Lin, L. Zhang, L. Zhang, B. Xiang, H. Xu, F. Klappenberger, J. V. Barth, S. Klyatskaya, and M. Ruben. "Surface-Dependent Chemoselectivity in CC Coupling Reactions". In: *Angewandte Chemie International Edition* 58.25 (2019), pp. 8356–8361. ISSN: 1433-7851 1521-3773. DOI: 10.1002/anie.201900636.

[168] C. Zhang, R. B. Jaculbia, Y. Tanaka, E. Kazuma, H. Imada, N. Hayazawa, A. Muranaka, M. Uchiyama, and Y. Kim. "Chemical Identification and Bond Control of π-Skeletons in a Coupling Reaction". In: *Journal of the American Chemical Society* 143.25 (2021), pp. 9461–9467. ISSN: 0002-7863 1520-5126. DOI: 10.1021/jacs.1c02624.

[169] B. Cirera, Y.-Q. Zhang, J. Bjork, S. Klyatskaya, Z. Chen, M. Ruben, J. V. Barth, and F. Klappenberger. "Synthesis of Extended Graphdiyne Wires by Vicinal Surface Templating". In: *Nano Letters* 14.4 (2014), pp. 1891–1897. ISSN: 1530-6984. DOI: 10.1021/nl4046747.

[170] T. Wang, H. Lv, Q. Fan, L. Feng, X. Wu, and J. Zhu. "Highly Selective Synthesis of cis-Enediynes on a Ag(111) Surface". In: *Angewandte Chemie International Edition* 56.17 (2017), pp. 4762–4766. ISSN: 14337851. DOI: 10.1002/anie.201701142.

[171] Y.-Q. Zhang, M. Paszkiewicz, P. Du, L. Zhang, T. Lin, Z. Chen, S. Klyatskaya, M. Ruben, A. P. Seitsonen, J. V. Barth, and F. Klappenberger. "Complex supramolecular interfacial tessellation through convergent multi-step reaction of a dissymmetric simple organic precursor". In: *Nature Chemistry* 10.3 (2018), pp. 296–304. ISSN: 1755-4330 1755-4349. DOI: 10.1038/nchem.2924.

[172] Y.-Q. Zhang, T. Paintner, R. Hellwig, F. Haag, F. Allegretti, P. Feulner, S. Klyatskaya, M. Ruben, A. P. Seitsonen, J. V. Barth, and F. Klappenberger. "Synthesizing Highly Regular Single-Layer Alkynyl–Silver Networks at the Micrometer Scale via Gas-Mediated Surface Reaction". In: *Journal of the American Chemical Society* 141.13 (2019), pp. 5087–5091. ISSN: 0002-7863 1520-5126. DOI: 10.1021/jacs.8b13547.

[173] B. Yang, N. Cao, H. Ju, H. Lin, Y. Li, H. Ding, J. Ding, J. Zhang, C. Peng, H. Zhang, J. Zhu, Q. Li, and L. Chi. "Intermediate States Directed Chiral Transfer on a Silver Surface". In: *Journal of the American Chemical Society* 141.1 (2019), pp. 168–174. ISSN: 0002-7863 1520-5126. DOI: 10.1021/jacs.8b05699. URL: https://www.ncbi.nlm.nih.gov/pubmed/30472840.

[174] A. Riss, A. P. Paz, S. Wickenburg, H.-Z. Tsai, D. G. De Oteyza, A. J. Bradley, M. M. Ugeda, P. Gorman, H. S. Jung, M. F. Crommie, A. Rubio, and F. R. Fischer. "Imaging single-molecule reaction intermediates stabilized by surface dissipation and entropy". In: *Nature Chemistry* 8.7 (2016), pp. 678–683. ISSN: 1755-4330 1755-4349. DOI: 10.1038/nchem.2506.

[175] L. Giovanelli, O. Ourdjini, M. Abel, R. Pawlak, J. Fujii, L. Porte, J.-M. Themlin, and S. Clair. "Combined Photoemission Spectroscopy and Scanning Tunneling Microscopy Study of the Sequential Dehydrogenation of Hexahydroxytriphenylene on Ag(111)". In: *Journal of Physical Chemistry C* 118.27 (2014), pp. 14899–14904. ISSN: 1932-7447. DOI: 10.1021/jp501849h.

[176] L. Feng, T. Wang, Z. Tao, J. Huang, G. Li, Q. Xu, S. L. Tait, and J. Zhu. "Supramolecular Tessellations at Surfaces by Vertex Design". In: *ACS Nano* 13.9 (2019), pp. 10603–10611. ISSN: 1936-0851 1936-086X. DOI: 10.1021/acsnano.9b04801.

[177] H. T. Zhou, J. Z. Liu, S. X. Du, L. Z. Zhang, G. Li, Y. Zhang, B. Z. Tang, and H. J. Gao. "Direct Visualization of Surface-Assisted Two-Dimensional Diyne Polycyclotrimerization". English. In: *Journal of the American Chemical Society* 136.15 (2014), pp. 5567–5570. ISSN: 0002-7863. DOI: 10.1021/ja501308s.

[178] A. Mistry, B. Moreton, B. Schuler, F. Mohn, G. Meyer, L. Gross, A. Williams, P. Scott, G. Costantini, and D. J. Fox. "The Synthesis and STM/AFM Imaging of 'Olympicene' Benzo[cd]pyrenes". In: *Chemistry - A European Journal* 21.5 (2015), pp. 2011–2018. ISSN: 09476539. DOI: 10.1002/chem.201404877.

[179] N. Pavliček, A. Mistry, Z. Majzik, N. Moll, G. Meyer, D. J. Fox, and L. Gross. "Synthesis and characterization of triangulene". In: *Nature Nanotechnology* 12.4 (2017), pp. 308–311. ISSN: 1748-3395. DOI: 10.1038/nnano.2016.305. URL: https://www.nature.com/articles/nnano.2016.305.

[180]   F. De Marchi, G. Galeotti, M. Simenas, E. E. Tornau, A. Pezzella, J. Macleod, M. Ebrahimi, and F. Rosei. "Room-temperature surface-assisted reactivity of a melanin precursor: Silver metal-organic coordination: Versus covalent dimerization on gold". In: *Nanoscale* 10.35 (2018), pp. 16721–16729. ISSN: 20403372. DOI: 10.1039/c8nr04002h.

[181]   F. De Marchi, G. Galeotti, M. Simenas, P. Ji, L. Chi, E. E. Tornau, A. Pezzella, J. MacLeod, M. Ebrahimi, and F. Rosei. "Self-assembly of 5,6-dihydroxyindole-2-carboxylic acid: polymorphism of a eumelanin building block on Au(111)". In: *Nanoscale* 11.12 (2019), pp. 5422–5428. ISSN: 2040-3364 2040-3372. DOI: 10.1039/c8nr09810g.

[182]   S. Kawai, O. Krejčí, A. S. Foster, R. Pawlak, F. Xu, L. Peng, A. Orita, and E. Meyer. "Diacetylene linked anthracene oligomers synthesized by one-shot homocoupling of trimethylsilyl on Cu(111)". In: *ACS Nano* 12.8 (2018), pp. 8791–8797. ISSN: 1936086X. DOI: 10.1021/acsnano.8b05116.

[183]   A. Sánchez-Grande, B. de la Torre, J. Santos, B. Cirera, K. Lauwaet, T. Chutora, S. Edalatmanesh, P. Mutombo, J. Rosen, R. Zbořil, R. Miranda, J. Björk, P. Jelínek, N. Martín, and D. Écija. "On-Surface Synthesis of Ethynylene-Bridged Anthracene Polymers". In: *Angewandte Chemie International Edition* 58.20 (2019), pp. 6559–6563. ISSN: 1433-7851 1521-3773. DOI: 10.1002/anie.201814154.

[184]   T. Wang, H. Lv, L. Feng, Z. Tao, J. Huang, Q. Fan, X. Wu, and J. Zhu. "Unravelling the Mechanism of Glaser Coupling Reaction on Ag(111) and Cu(111) Surfaces: a Case for Halogen Substituted Terminal Alkyne". In: *The Journal of Physical Chemistry C* 122.26 (2018), pp. 14537–14545. ISSN: 1932-7447 1932-7455. DOI: 10.1021/acs.jpcc.8b02893.

[185]   J. Liu, P. Ruffieux, X. L. Feng, K. Mullen, and R. Fasel. "Cyclotrimerization of arylalkynes on Au(111)". English. In: *Chemical Communications* 50.76 (2014), pp. 11200–11203. ISSN: 1359-7345. DOI: 10.1039/c4cc02859g.

[186]   C. Zhang, R. B. Jaculbia, Y. Tanaka, E. Kazuma, H. Imada, N. Hayazawa, A. Muranaka, M. Uchiyama, and Y. Kim. "Chemical Identification and Bond Control of π-Skeletons in a Coupling Reaction". In: *Journal of the American Chemical Society* 143.25 (2021), pp. 9461–9467. DOI: 10.1021/jacs.1c02624.

[187]   A. Wang, J. Li, and T. Zhang. "Heterogeneous single-atom catalysis". In: *Nature Reviews Chemistry 2018 2:6* 2.6 (2018), pp. 65–81. ISSN: 2397-3358. DOI: 10.1038/s41570-018-0010-1. URL: https://www.nature.com/articles/s41570-018-0010-1.

[188]   F. D. Natterer, K. Yang, W. Paul, P. Willke, T. Choi, T. Greber, A. J. Heinrich, and C. P. Lutz. "Reading and writing single-atom magnets". In: *Nature 2017 543:7644* 543.7644 (2017), pp. 226–228. ISSN: 1476-4687. DOI: 10.1038/nature21371. URL: https://www.nature.com/articles/nature21371.

[189]   A. A. Khajetoorians, J. Wiebe, B. Chilian, and R. Wiesendanger. "Realizing all-spin-based logic operations atom by atom". In: *Science* 332.6033 (2011), pp. 1062–1064. DOI: 10.1126/SCIENCE.1201725. URL: www.sciencemag.org/cgi/content/full/science.1201725/DC1.

[190] H. M. Sturmeit, I. Cojocariu, A. Windischbacher, P. Puschnig, C. Piamonteze, M. Jugo-vac, A. Sala, C. Africh, G. Comelli, A. Cossaro, A. Verdini, L. Floreano, M. Stredansky, E. Vesselli, C. Hohner, M. Kettner, J. Libuda, C. M. Schneider, G. Zamborlini, M. Cinchetti, and V. Feyer. "Room-temperature on-spin-switching and tuning in a porphyrin-based multifunctional interface". In: *Small* (2021), p. 2104779. ISSN: 1613-6829. DOI: 10.1002/SMLL.202104779. URL: https://onlinelibrary.wiley.com/doi/full/10.1002/smll.202104779%20https://onlinelibrary.wiley.com/doi/abs/10.1002/smll.202104779%20https://onlinelibrary.wiley.com/doi/10.1002/smll.202104779.

[191] P. Liljeroth, J. Repp, and G. Meyer. "Current-induced hydrogen tautomerization and conductance switching of naphthalocyanine molecules". In: *Science* 317.5842 (2007), pp. 1203–1206. DOI: 10.1126/SCIENCE.1144366. URL: https://www.science.org/doi/abs/10.1126/science.1144366.

[192] W. Auwärter, K. Seufert, F. Bischoff, D. Ecija, S. Vijayaraghavan, S. Joshi, F. Klap-penberger, N. Samudrala, and J. V. Barth. "A surface-anchored molecular four-level conductance switch based on single proton transfer". In: *Nature Nanotechnology* 7.1 (2011), pp. 41–46. ISSN: 1748-3395. DOI: 10.1038/nnano.2011.211. URL: https://www.nature.com/articles/nnano.2011.211.

[193] T. Tanaka and A. Osuka. "Conjugated porphyrin arrays: Synthesis, properties and applications for functional materials". In: *Chemical Society Reviews* 44.4 (2015), pp. 943–969. ISSN: 14604744. DOI: 10.1039/c3cs60443h.

[194] Y. Nakamura, N. Aratani, and A. Osuka. "Cyclic porphyrin arrays as artificial pho-tosynthetic antenna: Synthesis and excitation energy transfer". In: *Chemical Society Reviews* 36.6 (2007), pp. 831–845. ISSN: 14604744. DOI: 10.1039/b618854k.

[195] N. Aratani, A. Tsuda, and A. Osuka. "Discrete giant porphyrin arrays: challenges to molecular size, length and the extent of electronic p-conjugation". In: *Synlett* 11.11 (2001), pp. 1663–1674. ISSN: 0936-5214. DOI: 10.1055/s-2001-18073.

[196] M. C. O'Sullivan, J. K. Sprafke, D. V. Kondratuk, C. Rinfray, T. D. Claridge, A. Saywell, M. O. Blunt, J. N. O'Shea, P. H. Beton, M. Malfois, and H. L. Anderson. "Vernier templating and synthesis of a 12-porphyrin nano-ring". In: *Nature* 469.7328 (2011), pp. 72–75. ISSN: 00280836. DOI: 10.1038/nature09683.

[197] A. Bellamy-Carter, C. Roche, H. L. Anderson, and A. Saywell. "Self-assembly of a strapped linear porphyrin oligomer on HOPG". In: *Scientific Reports* 11.1 (2021), pp. 1–7. ISSN: 2045-2322. DOI: 10.1038/s41598-021-99881-x. URL: https://doi.org/10.1038/s41598-021-99881-x.

[198] H. Marbach. "Surface-mediated in situ metalation of porphyrins at the solid–vacuum interface". In: *Accounts of Chemical Research* 48.9 (2015), pp. 2649–2658. ISSN: 0001-4842. DOI: 10.1021/acs.accounts.5b00243. URL: https://pubs.acs.org/doi/10.1021/acs.accounts.5b00243.

[199] J. M. Gottfried. "Surface chemistry of porphyrins and phthalocyanines". In: *Surface Science Reports* 70.3 (2015), pp. 259–379. ISSN: 01675729. DOI: 10.1016/j.surfrep.2015.04.001. URL: http://dx.doi.org/10.1016/j.surfrep.2015.04.001.

[200] W. Auwärter, D. Écija, F. Klappenberger, and J. V. Barth. "Porphyrins at interfaces". In: *Nature Chemistry* 7.2 (2015), pp. 105–120. ISSN: 17554349. DOI: 10.1038/nchem.2159. URL: http://dx.doi.org/10.1038/nchem.2159.

[201] B. Mallada, P. Błoński, R. Langer, P. Jelínek, M. Otyepka, and B. de la Torre. "On-surface synthesis of one-dimensional coordination polymers with tailored magnetic anisotropy". In: *ACS Applied Materials & Interf.* 13.27 (2021), pp. 32393–32401. ISSN: 1944-8244. DOI: 10.1021/acsami.1c04693. URL: https://pubs.acs.org/doi/10.1021/acsami.1c04693.

[202] A. Saywell, A. S. Browning, P. Rahe, H. L. Anderson, and P. H. Beton. "Organisation and ordering of 1D porphyrin polymers synthesised by on-surface Glaser coupling". In: *Chemical Communications* 52.68 (2016), pp. 10342–10345. ISSN: 1364548X. DOI: 10.1039/c6cc03758e.

[203] E. Vogel, M. Köcher, H. Schmickler, and J. Lex. "Porphycene-a novel porphin isomer". In: *Angewandte Chem International Edition* 25.3 (1986), pp. 257–259. ISSN: 15213773. DOI: 10.1002/anie.198602571.

[204] E. Vogel. "The porphyrins from the 'annulene chemist's' perspective". In: *Pure & Appl. Chem.* 65.1 (1993), pp. 143–152.

[205] J. I. Wu, I. Fernández, and P. V. Schleyer. "Description of aromaticity in porphyrinoids". In: *Journal of the American Chemical Society* 135.1 (2013), pp. 315–321. ISSN: 00027863. DOI: 10.1021/JA309434T/SUPPL_FILE/JA309434T_SI_001.PDF. URL: https://pubs.acs.org/doi/abs/10.1021/ja309434t.

[206] K. Seufert, F. McBride, S. Jaekel, B. Wit, S. Haq, A. Steiner, P. Poli, M. Persson, R. Raval, and L. Grill. "Porphine Homocoupling on Au(111)". In: *Journal of Physical Chemistry C* 123.27 (2019), pp. 16690–16698. ISSN: 19327455. DOI: 10.1021/acs.jpcc.9b02770.

[207] Q. Sun, L. M. Mateo, R. Robles, N. Lorente, P. Ruffieux, G. Bottari, T. Torres, and R. Fasel. "Bottom-up fabrication and atomic-scale characterization of triply linked, laterally π-extended porphyrin nanotapes". In: *Angewandte Chemistry International Edition* 60.29 (2021), pp. 16208–16214. ISSN: 15213773. DOI: 10.1002/anie.202105350.

[208] B. Cirera, B. De La Torre, D. Moreno, M. Ondráček, R. Zbořil, R. Miranda, P. Jelínek, and D. Écija. "On-surface synthesis of gold porphyrin derivatives via a cascade of chemical interactions: Planarization, self-metalation, and intermolecular coupling". In: *Chemistry of Materials* 31.9 (2019), pp. 3248–3256. ISSN: 15205002. DOI: 10.1021/acs.chemmater.9b00125.

[209] K. Diller, A. C. Papageorgiou, F. Klappenberger, F. Allegretti, J. V. Barth, and W. Auwärter. "In vacuo interfacial tetrapyrrole metallation". In: *Chemical Society Reviews* 45.6 (2016), pp. 1629–1656. ISSN: 0306-0012. DOI: 10.1039/C5CS00207A. URL: http://xlink.rsc.org/?DOI=C5CS00207A.

[210] L. Zhang, Y. Q. Zhang, Z. Chen, T. Lin, M. Paszkiewicz, R. Hellwig, T. Huang, M. Ruben, J. V. Barth, and F. Klappenberger. "On-surface activation of trimethylsilyl-terminated alkynes on coinage metal surfaces". In: *ChemPhysChem* 20.18 (2019), pp. 2382–2393. ISSN: 14397641. DOI: 10.1002/cphc.201900249.

[211] S. Fatayer, F. Albrecht, Y. Zhang, D. Urbonas, D. Peña, N. Moll, and L. Gross. "Molecular structure elucidation with charge-state control". In: *Science* 365.6449 (2019), pp. 142–145. ISSN: 10959203. URL: https://www.science.org/doi/abs/10.1126/science.aax5895%20https://www.science.org.

[212] F. Albrecht, F. Bischoff, W. Auwärter, J. V. Barth, and J. Repp. "Direct identification and determination of conformational response in adsorbed individual nonplanar molecular species using noncontact atomic force microscopy". In: *Nano Letters* 16.12 (2016), pp. 7703–7709.

[213] M. Schwarz, A. Riss, M. Garnica, J. Ducke, P. S. Deimel, D. A. Duncan, P. K. Thakur, T.-L. Lee, A. P. Seitsonen, J. V. Barth, et al. "Corrugation in the weakly interacting hexagonal-BN/Cu (111) system: structure determination by combining noncontact atomic force microscopy and X-ray standing waves". In: *ACS nano* 11.9 (2017), pp. 9151–9161.

[214] A. Riss, M. Richter, A. P. Paz, X. Y. Wang, R. Raju, Y. He, J. Ducke, E. Corral, M. Wuttke, K. Seufert, M. Garnica, A. Rubio, J. V. Barth, A. Narita, K. Müllen, R. Berger, X. Feng, C. A. Palma, and W. Auwärter. "Polycyclic aromatic chains on metals and insulating layers by repetitive [3+2] cycloadditions". In: *Nature Communications* 11.1 (2020), pp. 1–8. ISSN: 2041-1723. DOI: 10.1038/s41467-020-15210-2. URL: https://www.nature.com/articles/s41467-020-15210-2.

[215] W. Auwärter, K. Seufert, F. Bischoff, D. Ecija, S. Vijayaraghavan, S. Joshi, F. Klappenberger, N. Samudrala, and J. V. Barth. "A surface-anchored molecular four-level conductance switch based on single proton transfer". In: *Nature Nanotechnology* 7.1 (2012), pp. 41–46. ISSN: 17483395. DOI: 10.1038/nnano.2011.211.

[216] V. D. Pham, V. Repain, C. Chacon, A. Bellec, Y. Girard, S. Rousset, A. Smogunov, Y. J. Dappe, and J. Lagoute. "Control of molecule–metal interaction by hydrogen manipulation in an organic molecule". In: *The journal of physical chemistry letters* 7.8 (2016), pp. 1416–1421.

[217] A. Sperl, J. Kröger, and R. Berndt. "Controlled metalation of a single adsorbed phthalocyanine". In: *Angewandte Chemie International Edition* 50.23 (2011), pp. 5294–5297.

[218] T. Kumagai, F. Hanke, S. Gawinkowski, J. Sharp, K. Kotsis, J. Waluk, M. Persson, and L. Grill. "Thermally and vibrationally induced tautomerization of single porphycene molecules on a Cu (110) surface". In: *Physical Review Letters* 111.24 (2013), p. 246101.

[219] J. Braun, M. Koecher, M. Schlabach, B. Wehrle, H.-H. Limbach, and E. Vogel. "NMR study of the tautomerism of porphyrin including the kinetic HH/HD/DD isotope effects in the liquid and the solid state". In: *Journal of the American Chemical Society* 116.15 (1994), pp. 6593–6604.

[220] L. Lauhon and W. Ho. "Single-molecule chemistry and vibrational spectroscopy: pyridine and benzene on Cu (001)". In: *The Journal of Physical Chemistry A* 104.11 (2000), pp. 2463–2467.

[221] T. Komeda, Y. Kim, Y. Fujita, Y. Sainoo, and M. Kawai. "Local chemical reaction of benzene on Cu (110) via STM-induced excitation". In: *The Journal of chemical physics* 120.11 (2004), pp. 5347–5352.

[222] H. Lesnard, M.-L. Bocquet, and N. Lorente. "Dehydrogenation of aromatic molecules under a scanning tunneling microscope: pathways and inelastic spectroscopy simulations". In: *Journal of the American Chemical Society* 129.14 (2007), pp. 4298–4305.

[223] M. Schlabach, H. Rumpel, and H.-H. .-. Limbach. "Investigation of the tautomerism of 15N-labeled hydroporphyrins by dynamic NMR spectroscopy". In: *Angewandte Chem. International Edition* 28.1 (1989), pp. 76–79. ISSN: 15213773. DOI: 10.1002/anie.198900761.

[224] F. Bischoff, K. Seufert, W. Auwärter, S. Joshi, S. Vijayaraghavan, D. Écija, K. Diller, A. C. Papageorgiou, S. Fischer, F. Allegretti, D. A. Duncan, F. Klappenberger, F. Blobner, R. Han, and J. V. Barth. "How surface bonding and repulsive interactions cause phase transformations: Ordering of a prototype macrocyclic compound on Ag(111)". In: *ACS Nano* 7.4 (2013), pp. 3139–3149. ISSN: 19360851. DOI: 10.1021/nn305487c.

[225] M. Schlabach, B. Wehrle, H. Rumpel, J. Braun, G. Scherer, and H.-H. Limbach. "NMR and NIR studies of the tautomerism of 5,10,15,20-tetraphenylporphyrin including kinetic HH/HD/DD isotope and solid state effects". In: *Ber. Bunsenges. phys. Chem.* 96.6 (1992), pp. 821–833. ISSN: 0005-9021. DOI: 10.1002/bbpc.19920960616.

[226] C. Storm and Y. Teklu. "Nitrogen-hydrogen tautomerism in porphyrines and chlorines". In: *Journal of the American Chemical Society* 94.5 (1972), pp. 1745–1747.

[227] R. M. Claramunt, J. Elguero, and A. R. Katritzky. "Tautomerism involving other than five-and six-membered rings". In: (2000).

[228] C. Brückner. "The Breaking and mending of meso-tetraarylporphyrins: Transmuting the pyrrolic building blocks". In: *Accounts of Chemical Research* 49.6 (2016), pp. 1080–1092. DOI: 10.1021/acs.accounts.6b00043.

[229] M. O. Senge, N. N. Sergeeva, and K. J. Hale. "Classic highlights in porphyrin and porphyrinoid total synthesis and biosynthesis". In: *Chemical Society Reviews* 50.7 (2021), pp. 4730–4789. ISSN: 14604744. DOI: 10.1039/c7cs00719a.

[230] P. R. Bell. "The theory of reactions involving proton transfers". In: *Proceedings of the Royal Society of London. Series A - Mathematical and Physical Sciences* 154.882 (1936), pp. 414–429. ISSN: 0080-4630. DOI: 10.1098/rspa.1936.0060.

[231] M. G. Evans and M. Polanyi. "Further considerations on the thermo-dynamics of chemical equilibria and reaction rates". In: *Transactions of the Faraday Society* 32 (1936), pp. 1333–1360. ISSN: 9363201333.

[232] T. M. Krygowski and M. K. Cyrański. "Structural aspects of aromaticity". In: *Chemical Reviews* 101.5 (2001), pp. 1385–1420.

[233] M. Garcia-Borràs, S. Osuna, J. M. Luis, M. Swart, and M. Solà. "The role of aromaticity in determining the molecular structure and reactivity of (endohedral metallo) fullerenes". In: *Chemical Society Reviews* 43.14 (2014), pp. 5089–5105. ISSN: 14604744. DOI: 10.1039/c4cs00040d.

[234] D. Yu, T. Stuyver, C. Rong, M. Alonso, T. Lu, F. De Proft, P. Geerlings, and S. Liu. "Global and local aromaticity of acenes from the information-theoretic approach in density functional reactivity theory". In: *Physical Chemistry Chemical Physics* 21.33 (2019), pp. 18195–18210. ISSN: 14639076. DOI: 10.1039/c9cp01623f.

[235] C. P. Frizzo and M. A. P. Martins. "Aromaticity in heterocycles: New HOMA index parametrization". In: *Structural Chemistry* 23.2 (2011), pp. 375–380. ISSN: 1572-9001. DOI: 10.1007/S11224-011-9883-Z. URL: https://link.springer.com/article/10.1007/s11224-011-9883-z.

[236] L. Gross, F. Mohn, N. Moll, B. Schuler, A. Criado, E. Guitián, D. Peña, A. Gourdon, and G. Meyer. "Bond-order discrimination by atomic force microscopy". In: *Science* 337.6100 (2012), pp. 1326–1329. DOI: 10.1126/SCIENCE.1225621. URL: https://www.science.org/doi/abs/10.1126/science.1225621.

[237] P. Hapala, R. Temirov, F. S. Tautz, and P. Jelínek. "Origin of high-resolution IETS-STM images of organic molecules with functionalized tips". In: *Physical Review Letters* 113.22 (2014), p. 226101. DOI: 10.1103/PhysRevLett.113.226101. URL: https://journals.aps.org/prl/abstract/10.1103/PhysRevLett.113.226101.

[238] M. K. Cyrański, T. M. Krygowski, M. Wisiorowski, N. J. van Eikema Hommes, and P. v. R. Schleyer. "Global and local aromaticity in porphyrins: An analysis based on molecular geometries and nucleus-independent chemical shifts". In: *Angewandte Chemie International Edition* 37.1-2 (1998), pp. 177–180.

[239] M. Islyaikin, V. Ferro, and J. G. de la Vega. "Aromaticity in tautomers of triazoleporphyrazine". In: *Journal of the Chemical Society, Perkin Transactions 2* 12 (2002), pp. 2104–2109.

[240] J. I. Aihara, E. Kimura, and T. M. Krygowski. "Aromatic conjugation pathways in porphyrins". In: *Bulletin of the Chemical Society of Japan* 81.7 (2008), pp. 826–835. ISSN: 00092673. DOI: 10.1246/bcsj.81.826.

[241] F. Bischoff, A. Riss, G. S. Michelitsch, J. Ducke, J. V. Barth, K. Reuter, and W. Auwärter. "Surface-mediated ring-opening and porphyrin deconstruction via conformational distortion". In: *Journal of the American Chemical Society* 143.37 (2021), pp. 15131–15138.

[242] J. Lu, B. Da, W. Xiong, R. Du, Z. Hao, Z. Ruan, Y. Zhang, S. Sun, L. Gao, and J. Cai. "Identification and electronic characterization of four cyclodehydrogenation products of H2TPP molecules on Au(111)". In: *Physical Chemistry Chemical Physics* 23.20 (2021), pp. 11784–11788. ISSN: 14639076. DOI: 10.1039/d1cp01040a.

[243] A. Wiengarten, J. A. Lloyd, K. Seufert, J. Reichert, W. Auwärter, R. Han, D. A. Duncan, F. Allegretti, S. Fischer, S. C. Oh, Ö. Salam, L. Jiang, S. Vijayaraghavan, D. Écija, A. C. Papageorgiou, and J. V. Barth. "Surface-Assisted Cyclodehydrogenation; Break the Symmetry, Enhance the Selectivity". In: *Chemistry - A European Journal* 21.35 (2015), pp. 12285–12290. ISSN: 15213765. DOI: 10.1002/chem.201502001.

[244] M. O. Senge, N. N. Sergeeva, and K. J. Hale. "Classic highlights in porphyrin and porphyrinoid total synthesis and biosynthesis". In: *Chemical Society Reviews* 50.7 (2021), pp. 4730–4789. ISSN: 14604744. DOI: 10.1039/c7cs00719a.

[245] A. R. Battersby. "Tetrapyrroles: The pigments of life". In: *Natural Product Reports* 17.6 (2000), pp. 507–526. ISSN: 02650568. DOI: 10.1039/b002635m.

[246] L. M. Mateo, Q. Sun, S. X. Liu, J. J. Bergkamp, K. Eimre, C. A. Pignedoli, P. Ruffieux, S. Decurtins, G. Bottari, R. Fasel, and T. Torres. "On-Surface Synthesis and Characterization of Triply Fused Porphyrin–Graphene Nanoribbon Hybrids". In: *Angewandte Chemie - International Edition* 59.3 (2020), pp. 1334–1339. ISSN: 15213773. DOI: 10.1002/anie.201913024.

[247] L. M. Mateo, Q. Sun, K. Eimre, C. A. Pignedoli, T. Torres, R. Fasel, and G. Bottari. "On-surface synthesis of singly and doubly porphyrin-capped graphene nanoribbon segments". In: *Chemical Science* 12.1 (2021), pp. 247–252. ISSN: 20416539. DOI: 10.1039/d0sc04316h.

[248] Z. Feng, S. Velari, C. Dri, A. Goldoni, M. Peressi, and G. Comelli. "Binary Conformational Switches in a Porphyrin Chain: Tautomerization and Stereoisomerization". In: *Journal of Physical Chemistry C* 124.21 (2020), pp. 11376–11382. ISSN: 19327455. DOI: 10.1021/acs.jpcc.0c00471.

[249] D. Heim, D. Écija, K. Seufert, W. Auwärter, C. Aurisicchio, C. Fabbro, D. Bonifazi, and J. V. Barth. "Self-assembly of flexible one-dimensional coordination polymers on metal surfaces". In: *Journal of the American Chemical Society* 132.19 (2010), pp. 6783–6790. ISSN: 00027863. DOI: 10.1021/ja1010527.

[250] F. Bischoff, Y. He, A. Riss, K. Seufert, W. Auwärter, and J. V. Barth. "Exploration of Interfacial Porphine Coupling Schemes and Hybrid Systems by Bond-Resolved Scanning Probe Microscopy". In: *Angewandte Chemie - International Edition* 57.49 (2018), pp. 16030–16035. ISSN: 15213773. DOI: 10.1002/anie.201808640.

[251] F. Xiang, Y. Lu, Z. Wang, H. Ju, G. Di Filippo, C. Li, X. Liu, X. Leng, J. Zhu, L. Wang, and M. A. Schneider. "On-Surface Synthesis of Chiral π-Conjugate Porphyrin Tapes by Substrate-Regulated Dehydrogenative Coupling". In: *Journal of Physical Chemistry C* 123.37 (2019), pp. 23007–23013. ISSN: 19327455. DOI: 10.1021/acs.jpcc.9b06025.

[252] T. Joshi, C. Chen, H. Li, C. S. Diercks, G. Wang, P. J. Waller, H. Li, J. L. Bredas, O. M. Yaghi, and M. F. Crommie. "Local Electronic Structure of Molecular Heterojunctions in a Single-Layer 2D Covalent Organic Framework". In: *Advanced Materials* 31.3 (2019), pp. 6–11. ISSN: 15214095. DOI: 10.1002/adma.201805941.

[253] F. Bischoff, Y. He, K. Seufert, D. Stassen, D. Bonifazi, J. V. Barth, and W. Auwärter. "Tailoring Large Pores of Porphyrin Networks on Ag(111) by Metal–Organic Coordination". In: *Chemistry - A European Journal* 22.43 (2016), pp. 15298–15306. ISSN: 15213765. DOI: 10.1002/chem.201602154.

[254] Y. Li, J. Xiao, T. E. Shubina, M. Chen, Z. Shi, M. Schmid, H. P. Steinrück, J. M. Gottfried, and N. Lin. "Coordination and metalation bifunctionality of Cu with 5,10,15,20-tetra(4-pyridyl)porphyrin: Toward a mixed-valence two-dimensional coordination network". In: *Journal of the American Chemical Society* 134.14 (2012), pp. 6401–6408. ISSN: 00027863. DOI: 10.1021/ja300593w.

[255] D. P. Goronzy, M. Ebrahimi, F. Rosei, Arramel, Y. Fang, S. De Feyter, S. L. Tait, C. Wang, P. H. Beton, A. T. Wee, P. S. Weiss, and D. F. Perepichka. "Supramolecular assemblies on surfaces: Nanopatterning, functionality, and reactivity". In: *ACS Nano* 12.8 (2018), pp. 7445–7481. ISSN: 1936086X. DOI: 10.1021/acsnano.8b03513.

[256] M. In't Veld, P. Iavicoli, S. Haq, D. B. Amabilino, and R. Raval. "Unique intermolecular reaction of simple porphyrins at a metal surface gives covalent nanostructures". In: *Chemical Communications* 13 (2008), pp. 1536–1538. ISSN: 13597345. DOI: 10.1039/b718865j.

[257] A. Floris, S. Haq, M. In't Veld, D. B. Amabilino, R. Raval, and L. Kantorovich. "Driving Forces for Covalent Assembly of Porphyrins by Selective C-H Bond Activation and Intermolecular Coupling on a Copper Surface". In: *Journal of the American Chemical Society* 138.18 (2016), pp. 5837–5847. ISSN: 15205126. DOI: 10.1021/jacs.5b11594.

[258] M. Di Giovannantonio, M. Tomellini, J. Lipton-Duffin, G. Galeotti, M. Ebrahimi, A. Cossaro, A. Verdini, N. Kharche, V. Meunier, G. Vasseur, Y. Fagot-Revurat, D. F. Perepichka, F. Rosei, and G. Contini. "Mechanistic Picture and Kinetic Analysis of Surface-Confined Ullmann Polymerization". In: *Journal of the American Chemical Society* 138.51 (2016), pp. 16696–16702. ISSN: 15205126. DOI: 10.1021/jacs.6b09728.

[259] G. Galeotti, M. Di Giovannantonio, J. Lipton-Duffin, M. Ebrahimi, S. Tebi, A. Verdini, L. Floreano, Y. Fagot-Revurat, D. F. Perepichka, F. Rosei, and G. Contini. "The role of halogens in on-surface Ullmann polymerization". In: *Faraday Discussions* 204 (2017), pp. 453–469. ISSN: 13645498. DOI: 10.1039/c7fd00099e.

[260] G. Galeotti, F. De Marchi, E. Hamzehpoor, O. MacLean, M. Rajeswara Rao, Y. Chen, L. V. Besteiro, D. Dettmann, L. Ferrari, F. Frezza, P. M. Sheverdyaeva, R. Liu, A. K. Kundu, P. Moras, M. Ebrahimi, M. C. Gallagher, F. Rosei, D. F. Perepichka, and G. Contini. "Synthesis of mesoscale ordered two-dimensional π-conjugated polymers with semiconducting properties". In: *Nature Materials* 19.8 (2020), pp. 874–880. ISSN: 14764660. DOI: 10.1038/s41563-020-0682-z. URL: http://dx.doi.org/10.1038/s41563-020-0682-z.

[261] B. de la Torre, A. Matěj, A. Sánchez-Grande, B. Cirera, B. Mallada, E. Rodríguez-Sánchez, J. Santos, J. I. Mendieta-Moreno, S. Edalatmanesh, K. Lauwaet, M. Otyepka, M. Medveď, Á. Buendía, R. Miranda, N. Martín, P. Jelínek, and D. Écija. "Tailoring π-

conjugation and vibrational modes to steer on-surface synthesis of pentalene-bridged ladder polymers". In: *Nature Communications* 11.1 (2020), pp. 1–8. ISSN: 20411723. DOI: 10.1038/s41467-020-18371-2. arXiv: 2004.04918.

[262] J. E. McMurry and M. P. Fleming. "New method for the reductive coupling of carbonyls to olefins. Synthesis of. beta.-carotene". In: *Journal of the American Chemical Society* 96.14 (1974), pp. 4708–4709.

[263] J. E. Mcmurry. "Carbonyl-Coupling Reactions Using Low-Valent Titanium". In: *Chemical Reviews* 89.7 (1989), pp. 1513–1524. ISSN: 15206890. DOI: 10.1021/cr00097a007.

[264] M. O. Senge, K. R. Gerzevske, M. G. H. Vicente, T. P. Forsyth, and K. M. Smith. "Models for the Photosynthetic Reaction Center—Synthesis and Structure of Porphyrin Dimers with cis-and trans-Ethene and Skewed Hydroxymethylene Bridges". In: *Angewandte Chemie International Edition in English* 32.5 (1993), pp. 750–753.

[265] R. Paolesse, R. K. Pandey, T. P. Forsyth, L. Jaquinod, K. R. Gerzevske, D. J. Nurco, M. O. Senge, S. Licoccia, T. Boschi, and K. M. Smith. "Stepwise syntheses of bisporphyrins, bischlorins, and biscorroles, and of porphyrin-chlorin and porphyrin-corrole heterodimers". In: *Journal of the American Chemical Society* 118.16 (1996), pp. 3869–3882. ISSN: 00027863. DOI: 10.1021/ja9541138.

[266] M. O. Senge, W. W. Kalisch, and K. Ruhlandt-Senge. "Synthesis and crystal structures of cofacial bischlorin. Octaethylchlorin-based structural models for the special pair in photosynthesis". In: *Chemical Communications* 18 (1996), pp. 2149–2150. ISSN: 13597345. DOI: 10.1039/cc9960002149.

[267] M. Shen and F. Zaera. "Coupling reactions in aldehydes adsorbed on V(100) single-crystal surfaces". In: *Journal of the American Chemical Society* 131.24 (2009), pp. 8708–8713. ISSN: 00027863. DOI: 10.1021/ja9023379.

[268] L. Benz, J. Haubrich, R. G. Quiller, S. C. Jensen, and C. M. Friend. "McMurry chemistry on TiO_2(110): Reductive C=C coupling of benzaldehyde driven by titanium interstitials". In: *Journal of the American Chemical Society* 131.41 (2009), pp. 15026–15031. ISSN: 00027863. DOI: 10.1021/ja905522c.

[269] M. Ebrahimi and K. T. Leung. "Selective surface chemistry of allyl alcohol and allyl aldehyde on Si(100)2×1: Competition of [2 + 2] C=C cycloaddition with O-H dissociation and with [2 + 2] C=O cycloaddition in bifunctional molecules". In: *Surface Science* 603.9 (2009), pp. 1203–1211. ISSN: 00396028. DOI: 10.1016/j.susc.2009.03.005. URL: http://dx.doi.org/10.1016/j.susc.2009.03.005.

[270] L. Cai, X. Yu, M. Liu, Q. Sun, M. Bao, Z. Zha, J. Pan, H. Ma, H. Ju, S. Hu, L. Xu, J. Zou, C. Yuan, T. Jacob, J. Björk, J. Zhu, X. Qiu, and W. Xu. "Direct formation of C-C double-bonded structural motifs by on-surface dehalogenative homocoupling of gem-dibromomethyl molecules". In: *ACS Nano* 12.8 (2018), pp. 7959–7966. ISSN: 1936086X. DOI: 10.1021/acsnano.8b02459.

[271] A. C. Papageorgiou, K. Diller, S. Fischer, F. Allegretti, F. Klappenberger, S. C. Oh, Ö. Sağlam, J. Reichert, A. Wiengarten, K. Seufert, et al. "In Vacuo Porphyrin Metalation on Ag (111) via Chemical Vapor Deposition of Ru3 (CO) 12: Mechanistic Insights". In: *The Journal of Physical Chemistry C* 120.16 (2016), pp. 8751–8758.

[272] M. Röckert, M. Franke, Q. Tariq, S. Ditze, M. Stark, P. Uffinger, D. Wechsler, U. Singh, J. Xiao, H. Marbach, H. P. Steinrück, and O. Lytken. "Coverage- and temperature-dependent metalation and dehydrogenation of tetraphenylporphyrin on Cu(111)". In: *Chemistry - A European Journal* 20.29 (2014), pp. 8948–8953. ISSN: 15213765. DOI: 10.1002/chem.201402420.

[273] D. Wechsler, M. Franke, Q. Tariq, L. Zhang, T. L. Lee, P. K. Thakur, N. Tsud, S. Bercha, K. C. Prince, H. P. Steinrück, and O. Lytken. "Adsorption Structure of Cobalt Tetraphenylporphyrin on Ag(100)". In: *Journal of Physical Chemistry C* 121.10 (2017), pp. 5667–5674. ISSN: 19327455. DOI: 10.1021/acs.jpcc.7b00518.

[274] G. Di Santo, S. Blankenburg, C. Castellarin-Cudia, M. Fanetti, P. Borghetti, L. Sangaletti, L. Floreano, A. Verdini, E. Magnano, F. Bondino, C. A. Pignedoli, M. T. Nguyen, R. Gaspari, D. Passerone, and A. Goldoni. "Supramolecular engineering through temperature-induced chemical modification of 2h-tetraphenylporphyrin on Ag(111): Flat phenyl conformation and possible dehydrogenation reactions". In: *Chemistry - A European Journal* 17.51 (2011), pp. 14354–14359. ISSN: 09476539. DOI: 10.1002/chem.201102268.

[275] A. C. Papageorgiou, S. Fischer, S. C. Oh, Ö. Sağlam, J. Reichert, A. Wiengarten, K. Seufert, S. Vijayaraghavan, D. Écija, W. Auwärter, F. Allegretti, R. G. Acres, K. C. Prince, K. Diller, F. Klappenberger, and J. V. Barth. "Self-terminating protocol for an interfacial complexation reaction in vacuo by metal-organic chemical vapor deposition". In: *ACS Nano* 7.5 (2013), pp. 4520–4526. ISSN: 19360851. DOI: 10.1021/nn401171z.

[276] C. Ruggieri, S. Rangan, R. A. Bartynski, and E. Galoppini. "Zinc(II) Tetraphenylporphyrin on Ag(100) and Ag(111): Multilayer Desorption and Dehydrogenation". In: *Journal of Physical Chemistry C* 120.14 (2016), pp. 7575–7585. ISSN: 19327455. DOI: 10.1021/acs.jpcc.6b00159.

[277] S. Fox and R. W. Boyle. "First examples of intramolecular Pd(0) catalysed couplings on ortho-iodinated meso-phenyl porphyrins". In: *Chemical Communications* 4.11 (2004), pp. 1322–1323. ISSN: 1364548X. DOI: 10.1039/b403466J.

[278] F. Bischoff, Y. He, A. Riss, K. Seufert, W. Auwärter, and J. V. Barth. "Exploration of Interfacial Porphine Coupling Schemes and Hybrid Systems by Bond-Resolved Scanning Probe Microscopy". In: *Angewandte Chemie International Edition* 57.49 (2018), pp. 16030–16035. DOI: https://doi.org/10.1002/anie.201808640.

[279] M. Schwarz, D. A. Duncan, M. Garnica, J. Ducke, P. S. Deimel, P. K. Thakur, T. L. Lee, F. Allegretti, and W. Auwärter. "Quantitative determination of a model organic/insulator/metal interface structure". In: *Nanoscale* 10.46 (2018), pp. 21971–21977. ISSN: 20403372. DOI: 10.1039/c8nr06387g.

[280] M. Di Giovannantonio, M. El Garah, J. Lipton-Duffin, V. Meunier, L. Cardenas, Y. Fagot Revurat, A. Cossaro, A. Verdini, D. F. Perepichka, F. Rosei, et al. "Insight into organometallic intermediate and its evolution to covalent bonding in surface-confined Ullmann polymerization". In: *ACS nano* 7.9 (2013), pp. 8190–8198.

[281] R. N. Mozhchil, A. M. Ionov, S. I. Bozhko, V. S. Bozhko, V. D. Rumyantseva, A. L. Trigub, and A. P. Menushenkov. "Electronic, local atomic structure of lutetium tetraphenyl-porfyrin: XPS and XAFS spectroscopy stadies". In: *Journal of Physics: Conference Series* 1238.1 (2019). ISSN: 17426596. DOI: 10.1088/1742-6596/1238/1/012002.

[282] K. Diller, F. Klappenberger, F. Allegretti, A. C. Papageorgiou, S. Fischer, D. A. Duncan, R. J. Maurer, J. A. Lloyd, S. C. Oh, K. Reuter, and J. V. Barth. "Temperature-dependent templated growth of porphine thin films on the (111) facets of copper and silver". In: *Journal of Chemical Physics* 141.14 (2014), p. 144703. ISSN: 10897690. DOI: 10.1063/1.4896605. URL: http://dx.doi.org/10.1063/1.4896605.

C. Acknowledgements

Despite there being only one author's name at the beginning, many have contributed directly or indirectly to this work. Here, I would like to thank everyone who contributed to this thesis.

First of all, I would like to thank my supervisor Prof. Dr. Johannes V. Barth, for offering me the opportunity to work in his group and for guiding me throughout this thesis. I especially appreciated his encouragement and continuous support. I thank Dr. Maryam Ebrahimi for her initial guidance in my first work in the lab and for guiding me through XPS techniques.

Especially, I want to thank Dr. Alex Riss who supervised me in the AFM lab, and gave invaluable guidance and meaningful discussion on the projects. I want to thank Eduardo Corral-Rascon for his continuous support during my slots in the AFM lab. I would also like to thank the other LT-AFM/STM members, Dr. Yang Bao and Dr. Ignacio Piquero-Zulaica for their many helpful discussions and assistance in the lab.

Since the projects were performed with several instruments, I would like to thank Prof. Dr. Willi Auwärter for allowing me to work in the LT-STM lab. I especially thank Dr. Knud Seufert, Dr. Aleksandr Baklanov, and Dr. Martin Schwarz for helping me get started in the lab at the beginning of my Ph.D. In addition, when working in the JT-STM lab, Dr. Biao Yang helped me a lot with experiments. His great guidance and discussions make the project proceed very well.

I would also like to thank Karl Eberle for his assistance when I worked in the ESCA lab, and thank him and Reinhold Schneider for always solving the technical and electrical problems in the lab. I would also like to thank our secretary Viktoria Blaschek for her help during my time in E20 and all other E20 members for easygoing communication and pleasant memories of lunchtime in our kitchen.

Furthermore, I especially thank Prof. Dr. Jonas Björk, who supervised me in the theoretical calculations for the works related to this thesis and greatly helped in the discussion and the understanding of the results. I also want to thank him for supporting my time in Linköping and continuing supervision when I went back to Munich.

I have to thank these chemists who synthesized the employed chemicals. H_2TFPP molecule was done by Prof. Dr. Mathias Senge and Dr. Alina Meindl, and TMS-alkyne substituted porphyrin molecules were done by Prof.Dr. Mario Ruben and Dr. Zhi Chen.

Moreover, I would like to thank Wei Ran, Hongxiang Xu, Wenchao Zhao, Shengming Zhang and Zhongliu Liu, the relaxed atmosphere and Chinese food at our parties made me feel very warm; thanks for your company during my stay in Munich.

Finally, I am very grateful to my family and friends, who have always given me so much support and understanding, especially Biao, for helping me work out my problems in my work and daily life.